UNIVERSITÉ DU LUXEMBOURG

PhD-FSTM-2021-079
The Faculty of Science, Technology and Medicine

DISSERTATION

Defence held on 13/10/2021 in Esch-sur-Alzette

to obtain the degree of

DOCTEUR DE L'UNIVERSITÉ DU LUXEMBOURG

EN PHYSIQUE

by

Joao Ricardo ANTUNES AFONSO
Born on 22 May 1994 in Almada, Portugal

OZONE GAS SENSORS BASED ON OFF-STOICHIOMETRIC COPPER-CHROMIUM-OXIDE THIN FILMS

Dissertation defence committee

Dr Damien LENOBLE, dissertation supervisor
Luxembourg Institute of Science and Technology

Prof. Dr Jean-Pierre Raskin
Professor, Université Louvain la Neuve

Prof. Dr Susanne SIEBENTTRIT, Chairman
Professor, Université du Luxembourg

Dr Romain GWOZIECKI
CEA-LETI

Prof. Dr Luis Pereira,
Professor, FCT – NOVA University of Lisbon

Acknowledgements

It has been more than four years working at LIST and I feel fortunate for the opportunity given to me to develop my work and to pursue my PhD degree. This undertaking could not have been accomplished without the help and assistance of many people, for so, I'd like to start by thanking all the LIST and university of Luxembourg staff for the help provided as well as the WELCOME lab staff in Leuven la Neuve.

I would like to thank Dr. Damien Lenoble, for giving me this opportunity, for all the fruitful discussions and creative input. I learned a lot not only in scientific terms, but also how to face a difficulty and solve the problems and how to be an autonomous independent worker. This is an unvaluable skill that will stick with me.

Next, I would like to thank Prof. Dr. Susanne Siebentritt and Prof. Dr. Jean-Pierre Raskin for being part of my CET and for all the valuable input given. Thanks to your knowledge and your directions I feel I was able to really improve my work in the past years. I gratefully thank Prof. Dr. Susanne Siebentritt for organizing and directing all the MASSENA program that I am a part of and for all the assistance provided.

The WELCOME lab in Leuven-la-Neuve always welcomed me to run hundreds of experiments. For this, I welcome Prof. Dr. Jean-Pierre Raskin, for opening me the doors and for all the discussions and regular feedback during my visits. I thank furthermore, Pascal Simon, Thomas Walewyns and the WELCOME support staff, for helping me setting up the experimental setup and for the constant support to my questions and difficulties.

I would like to thank Prof. Dr. Luis Pereira, Dr. Romain Gwoziecki and Giuseppe Bruno, for reading and reviewing my thesis and being part of my jury committee.

I would like to thank Dr. Petru Lunca-Popa for his expertise in MOCVD and for the constant help. At times you were like my second supervisor.

I would like to acknowledge Noureddine Adjeroud for his expertise and for his help in ALD deposition. I would like to thank Dr. Jérôme Guillot for XPS analysis, Dr. Nathalie Valle and Brahime El Adib for SIMS analysis, Dr. Yves Fleming for XRD training and assistance, Dr. Mael Guennou for Raman measurement training and assistance, Patrick Grysan for helping me with many KPFM and AFM measurements, Dr. Didier Arl for training and assistance on FIB-SEM, Dr. Stéphanie Girod for training on photolithography as well as help running many dose tests and Dr. Renaud Leturcq for training on electrical characterizations. Also, I would like to thank Jeremy Raguin and Julien Jacob for their valuable support.

Furthermore, I would like to thank Dr. Mark Greiner and Gudrun Klihm, for helping me setting up and all the NAP XPS analysis, as well as all the post analysis assistance in the understanding of the data and valuable explanations.

I would like to thank all the PhD students past and previous in F1.14, for their help and suggestions, moral support, and casual conversations. Thank you to Raúl, Sabrina, Antoine, Shiv, Marco, Matteo, Tai, Rutuja, Nikhar, Rishabh, Nohora, Sunil, Serena, Divya, Julien and David, for the fun moments. Lastly, I would like to thank my family and friends for their support.

Table of Contents

Abbreviation List

AFM – Atomic force microscopy

ALD – Atomic layer deposition

CB – Conduction band

CMVB – Chemical modulation of the valence band

CVD – Chemical vapour deposition

ITO – Indium Tin Oxide

KPFM – Kevin Probe Force Microscopy

MLA – Mask-less aligner

MOCVD – Metal Organic Chemical Vapour Deposition

NAP-XPS – Near ambient pressure X-ray photoelectron spectroscopy

PLD – Pulsed laser deposition

SEM – Scanning Electron Microscopy

TEM – Transmission Electron Microscopy

TFT – Thin Film Transistor

TCM – Transparent Conductive Material

TCO – Transparent Conductive Oxide

UV- Ultraviolet

VB – Valence Band

VBM – Valence Band Maximum

XPS - X-ray photoelectron spectroscopy

XRD – X-ray diffraction

General Introduction

Ozone (O_3) is a highly reactive and unstable gas, that is found naturally in the stratosphere. In this upper atmospheric layer, ultraviolet (UV) light from the sun, splits O_2 molecules into two atomic oxygen. When this atomic oxygen collides with an oxygen molecule it forms ozone. Stratospheric ozone is important for human life because it protects the earth's surface from hazardous ultraviolet light (UV-B and UV-C). However tropospheric ozone is an air pollutant playing a role in climate change, air quality and ecosystem health. Due to the increase of anthropogenic emissions of O_3 precursors, a steady rise of ozone level has been observed around the world since the 1950s [1]. Ozone regulated levels are regularly surpassed in the summer months in Europe. Besides the environmental problems derived from the usage of ozone in several industries, indoor office pollution is a major health concern according to the world health organization (WHO). It has been shown that ozone can be produced by laser and ink-jet printers, as well as other office equipment [2]. When inhaled ozone travels to the lungs, causing muscles to constrict, trapping air in the alveoli leading to inflammation of the airways and adverse respiratory effects. Long term exposure can cause chronic diseases, such as asthma and chronic obstructive pulmonary disease [3–5]. Recent studies have shown that daily exposure to high ozone levels may cause DNA damage, as previously reported for operators in photocopier centres [6].

Ozone can be efficiently detected using UV absorbance and chemiluminescence sensors. However, these methods rely on a periodic sampling with large and expensive stationary analytical devices. The creation of portable, low cost, efficient ozone sensors opens novel possibilities in sensor networks for indoor/outdoor monitoring of air pollution with wireless communications for the rapidly expanding Internet of Things.

Sensor networks are based on a group of sensors with different properties that can monitor (in some cases control) the physical conditions of the environment. Several sensor nodes are wirelessly connected, passing their data through the network to the central location. This allows fast data monitoring, with possibilities of hundreds of thousands of data collecting locations. After being developed by the military, sensor networks have grown into many industrial and consumer applications. The recent years have marked the increase in demand for low-cost sensor networks (LCSNs) [7]. The key to LCSNs is being able to produce low-cost sensors that are still reliable, in the target range whilst having low power consumption. Sensor networks will play a major role in the true deployment of internet of things (IoT), a fast pace growing market with an expected compound annual growth of 11%, potentially reaching 24 billion devices in 2030 and generating 1.5 trillion-dollar annual revenue. Physical events and conditions, such as temperature, pressure, atmosphere quality and radiation are continually measured, the collected data is transmitted to a monitoring centre and action can be swiftly taken (increasing the ventilation and evacuating the area).

With the integration of low-cost sensors onto portable devices, air quality can be monitored, in schools and office environments, saving billions of people from future health problems due to ozone exposure [8].

Solid state conductometric gas sensors have been presented as the solution, since they are simple to operate, have low production costs (since the techniques are batch fabrication compatible) and can be easily integrated into the sensor networks [9–11]. Even if these sensors are not as accurate and present lower selectivity, their robustness and longevity makes them the perfect candidates to be incorporated in sensor networks as alarm for dangerous gas concentrations.

Several materials have been proposed as ozone metal oxide conductometric sensors, namely In_2O_3, ZnO, SnO_2 and WO_3, with good responses. However, these materials, in general require high working temperature (usually above 250°C) to be able to produce reversible measurements, what bumps directly into the requirements for low-cost sensor networks. Room temperature compatible ozone sensors have been proposed, making resource to a UV light to assist in the oxidation/reduction process. Whilst an interesting proposal it is not a solution since it merely substitutes one cost for another and it becomes less practical for miniaturization and integration into the sensor networks. Delafossite based ($CuMO_2$ where M = Al or Cr) ozone sensors have been proposed, working with reversible reactions at room temperature [12,13]. These sensors have shown interesting response characteristics even if the lowest ozone concentration used, 50 ppm is about 500 times higher than the common health requirements for air safety (100 ppb for 8 hour exposure), these first studies create a research avenue for the use of p-type semiconductors into ozone gas sensing.

Delafossite materials are a very promising kind of p-type transparent conductive oxide (TCO), with some of the highest reported conductivities and decent transparency in the visible range. It is rather cheap to manufacture and easily scalable, when produced by metal-organic chemical vapour deposition (MOCVD).

Objectives and Outline of this work

The aim of this work is to fabricate and investigate the ozone sensing properties of off-stoichiometric copper chromium oxide. The study, by our research group, of this novel and original material has produced some of the best properties for p-type TCOs, in recent years [14]. The deposition by metal organic chemical vapour deposition (MOCVD) and the capability to produce thin films make it an ideal candidate for miniaturization and integration into sensor networks. We propose a deep study of the interplay between the deposition conditions, the post-deposition annealing treatments and the thin-film physical properties.

Furthermore, different conductometric sensors will be produced and tested, under ozone atmospheres, in order to study the relationship between the thin film properties and the sensing response behaviour. During this work, we propose an advanced understanding of

the chemical interactions between ozone and off-stoichiometric Cu-Cr-O delafossite thin-films, including the kinetics of the ozone – delafossite reaction. The sensors dependence on the film carriers concentration will first be characterized. Next, a study of the sensor under different ozone concentrations and working temperatures will be performed.

Near ambient pressure x-ray photoelectron spectroscopy coupled with all the electronic studies, might allow us to have an important understanding of the kinetic reaction and the driver of the changes in conductivity upon ozone introduction.

1. State of the Art

1.1. Ozone

Ozone, or trioxygen (O_3) is an allotrope of oxygen that is much less stable than the diatomic (O_2) allotrope. Ozone is formed from dioxygen by the action of ultraviolet (UV) light and electrical discharges, that break down oxygen molecules. Atomic oxygen can then react with molecular oxygen, to form ozone (see equations 1-4). If atomic oxygen reacts with an ozone molecule or with another atomic oxygen, then it will form molecular oxygen. This is usually referred as the Chapman cycle [15].

Ozone is essential for human life in the stratosphere, where the commonly known ozone layer, acts as a shield absorbing most of the sun's harmful UV-B and UV-C radiation (figure 2). Ozone's concentration is maximum between 17 and 25 km from the earth's surface. The ground concentration of ozone should me minimal, however in the last century this situation started to change. Ozone had been widely adopted in industrial processes, making ozone an urban pollutant. Due to its powerful oxidizing characteristic, ozone found mainstream usage for sterilization and purification in a panoply of industries, such as: pharmaceutical, food, textiles, water treatment, agriculture and medicine [9,16–19]. In addition, ozone has a significant effect on organic matter decay, with proven antibacterial and virus inactivation activity [20]. Environmental ozone in the troposphere is mostly a secondary pollutant, generated by photochemical reactions due to volatile organic compounds (VOCs) or oxides of nitrogen (NOx). Harmful concentrations of ozone in the environment are regularly coupled with high concentration of other pollutants [1,5,21–24]. Automobile nitrogen oxides emissions can be catalysed, mostly in the summer, due to sun radiation, into ozone (figure 1) [9]. Ozone is a contributing greenhouse gas, due to its absorptions of infrared radiation at 9.6 µm [25].

Oxygen decomposition	$O_2 + hv \rightarrow 2\,O$	(1)
Ozone Formation	$O + O_2 \rightarrow 2\,O_3$	(2)
Ozone decomposition	$O_3 + O \rightarrow 2\,O_2$	(3)
Oxygen recombination	$O + O \rightarrow 2\,O_2$	(4)

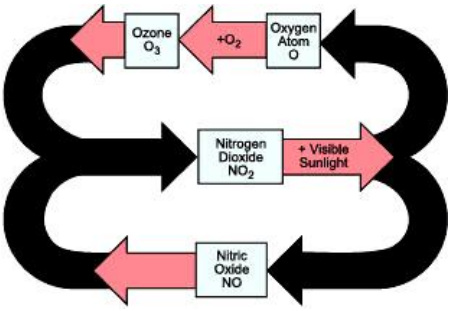

Figure 1 - Ozone production from NOx pollutants: Oxygen atoms freed from nitrogen dioxide by the action of sunlight attack oxygen molecules to produce ozone. Nitrogen oxide can combine with ozone to reform nitrogen dioxide, and the cycle repeats. From https://www.niehs.nih.gov/

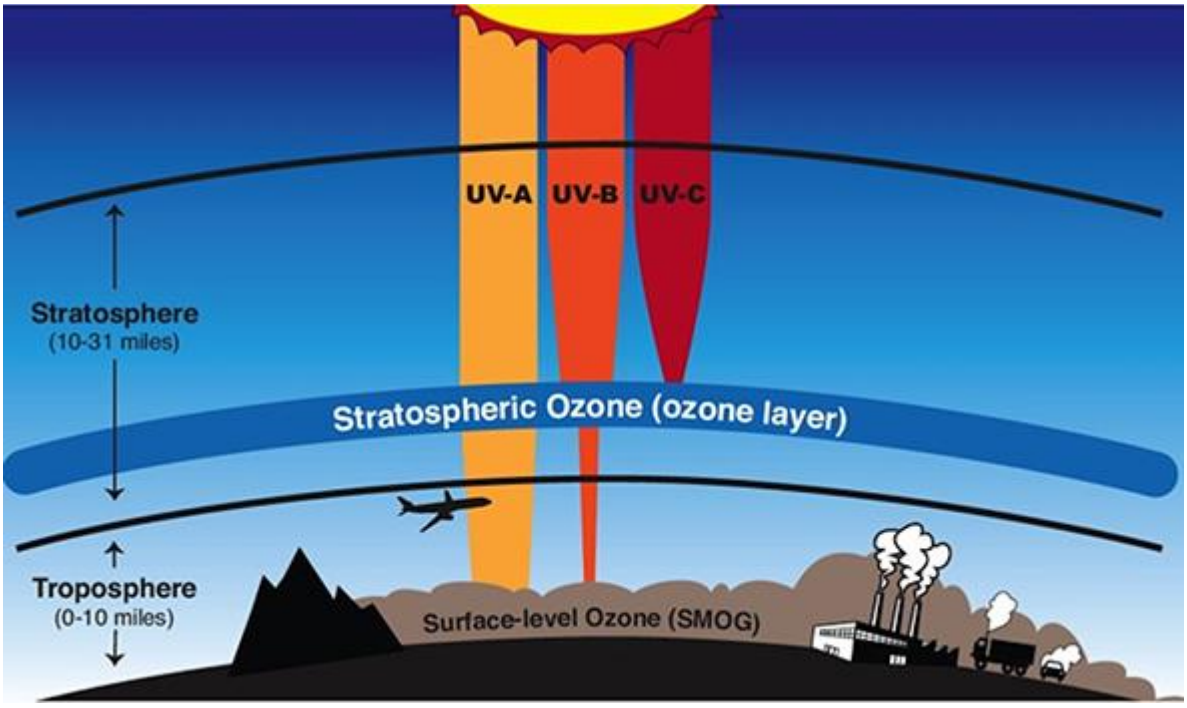

Figure 2 - The ozone layer in the stratosphere shields life on Earth from most UV-B and UV-C, the most harmful varieties of ultraviolet radiation. Surface-level ozone is however a pollutant. From https://scied.ucar.edu/learning-zone/atmosphere/ozone-layer

1.1.1. Ozone hazard

When ozone is inhaled it travels to the lungs. Its strong oxidizing properties make it very corrosive to the respiratory tract. Ozone can cause muscles to constrict, trapping air in the alveoli leading to inflammation of the airways and adverse respiratory effects, such as wheezing, shortness of breath, coughing, pain chest or sore throat. Exposure can aggravate lung diseases such as asthma, emphysema, and chronic bronchitis. Long-term exposure can be the cause for asthma and abnormal lung development in children as well as causing chronic obstructive pulmonary disease [3–5]. A summarized effect and ozone exposure consequence can be found in reference [26], a report by the World Health Organization (WHO).

Levy et al. [27], estimated a grand mean of 0.21% in mortality per 10 µg/m^3 increase of 1 hour maximum ozone, without controlling other air pollutants. Besides human health, ozone can also damage plants, trees, crops and vegetation [28,29]. Staehelin et al. [30], found an increase by a factor of 2, in ozone concentration, between the decades of the 1950s and the 1990s in Arosa (Switzerland).

The environmental protection agency (EPA), sets the limits of exposure at 70 ppb or 140 µg/cm^3 during 8 hours per day. A limit of 1 ppm for 15 minutes has been fixed as critical danger for human health. Due to an increase in anthropogenic emissions of O_3 precursors, a steady rise of O_3 levels has been seen, with legal limits set by the environmental agencies regularly surpassed every summer [1], as can be observed in the map in figure 3. Ozone formation is favoured by increased atmospheric temperatures. Based on this, it is expected that with the climate change and temperature rise, ozone can be an ever more present risk to human health [5].

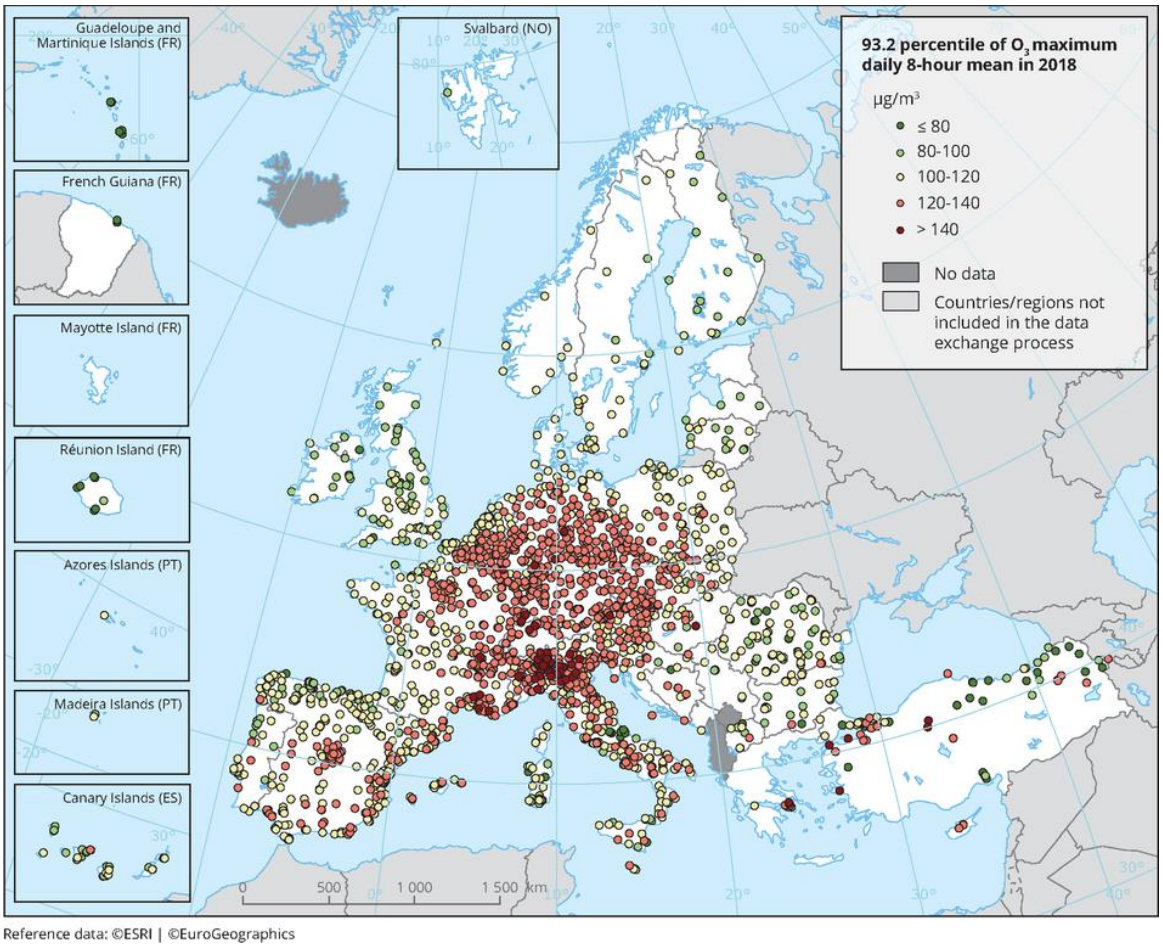

Figure 3- Observed concentrations of O_3 in 2018. The map shows the 93.2 percentile of the O_3 maximum daily 8-hour mean, representing the 26th highest value in a complete series. 41 % (895) of all stations reporting O_3, with the minimum data coverage of 75 %, showed concentrations above the target value for the protection of human health in 2018. Figure from [28].

1.1.2. Office environment ozone pollution

Indoor office pollution, where people spend a major portion of their days, is one of the most serious environmental risks to human health according to the World Health Organisation (WHO). Office equipment such as ink-jet and laser-jet printers or other laser-based equipment can produce ozone or volatile organic compounds (VOCs) that then may react with oxygen to form ozone [2]. Recent studies have shown that daily exposure to high levels of ozone may cause DNA damage, as previously reported for operators in photocopier centres [6]. It is therefore, of particular importance to monitor air quality and ozone levels in office environments and schools, where people spend a major part of their days. Several studies have found that air cleaning devices may increase indoor ozone concentrations to harmful levels [31].

A periodic sampling of air quality in office environment is key to act swiftly, thus requiring inexpensive, easy to integrate and miniaturizable, portable ozone sensors.

1.2. Ozone gas sensors

At present, several conventional analytical methods such as UV absorbance, optochemical (chemiluminescence, fluorescence), optical, electrochemical and mass spectrometry methods are available for the accurate detection of ozone concentration in air [9,19,39,20,32–38]. However, these methods rely on a periodic sampling with large and expensive stationary analytical devices. Besides the high cost, their implementation to control air quality distribution inside office environments is simply impractical. Solid-state conductometric gas sensors are attracting a great deal of research to be used for ozone monitoring, due to their low-cost and miniaturization possibilities. A comparison of the main types of ozone sensors and their advantages/disadvantages are shown in table 1.

Table 1 - Comparison of different available techniques for ozone detection; Refs. [9,19,20,37]

SENSING METHOD	ADVANTAGES	DISADVANTAGES
UV ABSORBANCE	High resolution; wide detection range; long lifetime; good selectivity; accuracy; quick response	Periodic air sampling; large and expensive stationary analytical devices; requires UV source; high energy consumption
OPTOCHEMICAL: CHEMILUMINESCENCE, FLUORESCENCE	High resolution; RT operation; wide detection range	Require light source; high cost; sensitive to temperature fluctuations; high energy consumption
ELECTROCHEMICAL	Low power consumption; RT operation; continuous monitoring; inexpensive	Less sensitive than optical technologies; cross-sensitivity to toxic gases and oxygen; short lifetime; periodic maintenance (every 2 months); limited operating conditions
MASS SPECTROSCOPY	High sensitivity; high selectivity	Complex; high costs; limited to laboratory usage
SOLID-STATE CONDUCTOMETRIC GAS SENSORS	High sensitivity to ozone; low-cost; miniaturizable; wide operating temperature range; long lifetime	Low selectivity; drift of operating characteristics; high power consumption (operating temperatures usually above 250°C)

1.3. Solid-state conductometric gas sensors

The main advantage of solid-state conductometric gas sensors is their ease of fabrication, using thin films, resulting in low production costs, as manufacturing techniques are easily scalable. These sensors are small and usually easy to miniaturize, being the ideal candidate for portable devices. Their fabrication technology is also easy to integrate into sensor networks processing [7,8]. They lack of selectivity and, in many cases, have presented a

baseline drift, however they can be used as an alarm for air pollution monitoring in low-cost wireless sensor networks [10,11,19].

Polycrystalline metal-oxide materials are the reference materials used in solid state gas sensors, due to a combination of benefiting factors: high surface area, small crystallite size, cheap design technology and stability of structural and physical-chemical properties. Amorphous materials are generally not stable enough for gas sensing, mainly at high temperature. Single crystalline or epitaxial materials face technological and cost limitations [40].

Several materials have been proposed as ozone metal oxide conductometric sensors, with In_2O_3 [9,41–47], ZnO [48–53] and WO_3 [21,32,54–60] driving most of the attention. Yet these sensors have an important drawback, the high working temperature required (usually above 250°C). Furthermore, the resistor responsible for the heating of the sensor may drift over time, with a reduction of the power output, leading to a decrease of the measuring temperature, causing an effect in the sensitivity as the sensor ages [16]. Room temperature ozone sensors have been proposed, making resource to a UV light to assist the oxidation/reduction process at the sensor's surface [42,48,50,58,61–63]. This introduction of a UV source increases the sensor cost and is not favourable to miniaturization and integration of the sensors into sensor networks. Besides, this solution may present selectivity problems towards molecular oxygen as the photoreduction promotes the dissociation of all oxidizing species present at the sensor's surface [64]. Long-term stability is also scarcely discussed for this kind of sensors. Table 2 gives an overview of some of the most commonly used materials for conductometric ozone sensors based on metal oxides. Delafossite based ($CuMO_2$ where M = Al or Cr) based ozone sensors have been proposed, with reversible reactions at room temperature [12,13]. These sensors have shown interesting response characteristics even if the ozone concentration used, 50 ppm is about 500 times higher than the common health requirements for air safety, these studies called for further studies related to the use of p-type semiconductors into ozone gas sensing.

Table 2 - Overview of some of the most commonly used materials for conductometric ozone sensors based on metal oxides

Material	Sensing Layer	Sensitivity	Detection range	Working temperature	Reference
ZnO	Nanorods	~ 9 at 1.2 ppm	0.1 – 1.2 ppm	250°C	[53]
In_2O_3	Thin film	$10^3 - 10^4$ at 1 ppm and 300°C	20 ppb - 1 ppm	200 – 300°C	[9,65]
	Thin film	~ 10	20 – 85 ppb	200°C	[66]

WO_3	Thin film	~ 6 at 68 ppb and 500°C	13 – 68 ppb	500 - 530°C	[32]
	Thin film	$\sim 10^2$ at 800 ppb and 150°C	30 - 800 ppb	150 – 400°C	[59]
SnO_2	Thin film	$10^3 - 10^4$	1 ppm	200 – 300°C	[9,65]
$NiCO_2O_4$	Nanostructures	12 at 560 ppb	30 – 560 ppb	200°C	[67]
CuO	Thin film	~ 2 at 300 ppb	50 – 300 ppb	250°C	[68]
$CuAlO_2$ + CuO + $CuAl_2O_4$	Thin film	$\sim 10^2$ at 350 ppb and 300°C	70 – 350 ppb	300 – 500°C	[69]
$CuCrO_2$	Nanocrystals	~ 2 at 200 ppm	50 – 200 ppm	RT	[12]

1.4. Metal oxide sensors: working principle and sensing mechanism

Electrical properties of semiconductor oxides depend on the composition of the surrounding gas atmosphere. The surface conductivity of the sensor is modified by the adsorption of reactive gas species and related space charge effects. In oxidizing atmosphere, the oxide surface is covered by negatively charged adsorbates and the adjacent space charge region is electron depleted, increasing the semiconductors' surface electron affinity and inducing a bandbending. For n-type oxides, the layer presents therefore an increased resistance, while for p-type oxides it presents a reduced resistance. Under reducing conditions, the oxygen adsorbates are removed by reaction with the reducing gas species and the electrons are re-injected into the space charge layers [54,57,70].

It is generally considered, for n-type materials, that the sensitivity to ozone is due to the presence of surface oxygen vacancies, which induce defect states in the band gap that act as electron donors. The filling of the vacancies by decomposing ozone, traps free charge carriers producing an associated shift in resistance [32,54]. It is known that ozone is a highly unstable molecule that readily donates its extra oxygen atom to free radical species. Upon ozone exposure, absorbates are created in the film's surface, due to the oxidizing nature of this species, creating a bandbending as represented in figure 4. Usually O_3 is adsorbed on the semiconductor surface as O^- or O_2^-, capturing an electron from the conduction band [45,69]. O_3^- can not be ruled out entirely at relatively low temperatures. This form of adsorbed oxygen is highly unstable at elevated temperatures, quickly being transformed into O^- or O_2^-. Only

one work, Naydenov et al. [71], in 1995, showed the formation of O_3^- on metal oxide surface (CeO_2), at temperatures of 65°C. Using Electron Paramagnetic Resonance (ESR) spectroscopy the study has shown that O_3^- easily dissociates into O^- even at temperatures below 70°C. To the best of our knowledge no other authors reported the formation of O_3^- [45,46]. It is still unknown however if ozone first adsorbs and then the molecule dissociates or the molecule dissociates during the adsorption, although the latter seems to be favoured in some cases [45,68,69]. Ozone has a much lower dissociation energy than oxygen: 1.2 eV and 5.1 eV respectively [72]. Ozone's half-life is fairly short, (25 hours at 24°C) and temperature dependent (2.5 s at 250°C). Upon reaction with the surface of the sensors it usually easily decomposes. The likely adsorption equations can be described as follows [73]:

Oxygen adsorption	$AS + O_2 + e^- \rightarrow AS - O_2^- \ (ads) + h^+$	(5)
Ozone adsorption	$AS + O_3 + e^- \rightarrow AS - O_3^- \ (ads) + h^+$	(6)
	$2AS + 2O_3 + 3e^- \rightarrow AS - 3O_2^- (ads) + 3h^+$	(7)
	$3AS + O_3 + 3e^- \rightarrow 3(AS - O^-(ads)) + 3h^+$	(8)
Desorption	$y(AS - O_x^-(ads)) + nh^+ \rightarrow \frac{xy}{2}(AS + O_2) + ne^-$	(9)

Where AS represent the adsorption sites in the sensing layer. In equation 6, it is likely that O_3^-, rapidly decomposes into $O^-(ads) + O_2(gas)$, as this form of adsorbed oxygen is unstable [45,71]. In figure 4 a schematic representing a p-type semiconductor material, when exposed to air a) and to ozone b) is shown. L_D represents the Debye length, that is the distance in a semiconductor over which chemical electrostatic effects can propagate. Related to materials physical properties, that affects the distribution of free charge carriers; L_D is dependent on the doping as per equation 10. Debye length is a key parameter in semiconductor gas sensors, since it can be understood as up to which depth in the grains the adsorbed species will impact the electronic properties.

$$L_D = \sqrt{\varepsilon * \frac{kT}{q^2 N_A}} \tag{10}$$

Where ε is the semiconductor permittivity, N_A is the acceptor density and kT are the Boltzmann constant and temperature, respectively.

When ozone is introduced, more species are adsorbed at the surface, increasing the bandbending observed. The Debye length will have a direct impact in the resistance relation between the R_s and R_b, that are respectively the resistance in the grain that is affected by the electrostatic effects of oxygen adsorbates and the region unaffected by it (schematic represented in figure 4). In an extreme case where the grain size is comparable to the Debye length, we can consider that all the grain is ionized and therefore we have $R_{total} = R_s$.

Sensor's response to ozone is usually calculated as the ratio of the resistances measured in the atmospheres containing and not containing ozone, $S = R_{ozone}/R_{air}$. Most metal oxide sensors show a better response above 200°C, when the sites are free from molecular water since the hydroxyl groups may limit the oxygen adsorption, by occupying the same adsorption sites. For so, working at lower temperatures might lead to saturation at lower ozone concentrations. Wagner et al. [42], showed for WO_3 the humidity interference was only noticeable for concentrations of ozone in the ppm range, where occupancy of adsorption sites by hydroxyl groups leads to a saturation of the sensors' response at lower ozone partial pressure, whilst measurements using ozone concentrations in the hundreds of ppb range at 20% and 40% relative humidity, didn't present a significative influence of humidity. Even if at $T \sim 100°C$, molecular water desorbs from the surface, hydroxyl groups may react with ozone to form intermediate species such as HO_2 and HO_3 [9]. Furthermore, these hydroxyl groups are known to catalyse ozone decomposition. This may lead to a weaker change in resistance upon exposure to ozone. At temperatures higher than 350°C the influence of relative humidity becomes insignificant [9,45]. Humidity interference has been shown to have a strong effect on SnO_2 and In_2O_3-based sensors and a moderate effect on WO_3 sensors [21,42].

While an increased working temperature is necessary for fully reversible measurements and to increase the sensing response, at high temperature (above 400°C) the desorption mechanism increases significantly, and the system may become less sensitive. Therefore, the coverage of chemisorbed species shows a maximum with increasing temperature (typically in the range 350° – 500 °C) [57]. This has lead in several works to show an optimum sensitivity temperature, where a maximum ratio of sensitivity upon ozone exposure was achieved [45,54,59,68,69]. Bendahan et al. [57], has shown that the optimum sensing temperature is dependent on the ozone concentration, for WO_3 sensors. In their work, they observed an ideal sensing temperature of 275°C for 0.1 ppm of ozone, whilst for 1 ppm it was observed 375°C as the optimum sensing temperature. In their review Korotcenkov et al. [9], suggests an optimal working temperature $T \sim 350 - 400°C$, for In_2O_3 and SnO_2 gas sensors. However, in the literature there is a scarcity of data regarding the influence of the measuring temperature regarding the selectivity of the films, namely towards molecular oxygen that may create the same adsorbate species.

The response and recovery time are directly related to the adsorption and desorption activation energies, respectively. This can be explained by considering the temperature dependence of the surface coverage of chemisorbed species. Since both these reactions are thermally activated, the response time is usually favoured at higher temperatures.

Most sensors operate at high temperature, for this purpose it is incorporated onto a resistive heater together with a microcontroller [9]. Ideally the adsorption reactions are reversible and have an equilibrium point determined by the sensor's working temperature,

however some reactions may be irreversible, leading to a poisoning of the sensor, decreasing its baseline resistance and its sensitivity [16].

Studies have shown, for metal oxides, such as SnO_2, TiO_2 and $SrTiO_3$ that in the temperature range below 500°C, the incorporation reaction of the adsorbed oxygen atoms into the lattice (bulk diffusion) is very slow. Therefore, for most sensors that actuate in this temperature range, chemisorption is the dominant effect that controls the sensing mechanism, as a general rule. Only at higher temperatures (500 – 700°C range), the incorporation of oxygen into the lattice of metal oxides, which takes place due to oxygen diffusion, becomes the dominant mechanism responsible of the change of their resistance, [9].

Few studies have been reported using p-type semiconductors, that are in general further behind of the most commonly explored n-type counterparts but may prove to be an interesting alternative for ozone sensing. Studies have shown that Copper based oxides (CuO and $CuAlO_2$), present a high catalytic activity for ozone decomposition [68,69]. In these works, it has been shown the sensitivity of copper oxides to relevant ozone concentrations, in the 50 – 100 ppb range, albeit working at temperatures above 250°C.

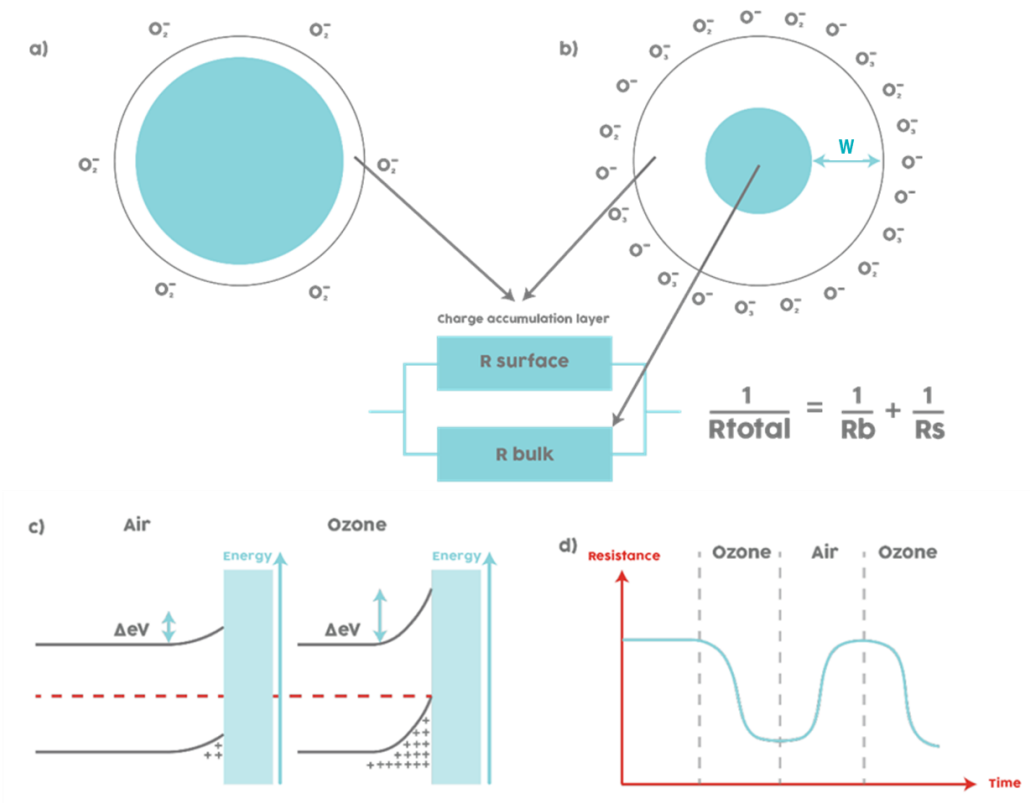

Figure 4 - Schematic representing the oxygen adsorbates on a grain of a p-type semiconductor sensing layer upon: a) exposure to air; b) exposure to ozone, depicting all the possible oxygen species formed at the surface. The equivalent circuit is represented with a parallel of resistors. The individual contribution of each is dependent on the Debye length (L_D); c) represents the expected bandbending of energy levels at the surface, upon exposure to atmospheric air and to ozone; d) represents the expected behaviour for a p-type semiconductor with the

decrease in resistance upon ozone exposure, until a plateau has been reached and the full reversibility of the measurements.

1.4.1 Response behaviour of semiconductor sensors

The gas sensors response to target gas, has been known empirically for several decades to follow a power law behaviour, of the type $S = AP_{gas}^{n}$, where A and n are constants and P is the gas partial pressure [41,45,70,74,75]. Yamazoe et al. [70], has been able to correlate the experimental results with the semiconductor theory, resulting in the theory of power laws. Hao et al. [76], was also able, combining the Schottky barrier model and the law of mass action to explain this power law behaviour, reaching similar results to those of Yamazoe, corroborating its validity. In their work they combined the depletion theory of semiconductor, which deals with the distribution of electrons between surface state (surface charge) and bulk, with the dynamics of adsorption and/or reactions of gases on the surface, which is responsible for accumulation or reduction of surface charges.

Gas sensors based on polycrystalline thin-films can be approximated to arrays of grains, considering enhanced diffusion of gas molecules along the grain's boundary. In cases where the grains are connected to their neighbour's through grain boundaries a potential barrier known as double Schottky barrier is formed (figure 5 a)) [77]. The barrier plays a key role in determining the total resistance of the sensor. For n-type metal-oxides semiconductor, upon exposure to an oxidizing gas, if the adsorption of the target gas is stronger than that of oxygen, the surface potential barrier will increase, resulting in an increase in the resistance of the material. Electrons can also be transported by tunnelling when the grains are a small distance apart albeit not in contact. Even in this case tunnelling current is attenuated in the same way by the surface potential on the oxide grains [70].

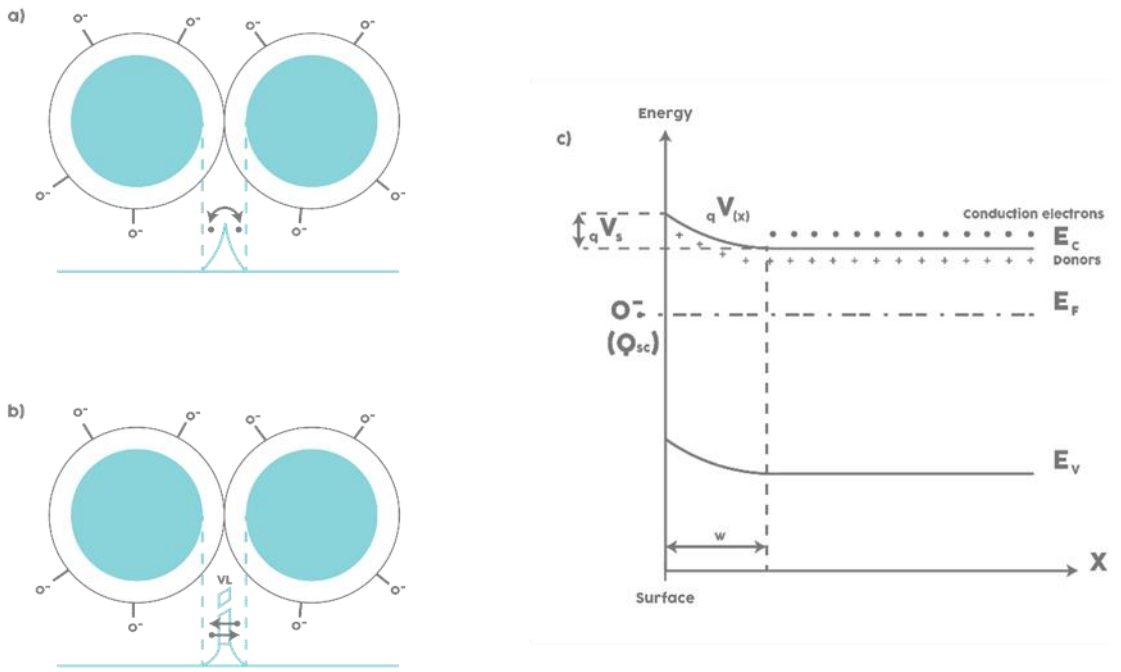

Figure 5 - Schematic of electron transfer in a grain conduction model: a) Double Schottky barrier b) Tunnelling model; c) Surface depletion layer formed by oxygen adsorption for a n-type semiconductor. From [70]

We approximate the accumulation layer in each grain, to a 1D model as depicted in figure 5 c), where x denotes the depth from the surface. When surface states are present at energies below Fermi levels in flat band conditions, in n-type materials electrons are transferred from the conduction band until Fermi level becomes constant (equilibrium) [70]. The resulting is a bandbending (depletion layer) that is described by a depth profile of potential energy of electrons $qV(x)$, and surface potential barrier qV_S, and depletion depth w, where q is the electron elemental charge and $V(x)$ and V_S are electric potential at given depth and surface, respectively. $V(x)$ is correlated with space charge density, $\rho(x)$, by Poisson's equation [70], as follows:

$$\frac{d^2V(x)}{dx^2} = -\frac{\rho(x)}{\varepsilon} \tag{11}$$

Where ε is the permittivity of the oxide. For n-type semiconductors $\rho(x) = q(N_d(x) - n(x))$, where N_d and n are the densities of ionized donors and conduction electrons at a given depth, respectively. For a case where all donors are ionized completely (shallow donors), $\rho(x)$ can be approximated by an abrupt change model [78], where $\rho(x) = qN_d$, for $0 < x < w$ and $\rho(x) = 0$, for $w < x$ and $Q_{sc} = -qN_dw$. Q_{sc} is the surface charge density. Based on this model the Poisson's equation can be solved to give an expression of $qV(x)$ as follows [70]:

$$qV(x) = \frac{q^2N_d}{2\varepsilon}(x - w)^2 \tag{12}$$

The height of potential barrier can be expressed, as surface potential is given by $qV_S = qV(0)$ leading to:

$$V_S = \frac{(w/L_D)^2}{q/kT} \tag{13}$$

The density of conduction electrons at the surface $[e]$ can be expressed in terms of surface potential as [70]:

$$[e] = N_d \exp\left(-\frac{qV_S}{kT}\right) \tag{14}$$

It can be rewrote as:

$$[e] = N_d \exp\left(-\frac{(w/L_D)^2}{2}\right) = N_d \exp\left(-\frac{m^2}{2}\right) \tag{15}$$

Where m is the reduction depletion depth defined by $m = w/L_D$. The conductance at each grain boundary is proportional to $[e]$ and hence the resistance of the sensing body according to Yamazoe et al. [70], can be considered inversely proportional to it.

$$\frac{R}{R_0} = \exp\left(\frac{m^2}{2}\right) \tag{16}$$

This equation shows that the resistance is uniquely determined by the reduced depletion depth. If we consider the response to ozone as:

$$O_3 + 3e^- \rightarrow 3O^-(ads) \tag{17}$$

The rate of accumulation of O^- is given by [70,76]:

$$\frac{d[O^-]}{dt} = k_1 P_{O_3}[e]^3 - k_{-1}[O^-]^3 \tag{18}$$

Since ozone decomposition is mostly an irreversible reaction, but ozone can desorb from the surface as per equation 18, a steady state will be reached, where $\frac{d[O^-]}{dt} = 0$

$$\frac{k_1}{k_{-1}} P_{O_3}[e]^3 = [O^-]^3 \tag{19}$$

Combining the chemistry taking place in the grains surface with the semiconductor's physics previously described. Assuming that there are no electrons-trapping except for O^- in the surface, then O^- would be solely responsible for the surface charge density [70,76]

$$[O^-] = -\frac{Q_{SC}}{q} = N_d w \tag{20}$$

If we combine equation 20 with 19 and 16, we can rewrite:

$$\left(\frac{k_1}{k_{-1}}P_{O_3}\right)^{1/3}\exp\left(-\frac{m^2}{2}\right)=w \tag{21}$$

$$\frac{R_0}{R}=\frac{\left(\frac{k_1}{k_{-1}}P_{O_3}\right)^{\frac{1}{3}}}{w} \tag{22}$$

The exponent that correlates the ratio of resistance, comes directly from the kinetics of the equation. This theoretical understanding derived by Yamazoe et al. [70], allowed to correlate what had been previously observed empirically with a fundamental understanding, explaining the power law behavior, $S = AP_{gas}^{n}$. In this case if we consider that the sole decomposition of ozone on surface reaction is into $[O^-]$, an exponent of 1/3 is to be expected. This formalism can be generalized as:

$$\frac{x}{a}O_3+\frac{a}{x}e^-\rightarrow\frac{a}{x}O_x^-+\frac{a}{x}p^+ \tag{23}$$

From this analysis, it is possible to understand that the exponent, of the power law is dependent on the reaction undergoing at the surface of the sensor [45]. Table 3 schematizes the different possible response functions for ozone.

Table 3 - Expected response function for O_3 gas sensors [45]

Gas	Adsorbed Species	Response ($S \sim P_{gas}^{n}$)
O_3	O_3^-	$S \sim P_{O_3}$
	$\frac{3}{2}O_2^-$	$S \sim P_{O_3}^{2/3}$
	$3O^-$	$S \sim P_{O_3}^{1/3}$

The exponent (n) of the power law is dependent on the gas and of the catalytic reaction with the metal oxide. Different materials have shown different exponent responses. Furthermore, studies have shown the exponent to be temperature dependent [76]. Yamazoe et al. [70], in their work, measured a constant exponent equal to one, for WO_3 based ozone sensors. For In_2O_3, Kiriakidis et al. [61], observed a linear increase in sensitivity with ozone concentration. Gurlo et al. [45] studied the variation of sensor response, for SnO and In_2O_3 materials, working at 250°C, with $0.7 < n < 0.5$. For n-type semiconductors, CuO has been reported to have $n = 0.53$ [68].

1.4.2 Langmuir Adsorption Theory

The interaction between the thin film and its environment is modelled by the Langmuir theory of adsorption-desorption balance [79]. The Langmuir isotherm has three major assumptions:

- Each active site interacts with only one adsorbate molecule (monolayer coverage)
- Adsorbate molecules are adsorbed on a finite number of well-defined localized sites (AS) and the saturation coverage corresponds to complete occupancy of these sites.
- The adsorption sites are all energetically equivalent, and there is no interaction between adjacent adsorbed molecules.

In that case Langmuir isotherm is represented by:

$$\theta = \frac{kP}{1 + kP} \tag{24}$$

θ is the fraction of sites that are filled on the surface with the adsorbed gas, P is the partial pressure of the gas and k is the reaction kinetic constant. At a given pressure the extent of adsorption is determined by the value of k, which is dependent upon both the temperature (T) and the enthalpy of adsorption. The adsorption enthalpy reflects the strength of binding of the adsorbate to the substrate [80]. The adsorption is proportional to the fraction of unoccupied sites, while desorption is proportional to the fraction of the adsorbent surface that is covered.

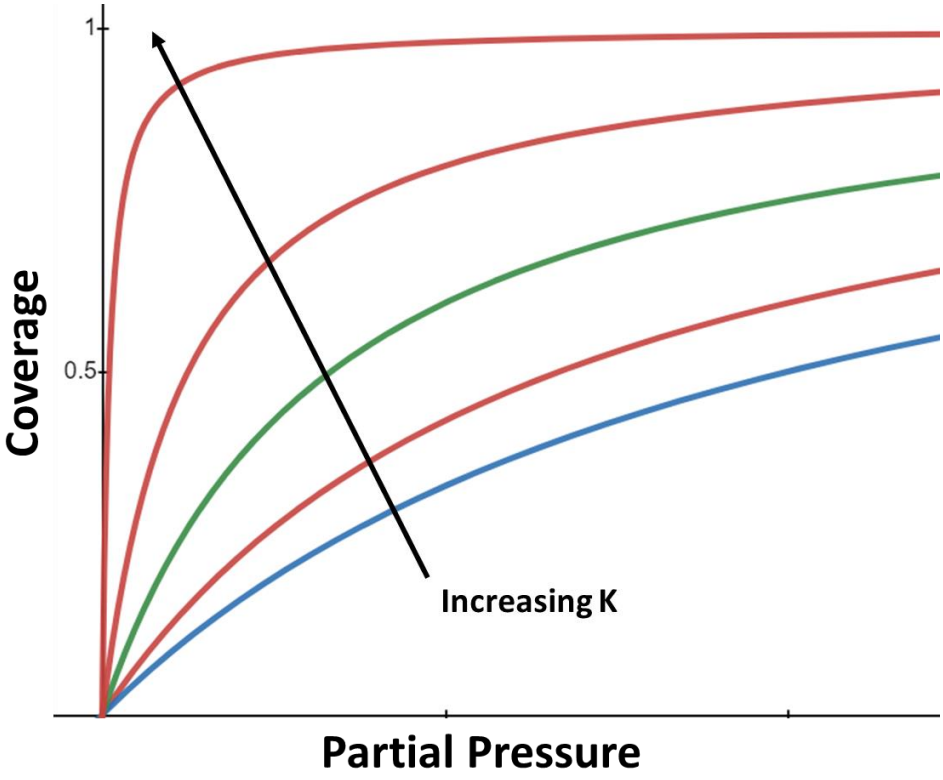

Figure 6- Langmuir isotherm expected dependence of coverage on pressure with increasing reaction constant k, reflecting either the increase in the adsorption enthalpy or a decrease in temperature.

The equation of evolution of θ overtime can be written as [32,54]:

$$\frac{d\theta}{dt} = k_1 P(\theta_{max} - \theta) - k_{-1}\theta \tag{25}$$

θ_{max} represents the total number of adsorption sites available. However, for the measurements of gas concentrations, a more relevant consideration related to the detection of ozone concentrations is a time-dependent dynamic model. Considering only O_3, as the interacting gas on the surface, and assuming no initial coverage (i.e. all adsorption sites are unoccupied), integrating the Langmuir isotherm as a function of time, leads to the following expression for the fraction of adsorption sites being occupied, upon O_3 exposure:

$$\frac{\theta(t)}{\theta_{max}} = 1 - \frac{k_{-1} + k_1 P e^{-(k_{-1}+k_1 P)t}}{k_{-1} + k_1 P} \tag{26}$$

When the target gas is an oxidizing gas and the gas pressure is high enough, there can be competitive adsorption and displacement of species, that have to be considered [45,70,76]. The formalism can be readily expanded to take oxygen adsorption into account by adding $k_2[O_2]$ [32].

$$\frac{\theta(t)}{\theta_{max}} = 1 - \frac{k_{-1} + (k_1 P + k_2[O_2])e^{-(k_{-1}+k_1 P+k_2[O_2])t}}{k_{-1} + k_1 P + k_2[O_2]} \quad (27)$$

The detection limit is dependent on k_1 and k_2. This means that materials with high adsorption constant for the target gas and a low one for O_2 will feature smaller detection limits. Surface dopants, stoichiometry, polarity, or surface energy and other changes in the materials properties can significantly change the ratio between k_1 and k_2 [76], that can be understood as the selectivity of the materials towards ozone compared with molecular oxygen.

Langmuir's theory has its disadvantages, based on the assumption it makes: each active site interacts with only one adsorbate molecule (monolayer coverage); adsorbate molecules are adsorbed on well-defined localized sites (AS) and the saturation coverage corresponds to complete occupancy of these sites; the adsorption sites are all energetically equivalent (homogeneous), and there is no interaction between adjacent adsorbed molecules [81]. The first assumption (adsorbates monolayer) is only possible for low partial pressure conditions. According to Guerin et al. [77], the Langmuir isotherm has however a good accuracy for describing the adsorption theory, even more so on lower covering ratio (less than 5×10^{-3}). Furthermore, there are possibly electrostatic interactions between the adsorbate species. The model has however a good accuracy when the bonding energy is comparable to a constant (due to the fact that all adsorbates are ionized), what is mostly the case as ozone sensing is mostly performed using low gas concentrations [32,77,82].

Other models have been proposed to study the interaction between the metal oxide semiconductor and the ozone adsorbates, namely the Wolkenstein adsorption theory [83], by Guerin et al. [57,59,77]. This model assumes, that the adsorption of an oxidizing gas species is carried out with two successive steps, a weak or neutral chemisorption and a strong or ionized chemisorption. During the first step, the bond is weak and does not involve electronic transfer. The second step leads to the transfer of an electron from the conduction band to the adsorbed species. The weak chemisorption is only limited by the number of adsorption sites, while the strong one is limited by the bandbending [77].

However, these models also present their own limitations. They cannot be solved analytically and only a numerical solution can be achieved, with a number of assumptions about the thin film [77]. The sensors are considered to consist of homogeneous stacking of identical grains (same size and shape, in this case the authors considered equal spherical grains), that each grain is single crystal, and that the resistivity of the layer results from the properties of only one grain [59]. It furthermore assumes that all chemical mechanisms are fully reversible in the whole range of temperature. All these claims are most likely not true for the case of polycrystalline materials, that have a wide variety of sizes and geometries. The authors made no studies to further justify these assumptions. As discussed, in many cases the reactions are also not fully reversible, mainly at room temperature.

Although the group proposes both models, Langmuir [54,57,84] and Wolkenstein [59,77] to study the interaction between ozone and WO_3, no conclusions or comparisons were drawn in between the two and the extracted parameters.

1.4.3 Morphology effect

Polycrystalline materials are very complicated to study, because the electro-conductivity and sensing properties of the materials depends on a great number of factors. The porosity, grain size, active surface area, thickness, crystalline structure and conductivity are some of the properties that modulate the sensing characteristics (selectivity, sensitivity and response time) of metal oxide sensors [40,44,57,72,84–86].

The sensing layer can either be more compact or more porous. For compact surfaces the gas interaction takes place mainly at the surface inducing a partly charged layer. Two resistances are formed in parallel. In the extreme opposite case, with highly porous layers, the gas may diffuse into the sensitive layer down to the substrate, bathing every grain [40,87]. The gas interaction can therefore take place at the surface of each individual grain, at grain boundaries, creating a fully charged regime depending on the grain size and doping of the oxide materials as per the Debye length (equation 10).

In most cases the sensitivity will be governed by the surface layer. It has been observed that the sensitivity has a negative correlation with the film thickness, when all other parameters are kept constant, in the case of polycrystalline ZnO ozone sensors [63]. The thickness however can't be thought as a standalone parameter, as it can be related with the porosity of the material. Thickness changes can lead to changes in the magnitude of the sensor's response and the ideal operating temperature. Increases in thickness can lead to slower response times. Most works have pointed out the benefits of using thin films instead of thicker ones: increasing the sensitivity and decreasing the response times [40,88,89]. The morphology of the films can have an impact since it may change the number of adsorption sites available and so control the sensitivity of the sensor. For thin films, thickness is key, since the grain size has regularly a direct increase with thickness [40].

Chemical composition and crystalline orientation can change the ozone catalysis process created by the oxide. Inter-grain contacts and gas permeability can be changed depending on the polycrystalline shaping. Every crystallographic plane has their surface state density and surface energy, creating changes in the adsorption/desorption activation energy. Golovanov et al. [90], has shown that the adsorption/desorption for humidity changes with different crystalline orientation of SnO_2 thin films. Gurlo et al. [45] noticed that the characteristics of In_2O_3 sensors strongly depend on the conditions of their preparation, which determines the structure, phase composition and indium electronic states. The surface stoichiometry changes the adsorption ability and controls the bandbending created by the adsorbates [40].

In general, metal oxide conductivity is described using a grain model [74,75,77,91–95], according to which, there are Schottky type contacts with the height of potential barrier depending on the surrounding atmosphere, such as represented in figure 7. The conductivity of the 3D networks of grains is controlled by the intergrain resistance contacts, as follows [40,72]:

$$R \approx \exp\left(\frac{qV_s}{kT}\right) \tag{28}$$

Where V_S is the height of the Schottky barrier at the inter-grain boundary, which can be modified with the adsorbed species. In general, it is established that a decrease in the grain size in metal oxide semiconductors should lead to an increased sensitivity of the sensors. A special strong increase has been shown, when grain sizes are comparable to the Debye length (extensive review can be found by Korotcenkov [40]). If we consider L_S, as the width of surface space charge region, as in equation 29, if $2L_s$ is larger than the grain size, then every grain will be fully involved in the space charged layer. This will mean when the model represented in figure 4 is considered, that the contribution of R_S is total.

$$L_S = L_D\sqrt{\frac{eV_S}{kT}} \tag{29}$$

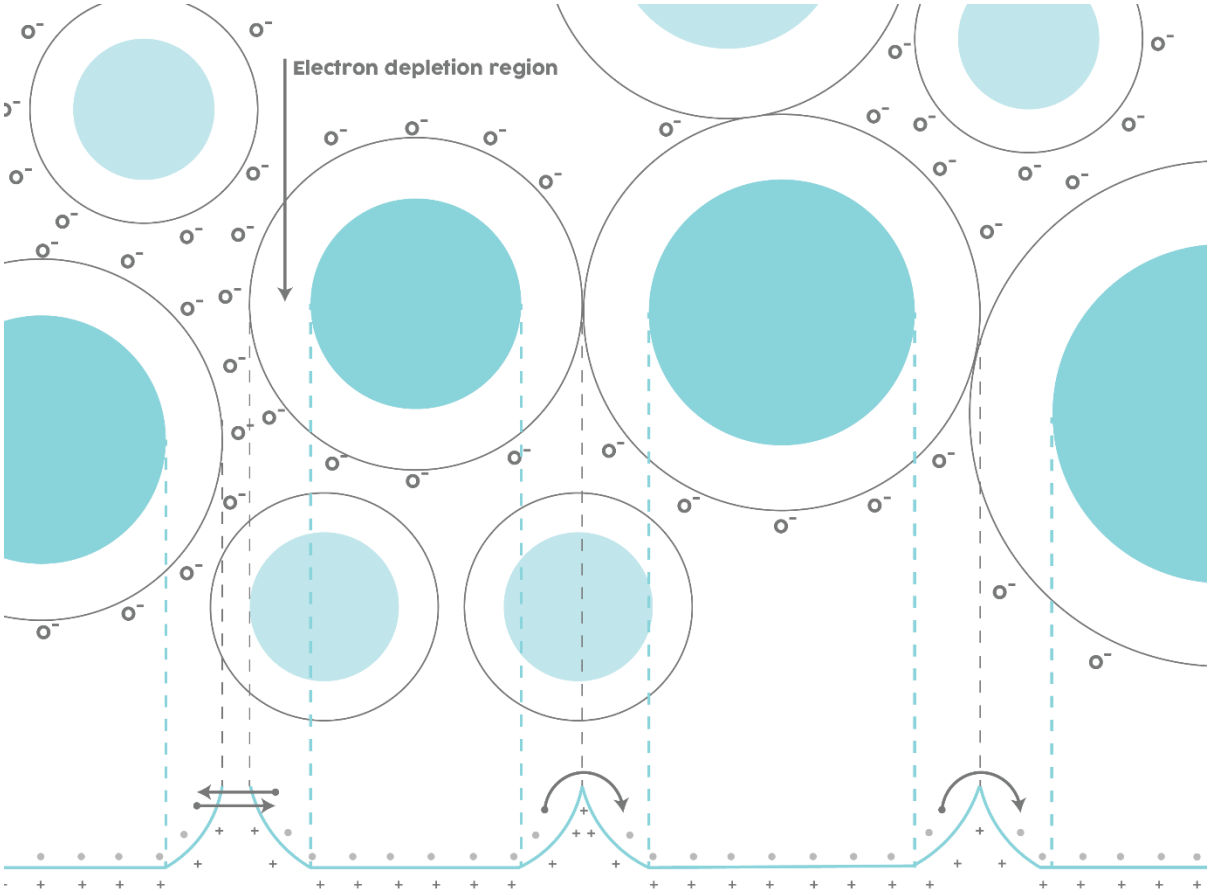

Figure 7 – Schematic model of the microstructure and energy bands, representing the potential barriers of the interface region between grains.

In most studies the grain size decrease has consistently shown an increase in sensing behaviour [61]. Vallejos et al. [21], claims that for WO_3 gas sensors it can be observed a clear impact on the sensors response based on the grain size and the number of free bonds. It was noted that a decrease in grain size from 24 to 17 nm promoted an increase in sensor response by a factor of ~ 2. For ZnO it was reported the decrease in sensitivity of the sensors with the increase in grain size [48,50]. Comparisons between micro and nanocrystals for p-type $CuCrO_2$ have shown an increase in response of 2.5 times, when nanocrystals are used [12]. Decrease in grain size, from 60 to 10 nm in In_2O_3 thin films has shown a considerable decrease in the response time, albeit not in the recovery time [65]. Some works have tried to correlate the grain size (D), with sensitivity. Rothschield et al [96], predicted that the sensitivity is inversely proportional to the grain size $S \sim D^{-1}$. However, this hasn't been corroborated by other authors, such as Suchea et al. [49,97], who observed a higher inverse dependence. Korotcenkov et al. [72], observed a dependence up to $S \sim D^{-3}$, in the range 10 to 50 nm with In_2O_3 thin films. The sensor behaviour sensitivity dependence, results from more than changes in grain size. The property engineering present to change the grain size, may involve the change of other properties, such as the porosity, the stoichiometry of the grains and the surface energy of the surface. These properties can affect the sensing behaviour. It has been

further shown by Korotcenkov [65,72], that In_2O_3 thin films show a much greater dependence on the grain size than SnO_2 based ones. In some cases, in these films, a quadratic kind of behaviour was observed, where a minimum has been reached at about 40 nm and either an increase or decrease of grain size proved to have an increase in sensitivity. According to the author this is due to the fact that the decrease in grain size is obtained by changes in the deposition temperature, that leads to a lower porosity. Liu et al. [88], observed that for films annealed at 500°C, despite the grain size increase the sensors performance increased due to the increase of porosity.

There are several routes of controlling the films properties, namely its grain size and porosity: by changing the deposition parameters or technological route, by post deposition thermal annealing, exposure to different atmospheres, via chemical attacks or etchings, in between others. Figure 8 schematically represents methods of thin film property engineering that can be used to change the properties of the sensing layers. The key is to understand which other parameters are also being modified simultaneously that can affect the sensors.

Determining which parameters are among the most important ones in a gas sensor depends on many factors, including the technological routes during the synthesis of the sensing layer and the thermal budget/atmosphere of the post-deposition treatments (when considering annealing). In general, it is impossible to determine in advance which parameter of the sensing layer will be the most effective to increase the gas sensitivity. The different parameters cannot be simply looked in a vacuum because they are mostly interdependent. The process of changing one of the properties of the material will invariably lead to changes in one or more of the other properties. Changes in the grain size can induce other changes such as [72]: tendency to agglomeration [98], porosity [88,99], specific surface area [100], transport and electronic properties [101], surface state density [102], crystalline structure [103,104], stoichiometry [105], adsorption capabilities [106,107] and the catalytic activity [107,108]. All these interdependencies on possibly inverse effects of the thin film sensing response, make it complicated to predict in a generic way the ideal parameters to be optimized for gas sensing [40]. These parameters will be always dependent on the sensing layer, the technological route and the gas to be detected.

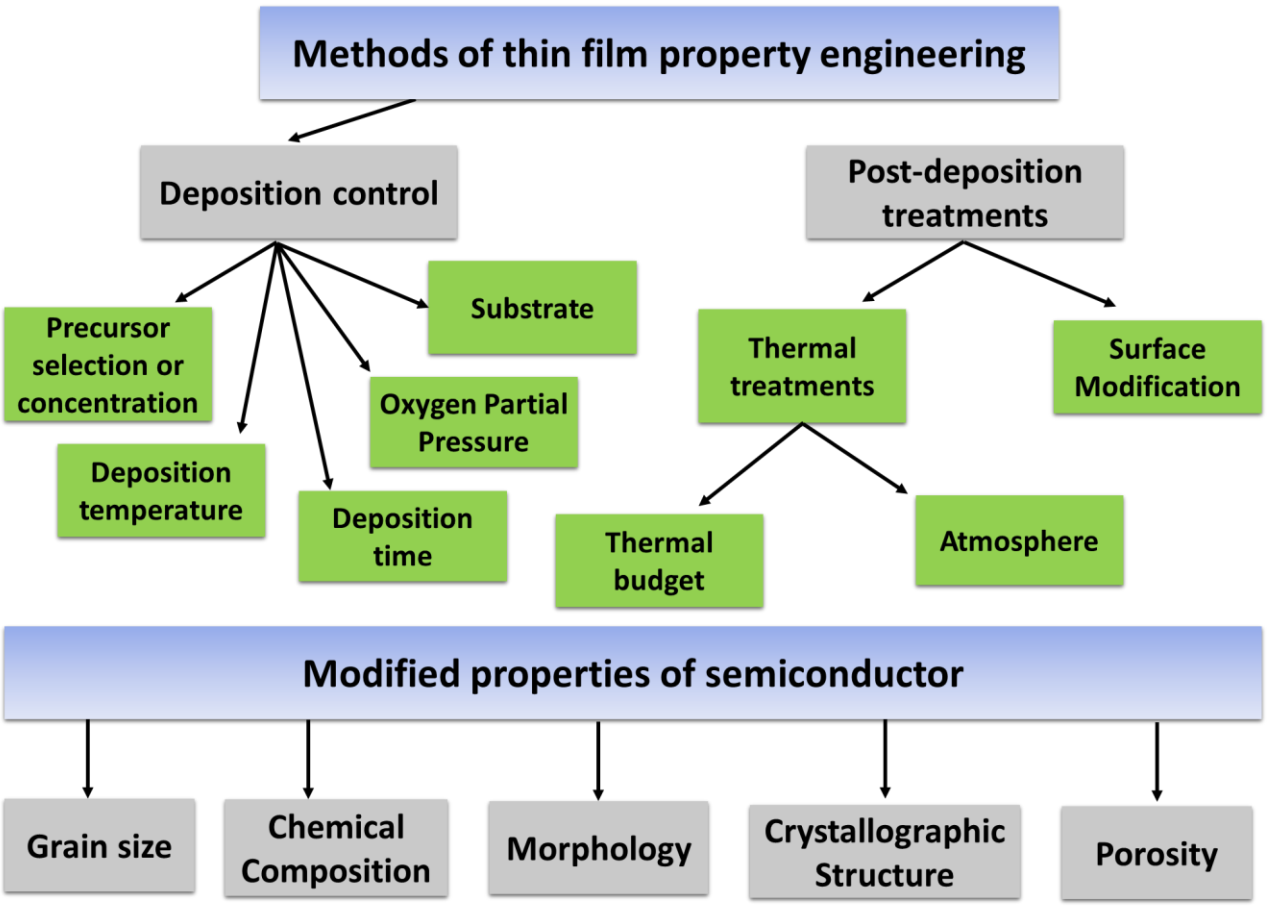

Figure 8 - Diagram illustrating methods of thin film property engineering that can be used in solid state gas sensors. Inspired from [40]

1.5. Delafossite Materials

Generally, high electrical conductivities and wide energetic bandgaps - leading to high optical transparencies - are sought for high figure of merit Transparent conductive oxides (TCOs), but seemingly mutually exclusive properties. TCOs are exceptional materials, combining high electrical conductivity, optical transparency and reasonable electrical mobility. Depending on the donor (electrons) or acceptor (holes) level in the bandgap of such material, they are either *n*- or *p*-type, with carrier concentration (n) and optical bandgap (E_g) typically above 10^{20} cm^{-3} and 3 eV, respectively. The most employed TCOs at industrial scale – Sn-doped In_2O_3 (ITO), Al-doped ZnO (AZO) and F-doped SnO_2 (FTO) – have *n*-type conductivity; among them, ITO stands out with electrical conductivity around 10^4 $S.cm^{-1}$ and transparency above 80 % in the visible range [109,110]. *N*-type TCOs have been reported and explored for more than half a century and they dominate the transparent electronics market, with their two main applications as transparent electrodes for flat panel displays and photovoltaic cells; and as active layer for transparent thin film transistors (TFT), UV light emitting diodes (LED), gas sensors and other transparent electronic devices [111]. However, challenges are still faced to find a matching *p*-type counterpart (extensive reviews can be found in [112,113]). The evolution of a capable *p*-type TCO would open a new era in transparent electronics, by promoting the fabrication of transparent active devices such transparent *p*-*n* junctions (diodes) [113,114] and complementary transistors [115,116] . This would open a new range of transparent electronics applications including: smart windows [117–120], transparent UV LEDs [121,122], heterojunction solar cell [123,124], advanced gas sensors [114,125–129], electromagnetic shielding [130].

A multitude of materials have been proposed as *p*-type TCOs, such as: ZnO [131,132], In_2O_3 [133], doped [134,135] or non-doped NiO [136], SnO [137–139] and β-Ga_2O_3 [140–142], mixture of In_2O-Ag_2O [143]; layered oxychalcogenides (LaCuCh, Ch = S [144–146], Se [147]); spinel oxides ($NiCo_2O_4$ [148,149], $ZnCo_2O_4$ [150,151] $ZnIr_2O_4$ [150] and $ZnRh_2O_4$ [150,152,153]); SnSeO [154]; Ba_2BiTaO_6 [155]; $SrCu_2O_2$ [121,156–158]; $LaCrO_3$ [159] and doped Cr_2O_3 [160,161]). Among the different *p*-type candidates, delafossite materials have shown promising conductivities and consistent optical transparency over the visible range as well as a very good stability in air (see reference [162] for an extensive review).

1.5.1. Delafossite properties

The challenge in improving optoelectronic properties of these *p*-type TCOs arises from their intrinsic electronic structure. The valence band edge of most oxide materials is composed by strongly localised oxygen *2p* levels, owing to its large electronegativity [163]. These levels lie far lower than the valence orbital of the metallic atoms, leading to a non-

dispersive valence band maximum (VBM); the high-electronegative oxygen atoms trap the holes, resulting in flat energy bands, therefore impeding the introduction of shallow acceptors and a high effective hole mass, leading thus to poor transport characteristics [163,164]. In a p-type crystalline solid, a few aspects might be considered to favour a considerable hole concentration:

i) a low formation energy of point defects that produce holes (e.g. native acceptors such as cation vacancies or oxygen interstitials).

ii) small ionisation energy of these defects, to release holes (i.e. a shallow acceptor level with respect to the host valence band).

iii) and most importantly, high formation energy of native defects that annihilate holes (e.g. native donors such as anion vacancies) [165],[166],[167].

Amidst all investigated p-type semiconducting materials, those having a delafossite structure were thoroughly investigated due to their interesting properties with applications in various fields.

Delafossite materials triggered a lot of interest as *p*-type TCOs candidates since 1997, when Kawazoe et al. [158,168], successfully fabricated a stable *p*-type undoped delafossite $CuAlO_2$ with a considerable conductivity (0.95 $S.cm^{-1}$) at the time. Although the value was about 3 orders of magnitude smaller than state-of-the-art *n*-type TCOs, the results were promising [158,169]. They proposed a strategy - the so-called chemical modulation of the valence band (CMVB) - for broadening the valance band and consequently achieve lighter effective mass/ higher carriers mobility [165]. Within this approach they outlined three criteria that must be met to manipulate the valence band edge of p-type TCOs without compromising their optical transparency. First, the energy levels *nd* of the shell of metallic cations and O *2p* should be similar to promote hybridization, forming strong covalent bonds, resulting in a more dispersive valence band edge pushed up above the bonding O *2p* or metallic cations *nd* states that furthermore ameliorates holes delocalisation, increasing the material mobility. Second, these levels should have closed electronic shells (nd^{10}) to avoid any coloration due by *d-d* excitations. Additionally, the coordination around oxygen atoms anions shall be tetrahedral, allowing to pair electrons in *2s* and *2p* orbitals of oxygen to bond with two other atoms; this configuration reduces the strong localisation of the carriers at the valence band maximum (VBM) [166]. From the theoretical point of view, the achievement of a p-TCO with improved characteristics relies on the delocalisation of the VB by promoting the orbital hybridization between metal cations nd^{10} and O 2p orbitals. This model explains thus the higher holes mobility (above 1 $cm^2\ V^{-1}\ s^{-1}$) achieved in this type of materials when comparing with other p-type TCOs.

Delafossite materials are ternary oxides compounds, with a layered structure AMO_2, where A and M are monovalent and trivalent cations, respectively. The A cations have small

size, favouring a linear (II) coordination; M cations and O anions have coordination (VI) and (IV), respectively. This structure allows to meet all the required criteria to modulate the VBM: the A cation has a closed-shell energy level close to (just above) the O *2p* level; M cations have a closed electronic shell nd^{10}; and oxygen ions with tetrahedral configuration. The A cation is a noble metal d^{10} cation, generally Ag, Cu, Pd and Pt; the latter two are known to create "metallic" delafossites [170,171]. Ag-based delafossites ($AgBO_2$) have been reported, but the deposition processes are very difficult and low electrical conductivities have been achieved until now [172–176]; despite that, these materials have shown promising results for biomedical applications due to their antimicrobial properties. Cu-delafossites have attracted attention due to their expected large hole mobility, resulted from the mixing of Cu *3d* and O *2p* states forming the valence band. It has been reported that the delafossite structure allows to host a multitude of M cations, namely *p*-block elements (Al [158,168,177,178], B [179–181], Ga [158,174,182,183] and In [184–187]), transition metals (Cr [188,189], Sc [190–192] and Y [191,193–195]), or lanthanides (La, Nd and Eu). These materials were thoroughly investigated as they demonstrated interesting antibacterial, (photo)catalytic [196–200], electrical, magnetic [201–205], multiferroic [206], optoelectronic [207,208], superconducting [209] and thermoelectric [196,202,210] properties. Among the Cu delafossites, copper chromium oxide delafossite ($CuCrO_2$) has been considered a promising candidate *p*-type TCO, due to covalent mixing between Cr^{3+} and O^{2-}, high density of Cr *3d* states near the VBM, wide bandgap, reasonable optical transparency and tuneable properties by allowing doping substitution with aliovalent and/or isovalent cations at the Cr site [176,189,211–216]. In addition, it has the lower synthesis temperature and a favourable thermal stability in air among all delafossites.

1.5.2. Delafossite crystalline structure

The $CuCrO_2$ delafossite structure is composed of two alternating layers: a close-packed layer of slightly distorted edge-shared CrO_6 octahedra sandwiching planes of close-packed Cu cations, in dumbbell-shape linear coordination to oxygen anions in the adjacent CrO_6 layers [217–219]. The Cr cation is located in a distorted edge shared CrO_6 octahedra with Cr as central position with a nominally +3 oxidation state. The oxygen ion is in pseudo-tetrahedral coordination with one Cu and three Cr cations. In a simpler way, the delafossite structure can be visualized as consisting of two alternating layers: a planar layer of Cu cations in a triangular pattern and a layer of edge-sharing CrO_6 octahedra flattened with respect to the c-axis. Depending on the orientation of each layer in the stacking, $CuCrO_2$ has two polytypes: ABABAB stacking leads to hexagonal α-2H polymorph (P63/mmc) [ICDD PDF 04-010-329] [220], whereas ABCABC leads to the rhombohedral α-3R polymorph (R-3m) [ICDD PDF 04-010-330] [221]. In the primitive rhombohedral cell, there are only four atoms: one Cu, one Cr and two O atoms [222,223]; however, the hexagonal cell is conventionally used to describe

rhombohedral structures [224]. Within the Cu based delafossites, the $CuCrO_2$ has relatively small a-axis and c-axis (a = 2.97-3.05 Å and c = 17.09-17.10 Å for rhombohedral crystal structure).

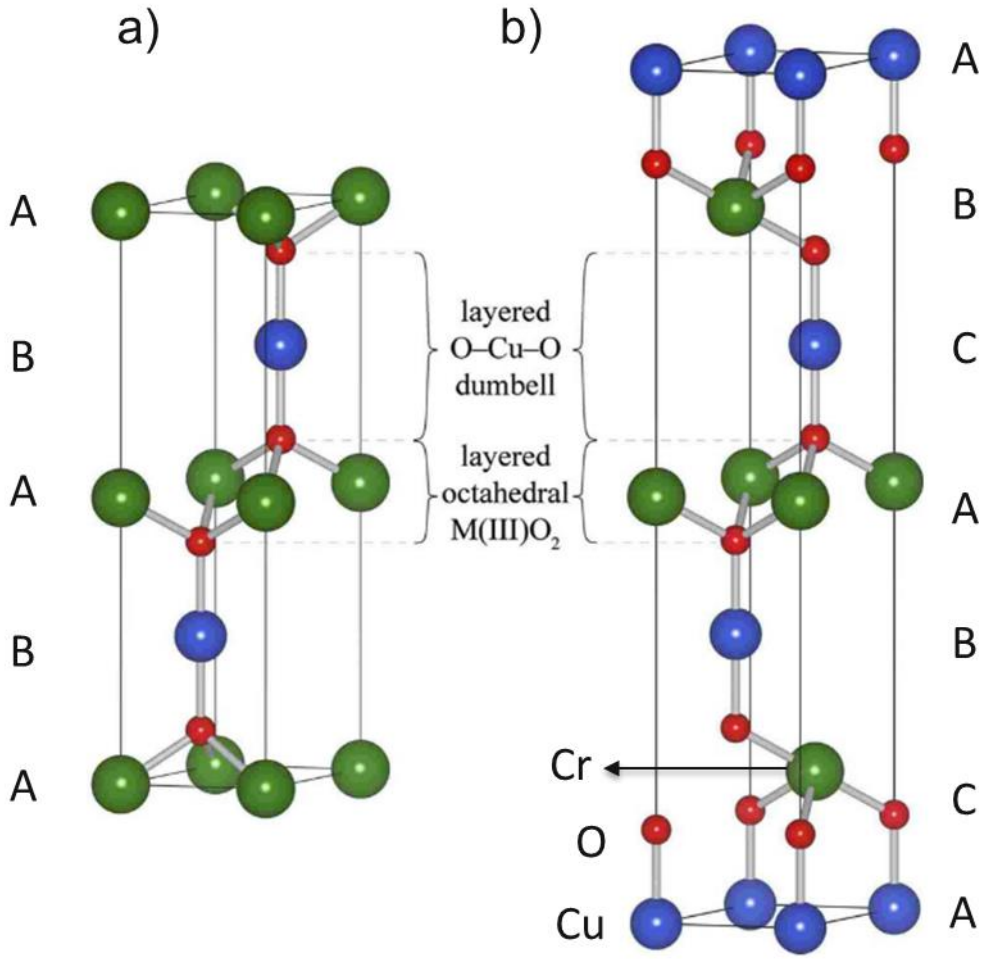

Figure 9 - Delafossite structure a) 2H polytype, P63/mmc space group symmetry; b) 3R polytype, R3¯m space group symmetry (rhombohedral unit cell). Adapted from [225].

It has been reported that the crystalline structure of delafossites has a large anisotropic electrical conductivity, with the in-plane (ab) conductivity (σ_{ab}) being far larger than along the *c*-axis (σ_c); [189,211,226–230]. $CuCrO_2$ was reported with a resistivity ratio of $\rho_c/\rho_{ac} \approx 35$ at 300 K, implying that [CrO_2] and/or [Cu^+] planes are better conducting path than Cr-O-Cu along *c*-axis [231]. According to electronic structure calculations performed for $CuCrO_2$ [232], the *d* orbitals of Cr^{3+} are mainly contributed near the Fermi level as compared to those of Cu^+, which could imply that the carriers would be mainly in the Cr planes rather than in the Cu ones. An increase in the (*00l*) orientation implies a greater presence of Cu^+ (*ab* planes) in the conduction path [232]. The effective mass is also affected by the B cation: a higher radius B leads to a larger *ab* lattice constant, increasing the Cu-Cu distances, reducing the VBM dispersion and therefore a higher effective mass, justifying the lower mobilities in delafossites compared with Cu_2O [112]. Nagarajan *et al.* reported that a B cation with smaller ionic radius

tends to decrease the lattice parameter in the Cu^{+} plane, increasing the overlap of Cu *d* orbital, hence improving the mobility [188]. However, results reported by Marquardt *et al.* [233] contradict this theory, where they measured a conductivity of $4x10^{-4}$ $S.cm^{-1}$ for $CuAl_{1-x}Mg_xO_2$, much lower for the reported one for $CuCr_{1-x}Mg_xO_2$ by Nagarajan et al. (220 $S.cm^{-1}$) and considering that Cr has a larger ionic radius than Al [193].

Delafossite has been consistently proposed to exhibit electrical transport limited by small polaron hopping [111,191,234–239]. This can be justified by the high effective mass, due to the polaronic interaction between carriers and the lattice [240]. In the case of small polaronic conduction, the distortion of the lattice extends over distances smaller than the lattice constant. The strong interaction between the lattice and the carrier, makes the latter become trapped by their own polarization [241]. Polaron conduction is characterized by hopping properties [242]. In contrast to other conduction mechanisms, lattice vibrations do not inhibit conduction but rather allow it, like as in ionic conductivity. Bywalez et al. [239], observed that the delafossite Seebeck coefficient was temperature-independent. This is in agreement with the theory of Nell et al. [243], that concludes that the small polaron conduction is characterized by a temperature-independent Seebeck coefficient. Similar results have been achieved by Ingram et al. [244] and Sinnarasa et al. [238]. The fact that the conductivity is thermally activated while the thermopower is temperature-independent is indicative of small polaron conduction [245]. In the case of small polarons the electrical conductivity is given by Mott and Davies [246]:

$$\sigma = \frac{A\sigma p}{T} e^{\frac{E_{\sigma p}}{k_b T}} \tag{30}$$

Where $E_{\sigma p}$ is the activation energy for polaronic conduction, k_b is the Boltzmann constant and $A\sigma p$ is a constant.

$CuCrO_2$ is a *p*-type semiconductor transparent to visible light, with a direct optical bandgap in the range of 2.95 - 3.30 eV [247]. It should be noted that in Cr *d-d* transitions are possible, inducing some coloration and decreasing transparency. The energy level of Cr^{3+} ions from partially filled *3d* shell will split into several levels according to the ligand field theory, the excitation of electrons from the lower to the upper of these levels could happen by absorbing photons in the visible range [248].

1.5.3. Delafossite deposition

Delafossites exhibit electrical conductivities ranging from insulating to semiconductive. Their electrical properties can be tuned, through different processing approaches, deposition techniques and conditions [233]. A myriad of deposition methods for $CuCrO_2$ have been reported, namely atomic laser deposition (ALD) [249], chemical vapour deposition [250], pulsed laser deposition (PLD) [205,251,252], sol-gel [253,254] , solid-state reaction

[196,199,255], spray pyrolysis [256,257] and sputtering [258,259]. Sol-gel techniques are more difficult to prepare high-quality films owing to the evaluation of thermodynamic and kinetic stability; nevertheless they are claimed to be more flexible regarding composition and stoichiometry control [218]. In some methods, such as ALD [249] and sputtering [238,258], annealing at high temperatures is needed to fully convert the parasitic phases (CuO, $CuCr_2O_4$ and Cr_2O_3) to the $CuCrO_2$ phase [223,226,238,260–266].

Pure (undoped) delafossite materials have relatively low conductivity (≈ 10^{-4} S cm^{-1}), due to low acceptor defects concentration [267]. There are usually two routes for $CuCrO_2$ thin films doping, intrinsic doping [154,258,268]: which is attributed to copper vacancies [229,230,269] and oxygen interstitials [190,194]; and extrinsic doping of which Mg substitution on the chromium sites is the most common [210,239,259,270–274], but also Fe, N, Al or Zn can be considered [203,275,276]. As shown by Chikoidze et al. [277], increasing Mg content will decrease oxygen vacancies and so enhance hole concentration, up to a maximum at 5% Mg. The same work shows an increase in conductivity up to 3 orders of magnitude with Mg concentration of 4.7%.

1.5.4. Delafossite post-deposition treatment

Post-deposition thermal treatment has been reported in delafossite for different purposes. Besides the conversion of parasitic phases to pure phase delafossite, when these are present, annealing the films may reduce the carrier concentration and increase transmittance values in the optical region up to 20% [260,262,265,278], as well as increase the crystalline quality. Changes of morphology and grain size have also been observed [200]. The preferred orientation (*001*) of $CuCrO_2$ films strengthens with increased temperature [265,279]. The optical bandgap of delafossite seems not to be affected by annealing processes [278]. Still in the literature there is a lack of quantitative studies, when it comes to $CuCrO_2$ without extrinsic doping, on the influence of the annealing processes on the electrical properties of the films.

1.5.5. Delafossite based gas sensing

$CuAlO_2$ delafossite thin-films, were first proposed in 2004, by Zheng et al. [13], as one of the first p-type semiconductor ozone sensors. They showed a sensitivity to ozone and reversible measurements using 0.1% ozone diluted in oxygen. Although this concentration is at least one million times bigger than the one that is required to be measured to be purposely used, it was still an important step in a direction of a low-cost p-type ozone sensor. When the ozone production was stopped, there was a recover of the baseline current. In figure 10 b) they presented the resistivity upon introduction of O_2 and Ar, showing no influence of these two atmospheres. The base resistivity seems however decreased when compared with the

base resistivity present in 10 a). In figure 10 c), they compared the influence of different film thicknesses, leading to the best response, for 0.1% of ozone, at 450 nm thick films. No further conclusions were drawn regarding the porosity change or other parameters with the different thicknesses.

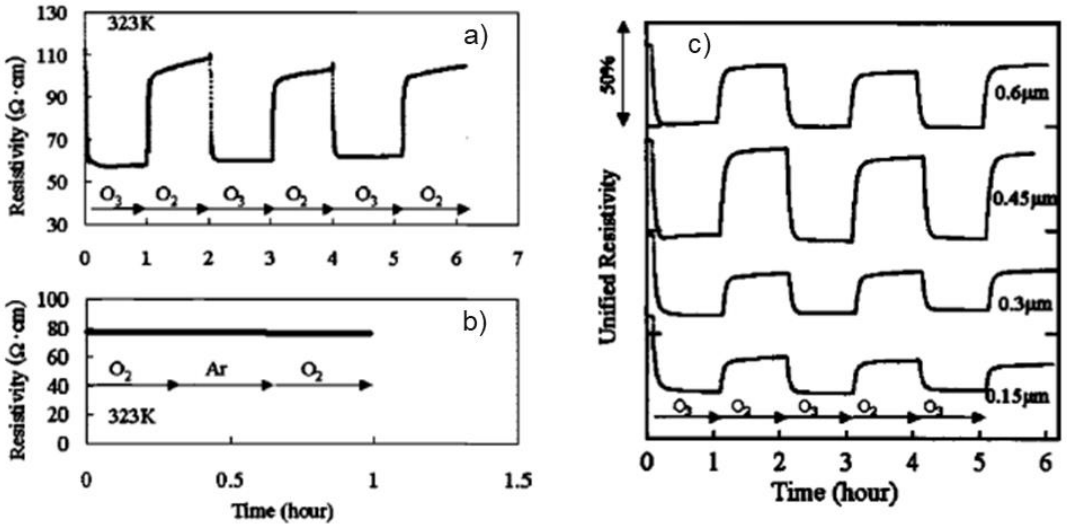

Figure 10 - Room temperature measurements by Zheng et al. [13]*, showing: a) reversible responses to 1000 ppm of ozone; b) response to O_2-Ar-O_2 cycles; c) comparison between different thin film thicknesses, with optimized response at 450 nm*

Later on, in 2009 [12,280,281], it was studied, the effect of ozone on $CuCrO_2$ thin films. In these works, it was compared the response of thin films prepared by PLD and thick films sintered using the sol-gel method, with a favouring of the latter. The author claims that PLD smooth and dense surface is the reason behind lower sensitivity compared with sol-gel that is prone to greater number of impurities. In their work [281], no thickness values or other thin film properties were studied, that would be key to enable this further discussion. Further on they compared the response of nanocrystals (10 - 80 nm) and microcrystals, when injecting different concentrations of ozone (50 ppm – 200 ppm), diluted in oxygen. The responses, depicted in figure 11, showed a clear improved response for the nanocrystal-based sensors, what the authors attributed to the increased surface area of sensing. In their work, no selectivity, or response comparisons were drawn in between oxygen response and air.

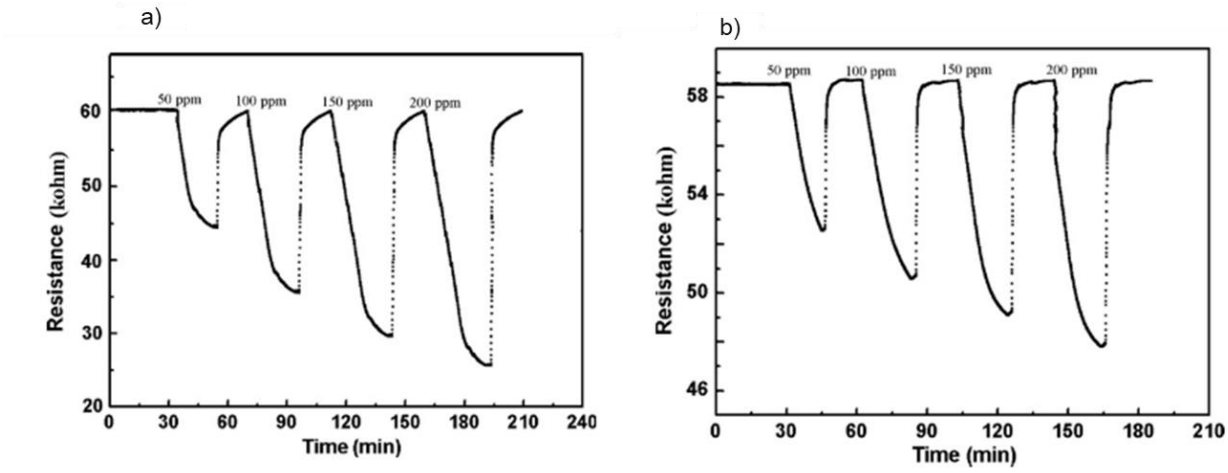

Figure 11 - Room temperature measurements by Zhou et al. [13]*, showing the response to increasing ozone concentrations of: a) $CuCrO_2$ nanocrystals and b) $CuCrO_2$ microcrystals.*

Nevertheless, the authors were able to show reversible measurements down to 50 ppm of ozone. In another work [280], they compared the results of different delafossite materials: $CuCrO_2$, $CuAlO_2$ and $CuYO_2$, with the first two showing very similar responses.

These results were a first step in the direction of integration of $CuCrO_2$ layers into gas sensing, in specific ozone sensing at low temperature (ideally at room temperature). Many limitations and a lack of data is still patent. The lowest studied ozone concentration was 50 ppm, with a sensitivity of 40%, whilst the limits imposed by the health agencies situate at 70 ppb for 8-hour exposure and 1 ppm can be considered immediate danger. There is still a gap of concentration to be filled of about 3 orders of magnitude. Furthermore, in these works, the authors scarcely related the material properties, electrical and morphological with the sensing responses. Selectivity was also barely addressed.

1.6. Conclusions

In this first chapter it was explored the ozone pollution dangers and presented the state of the art for ozone sensing. In particular, due to their small size and their potentially ease to be integrated into devices enabling the deployment of sensor networks, conductometric gas sensors were reviewed. In table 4, a comparison of different technologies for ozone sensing fabrication and the key features for usage in low cost sensor networks for air pollution monitoring is provided. Spectroscopy based sensors, have the best sensitivity and selectivity performance. They are however large equipments, expensive and impractical for integration. Optochemical based sensors, rely on change of optical properties of the materials used, upon ozone exposure. They suffer from cross-sensitivity problems and require an external light source, decreasing its integration potential.

Electrochemical based ozone sensors present good sensitivity to ozone. However, these sensors have a limited range of operation, since they need to be recalibrated upon changes of relative humidity and are quite susceptible to changes in oxygen content or other oxidizing gases [18,282]. These sensors are cheap to produce, but the periodic calibration and maintenance of the membrane and electrolyte required, drive up the long-term cost. The temperature range is also limited, as electrochemical sensors are temperature dependent.

Indeed, conductometric metal oxide ozone sensors seem to be the most promising for integration into this kind of devices. These can be split into two categories: standard conductometric ozone sensors, that work high temperature (usually above 250°C), thus increasing the power consumption due to constant heating and require a preheating time, up to 48 hours and photo-assisted conductometric ozone sensors, that albeit having the potential of working at room temperature require a UV-source, decrease the sensors selectivity and its integration potential. There is however still a strong lack of products based on conductometric gas sensors on the market.

Table 4 - Comparison of key features of different technologies used for ozone sensors for usage in low cost sensor networks for air pollution monitoring

Technology / Key Feature	Sensitivity (hundreds of ppb to ppm range)	Selectivity	Cost	Low power consumption	Response time	Miniaturization Integration
Spectroscopy						
Optochemical						
Conductometric metal oxide						
Photo-assisted conductometric						
Electrochemical						

In this work we are focusing on $CuCrO_2$, due to its promising electro-optical properties, low cost synthesis, possible miniaturization and preliminary studies indicating its capability to detect ozone at room temperature (even if the reported ozone concentrations are almost 3 orders of magnitude larger than desirable). The properties of p-type delafossites in general and $CuCrO_2$ in particular have been discussed. In comparison with others p-type TCM, the delafossite $CuCrO_2$ materials developed in LIST exhibit one of the highest trade-off: electrical

conductivity - visible transparency, with conductivities up to 100 S/cm and transparencies of about 50% in the visible range.

Off-stoichiometric copper-chromium-oxide, chromium rich, has been explored in the group [263,283–285], reaching some of the best electronic properties for undoped materials. Its conduction mechanism is directed by copper vacancies and unsaturated bonds. This makes it an interesting candidate that has never been deeply investigated for low temperature ozone sensing applications.

Films will be deposited by metal organic chemical vapour deposition (MOCVD), and the deposition parameters will be tailored in order to obtain different thin film properties. Post-deposition thermal annealing is another mechanism that will be on-purpose employed for the film property engineering. The interplay between the film's properties and the sensors response will be studied.

A deeper investigation and understanding of the chemistry and the kinetics of the reaction undergoing at the surface of the film will be studied to propose scientific rationales driving the sensing mechanisms of ozone onto off-stoichiometric copper-chromium-oxide, using the described power law behaviour, giving us insights of the reactions undergoing at the surface and a dynamic model based on the Langmuir theory of adsorption with the extraction of relevant kinetic parameters. Near ambient pressure X-ray photoemission spectroscopy (NAP-XPS) studies will give further insight about the ozone-delafossite reactions and its key feature drivers.

2. Experimental Methodologies

In this chapter, we present the original techniques developed during this work as well as the characterization techniques used. The core of this project is to develop conductometric gas sensors, based on off-stoichiometric copper chromium oxide, that are able to detect ozone concentrations in the tens/hundreds of ppb range. For this purpose, we have developed a totally new gas sensing setup, with the incorporation of ozone generators and a probe station. We furthermore took steps to introduce technological developments that can be key for the integration of delafossite thin films into active devices. These technological steps may allow new device architectures, leading to more complex gas sensing devices, such as p-n junction or back gate transistors-based sensors.

In a first part we describe the original techniques used. Firstly, is discussed the setup developed for gas sensing. Next, we discuss the thin film synthesis, using metal organic chemical vapour deposition. We then discuss the novel experiment in collaboration with Max-Planck institute in Germany, making resource to NAP-XPS, with the introduction of in-situ ozone, allowing us to study the interactions between the ozone molecules and the thin films surface. The preliminary research regarding $Cu_{0.66}Cr_{1.33}O_2$ etching is also discussed.

The sensor fabrication is discussed in the first part of this chapter, leading to the sensors schematically represented in figure 12. In this drawing: **1** - represents the substrate, in this case sapphire and silicon were used. **2**- is the delafossite thin film. Its thickness was changed between 32 and 150 nm and is represented by '**e**' in this schematic. The gold contacts (50 nm thick) are represented by the number **3**. The gold contacts are then connected to the electrical setup (number **4**), where a constant voltage is applied (1 V) and the current is measured. The distance between the pads (**L**) was kept constant at 500 µm, during this work.

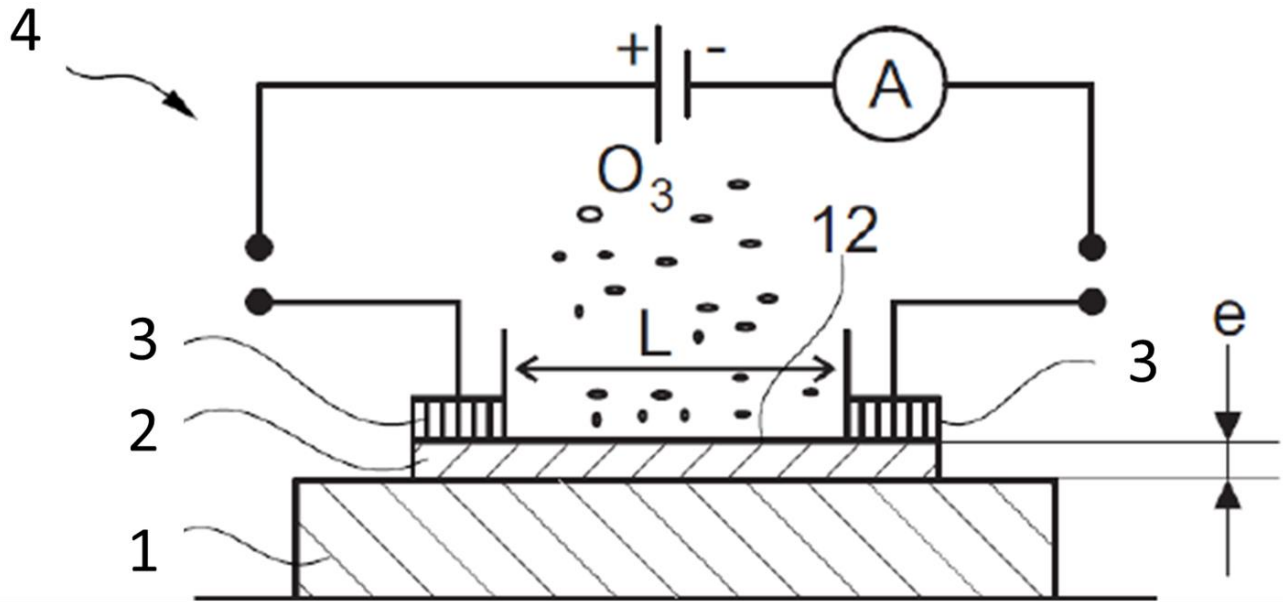

Figure 12 - Schematic drawing of the delafossite based sensor and the electrical measurements in the probe stage. 1 – Substrate, 2 – Delafossite thin film, 3 – Gold contacts, 4 – electrical apparatus, e -delafossite thickness, L – distance between contacts (500 µm).

The sensors properties were tuned by means of thermal annealing, which is discussed in sub-chapter 2.5. For the sensor fabrication, patterning processes were necessary, such as discussed in sub-chapter 2.7.

A p-n junction was fabricated, with copper-chromium-oxide and zinc oxide. The latter was deposited using atomic layer deposition (ALD), as is discussed in sub-chapter 2.6.

For the thin films and sensors characterization several techniques had to be used to extract important physical and chemical information, such as SEM, XRD, Raman, AFM and different electronic measurements (mainly I-V and Seebeck measurements).

2.1. Ozone setup development

An important part of this work was marked by the development of a gas testbench that allowed precise measurements of low ozone concentrations diluted in model gas. At the beginning of this project, no gas sensing measurements had been realized at LIST. Many of the studies here present were first developed in the WELCOME platform of the Université Catholique de Louvain-La-Neuve in Belgium. During the duration of the project, we have successfully created a gas sensing testbench that is fully operational, being currently used by several users of different projects. This involved: getting different quotations, run demos, installing the equipment and testing it. This is one of the important experimental accomplishments of this project.

For the development of this setup, a Linkam HFS359EV-PB4 model probe station, as shown in figure 13, was used. This probe stage was chosen due to the wide temperature range possibilities, from -195° to 600 °C and its small volume ($\sim 50\ cm^3$). This allowed us to make electrical measurements under controlled atmosphere and temperature. A limitation of this system is the manual placement of the probes, leading to necessarily large contact pads (ideally at least 500 x 500 μm^2). The ozone was generated from dry air, injected directly from a bottle, with a controlled flow. Analytik Jena UVP ozone generators (figure 14), 97-0066-01 and 97-0067-01, were used. The ozone generators are based on the photochemical reaction of ozone under shortwave UV (185 nm) to produce a continuous flow of ozone. A unit consists of a stable source of 185 nm radiation, based on a pen-ray mercury discharge lamp, a quartz reaction duct and radiation housing. This system, coupled with an appropriate supply of dry air or oxygen of uniform flow rate, will provide a stable source of ozone for hundreds of hours of operation. A graduated shield is used, for an accurate control of the length of exposed lamp, controlling the ozone concentration in the gas flow injected in the chamber. The calibration curves under dry air flow can be seen in figure 15. Two ozone generators are used to cover a wide range of ozone concentrations. While the first can produce concentrations from 50 to 600 ppb with a flow of 1 sccm/min of air, the second can produce concentrations up to 2.5 ppm, under the same conditions. Concentrations up to 5 ppm of ozone are possible by substituting the inlet of air by pure oxygen. This allows to control a wide range of ozone concentrations in the most relevant range for human life, i.e. from 50 ppb to 5 ppm.

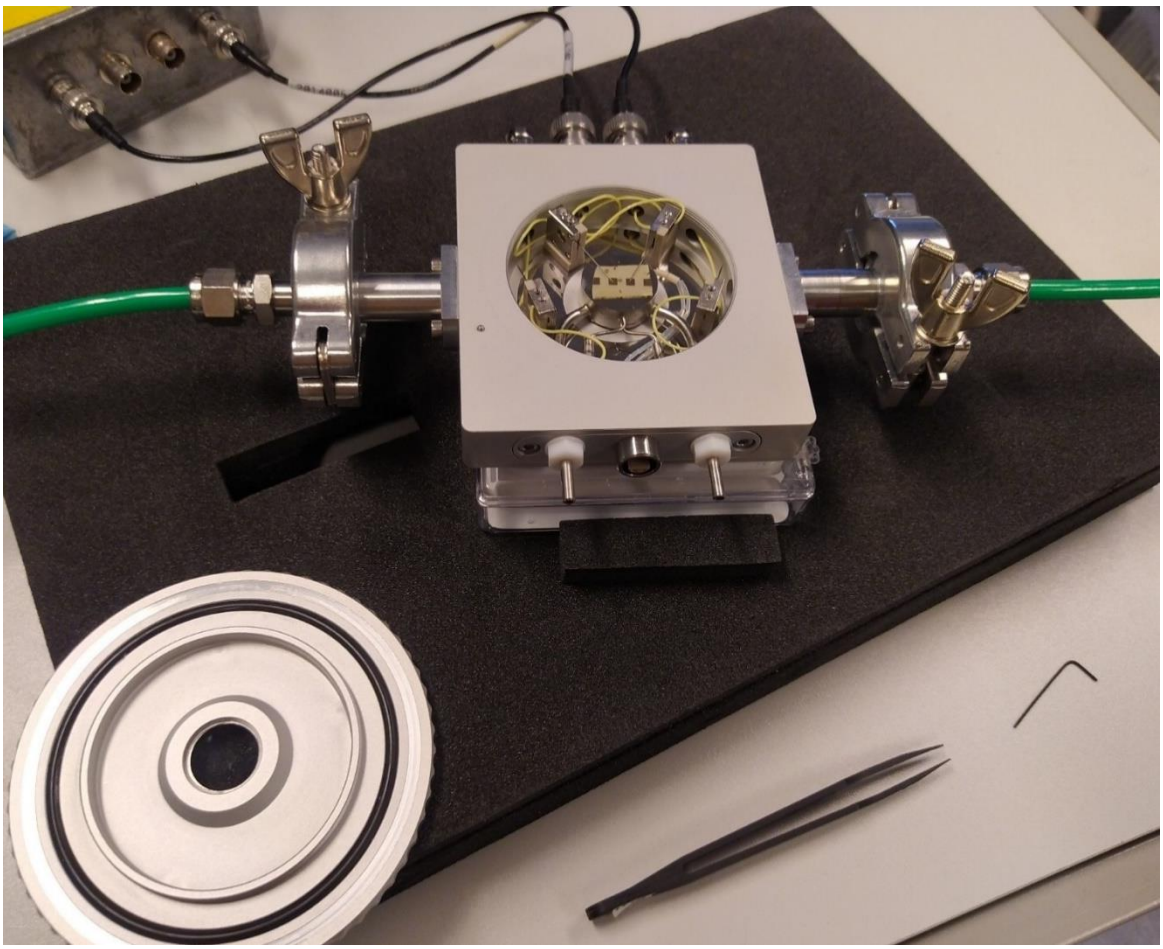

Figure 13 - Linkam HFS359EV-PB4 with testing delafossite sample with gold pads.

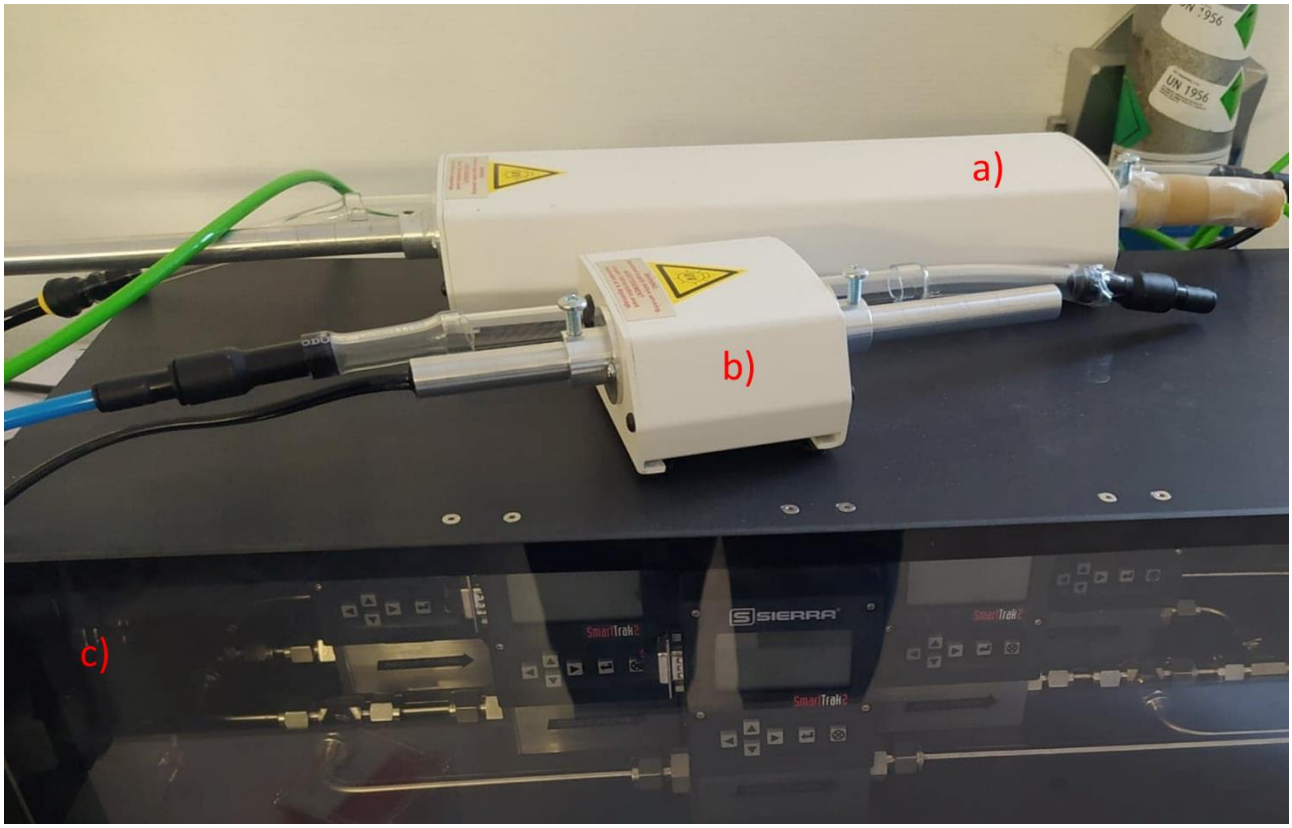

Figure 14 – a) Analytik Jena UVP ozone generator 97-0066-01; b) Analytik Jena UVP ozone generator 97-0066-02; c) Sierra mass flow meters for accurate gas flow control.

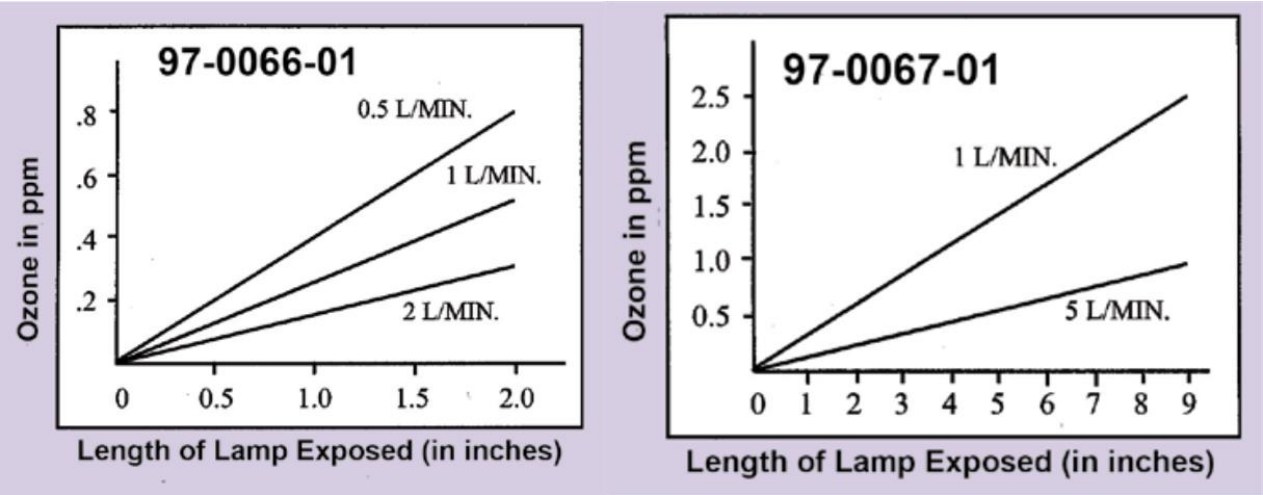

Figure 15 - Calibration curve under a constant flow of dry air for Analytik Jena UVP ozone generators (figure 12), 97-0066-01 and 97-0067-01.

A schematic representation of the gas sensing testbench is shown in figure 16. The gas is flown from the dry air bottle into a mass flow controller and through the ozone generator with a fixed aperture that allows a precise control of the ozone concentration. The ozone diluted in dry air is then flown into the probe station where the reaction takes place. The electrical measurements are done using a high impedance Keithley 2634B. The small chamber size, coupled with the room temperature gas flow, leading to an ozone half-life of 25 hours,

leads to a safe assumption that the ozone present inside the chamber, will be in the range given by the calibration curve of the ozone generator. PTFE tubbing was used for all connections, as it a material that does not assist in ozone decomposition.

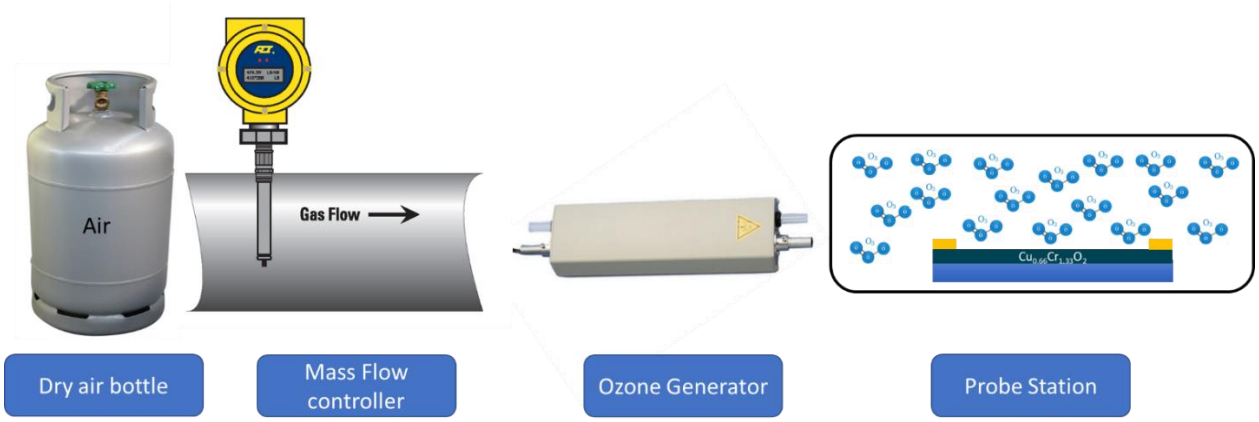

Figure 16 - Schematic of gas sensing testbench, with dry air being used; its flow controlled by a mass flow meter will pass through the ozone generator with a given aperture for a controlled ozone concentration. Lastly it will flow into the probe station where the ozone exposure to the delafossite will take place and the electrical measurements performed.

2.2. Metal Organic Chemical Vapour Deposition

Delafossite films were deposited using a Dynamic Liquid Injection - Metal Organic Chemical Vapour Deposition system (DLI-MOCVD), MC200 from Annealsys (Figure 17), which is a stagnation point-flow warm-wall reactor.

Chemical vapour deposition (CVD) is based on the injection of precursors (can be in solids sublimated, liquids evaporated or gases) that are transported to the chamber by a carrier gas and then can be mixed with other gases, such as oxygen for the formation of oxides. These gaseous reactants react or decompose into the substrate. This produces solid clusters in the solid-gas interface, creating a coating. In the case of Metal Organic CVD, metalorganic precursors are used, which are constituted of metal atoms bonded to organic radicals. Dynamic liquid injection refers to the fact that the precursors are actually injected in the liquid form. The precursors are kept under high pressure, 5 Bar and upon entering the reactor, the sudden decrease in pressure leads to a flash evaporation.

The used copper and chromium precursors are bis[2,2,6,6-tetramethyl-3,5-heptanedionato] copper(II) and tris[2,2,6,6- tetramethyl-3,5-heptanedionato]chromium(III), respectively ($Cu(thd)_2$ and $Cr(thd)_3$, Strem Chemicals). Cyclohexane solutions with a total precursor concentration of $[Cu(thd)_2] = [Cr(thd)_3] = 2,5$ mM were used. The total canister solution used was 1.075 g Cu(thd) + 1.5 g Cr(thd) diluted in one liter of Cyclohexane. The gas carrier used is N_2.

Deposition parameters were optimized as discussed in chapter 3. A table representing the best parameters, that were used for the deposition of the sensors studied in chapter 4, is presented.

Table 5 -Parameters used for delafossite deposition for ozone sensors studied in chapter 4.

Parameter	*Value*
Substrate temperature	450 °C
Reactor pressure	12 mbar
Precursor flow	2 g/min
Gas flow	2000 sccm
Gas carrier flow	350 sccm
Injector frequency	2.5 Hz
Rotation of Substrate holder	10 rpm
*Ratio of Precursors in solution (Cu/Cu+Cr) **	0.5
Deposition Time	450 – 1800 s

Figure 17 - Annealsys MC-200 DLI-MOCVD used for the growth of our delafossite thin films

2.3. In-situ ozone NAP-XPS analysis

X-ray photoelectron spectroscopy (XPS) is a surface analysis technique that provides valuable quantitative and chemical state information based on the photoelectric effect. The average depth for XPS measurements is usually up to 5 nm, with exponential weighting of the surface signal. XPS allows for the quantitative determination of the elemental composition, binding state and oxidation state [286]. The depth of the measurements is dependent on the elements analysed, as per their electron inelastic mean free path (λ), as represented in figure 18. In the case of Cr, O and Cu, one inelastic mean free path of 1.5 ± 0.3 nm is expected. This can be understood as that 66% of the signal comes from the top 1.5 nm, whilst 95% comes from the top 3 nm.

XPS spectra are obtained by exciting the sample surface with single energy Kα X-ray causing photoelectrons to be emitted from the surface, while simultaneously measuring the kinetic energy of electrons that are emitted from the material. The kinetic energy of the electrons depends upon the photon energy emitted by the x-ray source and the binding energy of the electron (i.e. the energy required to remove the electron from the surface). Peaks appear in the spectra from atoms emitting electrons with particular characteristic energies. The binding energy depends on the element from which the electron is emitted, the orbital that it was occupying and the chemical environment of the atom. From the binding energy and intensity of the peak, the chemical elements and their oxidation state can be identified and quantified. Therefore, XPS can be used to ascertain surface elemental composition. [286–290] An extensive review of thin film XPS analysis can be found in [290].

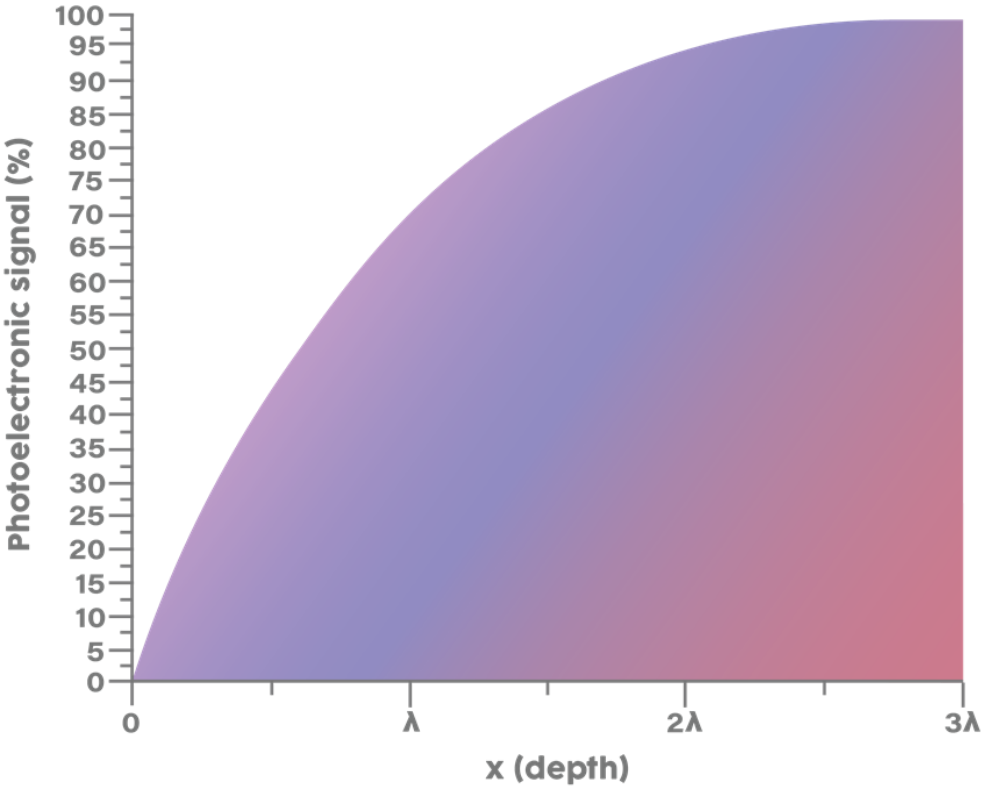

Figure 18 – XPS photoelectronic signal as function of depth, with each λ representing an inelastic mean free path of a photoelectron from an element

Traditionally, XPS is an ultra-high vacuum technique (< 10^{-8} mbar), due to inelastic scattering of the emitted electrons, leading to a poor signal noise ratio [291]. However in recent years, several efforts have led to the development of near ambient pressure (NAP) XPS, with the ability to work in pressures of tens of millibars [292,293]. The XPS working principle and the recent evolution of NAP-XPS, is carefully detailed elsewhere [294]. For this, however conductive layers are a must due to charging effect present in non-conductive samples leading to erroneous results. In a NAP-XPS measurement, a photoemission signal is measured from a sample, while the sample is exposed to a gas atmosphere. Pressures for NAP-XPS measurements typically range from 0.01 up to 100 mbar [291]. In this case, we present a study of the response of copper-chromium-oxide thin films to different ozone concentrations via XPS spectra. Different temperatures and gas environments lead to different core level and valence band maximum energies. A lower binding energy corresponds to a decrease in distance between the Fermi energy and the valence band maximum, (i.e. a more oxidized sample). A schematic representation of the expected behaviour of our copper-chromium-oxide thin films upon ozone exposure is present in figure 19. The bandbending in the different core levels and the valence band maximum is expected to be in the same range [295].

Different scan resolutions can reveal different information. A survey scan was first done in order to identify the elements present at the surface. A high-resolution scan of the most important elements, Cr, Cu and O were then performed to analyse the types of bonds and concentrations present at the surface. The valence state of Cu and Cr were carefully investigated, as different electronic states have different binding energies [296].

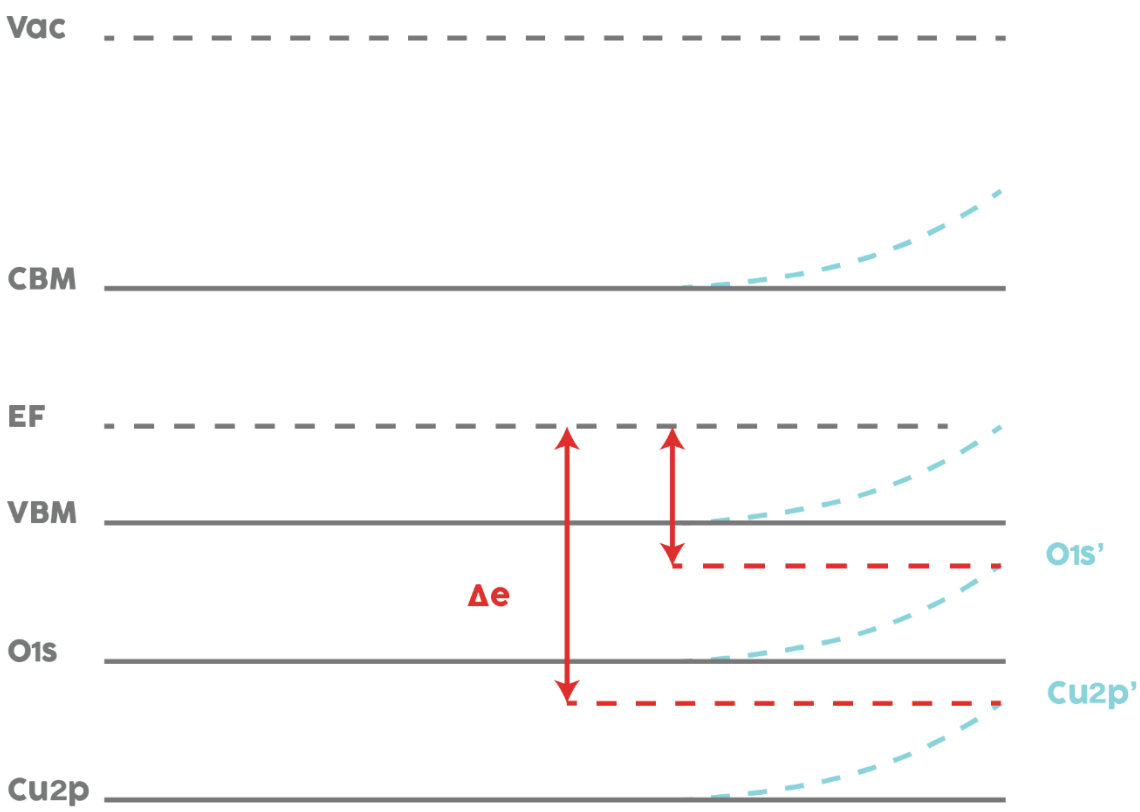

Figure 19 - Schematic representation of the band structure of copper-chromium-oxide, before and after ozone exposure, evidencing the expected bandbending

Furthermore, charge transfer can be observed, by shifts in the core-levels of the XPS peaks [297], as depicted in figure 19. Additionally, the electronic structure of the surrounding matrix can alter the screening properties of the photoemission process, giving rise to additional binding energy shifts and possible changes in peak line shape. In this case via the shift of core level peaks, information can be gathered about the charge transfer that happens upon ozone exposure.

The determination of surface potentials is straightforward using XPS, which allows the direct assessment of the Fermi level position with respect to the core levels. A higher binding energy corresponds to a larger distance between the Fermi energy and the measured electronic state, i.e. a more reduced sample [293].

All spectra presented in this work were measured using a Phoibos NAP-150 hemispherical analyser from Specs GmbH. The nozzle used to separate the sample environment from the electrostatic lens system had a diameter of 0.8 mm. The distance from the sample surface to the entrance aperture of the nozzle was always set to be equal to the nozzle diameter. Prior to the presented spectra, heating up to 600 °C under pure oxygen was performed to remove surface carbon. During XPS measurements gas was leaked into the sample chamber using a mass flow controller, and pressure was held constant during measurement by means of a throttle valve. The throttle valve controls the pumping cross section of a differential pumping stage. Pressure was measured using a diaphragm capacitance pressure. Nano ozone generator from absolute ozone was used, due to its high ozone production capacity and the low pressures required for performing the measurements. During ozone measurements presented, the flow was kept constant at 50 sccm/min, for a constant ozone production of 15 % in weight. The change in pressure was used to vary the ozone partial pressure and therefore its concentration. All peaks and atomic quantification were performed with Casa XPS software.

2.4. Delafossite Etching

In order to implement delafossite into applications, there are important process developments that need to be optimized. To pattern device structures, a key element is the etching process. There is however lack of literature regarding the etching of Cu-Cr-O delafossite. Only one group, Lim et al. [298,299], studied $CuCrO_2$ etching processes, to the best of our knowledge. Wet etching has been achieved using $(NH_4)_2Ce(NO_3)_6/HNO_3/H_2O$ solutions to produce microstructures of the order of 100 µm.

We studied the influence of a standard chromium etchant (Sigma Aldrich) in our off-stoichiometric delafossite. The product consists of a mixture of Amonium Cerium Nitrate (20 – 25 %) and Nitric Acid (5 – 10%) diluted in water. This solution was further diluted in water, in concentrations of 2.5 to 10 %. Standard polymeric photoresist was used for the masking process. Figures 20 and 21, show the results of sequential etched / non-etched lines, with 10 and 10 µm; 2 and 5 µm; 5 and 5 µm.

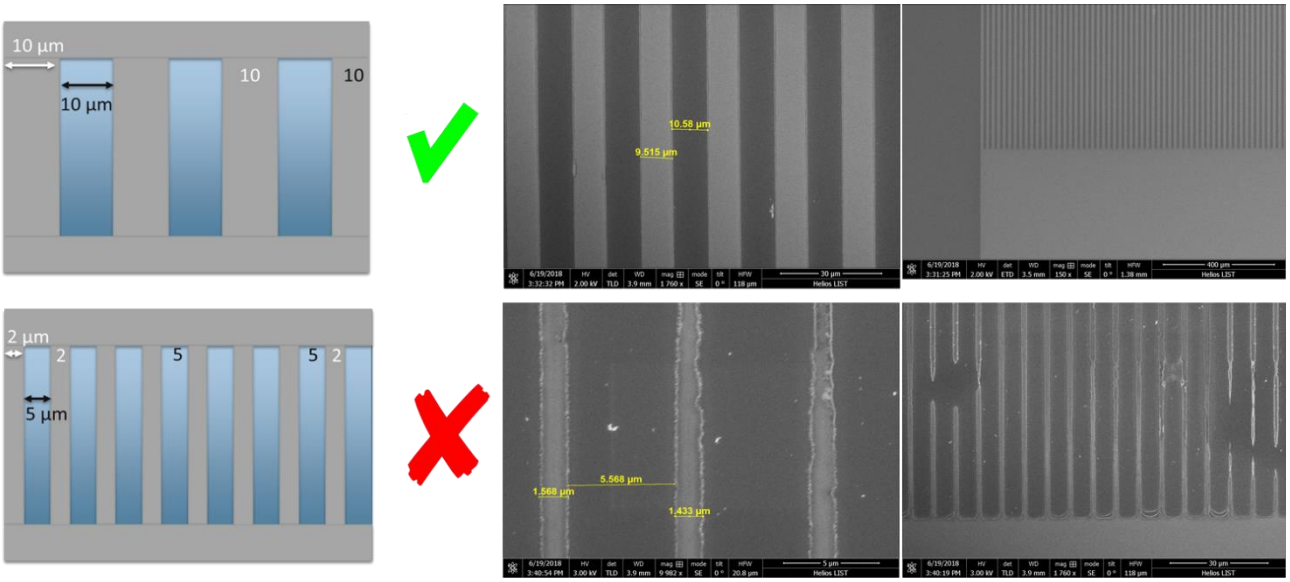

Figure 20 - Wet Etching of Cu-Cr-O delafossite using standard chromium etchant (5%) diluted in water, showing the ability to etch efficiently copper-chromium-oxide for microstructures down to 10 µm and the technology limitations when approaching the micrometric unit

For smaller lines (i.e. < 2 µm), the technology limitations are evidenced, with some of the copper chromium oxide lines being broken. The isotropic nature is characteristic of the wet etching processes, thus dry etchings are preferred when sub-µm resolutions are sought. Preliminary Dry etching studies PLASMATHERM 790 Reactive Ion Etching, with a mixture of 75 % Cl_2 / 25% Ar, were satisfactory, but need further confirmation regarding the resolution and the minimum thickness to be etched, that were out of the scope of this work.

All in all, it is noteworthy that our delafossite can be etched, using a cheap and standard solution for device scales within a few micrometre range, making it furthermore interesting for device applications.

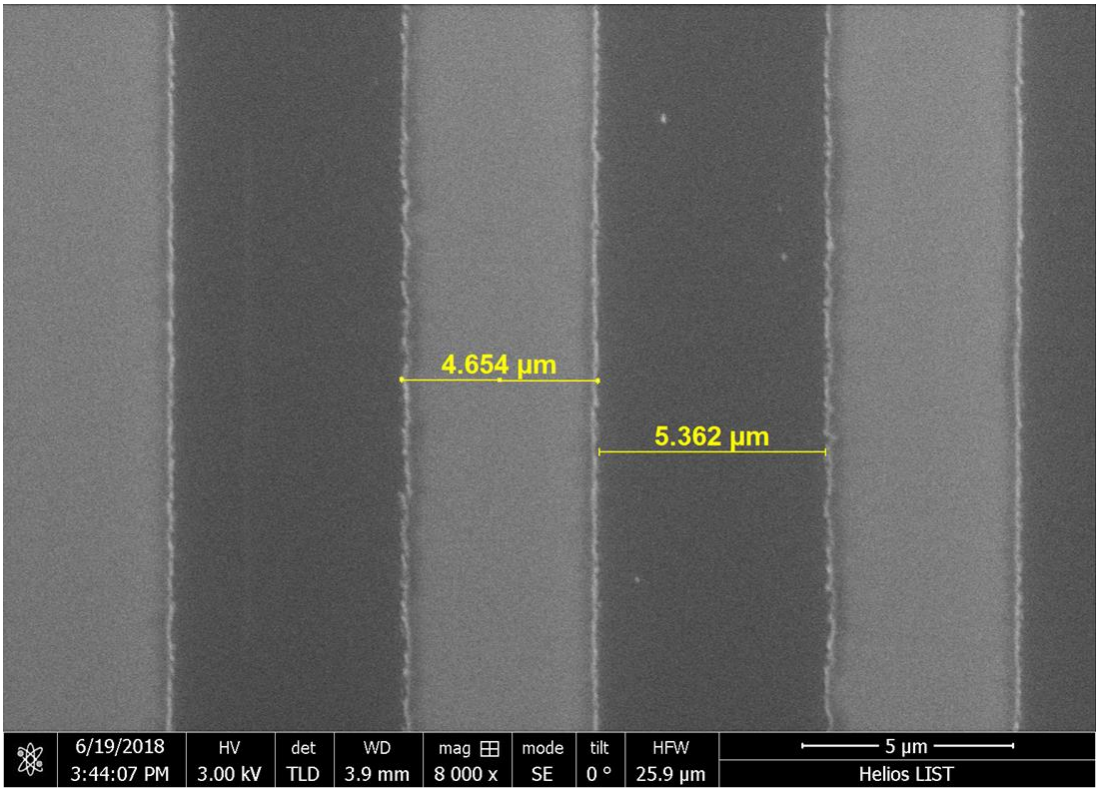

Figure 21 - Wet Etching of delafossite using standard chromium etchant (5%) diluted in water, showing the ability to etch efficiently copper-chromium-oxide for microstructures of 5 µm

2.5. Thermal Annealing

All the annealing processes were performed on a Rapid Thermal Annealing reactor (Annealsys), under vacuum (< 10^{-2} mbar). The annealing curve was first a heating ramp with 5 °C/s, a waiting time at constant peak temperature and a cooling ramp with -5 °C/s. The varied annealing time was the waiting time and the heating and cooling times are not considered.

2.6. Atomic Layer Deposition

Atomic layer deposition (ALD) was carried out in the ALD reactor Beneq TFS 200 (Figure 22). The deposition of ZnO followed the process described by Roge et al. [300], using in our case Argon as purge and carrier gas, for 500 cycles and with a pulse sequence: 1 - Diethylzinc (DEZ, $Zn(C_2H_5)_2$) pulse 150 ms; 2 - purge 10 s; 3 - H_2O pulse 200 ms; 4 – purge 10 s.

Figure 22 - ALD reactor Beneq TFS 200 used for ZnO for the transparent P-N junction developed.

2.7. Patterning Processes

Lithography processes were necessary for several parts of this work. The gold contact deposition on the sensors followed a standard lift-off process using a bilayer of photoresist LOR3A with 300 nm and on top a Shipley S1813 with 1.2 µm. The exposure was processed using Heidelberg Instruments MLA 150. The samples were developed using MF319 for 40 s. The gold contacts were deposited using a DC sputtering, Leica EM ACE 600. The lift-off was completed with remover PG.

For the P-N junction developed, an etching of ZnO was carried out. A similar lithographic process was used with a bilayer of photoresist. The samples were developed and etched in 0.1% $FeCl_2$ during 15 s.

2.8. Characterization techniques

Several techniques were used for the characterization of our thin films. Extensive reviews of these techniques can easily be found. It is not in the framework of this thesis to do so, only a brief description of the equipment used are provided.

2.8.1. Scanning electron microscopy

The surface morphology of the films was inspected by Scanning Electron Microscopy (SEM) with 10 kV of acceleration voltage, FEI Helios Nanolab 650 with EDX spectrum analysis connected to SEM Oxford Instrument Xmax 50mm^2. Thickness of the $CuCrO_2$ films was measured using the same equipment with a cross-section view on silicon. The analyses are performed under vacuum (≈ 10^{-6} mbar) and all images are obtained by secondary electron detection.

2.8.2. X-Ray diffraction

The film crystallographic structure was examined by X-ray diffraction (Diffractometer Bruker D8 Discover with Cu Kα radiation (l = 1.54 Å) at 40 kV and 40 mA, in Grazing incidence configuration. In GIXRD configuration, the X-ray beam enters the sample at a very low angle of incidence. The use of small incidence angles limiting the wave penetration and thus increasing top surface sensitivity leads to better signal for thin films due to a lesser contribution of the substrate, what is of critical importance for thin films. The incidence angle was kept at 0.5°.

2.8.3. Raman spectroscopy

Raman spectroscopy is based on an inelastic scattering of light by a material. Raman analysis may provide important structural properties. In this work, Raman spectra are performed by a Renishaw inVia confocal Raman microscope. It was used a laser beam with 442 nm wavelength to characterize the chemical structure of delafossite thin films.

2.8.4. Atomic force microscopy and Kelvin Probe force microscopy

Topography acquisitions were carried out with a Bruker's AFM Innova in tapping mode by maintaining the amplitude of the cantilever's resonance constant. The surface roughness was extracted via the NanoScope software.

Kelvin Probe Force Microscopy (KPFM) measurements have been performed in the same equipment using the amplitude modulation to determine the contact potential difference between the Pt-Ir coated tip and the sample surface. The analysis is done in one pass mode, the first resonance amplitude is used to track the topography while the KPFM signal is acquired at a second frequency (23 kHz). Freshly cleaved Highly-Oriented Pyrolytic Graphite (HOPG) is used as reference. Measurements are performed under dry N_2 atmosphere in order to avoid water condensation on the surface.

2.8.5. Electrical measurements

Resistivity was measured using four probes in linear configuration while for the Seebeck effect measurement a homemade system was used with a copper wire as reference. 4-Point-Probe measurements were realized on a Jendel Cylindrical four-point linear probes head with a Keithley Source Meter 2614B to extract the sheet resistance of the films according to:

$$Rs = 4.532 * 0.925 * \frac{V}{I} \tag{31}$$

The mobility of copper chromium oxide thin films is too low for the Hall effect measurement system, we have at our disposal. The mobility was therefore extracted from the Seebeck coefficient (equation 32). The set-up is shown in figure 23. It is made of two copper pieces attached to each other through an insulating plate in order to avoid thermal and electrical conduction between each piece. The larger copper piece is thermalized to the base temperature (room temperature during the experiments here), while the second smaller copper piece is heated through a resistive heater. The temperature of each piece is measured by two calibrated Pt100 resistive thermometers embedded in the copper pieces and thermally connected to them by Apiezon® grease. The thermo-voltage is measured by a high impedance source-measure unit Keithley 2634B, directly between each copper piece using a thermalized copper wire, which serves as reference material. The sample is mechanically pressed on both copper pieces, with the deposited film being directly in contact to each copper piece. Due to the temperature difference there is a small voltage build-up. The difference in voltage can be plotted as function of the difference in temperature to extract the Seebeck coefficient, as:

$$S = \frac{\Delta V}{\Delta T} \tag{32}$$

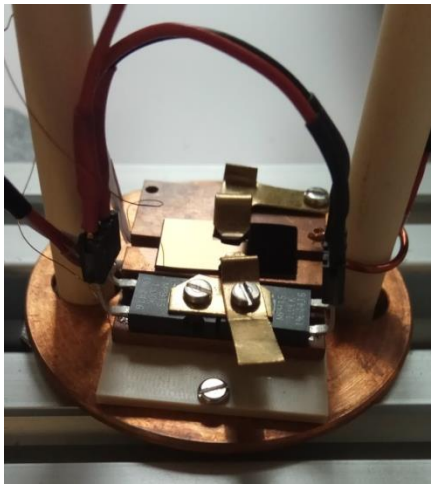

Figure 23 - Seebeck setup with a copper wire as a reference

Temperature dependence measurements were performed on the probe station cascade PM-8 connected to a Keithley 4200A. The electrical characterization of the junction was performed using a configuration with 2 point-probes biased at different voltage; when applying a voltage sweep, the current is measured between the two tungsten tips, as shown in figure 24. The Sweep tip was kept on the $CuCrO_2$ contacted with silver paste and the constant voltage 0 V was kept on ZnO pads.

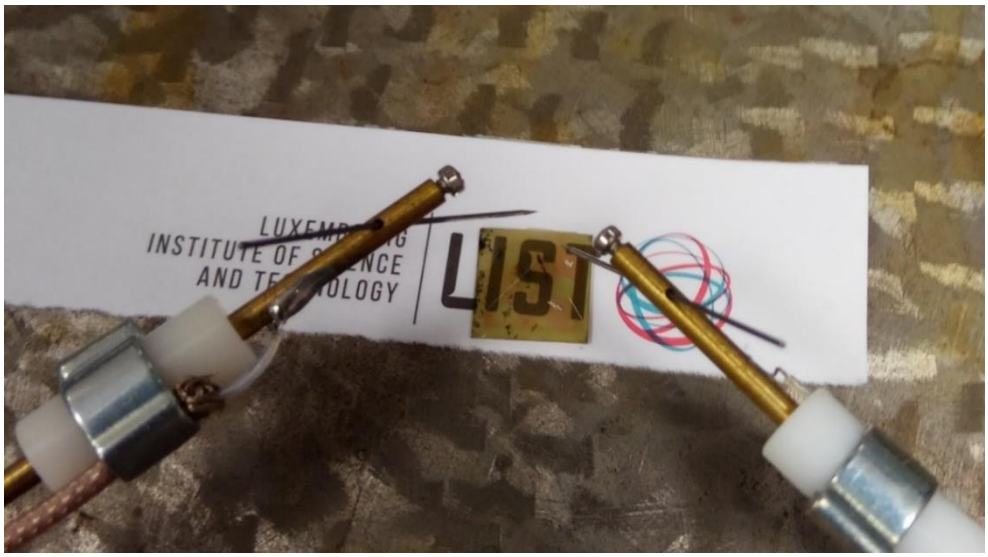

Figure 24 - P-N junction photography with the two contacts used for I-V Sweep

3. Copper-Chromium-Oxide Study

In this chapter we present, in a first part the previous studies done in the group that led to our basic understanding of the ideal conditions for pure delafossite copper-chromium-oxide growth. Next, we discuss the growth process and our fine tuning, by change of several deposition parameters and its influence on the conductivity of the thin films.

Ozone sensing is led by the trapping of electrons, in this case, since our thin film is a p-type semiconductor, it will lead to the injection of majority carriers (holes). Due to the nature of this reaction, the carrier concentration will be a key parameter for the sensing response. The mobility of the thin films on the other hand should be maximized, leading to a higher conductivity. There is an expected compromise between the increase in sensitivity of the films to ozone exposure and a high resistivity that would not be easy to characterize using a standard electronic system. Furthermore, the thickness of the films, porosity, the surface area, crystallite and grain size are all properties that will be studied and further correlated with ozone sensing response. It is expected that thinner films, increased porosity and decreased grain size should lead to better sensing responses.

The deposition parameters were optimized for maximum conductivity as per requirements in a common TCO. Then we present the study of the post-deposition thermal annealing on the defect healing in the material that lead to changes in the electronic properties. This approach leads to an intrinsically conductive material and with carefully studied annealing tune the electrical properties and morphological ones, such as the grain size and surface area. Ultimately, leading to the widest range of processing feature possibilities that can be optimized for reasonable conductivity with highest sensing response.

3.1. Previous studies – Delafossite deposition

$CuCrO_2$ delafossite can be deposited using many different methods. Among those, metal organic chemical vapour deposition (MOCVD) has showed a great potential, achieving the best reported conductivities without recourse to external doping and competitive optical transparency. It is also important for scalable processes due to its large area compatibility, high uniformity when compared with PLD or sol-gel technics and batch deposition possibilities. In previous works, done at LIST [212,234,269,301], it was reported the fabrication of a new peculiar stoichiometry of copper chromium delafossite characterized by an important deficit of copper, leading to conductivities higher than 100 $S.cm^{-1}$ without recourse to external doping [14,263,285]. This record value for intrinsically doped delafossite represents only one order of magnitude lower than its n-type counterparts. It should be noted

that the crystalline delafossite phase is however preserved. The off-stoichiometric $Cu_{0.66}Cr_{1.33}O_2$ was found in both as-deposited and annealed films whilst the delafossite structure remains unaltered [14]. As-deposited films present high carrier concentration, up to 10^{22} cm^{-3}. A new structural defect, consisting of chains of copper vacancies has been observed [176,285]. This defect was held responsible for the high level of p-type doping. Upon thermal annealing an important atomic rearrangement of atoms and defects occurs leading to the shrinkage of chains of vacancies almost until their extinction. This healing led to decreases of five orders of magnitude in the conductivity [176]. This has been confirmed by studies using a secondary ion mass spectroscopy (SIMS) system coupled with helium ion microscopy (HIM), specially developed at LIST and capable of producing high resolution elemental maps. Together with energy dispersive x-ray (EDX) and high-resolution transmission electron microscopy (TEM), it lead to further confirmation that the changes in conductivity observed were triggered by compositional rearrangement mechanism governed by a Ostwald ripening mechanism based on the dissolution of the chains of vacancies into single Cu vacancies migrating to grain boundaries [302].

Crêpellière et al. [234] and Lunca-Popa et al. [212,269], realized a profound study of the deposition conditions, in order to obtain pure phase delafossite materials as well as to optimize the films conductivity. A summary of this study is presented here.

3.1.1. Precursors Influence

Pulse direct liquid injection is an efficient process technology for the controlled supply of precursor solutions. The influence of the precursor concentration ratio, $Cu(thd)_2$ (bis[2,2,6,6-tetramethyl-3,5-heptanedionato]copper(II)) and $Cr(thd)_3$ (tris[2,2,6,6-tetramethyl-3,5-heptanedionato]chromium(III)), on the structure and electrical conductivity of the delafossite thin films, has been studied. The influence of the precursor copper fraction (χ) is represented in figure 25. As observed a fraction (χ) below 0.6 is necessary to avoid parasitic phases. This results in an excess Cr present in the thin films. The best conductivities were achieved at a fraction of 0.5. At the time the 17 S/cm were the best values obtained for undoped delafossites. A fraction of 0.5, leads to an off-stoichiometric delafossite ($Cu_{0.66}Cr_{1.33}O_2$), which is related with the increase in conductivity.

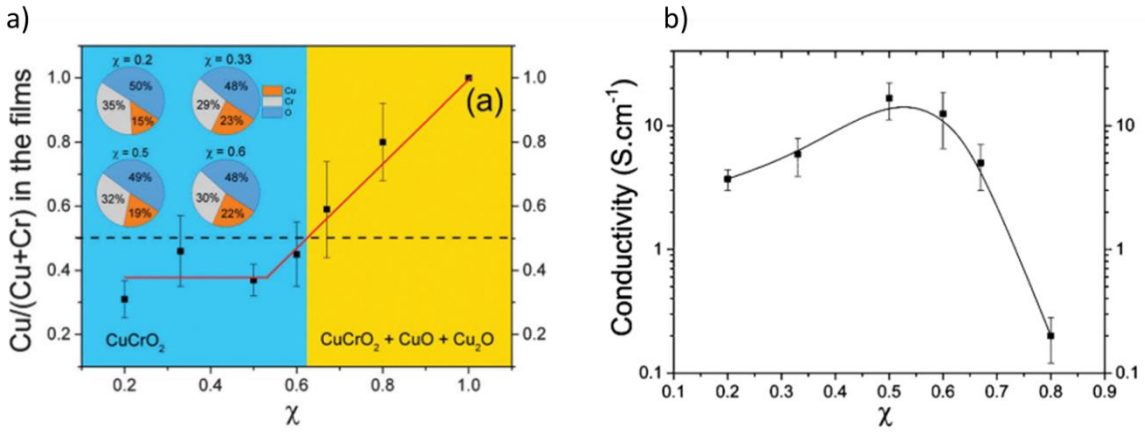

Figure 25 – a) Chemical composition of film growth at 370°C with precursor solutions featuring $0.2 \leq \chi \leq 0.8$ *as measured using XPS b) Conductivity as a function of the copper fraction w in the precursors' solution for films grown at 370°C. From* [284].

3.1.2. Parameters influence

Lunca Popa et al. [212], studied the influence of several deposition parameters on the electrical properties of the films. It was observed an increase of crystallinity with films deposited with higher precursors concentration and/or at higher temperature. The growth rate is also increased by the temperature of the reactor. Addition of a 150 W RF plasma discharge further increases the deposition rate, however at the cost of the conductivity. The best conductivities were achieved in the 400 – 500 °C temperature range. At higher temperatures (up to 650 °C), the native crystalline defects decrease, decreasing the carrier concentration of the thin films.

In this chapter, we report on the continuation of the study of the deposition parameters of copper-chromium delafossite, deposited by MOCVD with a further focus on the thin film properties that are essential for gas sensing, such as grain size, porosity and electrical conductivity. We then propose to use thermal annealing routes to better control the carrier concentration and tune ultimately the thin film properties for use in devices.

3.2. Copper-chromium-oxide growth

Herein we present the characterization results of delafossite copper-chromium-oxide thin films, grown by pulsed injection MOCVD, for the purpose of tailoring the main features impacting the sensing properties. The effect of the growth temperature, precursor mass injection, deposition pressure, substrate rotation and deposition time on the electronic and morphological properties of the films are studied.

As observed in the first chapter (state of the art), the morphological (grain size, porosity, surface area) and electrical properties (carrier concentration, mobility) of the materials can have a huge impact on the sensors behaviour. It is therefore key to explore these properties and understand how one can change them. Ultimately, a comparison is to be drawn between the ozone response or otherwise lack of it.

A summary of the input parameters in the pulsed injection MOCVD can be found on table 6.

Table 6 - Summary of main input parameters for deposition control in pulsed injection MOCVD - MC2000

Parameter	*Minimum*	*Maximum*
Substrate temperature	RT	750 °C
Reactor pressure	1 mbar	Atmospheric pressure
Precursor flow	0.5 g/min	3 g/min
Gas flow	0 sccm	5000 sccm
Gas carrier flow	50 sccm	500 sccm
P_{O2} +	0 mbar	ATM
Injector frequency	1 Hz	5 Hz
Rotation of Substrate holder	0	30 rpm
*Ratio of Precursors in solution (Cu/Cu+Cr) **	0.2	0.66
Deposition Time	0	N/A

+ Partial pressure of O_2 can be increased up to close to atmospheric pressure, considering a minimum gas carrier flow is necessary to inject precursors into the reactor.

***** Ratio of precursors to create pure phase delafossite, as per previous studies [234].

The ratio of precursors in solution, injector frequency, gas flows and oxygen partial pressure, have been thoroughly studied, so for the purpose of this work, their influence was not further investigated. Different substrates: Silicon (p-doped and undoped) with a silicon oxide passivation layer and sapphire were explored. Annex 1 depicts a summary of the deposition conditions studied and their influence on the thin film conductivities.

3.2.1. Rotation

The rotation effect on the thin films, has been investigated, while all other parameters are kept constant. In figure 26 a) we can see a thin film deposited without substrate rotation

and on 26 b) with a constant rotation of 10 rpm. As one can notice the homogeneity of the thin films is hugely impacted when depositions are made without substrate rotation. Increasing the rotation above 10 rpm, comes at a risk of mechanical damage to the susceptor. For this reason, further depositions were made with constant rotation at 10 rpm.

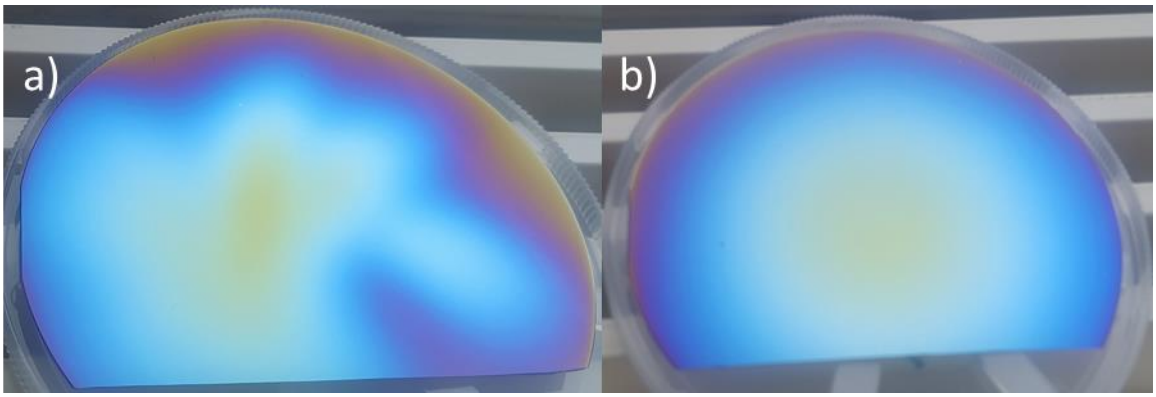

Figure 26 - Comparison between copper chromium delafossite deposited by MOCVD: a) without substrate rotation; b) with substrate rotation

3.2.2. Precursor mass rate

The influence of the precursor mass rate, injected into the chamber on the electrical properties of the films, was investigated using two deposition times: 900 and 1800 s (Table 7).

Table 7 - Effect of precursor injection on thin film's electrical properties and thickness

Deposition	Substrate	Substrate Temperature (°C)	Deposition time (s)	Injection (g/min)	Thickness (nm)	Conductivity (σ/cm)
S1	Si	450	900	2	75	5.71
S2	Si	450	1800	2	140	6.67
S3	Si	450	900	1	42	0.95
S4	Si	450	1800	1	68	0.48

The resulting conductivity of the films, is greatly reduced when the injection rate is decreased from 2 to 1 g/min. The injection frequency is kept constant at 2.5 Hz. This is the case for the two deposition times studied. The thickness of thin films was observed by cross-section SEM. As expected, the lower injection rate, results in lower thickness, when the deposition time is kept constant. The rate of precursor injection has been kept constant at 2 g/min, in all further referred depositions.

3.2.3. Deposition pressure

The pressure inside the chamber during the deposition step has been varied between 6 and 12 mbar, as depicted by table 8. Higher pressures (> 12 mbar) lead to possible parasitic

phases as previously discussed [212,234]. Pure phase delafossite results from samples P1 and P2. Higher electrical conductivity results are achieved for depositions at 12 mbar. This pressure is kept constant in all the other depositions mentioned.

Table 8 - Influence of the deposition pressure in the electrical properties of the thin films

Deposition	Substrate	Substrate Temperature (°C)	Deposition time (s)	Pressure (mbar)	Conductivity (σ/cm)
P1	Sapphire	450	900	12	34.7
P2	Sapphire	450	900	6	7.6

3.2.4. Substrate temperature

Previous reports by Crêpellière and Lunca Popa et al. [212,234], show that pure phase delafossite can be obtained at temperatures higher than 370 °C. However, above 550 °C, the electrical conductivity of the thin films has been shown to be severely negatively impacted. In table 9, we present our study, showing the influence of the deposition temperature, on the film's electrical conductivity, in the temperature window, 425 – 550 °C.

Table 9 - Study of the deposition temperature influence on the electrical properties of the thin films

Deposition	Substrate	Substrate Temperature (°C)	Deposition time (s)	Conductivity (σ/cm)
C1	Si	450	900	7.14
C2	Si	450	900	9.52
C3	Si	500	900	0.067
C4	Si	500	900	0.043
C5	Si	550	900	0.002
C6	Si	550	900	0.002
C7	p+ Si	450	900	7.16
C8	p+ Si	475	900	1.26
C9	p+ Si	450	900	8.19
C11	p Si	425	900	4.77
C12	p Si	450	900	9.74
C13	p Si	425	900	3.75

The increase in deposition temperature to 500 and 550 °C, leads to a severe decrease in the thin films conductivity, 2 and 3 orders of magnitude respectively. Pure delafossite phases are preserved, although higher temperature, leads to a lower amount of intrinsic defects, that governs the conductivity of our copper-chromium-oxide, explaining therefore the decreased conductivity. When comparing depositions made at 425 °C and 450 °C, the films conductivity is of the same order of magnitude. Tests were done using different substrate doping, from

undoped Si to p+ Si (boron concentration $N_A = 1 \times 10^{19}$). On top of the substrates was then grown a 20 nm thick silicon oxide layer, for electrical passivation. No relevant difference in the electrical conductivity of the thin films was found when comparing different doping levels of the silicon substrate.

3.2.5. Deposition time

Upon setting the other parameters, the influence of time can have a direct impact on the studied properties of thin films, that are key to gas sensing (conductivity, grain and crystallite size, surface area, roughness). In table 10 we analyse how changing the time of the depositions affects the electrical properties of the thin films.

Table 10 - Deposition conditions for relation between deposition time and conductivity of the thin films

Deposition	Substrate	Substrate Temperature (°C)	Deposition time (s)	Conductivity (σ/cm)
1	Si	450	900	7.14
2	Si	450	1800	6.67
3	Si	450	450	2.86

The thickness of grown films was measured by SEM cross-section, as shown in figure 27. It can be noted the almost linear increase in thickness with the increase in deposition time. From these cross-section analyses no further conclusion regarding the grain size or porosity could be obtained. In figure 28, the obtained diffractograms are displayed. According to the International Centre for Diffraction Data (ICDD) (pdf n°04-010-3330), the films obtained a pure rhombohedral delafossite structure belonging to the $\mathrm{R3m}$ space group. The evaluation of the relative intensity of the diffracted peaks shows the most intense peak is (012) (2θ = 36.42°), in the grazing incidence X-ray diffraction (GIXRD) configuration. Peaks (110), (104) and (018) are also present. There is a clear increase in signal intensity of the XRD spectra, that can be associated with the increase in film thickness. Scherrer equation can be used in order to estimate the size of the short-range crystalline order (that we will call "crystallite size") for the different thin films, according to:

$$\tau = \frac{K\lambda}{\beta \cos(\theta)} \tag{33}$$

where τ represents the volume weighted average crystallite size. λ is the x-ray wavelength, β is the full width at half maximum (FWHM) of the diffraction peak, K is a dimensionless shape factor (≈ 0.9, assuming perfect spherical crystallites) and θ is the Bragg angle. An absolute crystallite size cannot be determined with this method due to unknown shape factor, K, in the Scherrer equation and to the instrumental broadening. However, the crystallite size can be estimated. These results (table 11) show the increase in crystallite size with the

increase in deposition time, from 6.8 to 13.2 nm when the deposition time is increased 4-fold, from 450 to 1800 s.

Figure 29 shows the atomic force microscopy (AFM) analysis of the surface of the thin films. Measurements revealed an increase of the surface roughness, with the increase in deposition temperatures as can be seen in table 11. The crystallite size derivate from the XRD spectra, shows an increase trend with increased deposition time.

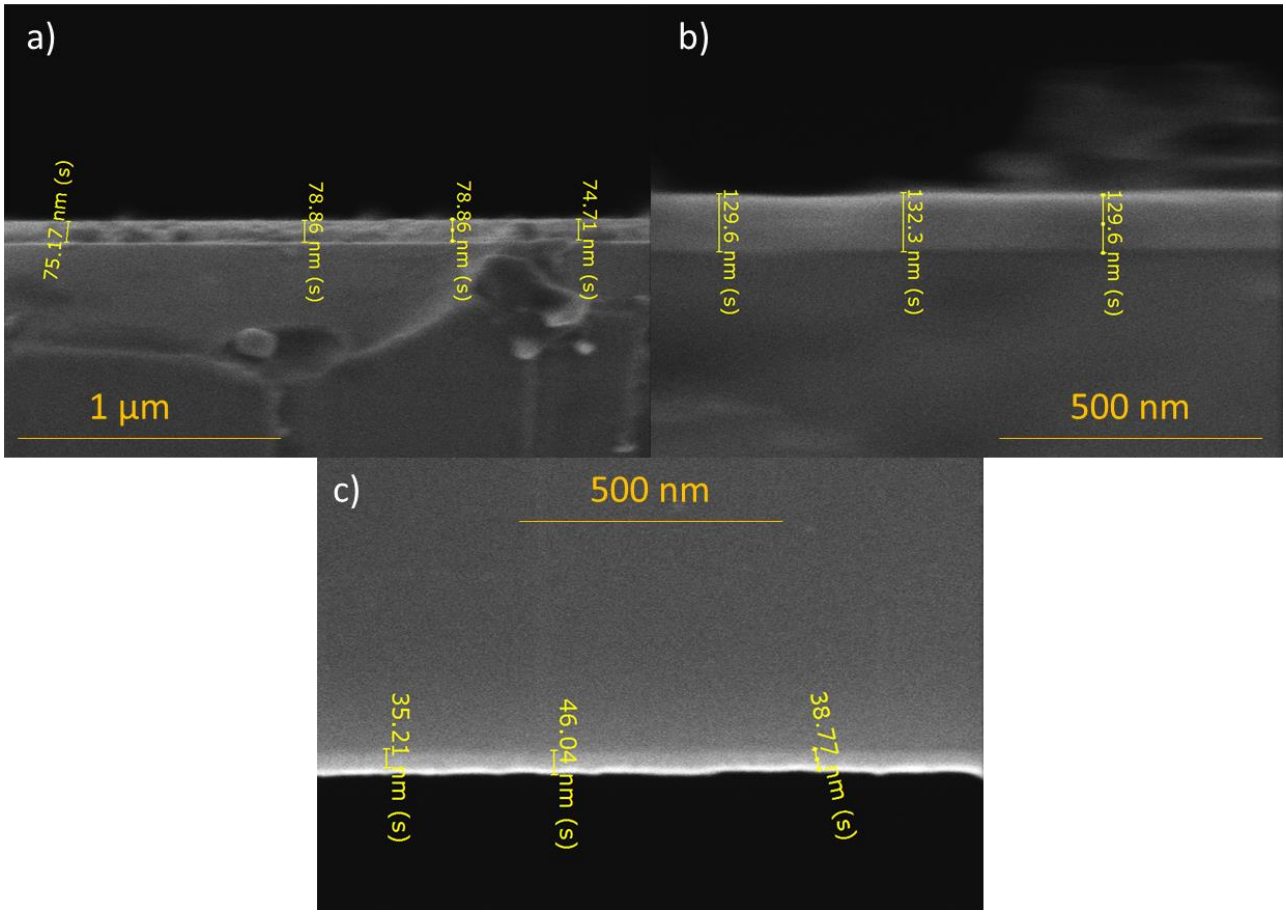

Figure 27 - Measured thickness on SEM cross-section of delafossite thin films with deposition time: a) 900 s; b) 1800 s; c) 450 s

The increase of deposition time leads to an increase in the thin films thickness, crystallite size and roughness. For this reason and to better understand the kinetic reactions undergoing by the delafossite grains upon ozone exposure, it is key to explore the sensitivity of sensors grown with different deposition times.

Table 11 - Summary of the thin film's electrical and morphological properties depending on deposition time

Deposition	Deposition time (s)	Conductivity (σ/cm)	Thickness (nm)	Crystallite size (nm)	Roughness (nm)
1	900	7.14	75 ± 5	9.5	2,1 ± 0,3
2	1800	6.67	132 ± 8	13.2	4,1 ± 0,5
3	450	2.86	40 ± 6	6.8	1,1 ± 0,1

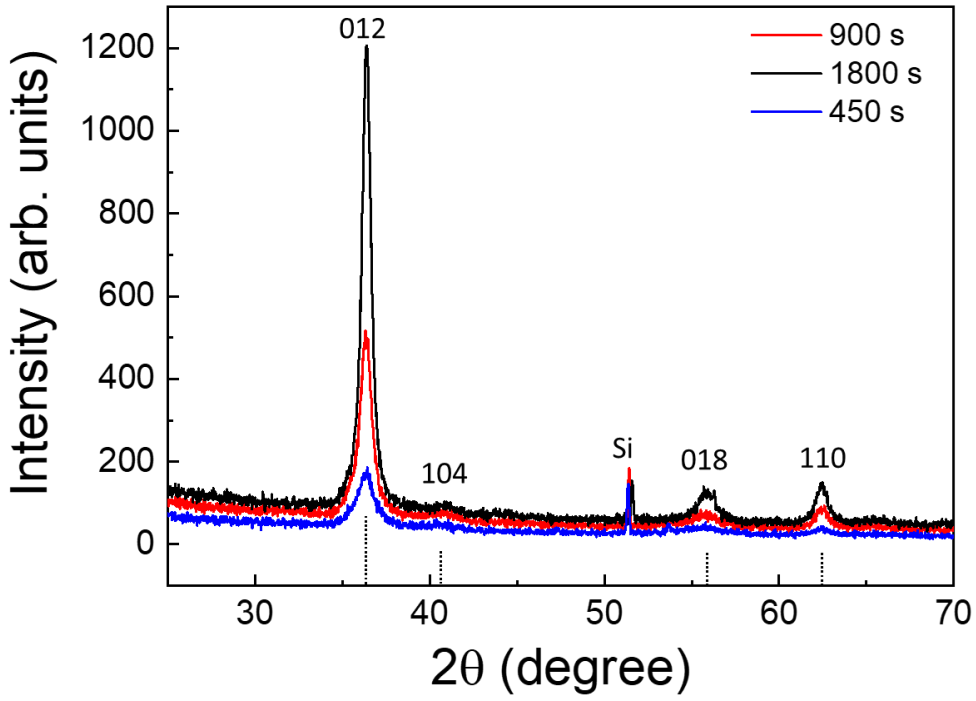

Figure 28 - Structural analysis of θ/2θ XRD diffractograms for films deposited for: a) 900 s; b) 1800 s; c) 450 s

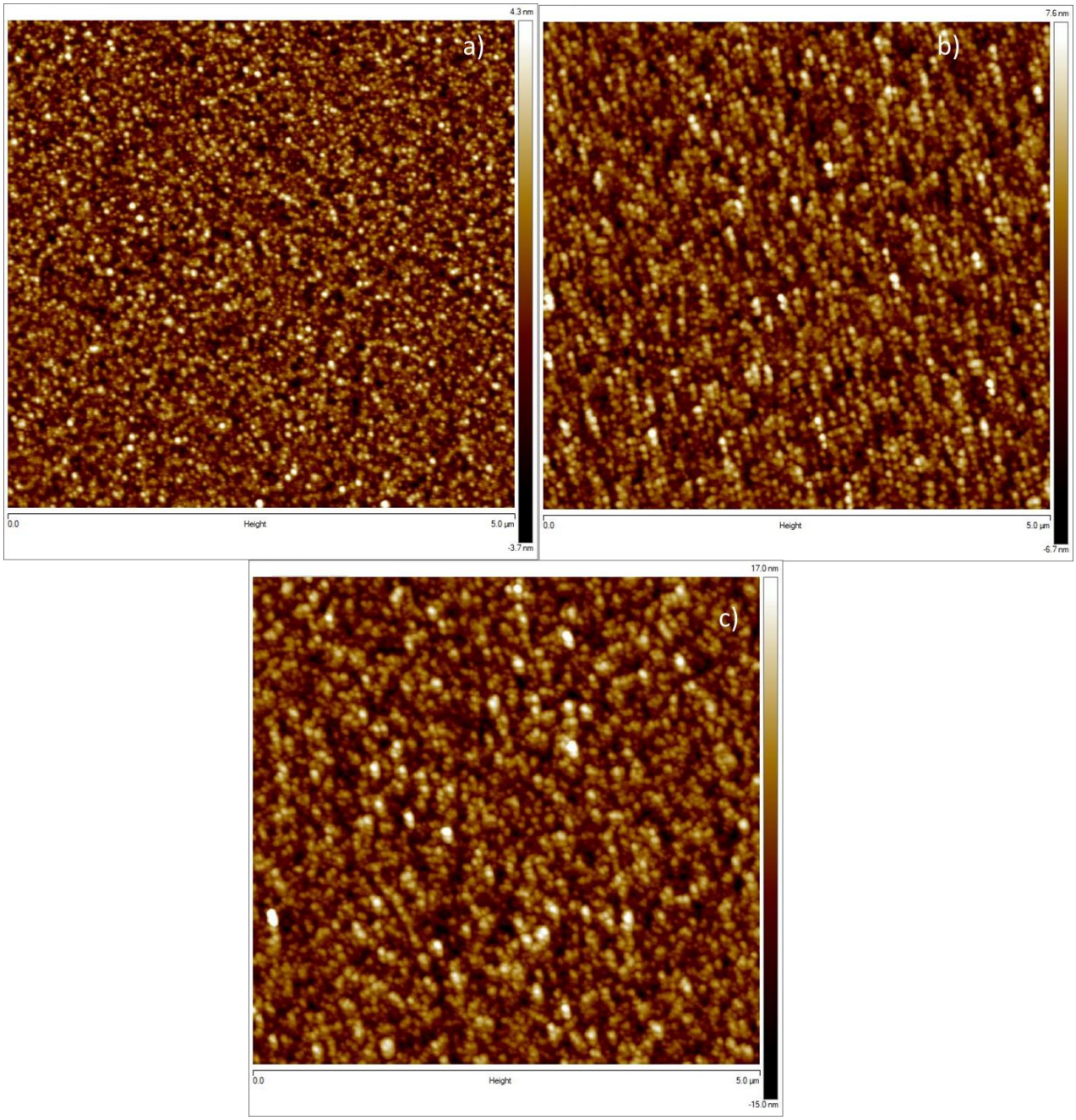

Figure 29 - Surface topography measured by AFM of delafossite thin films, deposited during: a) 450s; b) 900s; c) 1800s

3.2.6. Substrate

Depositions were done on silicon and sapphire substrates. While silicon is highly abundant and commonly used, sapphire is stable at higher temperatures and completely insulating. Delafossite phases could be achieved by depositing in any of the substrates, as well as in glass or quartz [283]. To isolate the thin film from the substrate an additional layer of SiO_2 is required. Delafossite is not affected by this intermediate insulating layer, as shown in the depositions represented in 3.2.4 and 3.2.5. There is no influence of the doping level of the

substrate, undoped (Si), lightly doped silicon (p-Si with a boron concentration $N_A = 5 \times 10^{15}$) and highly doped silicon (p+Si with a boron concentration $N_A = 1 \times 10^{19}$) on the conductivity of Cu-Cr-O delafossite thin-films (table 8). A Silicon oxide barrier has been used with at least 20 nm but for undoped silicon. Conductivity results are not significantly impacted by this barrier layer.

However, as it will be further discussed in chapter 5.4, Si substrate prove to have a major issue; upon annealing at high temperatures (above 900°C), copper diffuses into the silicon substrate, changing the delafossite structure. This is a commonly known fact in the literature [303,304]. Sapphire substrates (Al_2O_3) were preferably chosen due to their high thermal and chemical stability and insulating properties. Table 12 shows the main samples deposited on sapphire substrate.

Table 12 - Summary of the thin film electrical and morphological properties deposited on sapphire substrate

Deposition	Deposition time (s)	Conductivity (σ/cm)	Thickness (nm)	Crystallite size (nm)	Roughness (nm)
A	900	26.6	70	6.8	3,2 ± 0,3
B	1800	60.34	140	8.9	5,9 ± 0,4
C	450	12.32	32	4.0	1,8 ± 0,1

In figure 30, top view of thin films B (140 nm) and C (32 nm) are shown. The thinner film is less compact than the thicker one, what should lead to higher gas permeation and better responses for the thinner film, in line with the short-range crystallite size measured by XRD (4.0 and 8.9 nm for the films with 32 and 140 nm, respectively). Figure 31 shows the structural analysis of θ/2θ XRD diffractograms for both thin films. Pure delafossite phase is obtained for both. The (012) peak is the most intense, with a peak position (2θ = 36.28) slightly shifted towards smaller angles compared with the expected for pure phase delafossite of (2θ = 36.42), in both cases. This shift is associated with a change in the lattice parameters. For as-deposited delafossite the extracted parameter, for ''c'', along the z axis, results in 17.05 Å, smaller than the reported literature value for pure phase delafossite of 17.11, whilst the extracted ''a'' parameter is 2.98 Å, in good agreement with the expected value [305,306]. According to these results, it seems our delafossite lattice is slightly compressed by 0.3 %, along the c axis. Similar results were observed in previous reports for chromium rich – copper poor delafossite thin films and may be associated with the intrinsic doping due to the chains of copper vacancies defects [283,284].

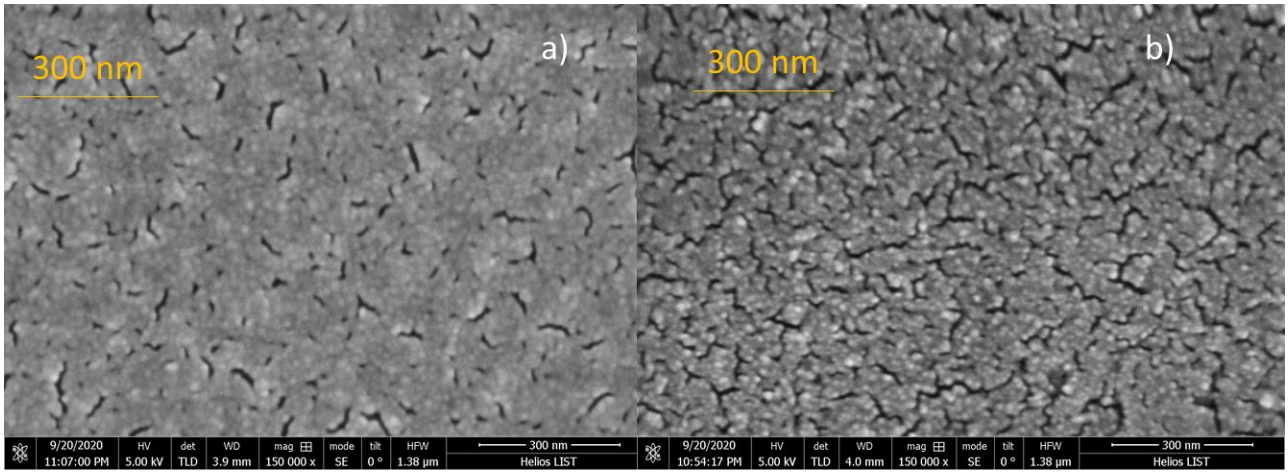

Figure 30 - SEM top view of $Cu_{0.66}Cr_{1.33}O_2$ thin films deposited on sapphire during: a) 1800 s and b) 450 s

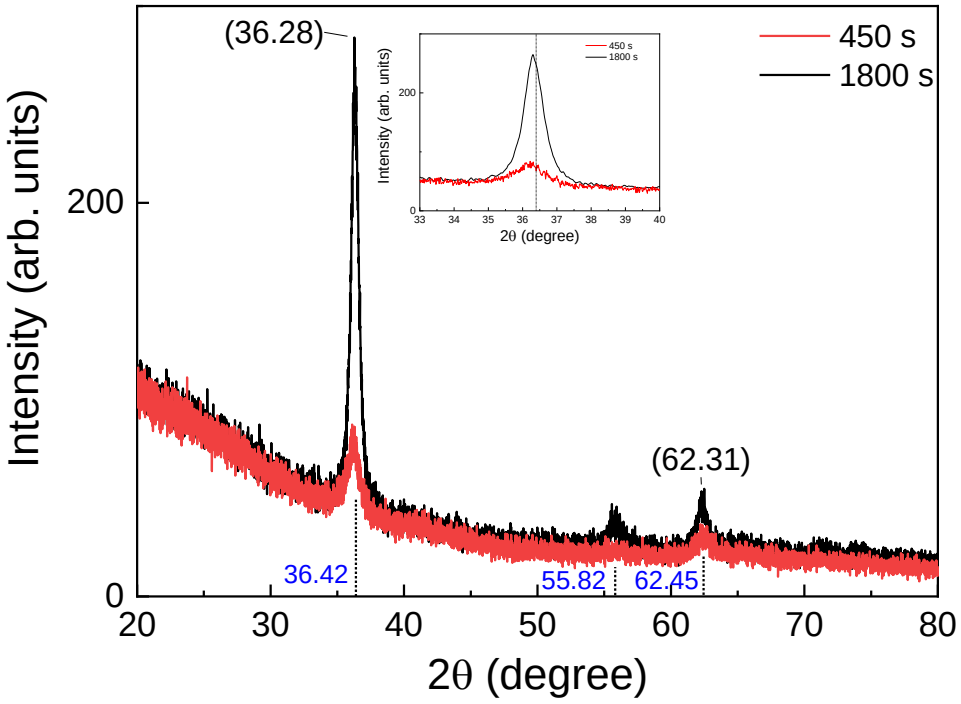

Figure 31 - Structural analysis of ϑ/2ϑ XRD diffractograms for films deposited for: a) 450 s; b) 1800 s

3.3. Annealing Process – Structural defect and electrical properties engineering

This subchapter is partially based on a publication. In this subchapter, we aim at the understanding on the material's electronic properties and the defect healing as function of the annealing conditions. We study the influence of annealing on the surface workfunction, carrier concentration and mobility. We observe that the chemical composition and the particular stoichiometry of our copper-chromium-oxide is unchanged by the annealing processes. The conduction mechanism and the p-type behaviour of our thin films is also retained. The dissolution of chains of copper vacancies into single point defects that migrate to the grain boundaries, can be associated with the decrease in carrier concentration. This defect healing was studied, and their activation energy was calculated to be 1.35 eV.

SCIENTIFIC REPORTS

OPEN

Tuning the electrical properties of the p-type transparent conducting oxide $Cu_{1-x}Cr_{1+x}O_2$ by controlled annealing

Received: 30 January 2018
Accepted: 18 April 2018
Published online: 08 May 2018

P. Lunca-Popa, J. Afonso, P. Grysan, J. Crêpellière, R. Leturcq & D. Lenoble

Off-stoichiometric copper chromium oxide delafossite received lately a great interest due to its high p-type electrical conductivity and adequate optical transmittance in the visible range. However, for a suitable integration in active devices such as p-n junctions, transistors or optoelectronic devices, the electronic properties must be efficiently tailored. Here, post-deposition thermal treatment is proven as an adequate approach for finely controlling the electrical properties of this former degenerate semiconducting material. The energetics of the annealing process are investigated using two different approaches, as a function of the annealing temperature and as a function of the annealing time, allowing the accurate determination of the activation energy of the annealing of defects. By using this method, the electrical carrier concentration was varied in the $10^{21}-10^{17}$ cm^{-3} range while the recorded changes in the drift mobility covered three orders of magnitude. Moreover, we demonstrate the ability to accurately manipulate the Fermi level of such materials, which is of great importance in controlling the carrier injection and extraction in optoelectronic active layers.

In the field of transparent conductive oxides (TCOs) copper-based delafossite materials are promising candidates as p-type transparent semiconductors closing the gap of optical and electrical properties towards current standard n-type semiconductors (a transmittance greater than 80% in the visible range and an electric conductivity up to 1000 S cm^{-1}). The interest in these peculiar delafossite compounds was ignited after the report of $CuAlO_2$ as a first p-type semiconductor with decent optical transparency[1] in the visible range and was reinforced after reporting a breakthrough of electrical conductivity up to 220 S cm^{-1} obtained for Mg-doped $CuCrO_2$[2]. Various copper-based delafossites $CuMO_2$ (M = Cu, Cr, Ga, In, Fe, B) were thoroughly studied[3] in the effort to understand the rationales of the p-type conductivity and the electrical transport mechanism within for optimizing subsequently theirs electrical and optical properties. Copper vacancies[4] or oxygen interstitials[1,5] were mainly suggested as the p-type doping source whilst small polaron[6,7] or band conduction models[8,9] were proposed to elucidate the conduction mechanism in such materials. Moreover, recent reports had shown large conductivity (larger than 10 S cm^{-1}) and adequate transparency for highly off-stoichiometric copper chromium delafossites.[10–13] In these particular compounds the crystalline phase of delafossite is preserved although a copper deficiency up to 33% is observed.

In our previous work[14] we reported the synthesis and the characterization of such off-stoichiometric Cu-Cr-O delafossite thin films with conductivities greater than 100 S cm^{-1} and optical transmittances up to 50%. Finite lines of copper vacancies chains randomly distributed within crystalline grains were observed (in Transmission Electron Microscopy) and furthermore suggested as the possible source of high doping in as-deposited films. A peculiar stoichiometry with a 33% copper deficiency compensated by a surplus of 33% chromium (i.e. $Cu_{0.66}Cr_{1.33}O_2$) was found in both as-deposited and annealed (900 °C) films whilst the delafossite crystalline structure remains unaltered. However, after annealing a drop of the carrier's concentration from 10^{21} to 10^{17} cm^{-3} or even lower was measured and associated with the healing of the chained defects. We then suggested that the main driving force leading the changes in the defect chemistry is the "healing" of defects, a process driven by short-range structural changes.

Materials Research and Technology Department (MRT), Luxembourg Institute of Science and Technology (LIST), 41 rue de Brill, L-4422, Belvaux, Luxembourg. Correspondence and requests for materials should be addressed to P.L.-P. (email: petru.luncapopa@list.lu)

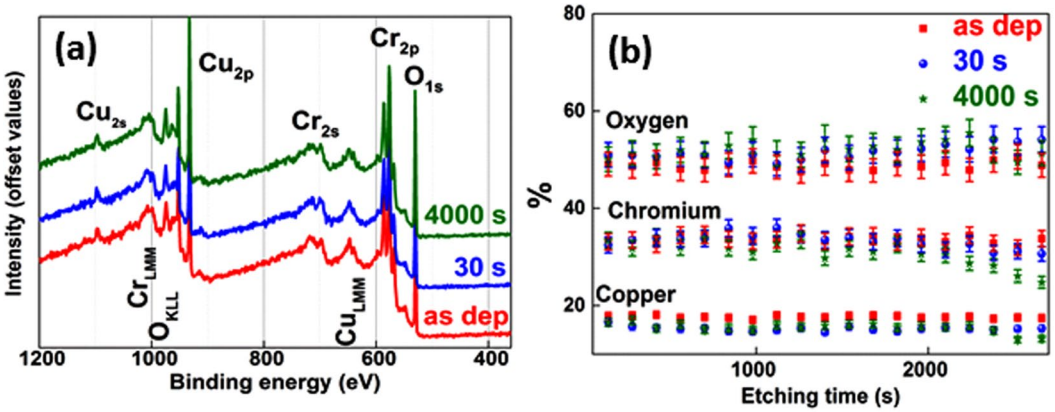

Figure 1. **(a)** Full XPS spectra for as-deposited and annealed films for 30 and respectively 4000 s; **(b)** measured chemical composition for same films; Annealing temperature: 900 °C.

In the present paper we further investigate how a controlled post-deposition thermal treatment can be used as a very effective approach for tailoring electrical properties of $Cu_{0.66}Cr_{1.33}O_2$. Such fine tuning is required for the electrical engineering of transparent devices such as p-n junctions or p-type transistors[15]. In order to achieve this goal, the metastable nature of the Cu-vacancies chains described above was investigated. Two different types of thermal treatments were used in the present study in order to investigate the thermodynamics of the annealing process: different annealing times at a fixed temperature (900 °C) or a fixed amount of time (900 s in this case) at various temperatures (from 650 °C to 850 °C). The first treatment demonstrates conditions for a fast process which is more adequate to technological applications where long lasting processes might be considered costly. The temperature is situated safely lower than 1100 °C, the reported limit of the materials stability for the copper delafossite phase[16]. The second treatment, involving lower temperatures, allows a better control due to the smooth variation of electrical properties. The experimental results show that the controlled thermal treatment can be used as a versatile process for controlling the holes concentration, the electrical mobility or even the electronic work function, all being key features for the engineering of electronic properties of transparent solid state devices.

Results and Discussions

We start by investigating the chemical composition of as-deposited and annealed films for various annealing time intervals in order to confirm the stability of the material's chemistry upon thermal treatment. Figure 1(a) depicts XPS results for as-deposited films and for films annealed for 30 s and respectively 4000 s. The XPS spectra look similar, suggesting no major changes of chemical concentrations. Besides XPS characteristic peaks for $Cu_{(2p,2s)}$, $Cr_{(2p,2s)}$ and O_{1s}, Auger O_{KLL} Cu_{LMM} and Cr_{LMM} peaks are present in the spectra[17]. The positions of Cu_{2p} peaks (1/2 at 932.6 eV and 3/2 at 952.5 eV) do not vary upon annealing. The distance between them is 19.9 eV, a clear indication of the delafossite phase. No satellite peak of Cu is observed, confirming that only Cu in +1 oxidation state is detected by XPS[13]. The Cr_{2p} peaks are observed at binding energies of 576.6 eV (3/2) and 585.6 eV (1/2) respectively. The distance between Cr_{2p} and O_{1s} remains at a constant value of 45.3 eV for all samples. Moreover, the Auger Cu_{LMM} peak observed at a binding energy of 568.6 eV confirms the purity of our delafossite phase[18].

The chemical compositions for as-deposited and annealed films are shown in Fig. 1(b). Concentrations around 16, 33 and 50% are measured (within the XPS measurement accuracy) for Cu, Cr and O respectively. This peculiar stoichiometry may lead to deviations in the partial charge of each atom as compared to the stoichiometric $CuCrO_2$. The bounds are known to be partially ionic and partially covalent and consequently the oxidation state of each atom in the crystal is not directly equal to the most stable oxidation state of each atom[19]. The X-Ray Diffraction, XRD, (Figure S1) analysis confirms furthermore the preservation of the delafossite phase after thermal treatments along with an increase of the crystalline grains' size and a relaxation of c lattice parameter (Figure S2). The change of the grains' size is also visible in AFM scans presented in Figure S3 from the supplementary information section.

Six samples with similar (averaged value: $15.6 \pm 6.9\,S\,cm^{-1}$) conductivities (Table 1) were used for each thermal treatment study (one was kept as reference in each case). Electrical conductivity values of tens of $S\,cm^{-1}$ are obtained using the set of deposition's parameters described within the experimental methods section. This level of conductivities is usually reported for off-stoichiometric delafossites thin- films fabricated using non-equilibrium chemical methods as dynamic liquid injection chemical vapour deposition[10,11,14] or chemical spray deposition[12,13]. These values are significantly higher than those reported for intrinsic[20,21] or some doped[22,23] $CuCrO_2$ delafossites thin-films.

Five of the samples were heated for 900 s at 650, 700, 750, 800 and 850 °C, respectively. For the first sample heated at 650 °C no change was observed after 900 s and consequently the time was furthermore increased up to 3600 s when a three times diminution of the electrical conductivity (σ_0/σ_f) was finally observed. This is in agreement with the work of Gotzendorfer *et al.*[23] where changes in electrical properties of $CuCrO_2$ were observed starting from temperatures around 620 °C. Second set of samples were heated at 900 °C for 30, 60, 200, 1000 and 4000 s respectively. For the last sample the measured conductivity was beyond the sensitivity of our apparatus ($10^{-4}\,S\,cm^{-1}$). For each sample the Seebeck coefficient and the conductivity were measured before and after the

t °C	σ_0 S/cm	$\frac{\sigma_0}{\sigma_f}$	S μVK^{-1}	p cm^{-3}	μ $cm^2V^{-1}s^{-1}$	t (s)	σ_0 S/cm	$\frac{\sigma_0}{\sigma_f}$	S μVK^{-1}	p cm^{-3}	μ $cm^2V^{-1}s^{-1}$
	15	1	100	1.7E + 21	0.08	0	17	1	110	1.5E + 21	0.070
650*	12	3	128	1.2E + 21	0.004	30	10	128	340	1.1E + 20	0.002
700	11	102	184	6.6E + 20	0.001	60	10	173	360	8.9E + 19	0.004
750	31	5500	257	2.9E + 20	0.002	200	7	4700	850	3.0E + 17	0.031
800	21	14000	374	7.3E + 19	0.0001	1000	19	12600	947	9.4E + 16	0.086
850	23	54000	753	9.3E + 17	0.007	4000	11	NA	NA	NA	NA

Table 1. Annealing times or annealing temperatures, initial electrical conductivities and the ratios after thermal treatment, Seebeck coefficients and calculated carrier's concentration and mobility (within small polaron model) for: left - films annealed for 900 s at different temperatures (*sample annealed for 3600 s); right - films annealed at 900 °C for different time intervals. NA – measures beyond the sensitivity of our apparatus.

thermal treatment and the results are presented in Fig. 2 and Table 1. The first observation is the negative slope of $\Delta V_{th}/\Delta T$ further proving the p-type nature of our films. For as-deposited samples values of S around 100–130 $\mu V\ K^{-1}$ were measured. For the sample heated at 650 °C a similar value (118 $\mu V\ K^{-1}$) of the Seebeck coefficient (Fig. 2(a)) is measured evidencing a slow healing of Cu-vacancies chains defects at this temperature. Beyond 700 °C important changes appear after 900 s of annealing. The electrical conductivity decreases monotonously with the annealing temperature until a diminution of 50 000 times, as measured in the case of the sample heated at 850 °C. The Seebeck coefficient follows an exponential decay (Fig. 2(c)) with the annealing temperature. This coefficient is directly related to the carriers' concentration which is further dependent on the concentration of defects. In the material investigated here, we have previously demonstrated that the defects are the chains of Cu vacancies observed by TEM experiments[14]. Therefore we may correlate the decrease of the carriers' concentration with the annihilation of these chains of Cu vacancies. A further indication will be presented later when analysing the thermodynamics of the annihilation reaction. The exponential decay confirms the metastable nature of defects and that a thermal activated law governs their healing. Similar healing of defects is observed when using the fast annealing process. The conductivity decreases by two orders of magnitude during short (30–60 s) thermal treatments, followed by a continuous decrease with the annealing time down to the 10^{-4} S cm^{-1} range for the sample heated during 4000 s. The values of the Seebeck coefficient can be regrouped in three main regimes as depicted in Fig. 2(b). Values around 100–130 μV^{-1} are measured for as-deposited high conductive samples. Similar values are usually reported for off-stoichiometric or doped delafossite thin-films with electrical conductivities around 10 S cm^{-1} or higher[2,10–14,24]. After short annealing times (up to 60 s) the coefficient increases up to values around 360 $\mu V\ K^{-1}$. Further increase of the annealing time results in values for Seebeck coefficient of 850 $\mu V\ K^{-1}$, similar with values reported for non-doped $CuCrO_2$[25]. Again the dependence of the Seebeck coefficient on the annealing time is exponential (Fig. 2(d)). It was previously reported[26,27] that performing Hall measurements on copper p-type delafossites is challenging due to very low values of mobility. Furthermore collected Hall voltage values are comparable with the background signal. Hall measurements at high magnetic fields (up to 9 T) were performed on our as-deposited sample and resulted in highly scattered data points[28]. An averaged value of 0.01 $cm^2\ V^{-1}s^{-1}$ can be extracted after making a large set of assumptions. This averaged value matches the mobility value as we extract it from our Seebeck measurements. This makes us confident that the combined Seebeck and conductivity measurements provide reliable values of electronic properties of our materials. From the electrical conductivity and the Seebeck coefficient measurements we extract the carriers' concentration of thin films. It is important to distinguish on one side the origin of holes in our system, which are related to peculiar defects (here chains of Cu vacancies), and on the other side the localisation of the free (mobile) holes in our system, which is related to the orbitals constituting the valence band maximum. In Cu-based delafossite materials, it has been widely assumed that the valence band is mainly made from d orbitals of Cu atoms, leading to a transition of the oxidation state of Cu^{I} to Cu^{II}. In conclusion whatever the origin of the holes (chains of Cu vacancies, isolated Cu vacancies, O interstitials, extrinsic dopants etc.), the free holes concentration corresponds to Cu atoms with + II oxidation state acknowledging that the oxidation state is an approximation and does not corresponds to the partial charge of atoms. Using this approach within the Heikes formalism, often used in the case of degenerate semiconductors[26], the following formula of the Seebeck coefficient is obtained:

$$S = \frac{k_B}{q} ln\left[\left(\frac{g_1}{g_2}\right)\frac{[Cu^+]}{[Cu^{2+}]}\right] \quad (1)$$

where $g_1 = 1$ and $g_2 = 4$ are electron degeneracies and of Cu^+ and Cu^{2+} while $[Cu^+]/[Cu^{2+}]$ is the ratio of Cu having +I and +II oxidation states, acknowledging that the oxidation state doesn't correspond to the spatial charge of atoms. This formula allows the calculation of Cu^{2+} fraction sites and furthermore p, the carriers concentration. Finally, the mobility μ can be estimated using $\boldsymbol{\sigma = pe\mu}$. The results are presented in Table 1. It should be mentioned here that for conductive samples ($\sigma > 1$ S cm^{-1}) the band degenerate[29] and the small polaron models lead to similar values[14]. Moreover for lower conductive samples a good agreement is observed using both small polaron and non-degenerate models[30]. The logarithmic dependence of the carriers' concentration and drift mobilities is depicted in Figs. 2(e and f) for both annealing processes. The decrease of the carriers' concentration is efficiently tailored by controlling the annealing temperature, as in this case a smoother variation is observed. However, if low values are aimed at, the fast annealing may be privileged. An interesting observation is related to the drift

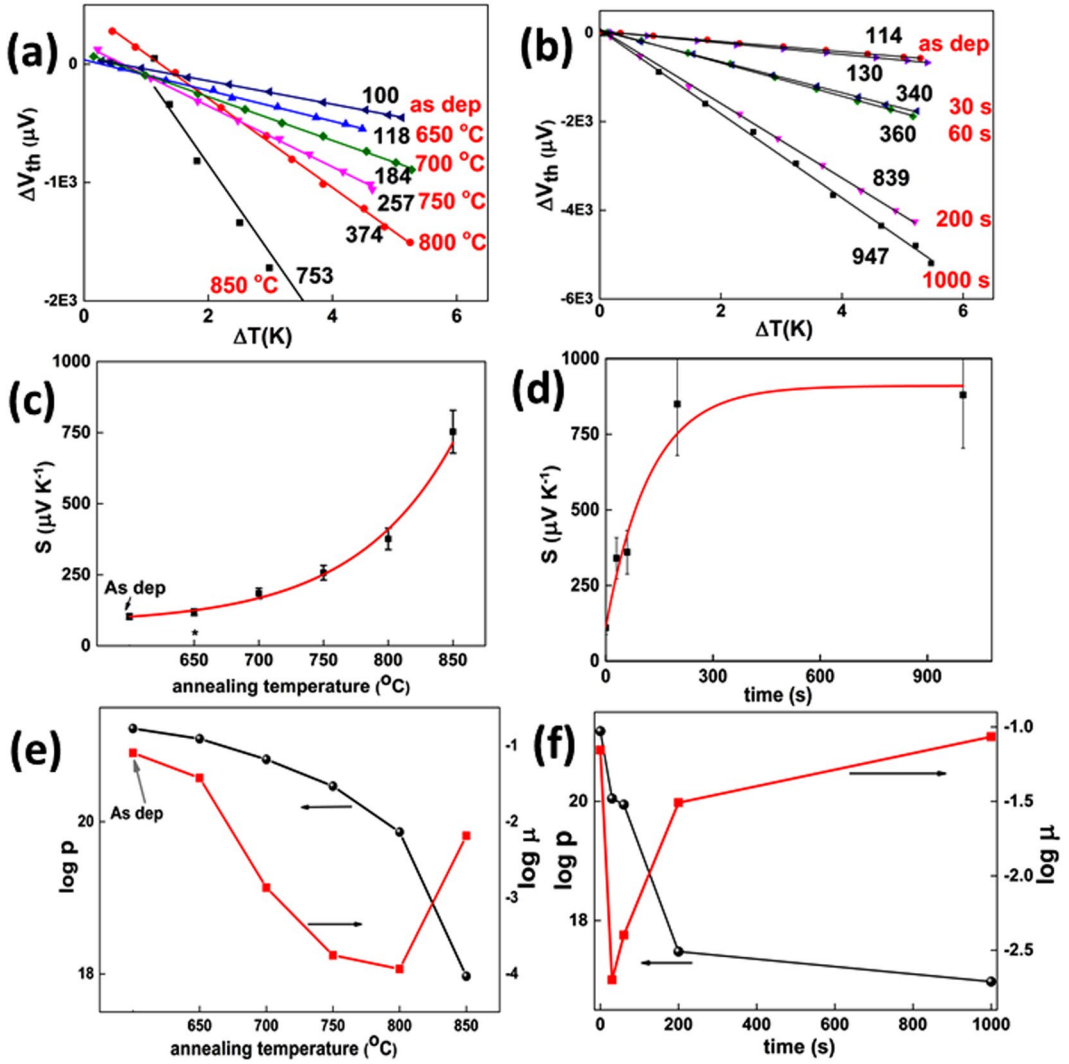

Figure 2. Seebeck coefficient measurement for Cu-Cr-O thin films **(a)** annealed at different temperatures; **(b)** annealed at 900 °C for various time intervals. Thermoelectric voltage $\Delta V_{th} = V_{hot} - V_{cold}$ is measured as a function of the temperature gradient ΔT applied across the sample, with copper wire as reference. The measurement has been performed with the cold contact maintained at room temperature (23 °C). The values of the Seebeck coefficient $S = -\Delta V/\Delta T$, determined from a linear fit, are indicated on the graph for each sample. The voltage offset is due to parasitic offsets from the measurement apparatus due to samples' high resistance; **(c)** Seebeck coefficient vs annealing temperature; **(d)** Seebeck coefficient vs annealing time for thermal treatments at 900 °C. Red curves are corresponding to exponential fits; Logarithm of the carrier concentration (black) and of drift mobility (red) **(e)** as function of annealing time for samples annealed at a fixed temperature 900 °C; **(f)** as function of the annealing temperature for samples annealed for a fixed time t = 900 s.

mobility. During both thermal treatments a minimum is observed: after 900 s of heating at 800 °C or after 30 s of heating at 900 °C. This behaviour might be related to the atomic rearrangement during the annealing process. In these conditions, the number of grain boundaries may increase to a maximum and furthermore scattering the carrier flow.

The results obtained after the two thermal processes described above are also used to investigate the energetics of doping defects. Assuming a first order kinetics law, the holes concentration p can be expressed as a function of the annealing time t in a general way as:

$$p(t) \approx N_a(t) = N_i e^{-kt} + N_{res} \equiv N_0 e^{-kt} + N_{res} \text{ with } N_o \gg N_{res} \quad (2)$$

where N_a is the acceptor dopant concentration, N_{res} is the residual acceptor concentration after an infinite annealing, $N_i = N_0 + N_{res}$ is the initial carrier concentration (as-deposited) and k is the rate constant. The assumption of a first order kinetic is validated by the observed linear dependence when plotting ln(p) vs. t for the data taken at 900 °C (Fig. 3(a)). Since the data point at 1000 s is already very close to the residual holes concentration p_{res}, only data up to 200 s of annealing are fitted. Consequently a rate constant $k = 0.040 \pm 0.005\ s^{-1}$ is obtained. Assuming

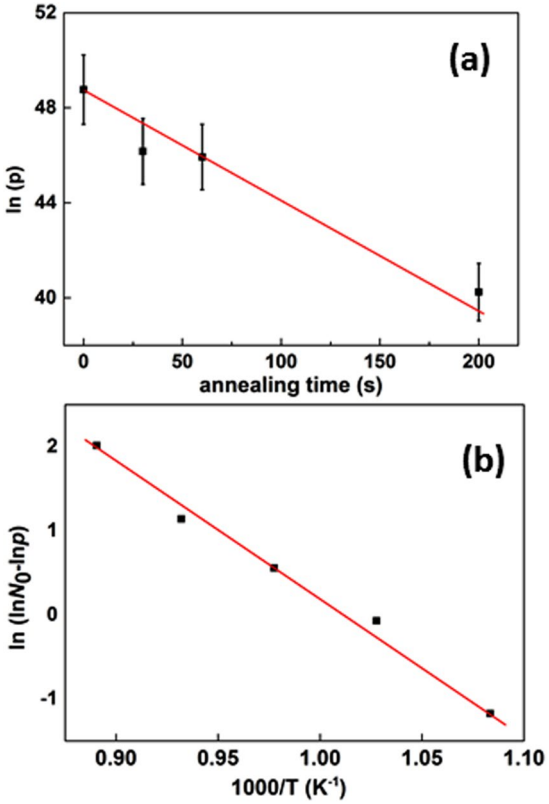

Figure 3. **(a)** Natural logarithm of the carrier concentration as a function of annealing time for Cu-Cr-O films annealed at a fixed temperature T = 1173 K; **(b)** Arrhenius plot of the difference of the natural logarithm of carrier concentration and initial doping, $\ln N_0 - \ln p$, as a function of the annealing temperature for $CuCrO_2$ annealed during a fixed time t = 900 s. The size of error bar is comparable with the symbol 'size. Red lines: linear fits to the data.

that the reaction is thermally activated, the reaction constant k can be expressed as a function of the annealing temperature T using an activation energy E_a:

$$k(T) = Ae^{-\frac{E_a}{k_B T}} \tag{3}$$

where A is a constant and k_B is the Boltzmann constant. Relating equations (2) and (3), we can express the carrier concentration as a function of the annealing temperature *T* and annealing time t:

$$p(T, t) = N_0 \exp\left(-At \exp\left(-\frac{E_a}{k_B T}\right)\right) + N_{res} \tag{4}$$

The residual dopant concentration can be neglected and the relationship can be thus expressed:

$$\ln(\ln N_0 - \ln p(T, t)) = \ln(At) - \frac{E_a}{k_B T} \tag{5}$$

Taking the as-deposited carrier concentration as the initial dopant concentration $N_i = N_0 = 1.68 \times 10^{21}\ cm^{-3}$, we can plot $\ln(\ln N_0 - \ln p(T, t))$ at fixed annealing time (t = 900) s as a function of $1/T$ (Fig. 3(b)).

The data fit well with the activation energy model, and an activation energy of $E_a = 1.35 \pm 0.07$ eV is obtained. In the case of ZnO[31] the activation energy for the annihilation of Frenkel pairs (annihilation of vacancies with nearby interstitials) is about 1 eV while the energy barriers for the migration of zinc and oxygen vacancies are 1.4 eV and 2.4 eV, respectively. Based on this quantitative comparison and on our previous microscopic analysis of defects showing the presence of Cu vacancy chains in as-deposited material, we suggest that the changes in electrical conductivities in our system are triggered by Ostwald ripening mechanisms based on the dissolution of shorter chains of vacancies into single Cu vacancies migrating to grain boundaries or longer chained vacancy defects. In our case, the activation energy would preferably correspond to the energy of migration of single Cu vacancies through the crystal. A detailed analysis of the structural evolution of defects goes beyond the present study but it is noteworthy that our measured activation is in the same range as the migration energy of cations vacancy in oxide semiconductors[32,33].

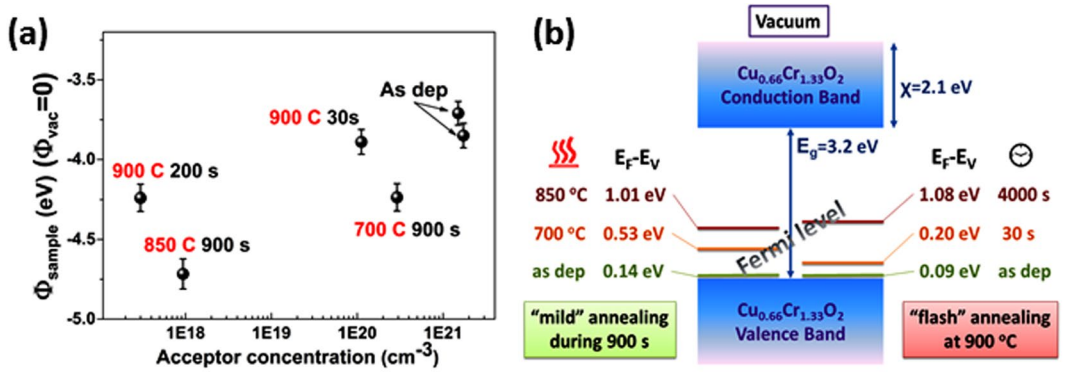

Figure 4. (**a**) work-function difference as a function of the carrier concentration); **(b)** calculated Fermi level for delafossite film annealing at different temperatures and for various time intervals.

KPFM measurements were performed on six samples: both reference samples plus two samples from the first set (900 s, 700 °C and 850 °C) and two from the last set (900 °C, 30 s and 4000 s). The measurements were performed alternatively between the HOPG reference and one of the samples. The values are always compared to the latest reference value to avoid possible fluctuations of the tip work function (e.g. due to contaminations). In order to compensate the vacuum levels misalignment KPFM insert a voltage $V_{DC} = (\Phi_{tip} - \Phi_{sample})/e$ where $\Phi_{tip(Pt\text{-}Ir)} = 5.5$ eV. The samples have different doping levels and different Fermi levels (E_F) are expected. An increase of the work function $\Delta\Phi$ is measured according to:

$$E_F - E_V = (\chi + E_g) - \Delta\Phi \tag{6}$$

where χ is the electronic affinity (2.1 eV for copper delafossites[34]), Eg is the band gap 3,2 eV[2,12,14]. This value is insignificantly affected by annealing[14] and thus holds for both cases of annealed and as-deposited (transmittance spectra and Tauc plots for as deposited and annealed samples are presented in Figure S5). The results are depicted in Fig. 4(a), where the work-function referenced to the vacuum (knowing that $\Phi_{HOPG} = 4.6$ eV) is shown as a function of the carriers' concentration. For as deposited samples, the Fermi level is situated at 90 meV above the valence band maximum, an ordinary value for degenerate semiconductors. Upon thermal treatment the Fermi level can be tailored upwards to 1.08 eV above the valence band maximum; this corresponds to the samples annealed for 4000 s at 900 °C (Fig. 4(b)). The Fermi level is thus gradually tailored within this range of energy (90 meV to 1.08 eV) when the thermal treatment is tuned.

Conclusions

We proved that the controlled thermal treatment is an efficient approach for controlling electronic properties of $Cu_{0.66}Cr_{1.33}O_2$, a highly conductive p-type transparent oxide. The holes concentration, the electrical mobility and the electronic work function are key features for transparent solid-state devices and for a suitable integration in any active devices (such as p-n junction, transistors or optoelectronic devices) these properties must be tailored in order to tune the required properties of such devices. Therefore we showed that the carrier concentration was smoothly varied from 10^{21} to 10^{17} cm^{-3}, the electrical conductivity swaps down 5 orders of magnitude while the recorded changes in drift mobility covered three orders of magnitude. Moreover, we accurately control the Fermi level which is of critical importance in controlling the carrier injection and extraction in electronic devices. Depending on the aimed final values we proposed a time driven or a temperature driven thermal treatment. From the value of 90 meV for as-deposited samples, the Fermi level can be tailored upwards up to 1.08 eV above the valence band maximum; this is achieved via the annealing of as-deposited sample for 4000 s at 900 °C. The energetics of singular Cu-vacancies chain defects responsible of the high conductivity in this peculiar material is also studied. An activation energy model is used to extract the averaged activation energy of the annihilation of Cu-vacancies chains. We found $E_a = 1.35$ eV which is very similar to the energy of the migration of Zn-vacancies in n-type ZnO-based TCOs.

Methods

Thin films with a thickness around 200 nm were deposited on Al_2O_3 c-cut substrates using a Dynamic Liquid Injection - Metal Organic Chemical Vapour Deposition system (DLI-MOCVD, MC200 from Annealsys) whilst bis 2,2,6,6-tetramethyl-3,5-heptanedionate compounds were used as precursors for copper and chromium. The deposition parameters are: temperature substrate = 450 °C; oxygen flow = 2000 standard cubic centimetres (sccm); nitrogen flow = 850 sccm; total process pressure = 12 mbar. A detailed description of the deposition approach fabrication can be found elsewhere[35]. The annealing processes were performed in a Rapid Thermal Annealing reactor (Annealsys) under Argon, under vacuum or at high oxygen partial pressure (in same conditions as during the deposition) and the changes in conductivity were not significantly depending on the annealing atmosphere. For the present work the annealing was performed under $N_2 + O_2$ mixture for the fast annealing and under vacuum for the annealing at various temperatures. Electrical properties were measured using four probes in linear configuration while for the Seebeck effect measurement a homemade system was used with a copper wire as reference. A detailed description of this system is presented on supplementary information section (Figure S5).

For X-Ray Photoemission Spectroscopy (XPS) analysis a Kratos Axis Ultra DLD system using a monochromated (Al Kα: hν = 1486.7 eV) X-ray source was used. Kelvin Probe Force Microscopy (KPFM) measurements have been performed on a Bruker Innova using the amplitude modulation to determine the contact potential difference between the Pt-Ir coated tip and the sample surface. The analysis is done in one pass mode, the first resonance amplitude is used to track the topography while the KPFM signal is acquired at a second frequency (23 kHz). Freshly cleaved Highly-Oriented Pyrolytic Graphite (HOPG) is used as reference. Measurements are performed under dry N_2 atmosphere in order to avoid water condensation on the surface.

References

1. Kawazoe, H. *et al*. P-type electrical conduction in transparent thin films of $CuAlO_2$. *Nature* **389**, 939–942 (1997).
2. Nagarajan, R., Draeseke, A. D., Sleight, A. W. & Tate, J. P-type conductivity in $CuCr_{1-x}Mg_xO_2$ films and powders. *J. Appl. Phys.* **89**, 8022–8025 (2001).
3. Nagarajan, R. *et al*. p-Type conductivity in the delafossite structure. *Int. J. Inorg. Mater.* **3**, 265–270 (2001).
4. Scanlon, D. O. & Watson, G. W. Understanding the p-type defect chemistry of $CuCrO_2$. *J. Mater. Chem.* **21**, 3655–3663 (2011).
5. Banerjee, A. N., Ghosh, C. K. & Chattopadhyay, K. K. Effect of excess oxygen on the electrical properties of transparent p-type conducting $CuAlO_{2+x}$ thin films. *Sol. Energy Mater. Sol. Cells* **89**, 75–83 (2005).
6. Tuller, H. L. & Nowick, A. S. Small polaron electron transport in reduced CeO_2 single crystals. *J. Phys. Chem. Solids* **38**, 859–867 (1977).
7. Ingram, B. J., Mason, T. O., Asahi, R., Park, K. T. & Freeman, A. K. Electronic structure and small polaron hole transport of copper aluminate. *Phys. Rev. B* **64**, 155114 (2001).
8. Bosman, A. J. & van Daal, H. J. Small-polaron versus band conduction in some transition-metal oxide. *Adv. Phys.* **19**, 1–117 (1970).
9. Nagaraja, A. R. *et al*. Band or Polaron: The Hole Conduction Mechanism in the p-type spinel Rh_2ZnO_4. *J. Am. Ceram. Soc.* **95**, 269–275 (2012).
10. Crêpellière, J. *et al*. Transparent conductive $CuCrO_2$ thin films deposited by pulsed injection metal organic chemical vapour deposition: up-scalable process technology for an improved transparency/conductivity trade-off. *J. Mater. Chem. C* **4**, 4278–4291 (2016).
11. Lunca-Popa, P., Crêpellière, J., Leturcq, R. & Lenoble, D. Electrical and optical properties of Cu-Cr-O thin films fabricated by Chemical Vapour Deposition. *Thin Solid Films* **612**, 194–201 (2016).
12. Farrell, L. *et al*. Spray pyrolysis growth of a high figure of merit, nano-crystalline, p-type transparent conducting material at low temperature. *Appl. Phys. Lett.* **107**, 031901 (2015).
13. Farrell, L. *et al*. Synthesis of nanocrystalline Cu deficient $CuCrO_2$ – a high figure of merit p-type transparent semiconductor. *J. Mater. Chem. C* **4**, 126–134 (2016).
14. Lunca-Popa, P., Crêpellière, J., Nukala, P., Leturcq, R. & Lenoble, D. Invisible electronics: Metastable Cu-vacancies chain defects for highly conductive p-type transparent oxides. *Appl. Mater. Today* **9**, 184–191 (2017).
15. Lenoble D. *et al*. Proceedings of 13th International Conference on Ion Implantation Technology- IIT, Alpbach, Austria, 17-22 September, 468-471 (2000).
16. Lalanne, M., Barnabé, A. & Mathieu, F. Tailhades, Ph. Synthesis and Thermostructural Studies of a $CuFe_{1-x}Cr_xO_2$ Delafossite Solid Solution with 0 x 1. *Inorg. Chem.* **48**, 6065–6071 (2009).
17. Wagner, C. D. *et al*. in *Handbook of X-Ray Photoelectron Spectroscopy*, (ed.Perkin-Elmer, Minnesota 1979).
18. Arnold, T. *et al*. X-ray spectroscopic study of the electronic structure of $CuCrO_2$. *Phys. Rev. B* **79**, 075102 (2009).
19. Scanlon, D. O., Godinho, K. G., Morgan, B. J. & Watson, G. W. Understanding conductivity anomalies in CuI -based delafossite transparent conducting oxides: Theoretical insights. *The Journal of Chemical Physics* **132**, 024707 (2010).
20. Sun, C.-S., Tsai, D.-C., Chang, Z.-C., Chen, E.-C. & Shieu, F.-S. Effects of annealing time on the structural and optoelectronic properties of p-type conductive transparent Cu–Cr–O film. *J Mater Sci: Mater Electron* **27**, 9740 (2016).
21. Tripathi, T. S., Niemelä, J. P. & Karppinen, M. Atomic layer deposition of transparent semiconducting oxide CuCrO2 thin films. *J. Mater. Chem. C* **3**, 8364 (2015).
22. Sinnarasa, I., Thimont, Y., Presmanes, L., Barnabé, A. & Tailhades, P. Thermoelectric and transport properties of Delafossite $CuCrO_2$:Mg thin films prepared by RF magnetron sputtering. *Nanomaterials* **7**, 157 (2017).
23. Götzendörfer, S., Bywalez, R. & Löbmann, P. Preparation of p-type conducting transparent $CuCrO_2$ and $CuAl_{0.5}Cr_{0.5}O_2$ thin films by sol-gel processing. *J Sol-Gel Sci. Technol.* **52**, 113–119 (2009).
24. Okuda, T., Jufuku, N., Hidaka, S. & Terada, N. Magnetic, transport, and thermoelectric properties of the delafossite oxides $CuCr_{1-x}Mg_xO_2$ ($0 < x < 0.04$). *Phys. Rev. B* **72**, 144403 (2005).
25. Ngo, T. N. M., Palstraa, T. M. & Blake, G. R. Crystallite size dependence of thermoelectric performance of $CuCrO_2$. *RSC Adv.* **6**, 91171 (2016).
26. Barnabé, A., Thimont, Y., Lalanne, M. & Presmanes, L. & Tailhades, Ph. p-Type conducting transparent characteristics of delafossite Mg-doped $CuCrO_2$ thin films prepared by RF-sputtering. *J. Mater. Chem. C* **3**, 6012–6024 (2015).
27. O'Sullivan, M., Stamenov, P., Alaria, J., Venkatesan, M. & Coey, J. M. D. Magnetoresistance of $CuCrO_2$-based delafossite film. *J. Phys.: Conf. Ser.* **200**, 052021 (2010).
28. Werner, F. Hall measurements on low-mobility thin films. *Journal of Applied Physics* **122**, 135306 (2017).
29. Cui, J., Li, Y., Du, Z.-L., Meng, Q. & Zhou, H. Promising defect thermoelectric semiconductors $Cu_{1-x}GaSb_xTe_2$ ($x = 0$–0.1) with the chalcopyrite structure. *J. Mater. Chem. A* **3**, 677–683 (2013).
30. Hossain, M. S., Islam, R., Shahjahan, M. & Khan, K. A. Studies on the thermoelectric effect in semiconducting ZnTe thin films. *J. Mater. Sci. Mater. Electron.* **19**, 1114–1121 (2008).
31. Meljanac, D. *et al*. The influence of thermal annealing on the structural, optical and electrical properties of AZO thin films deposited by magnetron sputtering. *Surface and Coatings Technology* **32**, 292–299 (2017).
32. Erhart, P. & Albe, K. Diffusion of zinc vacancies and interstitials in zinc oxide. *Appl. Phys. Lett.* **88**, 201918 (2006).
33. McCluskey, M. D. Chapter eight: point defects in ZnO. *Semiconductors and Semimetals* **91**, 279–313 (2015).
34. Wang, J., Lee, Y.-J. & Hsu, J. W. P. Sub-10 nm copper chromium oxide nanocrystals as a solution processed p-type hole transport layer for organic photovoltaics. *J. Mater. Chem. C* **4**, 3607–3613 (2016).
35. Bahlawane, N., Kohse-Höinghaus, K., Premkumar, P. A. & Lenoble, D. Advances in the deposition chemistry of metal-containing thin films using gas phase processes. *Chem.Sci.* **4**, 929–941 (2012).

Acknowledgements

This project was supported by the National Research Fund (FNR), Luxembourg (DEPTOS – Defect Engineering in p-type oxides semiconductors - project number C12/MS/3959502).

Author Contributions

P.L.P., R.L., J.C. and D.L. conceived and designed the experiments. P.L.P. prepared the figures and wrote the manuscript with the assistance of all authors. P.L.P. and J.A. performed annealing experiments. P.G. performed and interpreted the Kelvin probe measures.

Additional Information

Supplementary information accompanies this paper at https://doi.org/10.1038/s41598-018-25659-3.

Competing Interests: The authors declare no competing interests.

Publisher's note: Springer Nature remains neutral with regard to jurisdictional claims in published maps and institutional affiliations.

3.3.1. Annealing influence on conductivity

An in-depth study, presented in figure 32, shows the logarithmic decrease in conductivity with the increase in annealing temperature studied in the range of 600 to 900 °C. It can also be noted the impact each step of increase in annealing temperature takes in the decrease in conductivity.

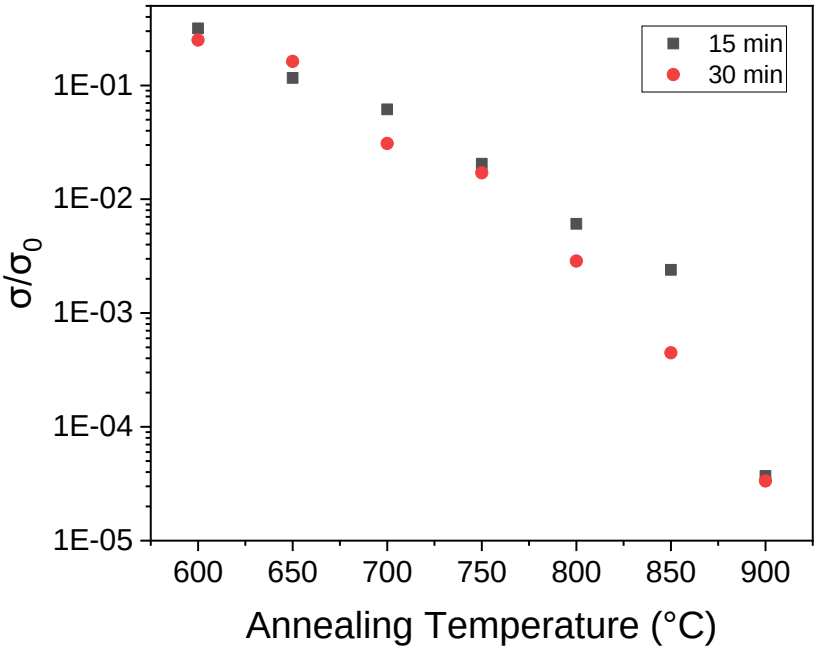

Figure 32 - Study of change in conductivity with annealing temperature of $CuCrO_2$ from 600° to 900°C

3.3.2. Temperature dependent response

The temperature dependent I-V curves of a thin film annealed at 700° is depicted in figure 33 a). The decrease in resistivity with increase in measuring temperature, as observed in 33 b) is in line with a semiconductor behaviour expected for our Cu-Cr-O thin films. The resistance decreases monotonically with the increase of temperature, due to the thermoionic generation of free charge in the semiconductor.

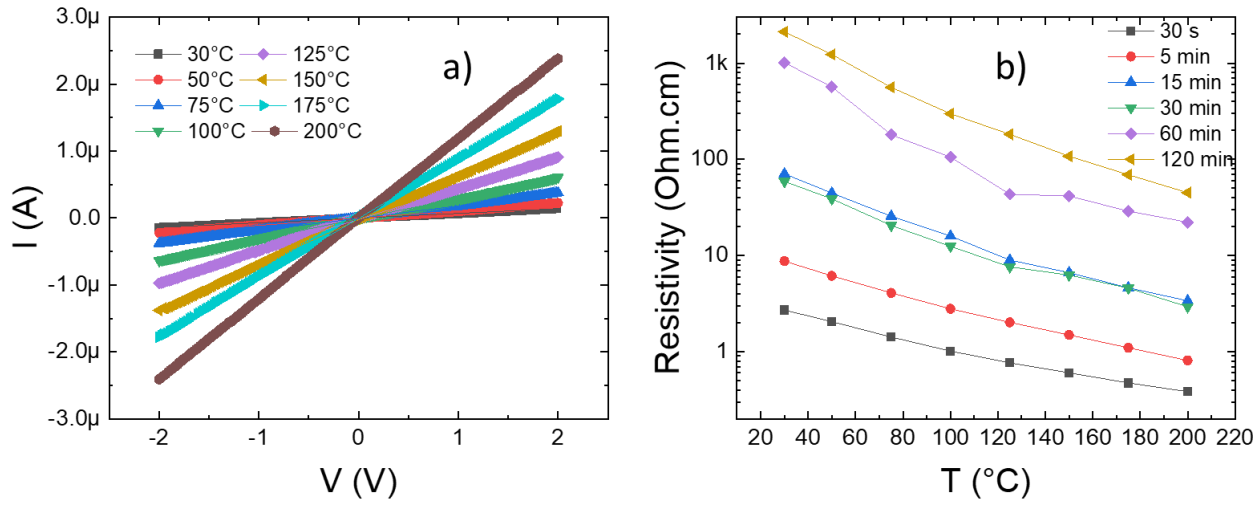

Figure 33 – Temperature response of delafossite thin films annealed at 700°C: a) With increasing temperature from 30 to 200°C b) Resistivity dependence on measuring temperature for films with different annealing durations

For small polaronic conductions, as is normally considered the case for delafossite films, the conduction is given by Mott and Davies. It can be rewritten as:

$$\ln(\sigma T) = \ln(A\sigma p) + \frac{E_{\sigma p}}{k_b T} \tag{34}$$

Where $E_{\sigma p}$ is the activation energy for polaronic conduction. The natural logarithm dependence of the conductivity times the temperature is plotted in figure 34, as function of the inverse of the temperature.

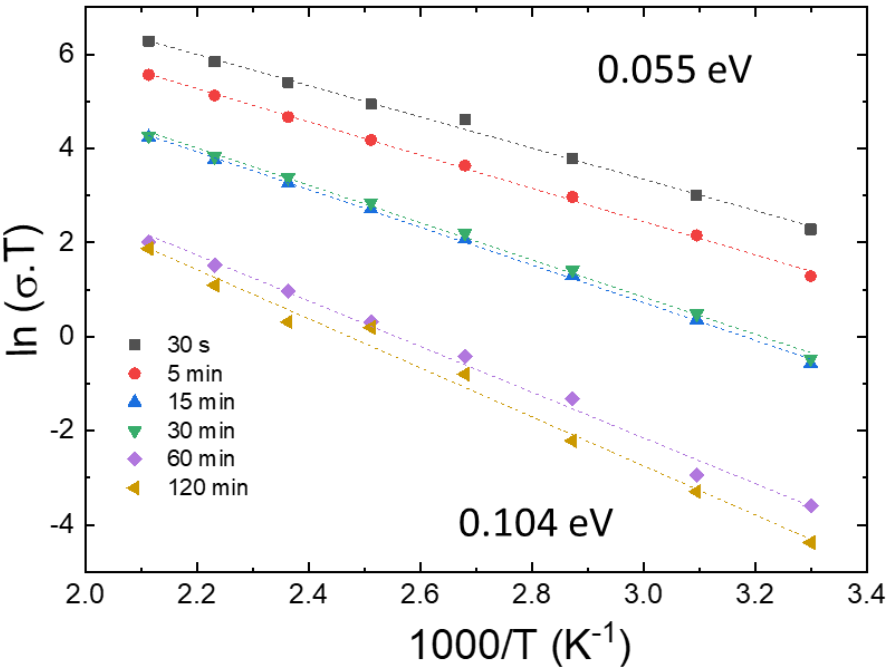

Figure 34 - Natural logarithm of the conductivity times the temperature as function of measuring temperature, for thin films annealed at 700°C during for different durations from 30 s to 120 min

From figure 34, it is possible to extract the $E_{\sigma p}$, the activation energy for polaronic conduction, resulting in the values in table 13. It is noteworthy the increase of activation energy with the increase in annealing time, in line with the increase in resistivity. These values ranging from 55 to 104 meV, are well in line with the data reported by Crêpellière et al. [284] and Barnabe et al. [278]. These results show that the conduction mechanism is unchanged by the thermal treatment here studied.

Table 13 - Extracted activation energy for polaronic conduction as function of annealing time at 700°C

Annealing	***30 s***	***5 min***	***15 min***	***30 min***	***60 min***	***120 min***
Eσp (meV)	55	61	73	72	95	104

3.3.3. Annealing dependent Raman spectroscopy

To further study the influence on the thin films of the annealing conditions, Raman spectroscopy was performed with a 442 nm laser. This allows us to further investigate, the correlation of the defect healing and the thin film crystallinity with the thermal treatments. Two Raman scattering peaks were observed for delafossite thin films (whilst not for the silicon substrate reference sample), at 457 cm^{-1} and at 709 cm^{-1}, as can be seen in figure 35, in good agreement with the results reported in the literature [255,265,307,308].

Delafossite compounds (space group R3m) such as $CuCrO_2$ have one formula unit per unit cell with a total of 12 possible vibrational modes. Among these modes only two are Raman active with E_g and A_g symmetry [308]. The A_{1g} mode corresponds to vibrations of the Cu-O bonds along the c-axis whilst the E_g mode represents the vibrations in the triangular lattice perpendicular to the c-axis. According to Aktas et al. [308], the vibration modes ωA_{1g} and ωE_g, can be attributed to the peak at 457 and 709 cm^{-1} respectively. It is noteworthy the increase in intensity of the peaks, after any annealing, when compared with as deposited thin films (depicted in red). This is in good alignment with the XRD spectra, increase in the (012) Cu-Cr-O peak, shown in figure 31, representing the increase in crystalline quality (long-range order) of the material. In the case of as-deposited thin films, defects annihilated most of Raman vibrational modes signal. Raman scattering is dependent on the surface morphology and related to grain size, crystalline quality and tensile stress in the films [265]. Post-deposition thermal treatments here studied lead to an increase of the Raman signal associated with the vibrational modes, ωA_{1g} and ωE_g, suggesting an atomic rearrangement for healing of structural defects, leading to a decrease in conductivity. This increase in peak intensity is furthermore visible with the increase in annealing time at 700 °C. The relative increase of ωA_{1g} vibrational mode compared with ωE_g, is interesting following the analysis of the lattice parameters, where a compression exists for as-deposited samples along the c-axis that is further relaxed upon annealing. These results can be associated with the dissolution of chains of copper vacancies and to an increase in the crystallinity of the thin films.

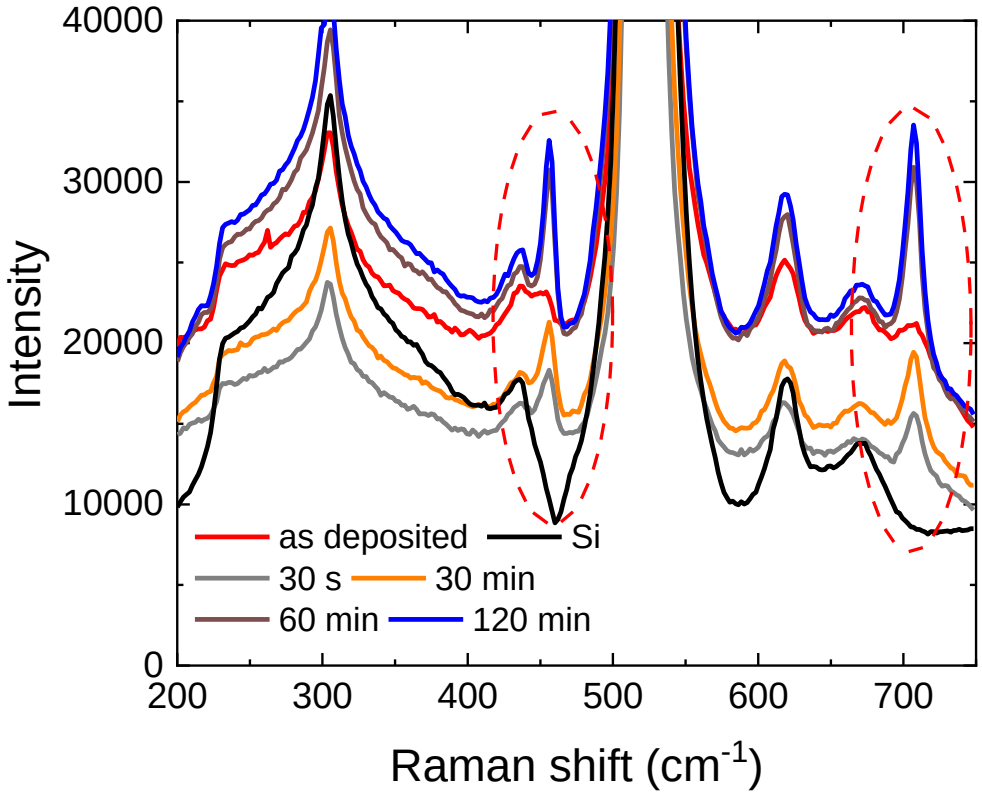

Figure 35 - Raman scattering spectra of samples with increasing annealing time

3.4. Conclusion

Delafossite thin film growth conditions were discussed and optimized for high conductivity thin films. One of the highest conductivity films were achieved for this kind of material, without recourse to external dopants. We explored the controlling of the carrier concentration, by means of post-deposition thermal annealing that will be a relevant parameter for ozone sensing due to the majority carrier injection expected in the thin films and the relation with the Debye length, that is key to the ionization of the grains. A controlled carrier concentration might be key to increase the sensitivity keeping the sensor with a minimum conductivity for standard electronic systems used in gas sensors. Films were produced using different conditions while preserving the delafossite structure. The highest conductivity thin films were selected, with different deposition times, leading to different film thickness for further study of post deposition thermal annealing processes. This allows us to have the widest study range in terms of conductivity and morphological properties to be tuned by post-deposition thermal annealing. Annealing steps increase the thin film crystallinity by healing of defects. This effect is triggered by Ostwald ripening mechanism

based on the dissolution of chains of copper vacancies. However, the stoichiometry of the thin film remains constant after annealing.

We proved that the controlled thermal treatment is an efficient approach for controlling electronic properties of $Cu_{0.66}Cr_{1.33}O_2$, a highly conductive p-type transparent oxide. The holes concentration, the electrical mobility and the electronic work function are key features for transparent solid-state devices and for a suitable integration in any active devices (such as p-n junctions, transistors or optoelectronic devices) these properties must be tailored in order to tune the required properties of such devices. Therefore, we showed that the carrier concentration could be smoothly tuned. Depending on the aimed final values we proposed a time driven or a temperature driven thermal treatment. From the value of 90 meV for as-deposited samples, the Fermi level can be tailored upwards up to 1.08 eV above the valence band maximum. The energetics of singular Cu-vacancies chain defects responsible of the high conductivity in this peculiar material was proposed. An activation energy model is used to extract the averaged activation energy of the annihilation of Cu-vacancies chains. We found $E_a = 1.35$ eV.

The changes in carrier concentration and conductivity can prove to be an important point for ozone sensing response.

4. Copper-Chromium-Oxide electrical and morphological properties tuning for sensing applications

Beside the tailoring of defects, of the carrier's mobility and concentration, the annealing process may have a severe impact on morphological factors that can change the ozone sensing response of the copper chromium oxide thin films. In this chapter we study the electrical and morphological properties of the thin films (such as roughness, crystallite size, surface area, crystal orientation) that directly impact ozone sensors response upon annealing processes at 900 and 1050°C.

Temperatures above 1100 °C promoted delafossite evaporation, what is in line with the temperature stability limit reported in the literature for $CuCrO_2$ [285]. For this were considered samples with two thicknesses, 32 and 140 nm deposited on a sapphire substrate. The annealing influence on the morphological and electrical properties of the thin films, represented in table 14, are specifically explored in this chapter.

Table 14 - Properties of as-deposited copper-chromium-oxide thin films with 32 and 140 nm

Deposition	Deposition time (s)	Conductivity (σ/cm)	Thickness (nm)	Crystallite size (nm)	Roughness (nm)
H	1800	60.34	140	8.9	5,9 ± 0,4
F	450	12.32	32	4.0	1,8 ± 0,1

In figure 36, the SEM top view of the thin films, as deposited and after a thermal annealing at 900 and 1050 °C, during respectively 900 and 300 s, can be observed. It is noticeable when comparing the as-deposited thin films, that the thicker films, F (140 nm), is quite more compact. After thermal annealing, in both cases the films roughness and porosity are increased, what becomes even more evident after the thermal treatment at 1050 °C. The films present a wide range of grain sizes with a rugged profile. In this case the grains seem to coalesce and porosity increases, what can create more pathways for the gas permeation and more active surface area. Using ImageJ software data treatment to study the surface coverage of the films, that represents the percentual area of the surface of the thin film that is covered by the material, as shown in figure 37, one can arrive at the values shown in table 15. This is in line with what can be observed in the top view images, showing the decrease of surface coverage with increase in annealing temperature.

This is further confirmed by the AFM analysis depicted in figure 38. It can be observed the increase in the morphological grain size as well as an important increase in roughness and

porosity of the thin films. Using Nanoscope Analysis tools, an image surface area differential can be calculated. This value is obtained by calculating the actual surface area measured by the AFM tip during the scan and dividing it by the projected surface (1 μm^2). Thermal treatment at 1050 °C greatly increases roughness, in the case of H sample (32 nm) from 1.8 to 5.5 nm and surface differential is increased by an order of magnitude, from 0.9 to 11.7 %. These results are instrumental to better understand the semiconductor morphological properties and being able to correlate them, among other parameters, to the gas sensing response.

GIXRD spectra is presented in figure 39. A clear increase of delafossite main diffraction peak (012) upon annealing is observed, what corresponds to a reorganization of the thin film and healing of defects, as previously observed. A shift of the peak angle, from (2θ = 36.28°) to (2θ = 36.53°) is evidenced, after annealing at 1050 °C. This shift may be associated with a change in the lattice parameters. Prior to thermal treatment, the extracted parameter, for "c", along the z axis, is 17.05 ± 0.02 Å, whilst the extracted value after annealing at 1050 °C, increases to 17.11 ± 0.02Å, without a relevant change in "a" parameter ($a = 2.975 \pm 0.01$). As previously reported [263,284,285], our as-deposited delafossite lattice is slightly compressed along the "c" axis. The increase in annealing temperature leads to a relaxation of the lattice to the expected values for pure $CuCrO_2$. This can be associated with the healing of Cu vacancies by atomic rearrangement, as no change in stoichiometry was observed. The increase in intensity can also be observed in $CuCrO_2$ (110) and (108) peaks, as well as a small shift to higher diffraction angles. For the samples annealed at 1050 °C, gold peaks can be observed due to the contact pads added for ozone measuring devices. No other peaks can be observed, showing the preservation of delafossite structure.

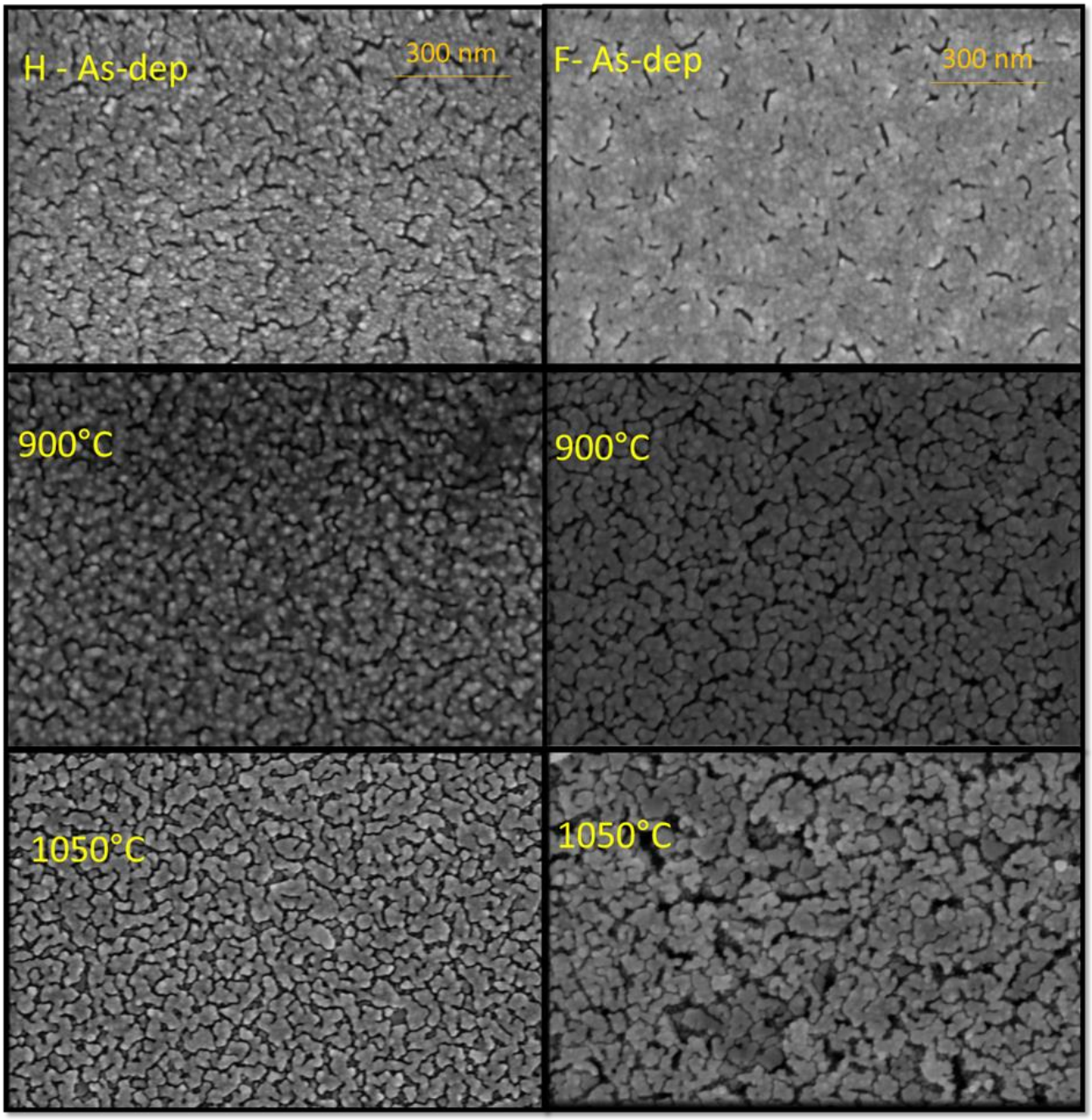

Figure 36 - SEM top view of delafossite thin films, as deposited, annealed at 900 °C and 1050 °C: on the left sample H, with 32 nm and on the right sample F, with 140 nm

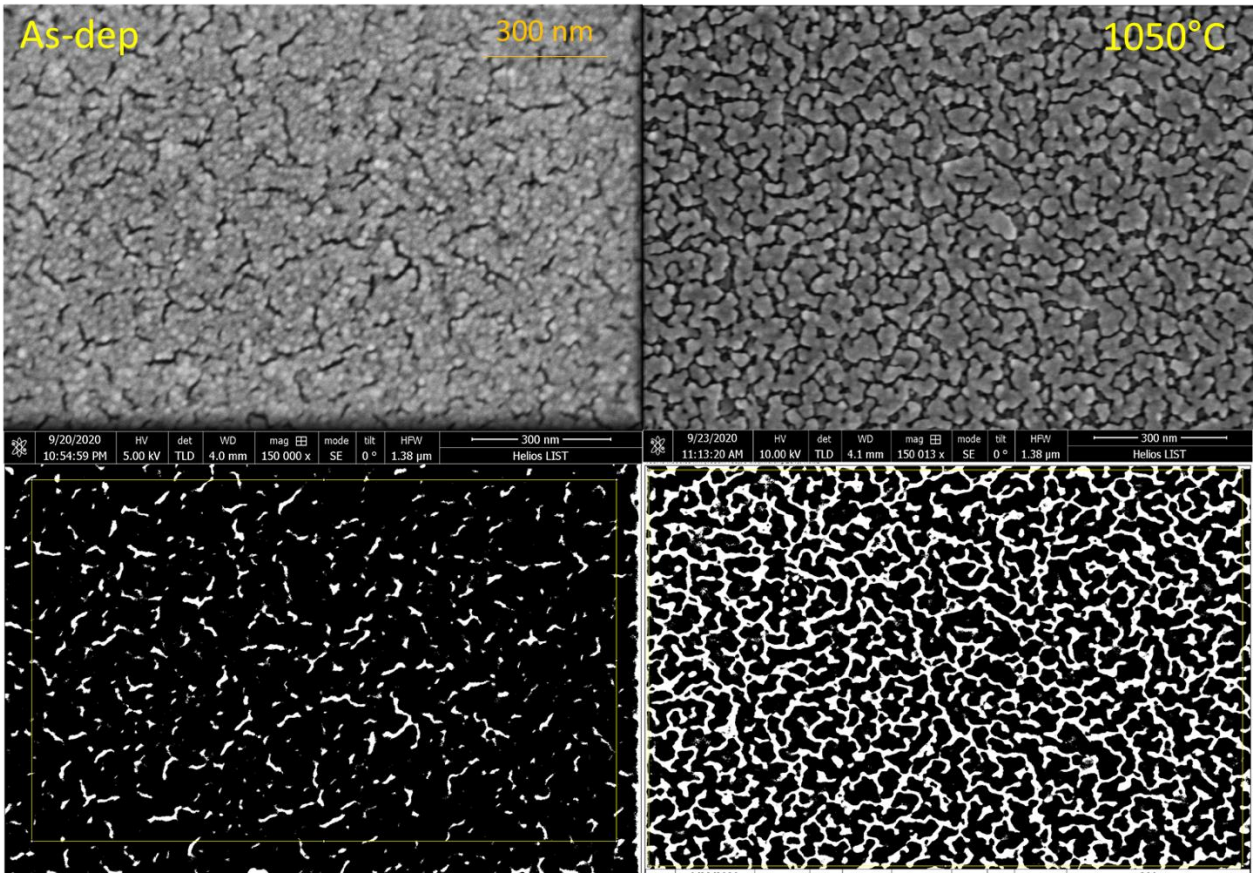

Figure 37 - 32 nm films as deposited and annealed at 1050 C top view images and ImageJ data treatment to calculate surface coverage

Table 15 - Summary of electrical and morphological properties of delafossite thin films with 32 and 140 nm: as deposited, annealed at 900 °C and 1050 °C

			32 nm			**140 nm**
Annealing temperature	As-dep	900°C	1050°C	As-dep	900°C	1050°C
Conductivity (S/cm)	12	7.3×10^{-4}	4.6×10^{-7}	60	2.1×10^{-3}	4.5×10^{-7}
Avg. Roughness (nm)	1.8	2.1	5.5	5.6	5.3	8.4
Surface Coverage (%)	94	87	71	98	88	82
AFM - Surface area differential (%)	0.9	1.2	11.7	2.4	2.9	14.7

Crystallite size (nm)	4.0	9.3	13.9	8.9	13.0	19.9

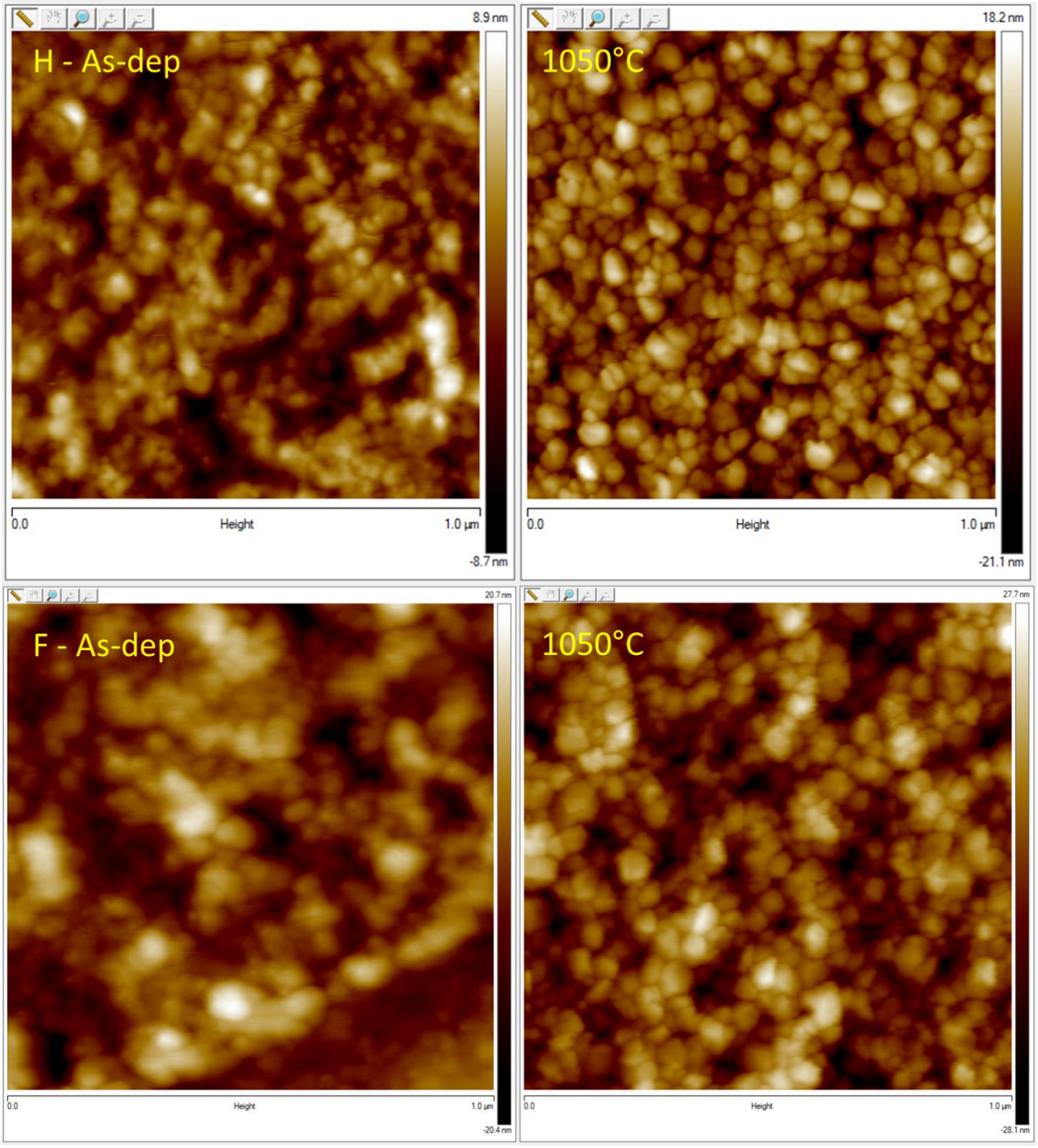

Figure 38 – AFM images 1 x 1 µm showing the surface morphology of copper chromium oxide thin films, with 32 and 140 nm, as deposited and annealed at 1050 °C

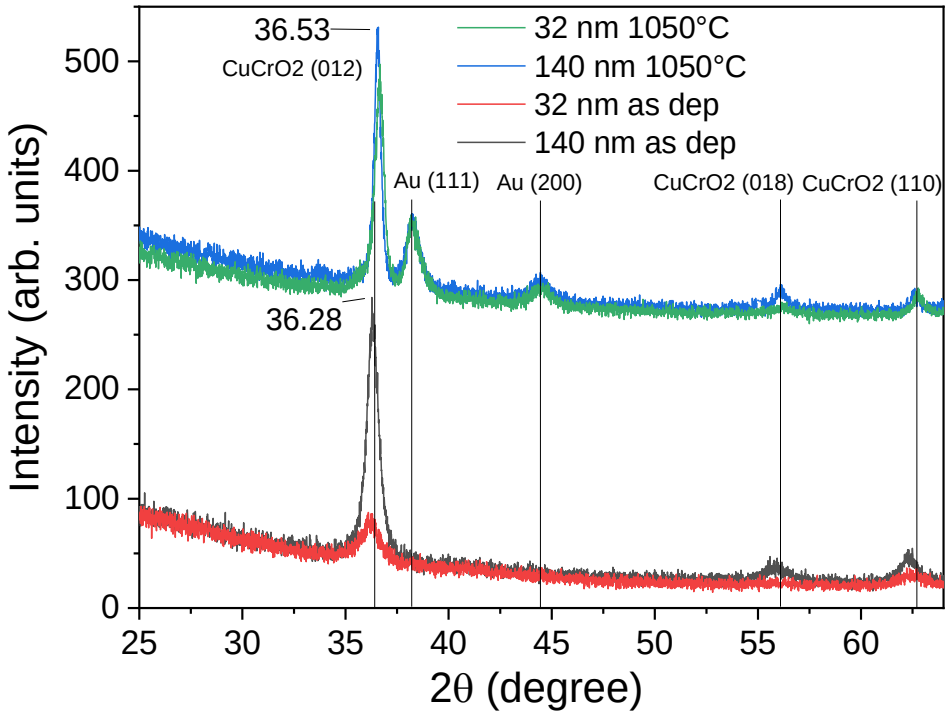

Figure 39 - GIXRD spectra for films (32 and 140 nm) as deposited and annealed at 1050 °C.

Delafossite thin film properties were tuned, using a wide range of annealing conditions. As discussed in chapter 1.4, metal oxide sensors response depends greatly on the thin film properties. Morphological properties, such as porosity and surface area were studied with the objective of maximizing them, since these properties can directly control the sensing response of the thin films.

Thermal treatments have impact on the morphology of the thin films, by increasing the grain size and crystallite size. There is an increase in roughness and porosity that was quantified using the surface area differential, extracted from AFM measurements and the surface coverage extracted from SEM top view images. These changes in morphology indicate that annealed thin films should present a bigger response to ozone sensing, due to the much-increased surface area. The increase in porosity might furthermore implicate the change from a pure surface reaction, where the ozone sensing is surface only, to a reaction throughout the full thickness of the film.

5. Ozone Sensing

Off-stoichiometric copper chromium delafossite thin films sensing activities towards O_3 are studied in this chapter. The influence of the thin films properties on the sensing behaviour is discussed. Furthermore, the measurements varying the gas concentration and the temperature are also explored. Annealed samples, over a wide range of temperature, starting from 700° to 1050 °C are compared with non-annealed thin films, which allows us to derive an understanding of the impact of the carrier concentration/conductivity. The influence of the thickness and morphological properties is studied. An understanding model of the ozone delafossite reaction, using the power law theory, for static response is used. A dynamic model is proposed, based on the Langmuir theory of adsorption to better understand the reaction undergoing on the grain's surface. Physical and kinetic parameters are derived to get scientific insights of the surface reactions.

The electrical measurements in this chapter are done using two probe I-V measurements. 4-point probe measurements were performed in several cases to confirm the validity of the measurements.

5.1. $Cu_{0.66}Cr_{1.33}O_2$ sensing response

The change of the electronic properties of semiconductor oxides depends on the composition of the surrounding gas atmosphere. The surface conductivity of the sensor is modified by adsorption of gas species and related space charge effects. In oxidizing atmosphere, the oxide surface is covered by negatively charged adsorbates and the adjacent space charge region is electron depleted, increasing surface potential and the semiconductor's workfunction. As shown in chapter 3, $Cu_{0.66}Cr_{1.33}O_2$ is a p-type semiconductor. Upon interaction with ozone, chemisorbed oxygen species are created in the film's surface, normally O^- or O_2^- (O_3^- cannot be fully excluded for short periods of time [71]). These adsorbate species will trap electrons from the conduction band, creating a bandbending of the energy levels on the grain surface. A surface accumulation layer which has a higher concentration of majority carriers (holes) is generated. In this situation the local conductivity of the films will increase. The sensing response to a gas is then defined as the relative conductivity ratio:

$$S = \frac{\sigma}{\sigma_0} = \frac{I}{I_0} \tag{35}$$

where, σ is the conductivity when exposed to ozone and σ_0 is the conductivity in dry air. I and I_0 are the currents measured when exposed to the target gas and in dry air respectively.

In this chapter we will explore $Cu_{0.66}Cr_{1.33}O_2$ response to ozone at low temperature (up to 200 °C). Prior to our work, the best results using a delafossite material at room temperature achieved a minimum detection limit of 50 ppm of ozone (with a response of about 40%) [12,281], a value 500 times higher than the limits imposed by the governmental health and safety agencies. In this work we explore the sensitivity of this off-stoichiometric material as well as the influence of the electrical and morphological changes promoted by post-deposition thermal treatment to improve the sensing response, as per equation 35. A study of the selectivity of the sensors when compared with molecular oxygen is performed. A theoretical model of the delafossite-ozone reaction is also proposed.

5.1.1. Annealing conditions

The response of delafossite thin films, deposited on a silicon substrate with thicknesses of 45, 75 and 150 nm, to 5 ppm of ozone diluted in air at room temperature is shown in figure 40, as function of time. As-deposited thin films present a very low sensitivity to ozone. One can still notice the increase in sensitivity with decreasing the films' thickness. The best response was observed for films with 45 nm, whilst 150 nm presented the poorest performances. A change in conductivity in the thinnest film of about 1% was recorded upon ozone introduction. This is however insufficient mainly when considered the high ozone concentration used, 5 ppm. The p-type behaviour of the sensors was confirmed, with the increase in conductivity upon ozone exposure due to the trapping of electrons.

As observed in chapter 4, our as-deposited delafossite thin films, do not present the ideal morphological properties for ozone sensing, due to their compact surface, high surface coverage and low roughness. Furthermore, the high carrier concentration present in these films is unsuitable, since a high amount of electron trapping due to ozone adsorption would be necessary for a noticeable increase of the films conductivity. A similar study to the one present in figure 40, was performed using thin films annealed at 700 °C during 900 s. It is presented in figure 41. Several conclusions might be drawn. The annealing process increases the sensitivity of delafossite thin films by a factor of 10. This increase is seen in any of the films thickness studied. The thinner film (45 nm) presents better sensing response after 1 hour of ozone exposure. The thicker film (150 nm) presents the lowest sensing response. The saturation of current reached suggests that a steady state equilibrium between adsorption and desorption of oxygen adsorbates was reached, at the measurement temperature. The responses for the case of figure 40 and 41, were performed at room temperature. The small conductivity changes observed upon gas introduction for non-annealed samples and samples annealed at 700°C lead to rather small conductivity changes (below 1 and 10 %, respectively). Even if a general trend might be analysed, comparison sample to sample must be done carefully due to the low current changes leading to values close to the measuring apparatus error.

Further annealing temperatures are then studied, for so the samples discussed in chapter 4 are used. Delafossite thin films, deposited on sapphire substrate, due to its high thermal stability, annealed at 900 °C and 1050 °C sensitivity to ozone is discussed. Three thicknesses were deposited: 32, 70 and 140 nm. The influence of the films thickness is furthermore discussed.

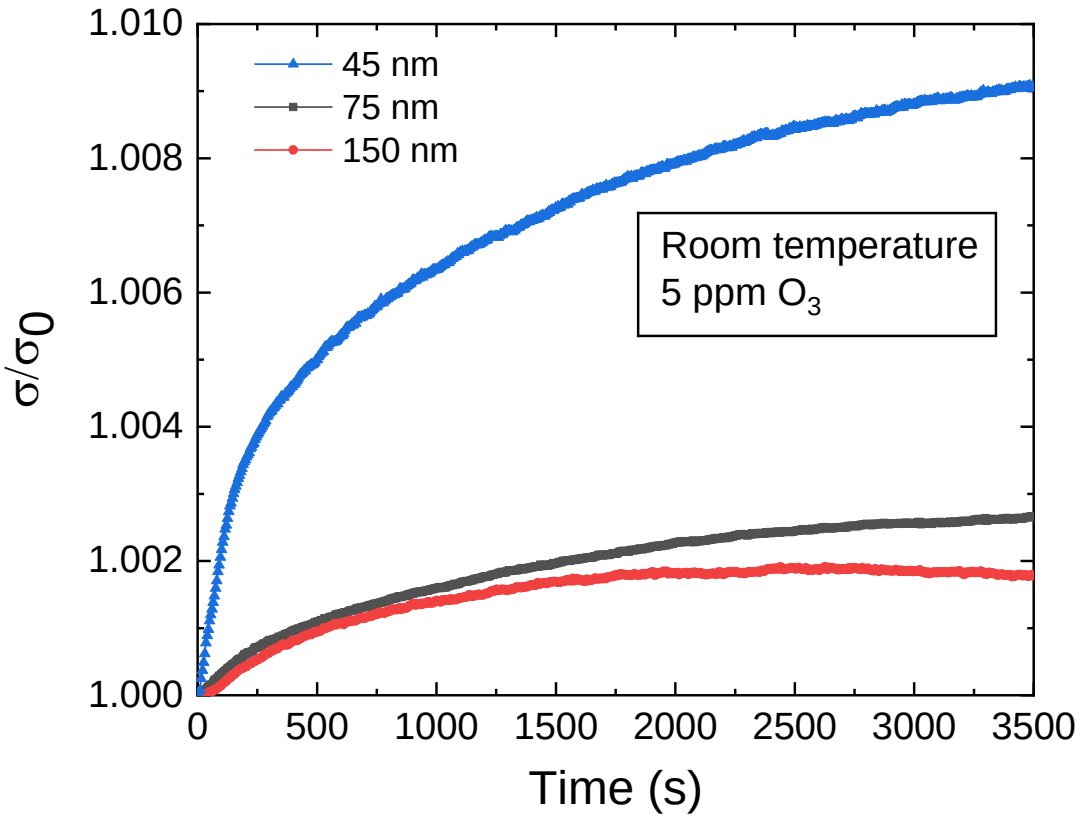

Figure 40 - Sensing characteristics of as-deposited Cu-Cr-O delafossite with different thicknesses, 45, 75 and 150 nm, upon exposure to 5 ppm of ozone diluted in dry air, at room temperature.

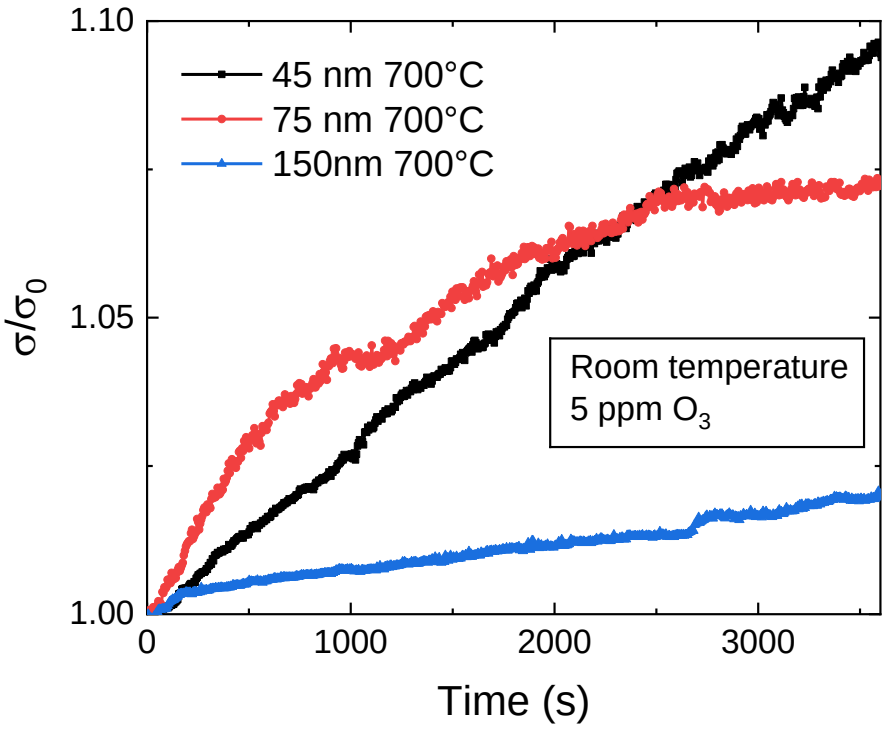

Figure 41 - Sensing characteristics of Cu-Cr-O delafossite annealed at 700 °C for 900 s upon exposure to 5 ppm of ozone diluted in dry air, at room temperature.

For Cu-Cr-O delafossite thin film with 32 nm thickness and annealed at 900 °C, its response to 5 ppm of ozone at room temperature is shown in figure 42. A sensing response of 1.57 was calculated, what corresponds to an increase in conductivity of 57%, upon ozone exposure. In figure 43, is shown the response to 5 ppm of ozone of the 32 nm copper chromium oxide thin film, annealed at 1050°C. A response leading to a fivefold increase in conductivity is remarkable. Similar results were observed for the samples of 70 and 140 nm, as shown in table 16. It should be noted however, the decrease in conductivity by the high temperature annealing leads to a decrease in the measured current, with measurements in the picoampere range, that can be a limiting factor for integration into traditional electronics used in sensor networks. These results can be understood by reminding the conclusions drawn in chapter 4. The increase in porosity allowing a higher gas permeation and the increase in roughness resulting in a bigger surface area, allows the ozone reaction to extend beyond the surface of the thin films, greatly increasing its sensitivity. This can be further observed by the 3D representation of AFM images taken of the thin films, as deposited, annealed at 900° and 1050°C, shown in figure 44. In these images one can see the very clear increase of surface area, after the high temperature annealing process.

Furthermore, the high temperature annealing leads to a decrease in the Debye length (equation 10), that represents in the case of a polycrystalline semiconductor, the distance over which the chemical electrostatic effects can propagate, changing the free charge

carriers. It is possible, that the decrease in carrier concentration observed leads to a higher ionization of the individual grains. In a parallel resistor model, as the one represented in figure 45, this is represented, by a decrease of the contribution of the bulk resistance, where $R_{total} = R_s$. In this model it is considered that the bulk resistance is independent of ozone concentration while the surface resistance is inversely correlated to it. The particle boundary resistance will also be influenced by the ozone adsorbate species due to the bandbending induced in the grain surface. The particle boundary is situated at a distance from the grain surface equal to the Debye length. When coupled with the increase in porosity, this can lead to gas interaction at the surface of each individual grain, creating a fully charged regime. Technological limitations exist when trying to extract the carrier concentration of such copper-chromium-oxide thin films with our setup. Due to the low mobility, Hall effect measurements are not suitable and our homemade Seebeck system is not reliable in the studied range. However, an order of magnitude can be estimated if certain assumptions are made: i) due to lack of bibliographic data, the dielectric constant was considered 15. This is based on the dielectric constant of Cr_2O_3, estimated to be 13 [309] and Cu_2O estimated at 18.1 [310]. ii) considering a mobility of 0.01 and 0.0001 cm^2/Vs, similar to the highest and lowest extracted for the samples studied in chapter 3.3, would result in $10 < L_D < 100$ nm, for the 32 nm copper-chromium-oxide thin film annealed at 1050 °C and $0.8 < L_D < 8$ nm, for the 32 nm thin film annealed at 900°C. These results would suggest that for the higher annealing temperature (1050 °C), it would likely result in a fully charged regime, even if grain size estimation is difficult to the grain heterogeneity observed.

The gradual increase in sensing response (as considered by the sensitivity) increases from below 1% for as-deposited films to a 5-fold response (precisely, 464%) for films annealed at 1050°C. These improvements are associated with the variation in carrier concentration of the films and the morphological changes observed leading to a higher surface area.

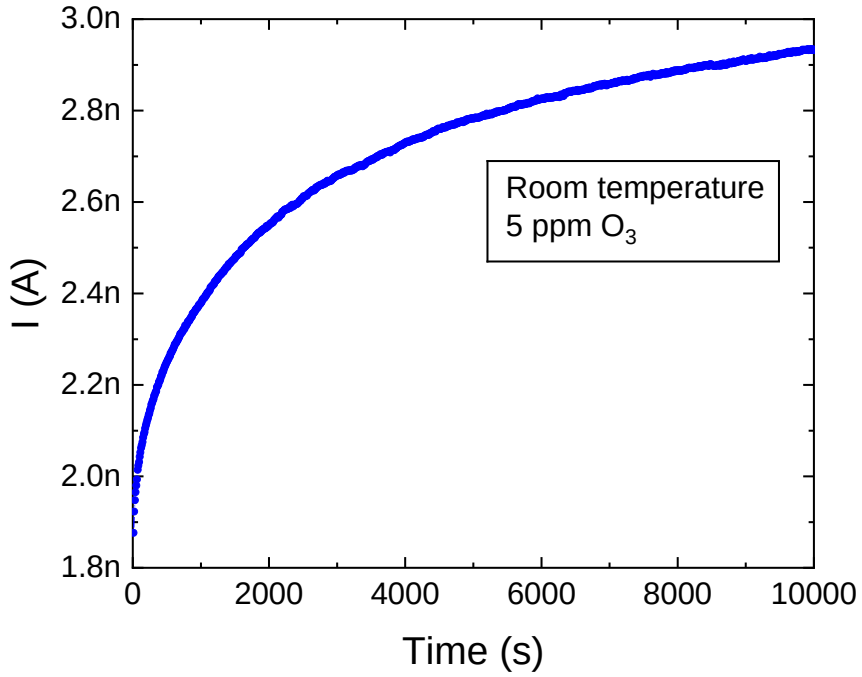

Figure 42 - Sensing characteristics of Cu-Cr-O delafossite (32 nm) annealed at 900 °C for 900 s, upon exposure to 5 ppm of ozone diluted in dry air, at room temperature.

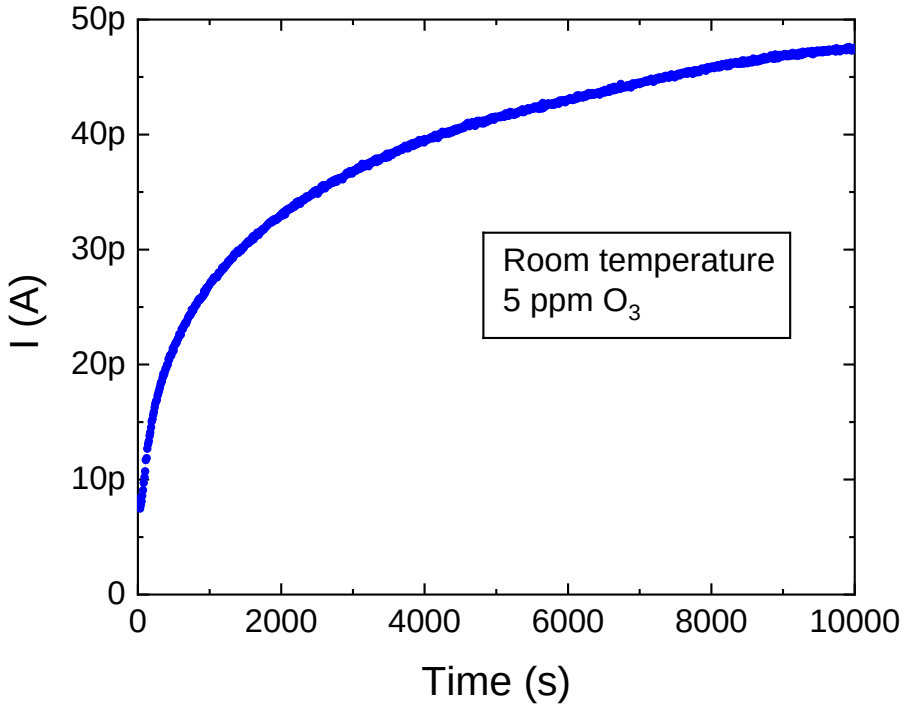

Figure 43 - Sensing characteristics of Cu-Cr-O delafossite (32 nm) annealed at 1050 °C for 300 s, upon exposure to 5 ppm of ozone diluted in dry air, at room temperature.

Table 16 – Maximum sensing response, as a % increase in conductivity, when exposed to 5 ppm of ozone depending on the thin films' annealing conditions.

Deposition	As deposited	700 °C	900 °C	1050 °C
Thinner (32 – 45 nm)	0.9 %	9 %	57 %	464 %
Medium (70 – 75 nm)	0.3 %	7 %	28 %	360 %
Thicker (140 – 150 nm)	0.2 %	2 %	33 %	239 %

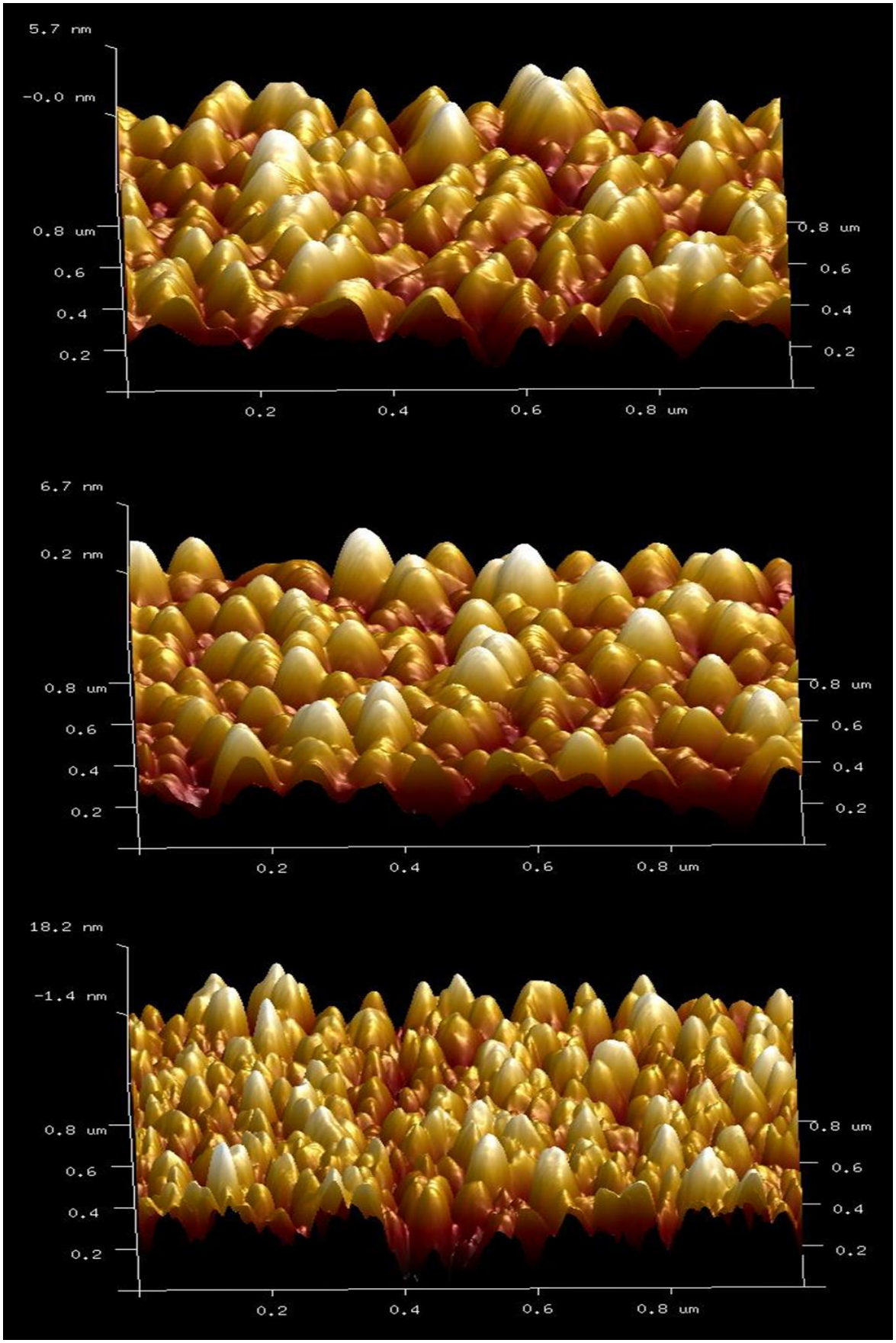

Figure 44 - 3D AFM pictures of delafossite thin films from top to bottom: as deposited, annealed at 900°C and annealed at 1050°C.

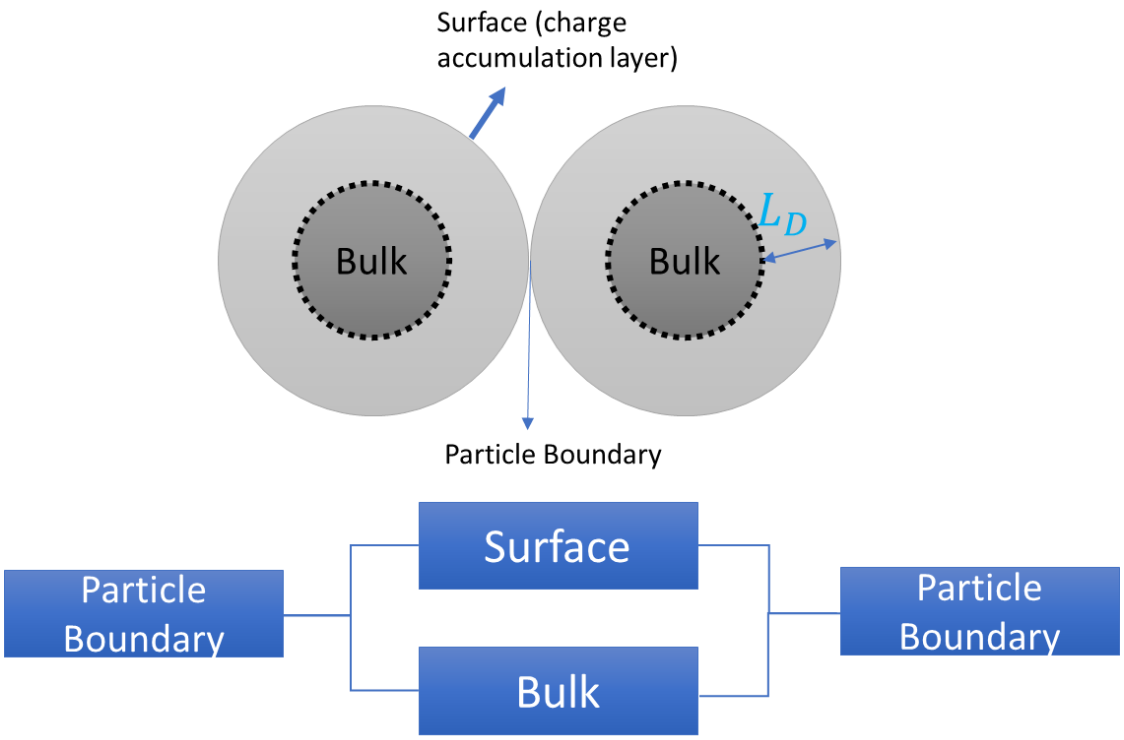

Figure 45 - Model representing the grain particles, the surface and the bulk and how their geometry can be derived into a resistance model

5.1.2. Thickness influence

Thin film thickness is an important parameter for ozone sensitivity as discussed in chapter 1.4. From our previous results it seems clear that the thinner films present higher sensitivity. Figure 46, further corroborates this assumption, when we compare the sensing response at room temperature of 32, 70 and 140 nm thin films annealed at 1050 °C. The sensing response of 32 nm films is 5.64, while it is 3.39 for 140 nm films. The inset shows the response for the first 500 s of ozone exposure, showing a response of more than 2.5 times for the thinner film and only about 1.5 for the thicker film. Whilst for lower annealing temperatures the difference in response might be correlated with different conductivities (the thicker films are more conductive), as shown in table 16, the conductivity for the 32 and 140 nm samples annealed at 1050 °C are comparable (4.6×10^{-7} and 4.5×10^{-7} S/cm, respectively). This further corroborates the hypothesis of the kinetics of ozone sensing being driven by surface reaction of the delafossite grains. When exposed to ozone the polycrystalline material grain boundaries, their Schottky potential barrier is decreased, favouring its conductivity. The thicker film also presents a very noisy response. This can partially be associated with the low conductivity, but it doesn't explain the increased noise for the thicker film, that has been observed in several experiments.

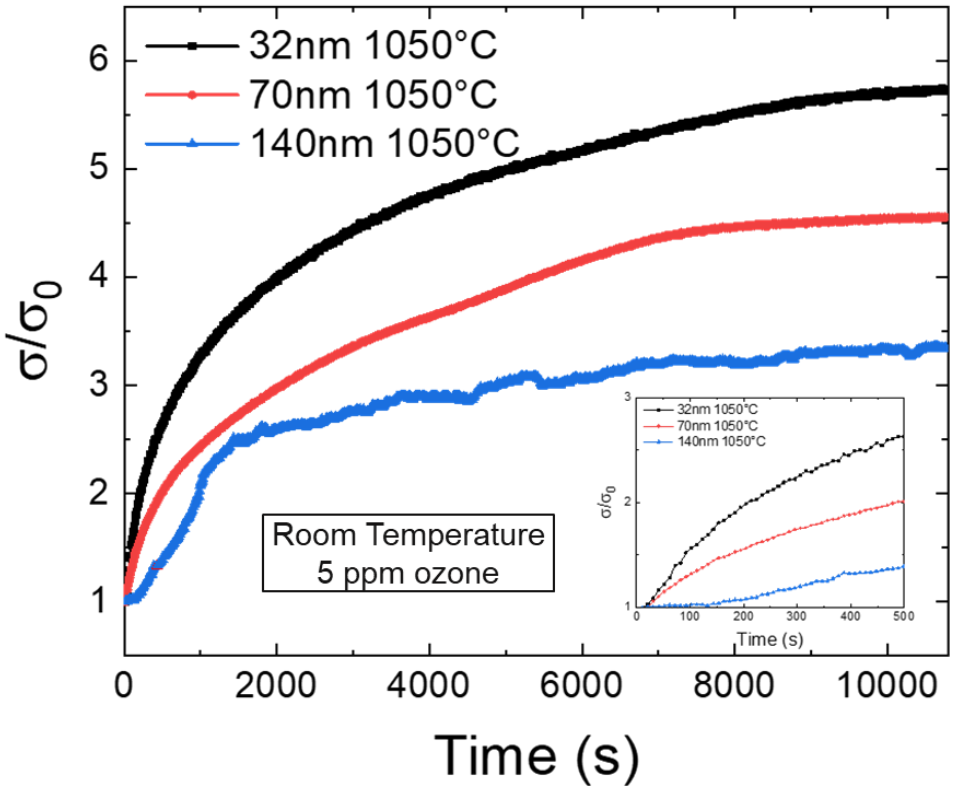

Figure 46 - Sensing characteristics of Cu-Cr-O delafossite thin films annealed at 1050 °C for 300 s, upon exposure to 5 ppm of ozone diluted in dry air, at room temperature, with 32, 70 and 140 nm. Inset showing the response during the first 500 s of exposure to ozone.

5.1.3. Temperature dependence

The influence of the measurement temperature on the thin films response was investigated. For this, the delafossite thin film of 32 nm annealed at 1050°C was purposely considered. In a first cycle, the I-V curve of the film was measured at 25, 50, 100, 150 and 200 °C, with a flow of dry air. A cool down cycle followed and then ozone in the concentration of 2.5 ppm was injected. It was waited until a plateau was reached. Next the temperature was further increased to the next value. The experimental results are shown in figure 47. One can notice the relative stability in the ratio of current under ozone and dry air in between 25 and 150 °C. Furthermore, the almost parallel behaviour of the dotted lines, showing a logarithmic increase of the current with the temperature, as expected for a semiconductor, shows a likely similar activation energy and no change of conduction mechanism.

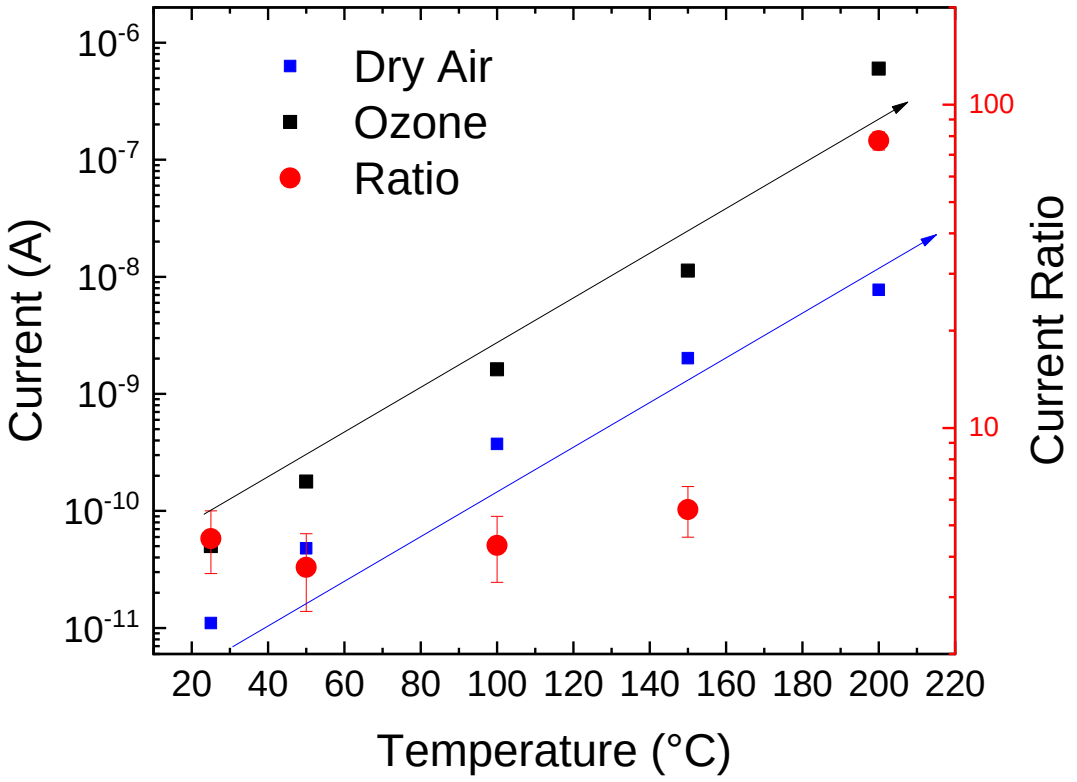

Figure 47 – 32 nm thin film annealed at 1050 °C current, with a bias of 1V, at increasing temperatures from 25 to 200 °C. The response is shown under dry air and under 2.5 ppm of ozone after a steady-state has been reached. In red is the current ratio (Current under ozone/Current under dry air). Arrows for guiding eyes, showing the two cycles of response, with increasing temperature under dry air exposure and ozone, considering the data up to 150°C.

Data at 200 °C however suggest a significant change of the mechanism of the sensing reaction. A huge increase in the current ratio, more than one order of magnitude is observed; the time to reach a plateau is greatly increased, from about 1 hour to more than 15 hours. These results will be further discussed in chapter 5.

Delafossite conductivity is known to be limited by small polaron hopping (discussed in chapter 1.5). The conductivity dependence on temperature, given by Mott and Davies [246], was presented in equation 34.

$E_{\sigma p}$ is the polaronic activation energy. By fitting the data of the films under dry air and ozone exposure, $E_{\sigma p}$ was extracted, with values of 149 meV and 143 meV, respectively. The activation energies extracted for this samples are considerably higher than the ones extracted in table 13, for samples annealed at 700°C (values ranging from 55 to 104 meV, for samples annealed for 30 s and 120 minutes, respectively) as would be expected due to the much higher annealing temperature (1050°C). From this analysis we may conclude that ozone exposure does not induce a change in the conduction mechanism, but merely an offset of the

baseline conductivity due to injection of majority carrier due to ozone exposure. This is the case in the range of temperatures 25 - 150°C.

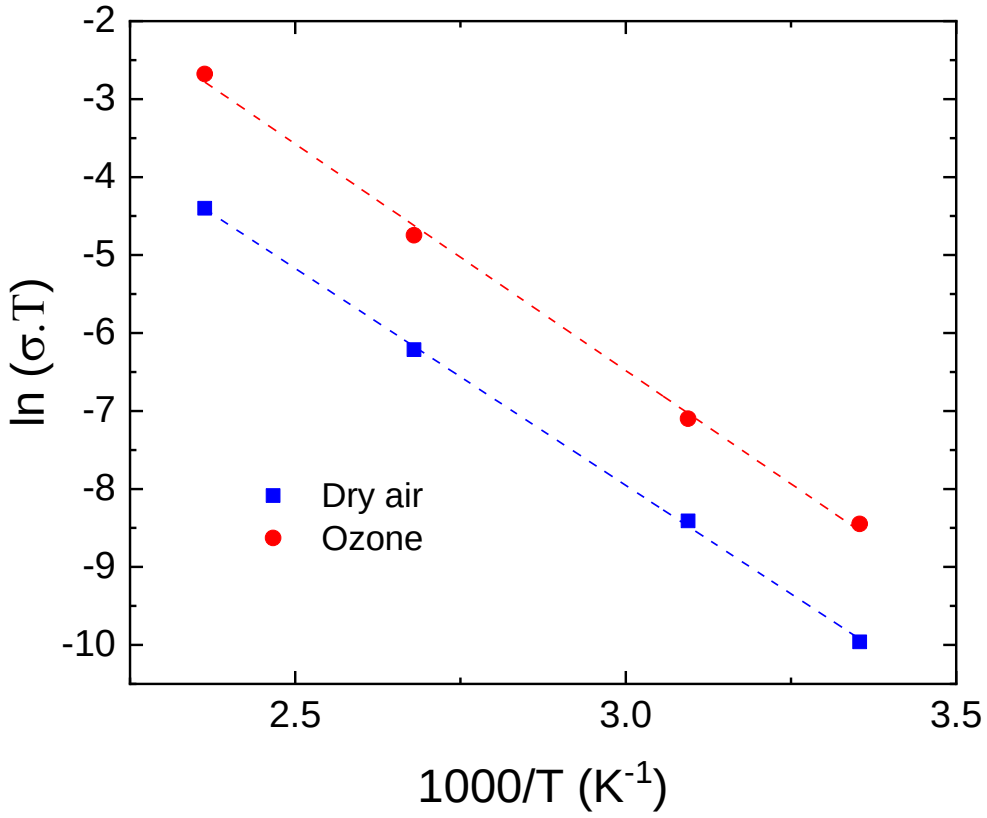

Figure 48 – Mott and Davies small polaronic conduction fit, using the natural logarithm of the conductivity times the temperature as function of measuring temperature, for 32 nm delafossite thin film annealed at 1050 °C, under dry air and 2.5 ppm ozone exposure.

In figure 49, is presented the sensing response of 32 nm copper-chromium-oxide thin film upon exposure to 50 ppb of ozone. In this case one can observe an increased response for the 125°C in comparison with the 75 and 100°C measurements.

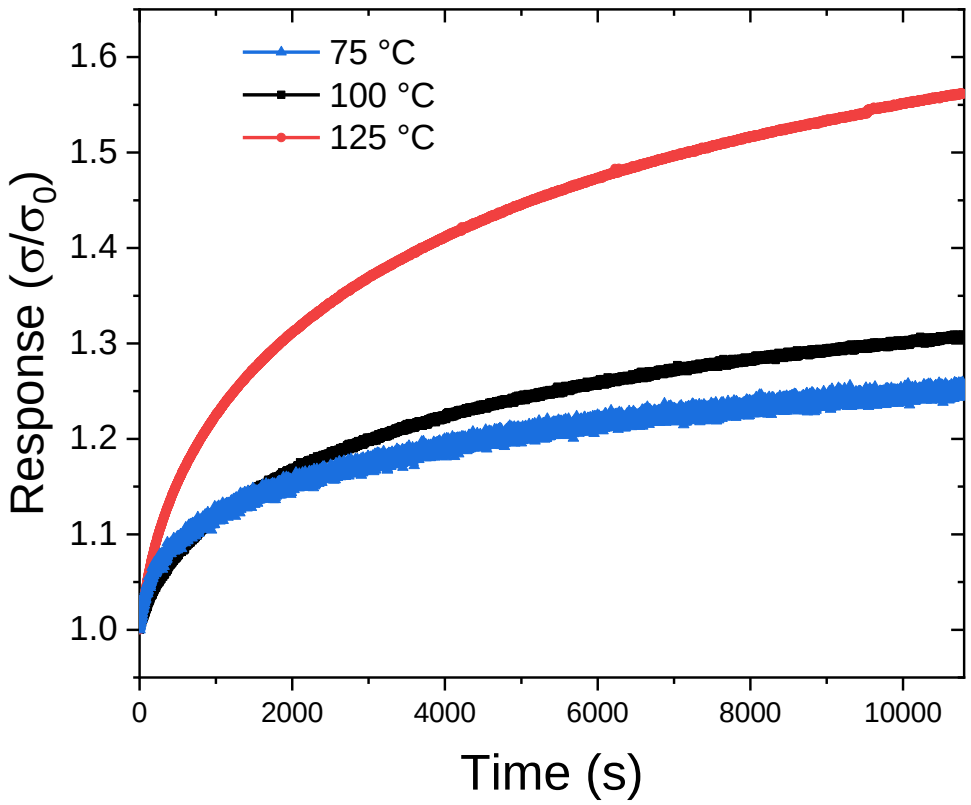

Figure 49 - Sensing response of 32 nm copper-chromium-oxide annealed at 1050 °C for 300 s, to 50 ppb of ozone diluted in dry air, at 75°, 100° and 125°C.

The temperature dependence analysis of the delafossite thin films, shows the sensor might be applied at the temperature range, 25 – 150 °C, showing the great potential of off-stoichiometric delafossite thin films for low temperature ozone sensing.

5.1.4. Influence of ozone concentration

Ozone concentration limits imposed by the health and environmental agencies are in the range of 70 – 100 ppb per 8 hours / day exposure and 1 ppm as a danger level, for 15 minutes.

In figure 50, we present the study of consecutive ozone exposures to our 32 nm copper-chromium delafossite thin films annealed at 1050°C with ozone concentrations from 50 ppb to 350 ppb, with its reversible reaction. The figure shows the consecutive increase in conductivity upon ozone exposure, first when exposed to 50 ppb, until a plateau was reached. Next ozone injection was stopped, and the recovery under dry air can be observed almost to the base value. This is an advantage to the commonly proposed sensors, based on In_2O_3 and SnO_2, that have been shown to require temperatures above 300°C for fully reversible reactions [40,44]. A next injection of 100 ppb shows the increase in conductivity to a higher

degree than the one at 50 ppb. This is furthermore observed at 350 ppb. A close to total recovery is achieved in this timeframe. It can be noted in the recovery phase a small drift of the baseline current (less than 5%), in the time range given. It should however be noted that if enough time is given (at least 12 hours), a total reversibility of the measurements is achieved in the studied temperature range. These results show for the first time, to the best of our knowledge, the sensitivity of copper-chromium delafossite thin films to this range of ozone concentrations. The electrical and morphological property engineering done during this work, was able to decrease the detectable ozone concentrations by a factor of 1000, when compared with the stoichiometric delafossite [12,281]. Furthermore, the response to only 50 ppb of ozone is of the same magnitude as the one presented by Zhou et al. [12], for 50 ppm of ozone, for pure phase $CuCrO_2$.

The I-V characteristics of the sensor response, using different ozone concentrations, from 50 ppb to 2.5 ppm, are depicted in figure 51. It can be observed the different sensing behaviour depending on the ozone concentration. A higher plateau is reached for higher ozone concentrations. This thus allows to use our delafossite thin-film as a chemiresistive sensor for ozone in a suitable range of concentrations for a widespread usage. This can help confirming the reaction of ozone being derived by the occupation of surface states, leading to changes in the local resistance. However, the time to reach a steady state (usually above 3 hours) is a severe obstacle for the sensor usage in some practical cases. In general, in the literature, the response time is presented as T90 (the time required to reach 90% of the equilibrium signal) [32,35,51]. However, considering figure 50, an equilibrium has not been fully reached even after 3 hours, rendering this response time unsuitable, for practical usage.

To overcome this problem another detection method is suggested, based on the dynamic rate of increase of current with time or the slope of the sensing response during the first 200s. As shown in figure 52, the difference in ozone concentration can be well observed in this time range. During the first period the increase in current as function of time is linear. In the figure inset is plotted $\frac{dI}{dt}$, as function of ozone concentration, showing a linear increase. This method suggests that by periodic data acquisition, our sensors can have a quick response, in a hundred seconds or less, while working at low temperatures (< 100°C).

Yet another practical usage possibility is the recording of the current after a fixed time of ozone response, as shown in figure 53. The current is recorded 200 seconds after ozone exposure for different ozone concentrations. This is another practical mechanism that would allow the integration of our sensors into low-cost sensor networks.

Figure 54, shows consecutive exposures to a) 50 ppb and b) 100 ppb of ozone, showing the full reversibility of our sensors as well as the repeatability of the measurements. Thicker films (140 nm) also present reversible response to ozone at 50 ppb as shown in figure 55, albeit its sensitivity being greatly diminished. However, no limitations in terms of ozone detection limit were found when comparing the response of films with different thicknesses,

ranging from 32 to 140 nm. From figure 50, can be extracted a T90 for response, of 2000 s and T90 for recovery of 10750 s. The correlation $\tau_{rec} > \tau_{res}$, that is the total recovery time being larger than the response time until saturation, was observed in every case, what is typical for sensors controlled by adsorption/desorption mechanisms [72].

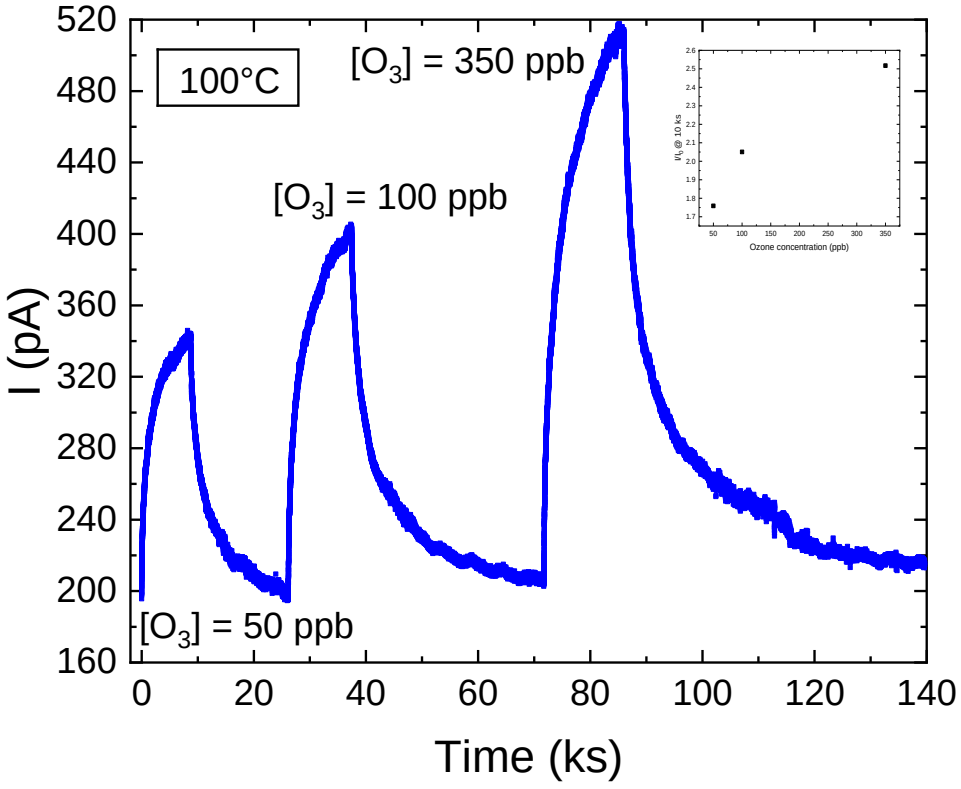

Figure 50 - Sensing characteristics at 100°C of 32 nm Cu-Cr-O delafossite thin films annealed at 1050 °C for 300 s, with consecutive exposures using ozone concentrations of 50, 100 and 350 ppb and the recovery periods in between. Inset shows the current ratio after 10 ks exposure for each cycle as function of ozone concentration.

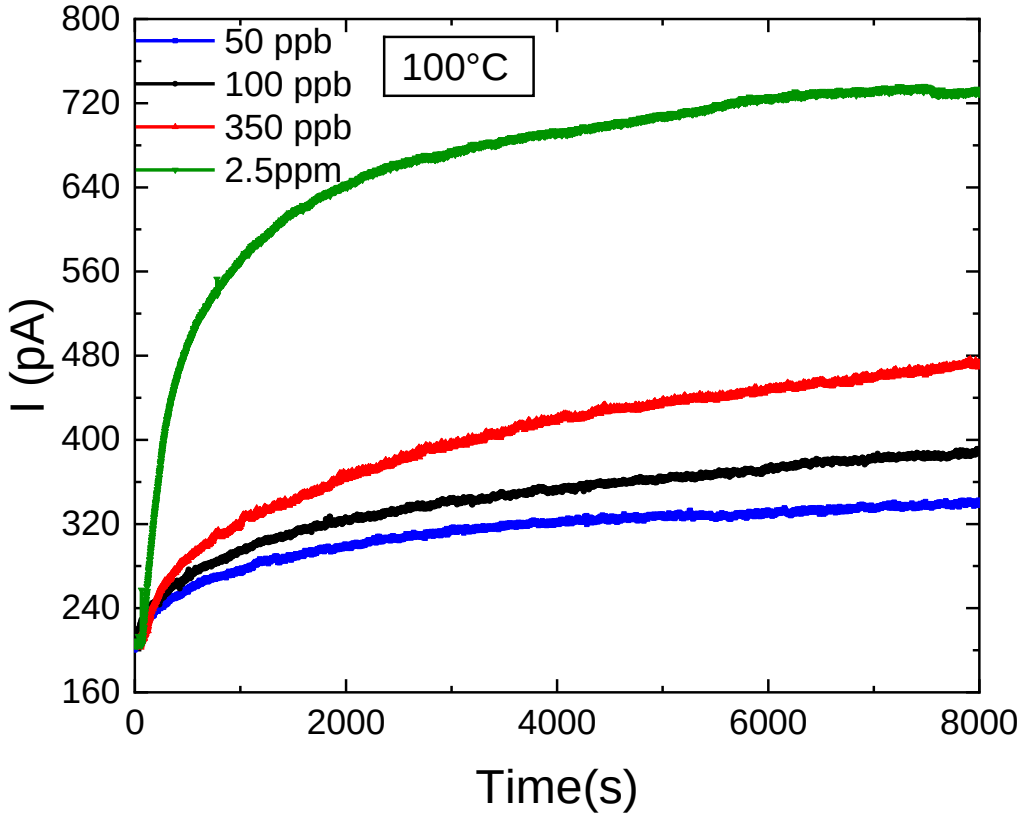

Figure 51 - Sensing characteristics at 100°C of 32 nm Cu-Cr-O delafossite thin films annealed at 1050 °C for 300 s, upon exposure to ozone diluted in dry air, 50, 100, 350 and 2500 ppb.

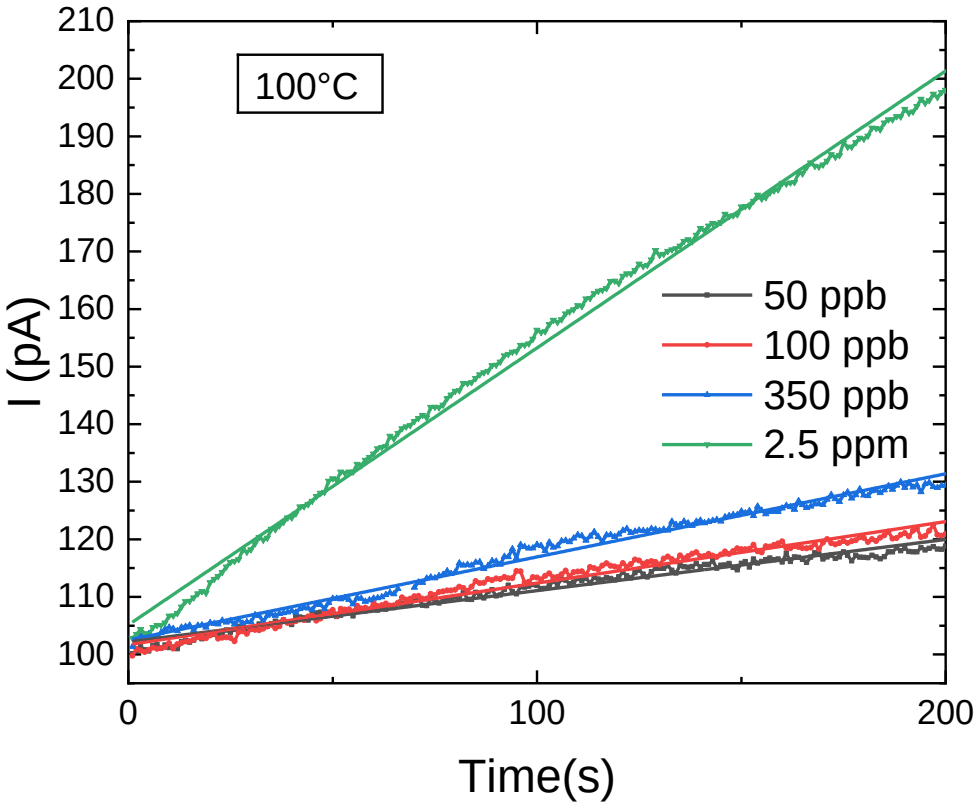

Figure 52 - Sensing characteristics at 100°C of 32 nm Cu-Cr-O delafossite thin films annealed at 1050 °C for 300 s, upon exposure to ozone diluted in dry air, 50, 100, 350 and 2500 ppb, for the first 200 s of ozone exposure.

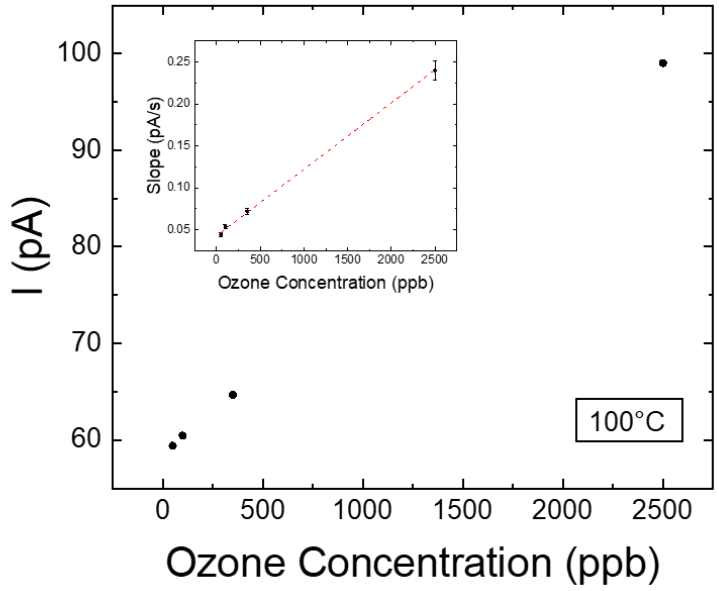

Figure 53 – Current values measured for 32 nm copper-chromium-oxide ozone sensor annealed at 1050°C after 200 s of ozone response to increasing ozone concentration. Inset: $\frac{dI}{dt}$ of ozone characteristics as function of ozone concentration, showing a linear dependence.

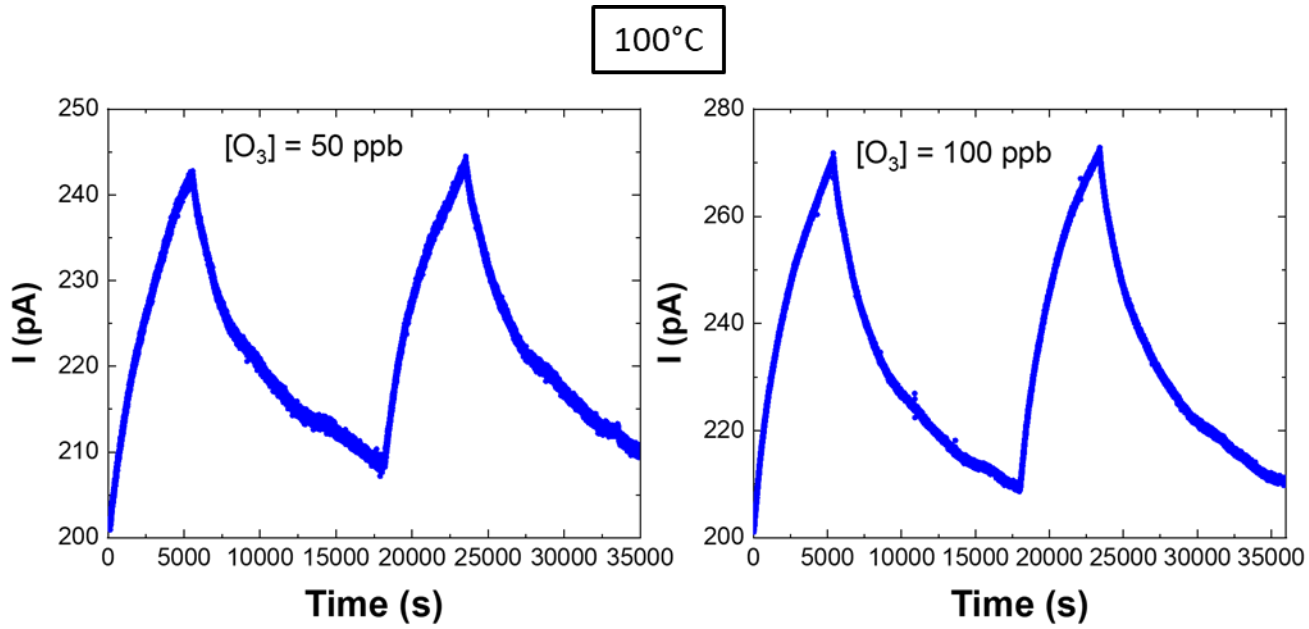

Figure 54 - Consecutive exposures to 50 and 100 ppb of ozone of 32 nm delafossite thin films annealed at 1050 °C for 300 s, at 100°C, showing the reversible behaviour and repeatability of our measurements.

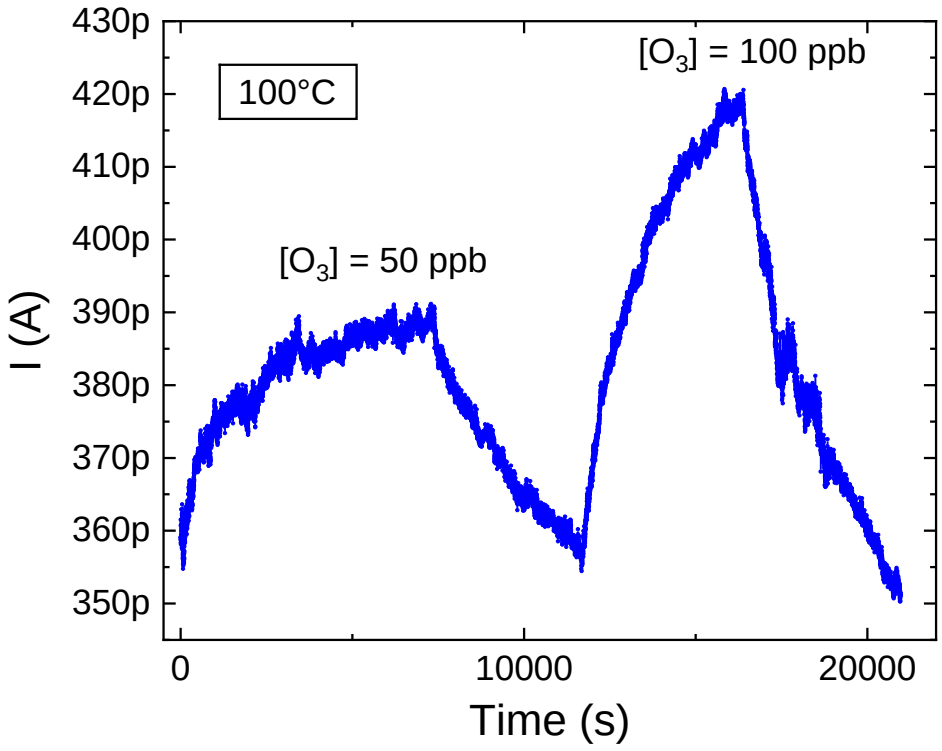

Figure 55 - Sensing characteristics at 100°C of 140 nm Cu-Cr-O delafossite thin film annealed at 1050 °C for 300 s, with concentrations of 50, 100 ppb and the recovery period in between.

5.1.5. Selectivity

Due to the nature of ozone adsorption, being led by the adsorption of oxygen species, one of the biggest cross-selectivity challenges might arise from changes induced by molecular oxygen, reminding that all of our previous measurements were obtained in dry air. For this we propose a study where we consecutively injected pure nitrogen (leading to the desorption of oxidant surface species, (i.e transduced by a continuous decrease of current) for 30 minutes, next we injected dry air, for 10 minutes, and after we injected a mixture of 40% O_2 / 60% N_2, for 30 minutes. Lastly ozone (50 ppb), diluted in dry air was injected for 30 minutes. During the first step there is a likely desorption of the surface species, present in the thin films. This leads to a small decrease of the conductivity. The injection of air does not cause any noticeable impact and the following injection of 40% O_2, double the oxygen concentration that can normally be found in ambient air, for 30 minutes, causes a small increase in conductivity (about 1% maximum). This is marginal when compared with the following injection of 50 ppb of ozone, less than the regulatory limit for 8 hours exposure, that causes an increase of conductivity of 14% after 30 minutes. This allows us to conclude that our sensor is very selective towards molecular oxygen. Any reasonable changes in the oxygen level that

may happen in the office environment will not be detected by the sensor, showing its very high selectivity when comparing O_3 and O_2.

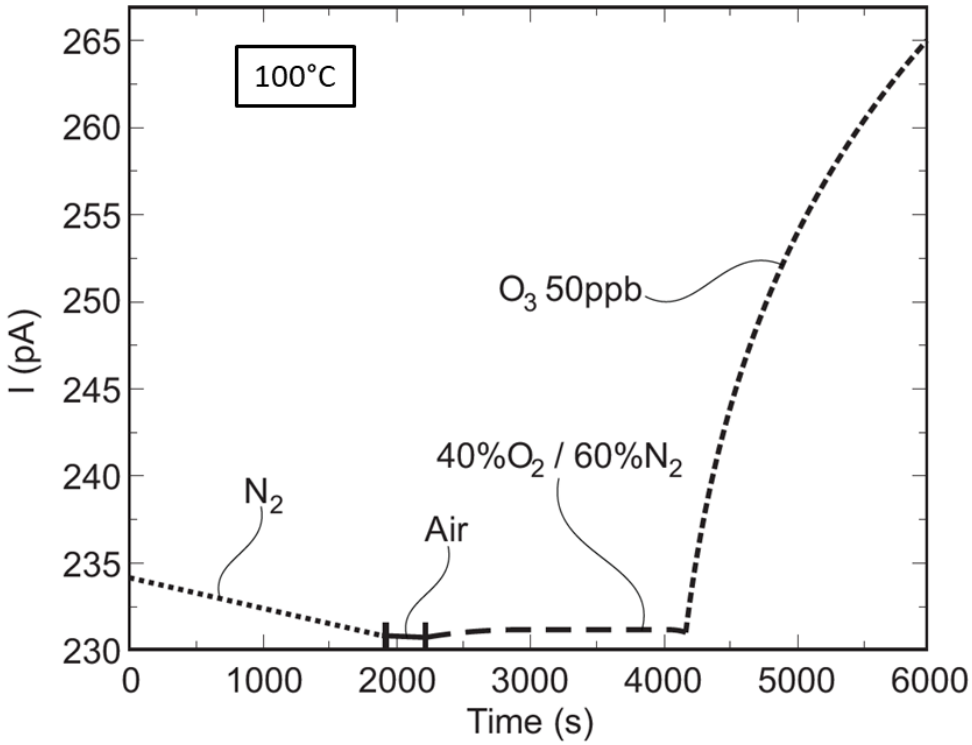

Figure 56 - Sensing characteristics of 32 nm Cu-Cr-O delafossite annealed at 1050 °C for 300 s, at 100 °C, upon consecutive exposures to N_2 (30 minutes), Air (10 minutes), a mixture of 40% O_2 / 60% N_2 (30 minutes) and 50 ppb of ozone diluted in air (30 minutes) showing the selectivity of our delafossite towards ozone

5.2. Investigating the surface delafossite – ozone reactions

5.2.1. Static Model – Power law behaviour

We have studied the interplay of the film properties and how to maximize our sensors performance, for low temperature measurements. We now turn our attention to investigate the reaction mechanism that drives the behaviour of our sensor. From our measurements, we studied the interaction between the ozone and the delafossite surface. Firstly, we use the measurements on an equilibrium state, so after a plateau has been reached. This is the commonly known power law behaviour, that has been discussed in detail in chapter 1.4.1. A semiconductor gas sensor follows a behaviour characterized by type $S = AP_{gas}^{n}$, where A and n are constants and P is the gas partial pressure. This behaviour is directly correlated with the species involved in the adsorption reaction. The analysis can be seen in figure 57. The study was performed at 75° and 100 °C. The data fits very well with the expected behaviour and the exponent was extracted $n = 0.30 \pm 0.02$ at 75 °C and $n = 0.31 \pm 0.02$ at 100 °C. Looking at table 3, that schematizes the different possible response functions for ozone and comparing with this analysis it is possible to better understand the reaction undergoing at the sensors' surface. The exponent close to 1/3 indicates that the reaction is mainly governed by the direct decomposition of ozone molecules into monoatomic oxygen, in the studied temperature range. These results diverge from the commonly reported exponents for ozone sensors of $n \sim 1$, which represent that each molecule of ozone is trapping one electron. In our case the reaction seems to be governed by the following equation:

$$3AS + O_3 + 3e^- \rightarrow 3(AS - O^-(ads)) + 3h^+ \quad (36)$$

Where one ozone molecule is decomposed into 3 monoatomic oxygen. This catalytic activity is in line with the previously reported by Bejaoui et al. [68], for CuO based sensors, but was so far never found for Cu-Cr-O delafossite systems. The authors measured $n = 0.53$, at 250 °C, that although it shows catalytic decomposition of ozone, is not favouring monoatomic oxygen and the selectivity vs. di-oxygen, being one of the critical challenge of ozone sensors operating in ambient air. This is the first-time that a direct ozone catalytic decomposition into monoatomic oxygen at low temperature is being reported, to the best of our knowledge. The nature of this reaction may well be the reason behind the high sensitivity of the sensors at low temperature as well as its very good selectivity compared with molecular oxygen.

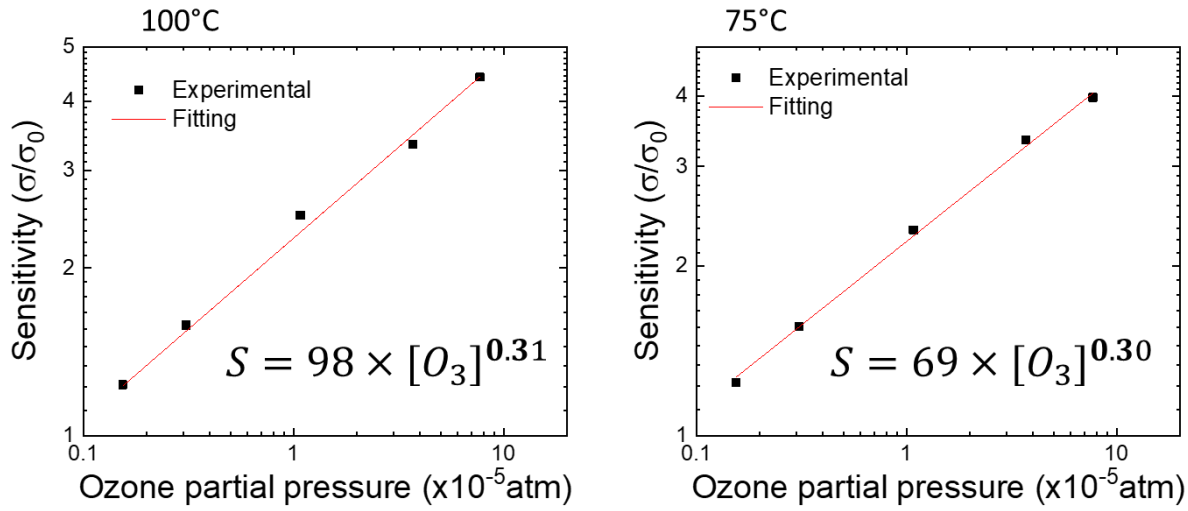

Figure 57 - Logarithm of the sensitivity (σ/σ_0) with the ozone partial pressure, after a steady state was reached, showing the power law behaviour of our sensors, with an approximate exponent of $\frac{1}{3}$ at a) 100 °C and b) 75 °C.

Assuming the validity of the derived equation at low gas concentrations and considering a change in sensitivity of 10% as the minimum significant response value, we can assume the detection limit for ozone would be 15 ppb at 100°C. Unfortunately, the current experimental setup at our disposal is not able to produce in a coherent way such low values of ozone concentration. The high catalytic activity for ozone decomposition can help explaining the low detection limits observed even at low temperatures.

5.2.2. Dynamic Model

We have used the equilibrium data fitting with the power law behaviour to identify monoatomic oxygen as the preferred adsorbed spices. Here we propose a study of the dependence of our sensors versus time with the ongoing surface-ozone reactions. By combining the kinetics of the equation, with the semiconductor's conduction mechanism, we propose a dynamic model of the change of conduction for our gas sensor, as discussed in chapter 1.4.2. Considering only O_3 and assuming no initial coverage, integrating the Langmuir isotherm as function of time, leads to the following expression for adsorption sites coverage, upon O_3 exposure:

$$\theta_v(t) = 1 - \frac{k_{-1} + k_1 P_{[O_3]} e^{-(k_{-1}+k_1 P_{[O_3]})t}}{k_{-1} + k_1 P_{[O_3]}} \quad (37)$$

Where $\theta_v(t)$, represents the fraction of occupied adsorption sites at a given time. $k_1$and k_{-1} are the adsorption and desorption reaction constants respectively. $P_{[O_3]}$ is the ozone partial pressure.

Considering that the sensors' conductivity is dependent on the surface coverage and that according to its identified behaviour, where each adsorbed monoatomic oxygen is trapping one electron, we can propose the relation between the conductivity, the ozone partial pressure and reaction kinetics. We consider that, the conductivity as function of time is given by:

$$\sigma(t) = p(t)e\mu = p_0 e\mu + \Delta p(t)e\mu \tag{38}$$

where $p_0 e\mu$ is the base conductivity and Δp is the change in carrier concentration derived by the injection of majority carriers due to atomic oxygen adsorption. It can be written as:

$$\sigma(t) = \sigma_0 + N.\theta_v(t) \tag{39}$$

with $N = e\mu\theta_0$. θ_0 represents the total number of adsorption sites available at a given temperature. σ_0 is the conductivity under dry air conditions at a given temperature.

We can further expand the formalism, considering the kinetic reactions are thermally activated:

$$k_i = k_{i0}\exp\left(-\frac{E_{ai}}{kT}\right) \tag{40}$$

Where E_{ai} is the activation energy of a given reaction. The number of adsorption sites can also be considered to be temperature dependent as the surface features and lattice parameters will change in temperature. We can therefore consider that the conductivity is given as function of time and temperature upon ozone injection by:

$$\sigma(t,T) = \sigma_0(T) + e\mu\theta_0(T)(1 - \frac{k_{-1}(T) + k_1(T)P_{[O_3]}e^{-\left(k_{-1}(T)+k_1(T)P_{[O_3]}\right)t}}{k_{-1}(T)+k_1(T)P_{[O_3]}}) \tag{41}$$

Or it can be further simplified to the current dependence on time and temperature as:

$$I(t,T) = I_0(T) + V.\frac{A}{l}e\mu\theta_0(T)(1 - \theta_v(t,T)) \tag{42}$$

This model has several limitations that can be pointed out: It considers that there is no surface coverage when ozone is introduced, and that ozone is the sole responsible for the change in carrier concentration. The formalism can be readily expanded to take oxygen adsorption into account as previously discussed, but due to the high selectivity found to molecular oxygen a model simplification was preferred. The model considers an immediate change of regime, from no ozone, to a static partial pressure, not considering the filling of the chamber (a few minutes) and stabilization of the ozone generator. Albeit the limitations, we believe this model can provide a good first order approximation, for the dynamic behaviour of our sensors, in the study range. Approximated kinetic parameters of the reaction can be

derived as well as physical parameters such as the total number of adsorption sites at a given temperature for our samples.

Figure 58, shows the response of $Cu_{0.66}Cr_{1.33}O_2$ to 50 and 100 ppb of ozone at different operating temperatures: 75°, 100° and 125°C. It presents also the fitting using the dynamic model in equation 43. Two distinct analysis at a given temperature and ozone concentration are performed. Table 17 presents the results derived from this analysis with the average and standard deviation found for each temperature of the kinetic constants and the total number of adsorption sites of the material. A trend can be observed, as the kinetic decomposition of ozone and its adsorption are favoured at higher temperatures, as would be expected for a thermally activated reaction (as shown in figure 59). The total number of adsorption sites seems however to not be changed when the temperature is increased from 75 to 100 °C. Temperatures above 100 °C promote the desorption of hydroxyl groups that may limit the number of adsorption sites. A further increase to 125 °C promotes an increase of the total number of adsorption sites from about 1.8×10^{13} to 5.1×10^{13}. This increase can be driven by the changes of the material at higher temperature or due to desorption of other adsorbate molecules, mainly -OH groups or carbon present at the surface. However, the high catalytic activity of our sensors at temperatures below 100 °C, make it the perfect candidate for low cost sensor network integration. Nevertheless, it might still be advisable in the case of metal oxide conductometric gas sensors, to operate at temperatures above 100 °C, due to the reduction of hydroxyl groups influence.

Table 17 -Parameters derived from dynamic model in equation 43, presenting the average of the kinetic constants and maximum number of adsorption sites, of two measurements for each ozone concentration, 50 and 100 ppb.

Temperature	$\boldsymbol{k_{-1}}$ $(\boldsymbol{s^{-1}})$	$\boldsymbol{k_1}$ $(\boldsymbol{s^{-1}})$	$\boldsymbol{\theta_0}$ $(\boldsymbol{cm^{-3}})$
75°C	$4.9 \times 10^{-4} \pm 2.8 \times 10^{-4}$	8.5 ± 0.8	$1.6 \times 10^{13} \pm 0.8 \times 10^{13}$
100°C	$4.3 \times 10^{-4} \pm 2.9 \times 10^{-4}$	21.9 ± 1.9	$1.8 \times 10^{13} \pm 0.18 \times 10^{13}$
125°C	$4.1 \times 10^{-4} \pm 0.2 \times 10^{-4}$	44.7 ± 0.75	$5.1 \times 10^{13} \pm 1.4 \times 10^{13}$

According to the literature results, at high temperature (above 400°C) the efficiency of the desorption mechanism of target molecules increases, and the system can become less sensitive. This has lead in several works to show a maximum, optimum response temperature [45,54,59,68,69]. This was not observed in our study range (up to 125°C). The desorption efficiency in the range of 75 ° - 125 °C seems to be of the same order of magnitude. The kinetic

reaction parameters extracted are independent of ozone concentration, in the temperature range studied. The activation energy was further extracted with a value of 0.4 eV.

Langmuir theory analysis of dynamic model for ozone sensing reaction in semiconductor sensors has been proposed in different works [32,54]. From these works the total density of adsorption sites for WO_3 was derived as 8×10^{12}, at 325°C. Simulation works based on Wolkenstein models were used by Bejaoui et al. [68] and Guerin et al. [57,59], to study the dynamic response of p-type CuO and n-type WO_3, respectively to ozone exposure. In first case, a rate constant for ozone was found as 24 s^{-1} and the extracted total density of adsorption sites estimated at $1 \times 10^{14}\ cm^{-3}$ at 250°C. These values are in line with our reported values (rate constant of 22 s^{-1} and estimated adsorption sites $2 \times 10^{13}\ cm^{-3}$) at a much higher temperature (250°C, compared with our 100°C), further justifying the potential of our sensors for low temperature (< 100 °C) ozone sensing.

Limitations can be found in the fittings present in figure 58, as the response does not fully saturate after 3 hours, as predicted in the model. This might be due to an additional slower mechanism present and additional reactions not taken into account in this model. It can be observed in the different ozone response as function of time plots, throughout this chapter, that a faster response is observed in the first $\sim$ 1000 s, and afterword a slow response continues instead of the expected saturation. This additional mechanism can be due to oxygen adsorbate species diffusion, likely through the grain boundaries.

Based on the fundamental reactions occurring at the surface of the oxide, a Langmuir based model is able to approximate the behaviour of the sensor to changes in ozone concentration, within the temperature range studied.

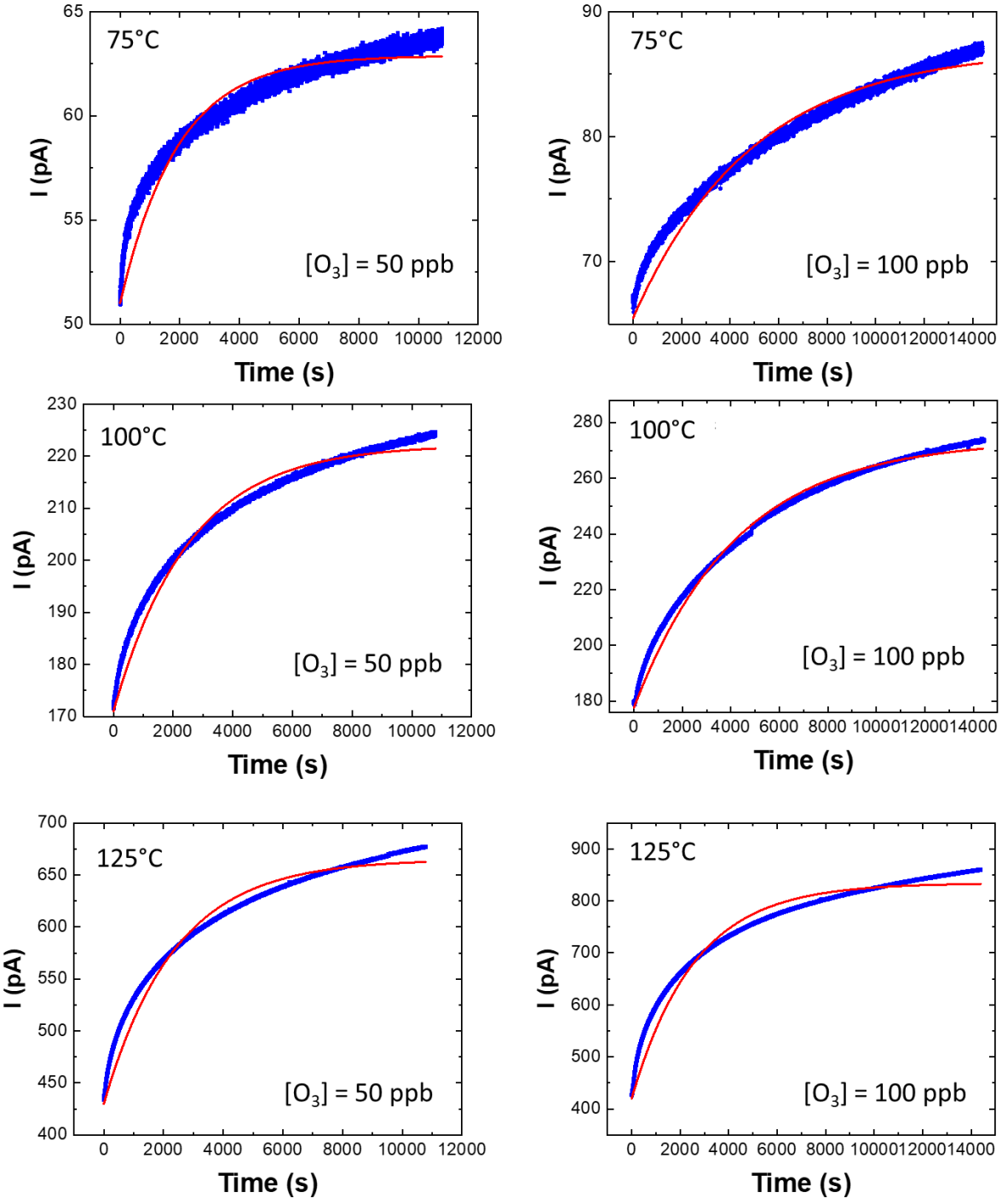

Figure 58 - Sensing characteristics of 32 nm Cu-Cr-O delafossite annealed at 1050 °C for 300 s, when exposed to 50 and 100 ppb of ozone at 75, 100 and 125 °C. Fit of dynamic model presented in equation 43, in each case allowing for extraction of parameters present in table 17.

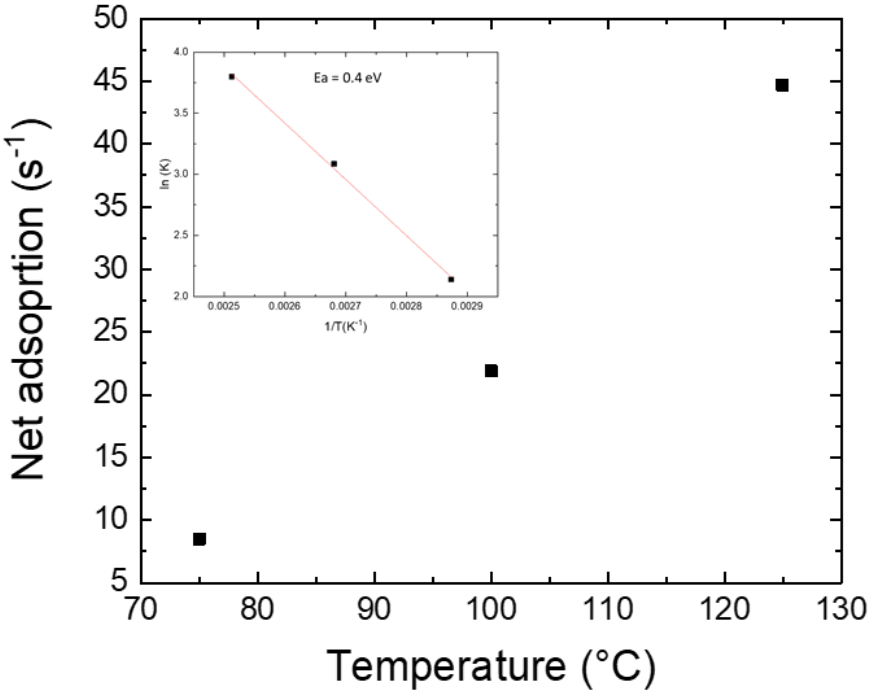

Figure 59 - Net adsorption (k_1 -k_{-1}) as function of sensor working temperature as extracted by the model present in figure 58. Inset showing the activation energy extraction leading to 0.4 eV

5.3. In-situ ozone NAP-XPS

In this sub-chapter, we present a study of the response of copper-chromium-oxide thin films to different ozone concentrations via NAP-XPS spectra. Different temperatures and gas environments lead to different core level and valence band maximum energies. A lower binding energy corresponds to a decrease in distance between the Fermi energy and the valence band maximum, (i.e. a more oxidized sample). This novel experiment can bring important information about the ozone decomposition and surface reactions undergoing at the thin film surface.

Several technical hurdles had to be overcome for the realization of this experiment: the insulating nature of the substrate used for the ozone sensing devices (sapphire) led to charging response and unreliable information. This substrate was subsequently substituted by a highly doped p-type silicon. However, upon annealing steps, copper diffuses into the silicon substrate, changing the chemical composition of the layer. This is a commonly known fact in the literature [303,304]. Titanium nitrate was further deposited as a barrier layer for copper diffusion [303], due to its high conductivity. However, TiN diffusion barrier layer is of limited efficiency with annealing temperatures above to 800°C [311,312] and there is a lack of viable alternatives at our disposition.

For this reason, thin copper-chromium-oxide films were deposited on p^+ Si and TiN, as represented in figure 60. The film was annealed at 750°C for 15 min. The sample was first heated up to 600 °C for removal of surface carbon. A first survey spectra was taken and sequentially the sample was exposed to pure oxygen at increasing pressures.

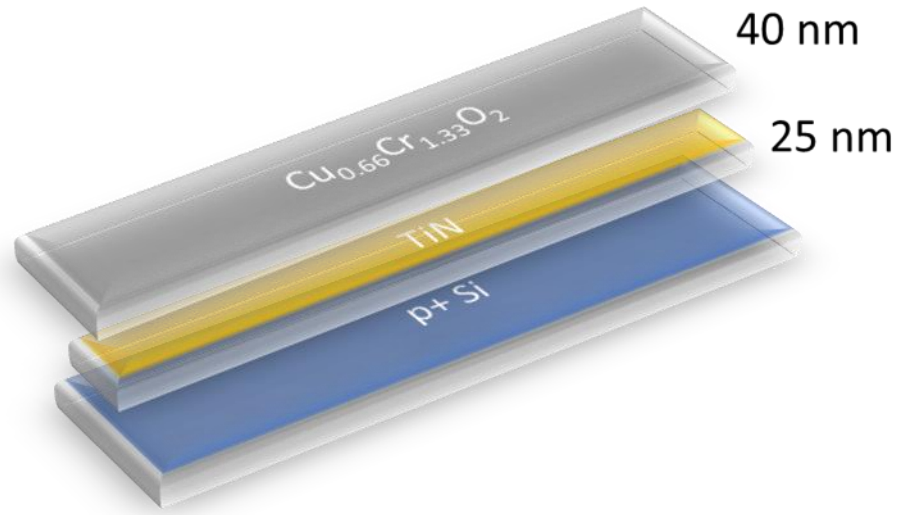

Figure 60 - Schematic representation of the sample used, evidencing the p-doped silicon as substrate, titanium nitrate as a diffusion barrier with 25 nm and our copper-chromium-oxide thin film

Afterwards the ozone generator was turned on, with a flow of 50 sccm/min, leading to a concentration of ~ 15% O_3, diluted in oxygen. The pressure of the chamber leads to ozone partial pressure. Measurements were performed with pressures ranging from 0.05 mbar to 2 mbar. By changing the total chamber pressure, the ozone partial pressure is controlled. Assuming standard temperature and pressure conditions this can be easily converted into ozone concentrations, that would range from 250 ppb (total pressure of 0.05 mbar) to 10 ppm (total pressure of 2 mbar), allowing for a wide studying range. The total number of ozone interactions with the surface material is in this way comparable with our previous measurements, acknowledging that even if ozone partial pressure is comparable, the ones of oxygen and nitrogen are not, being several orders of magnitude lower, leading to a relative number of interactions ozone – surface to be overestimated, even if these gases are normally not as reactive with the surface. All the concentrations of ozone discussed in this chapter were extracted in this way.

The sample was first studied at 100 °C and sequentially ozone exposure measurements were performed at 50 and 150 °C.

In figure 61, a first survey scan was performed, leading to the identification of Cu 2p, Cr 2p and O 1s characteristic peaks in the spectra, as well as small Ti 2p, Si 2p and C 1s peaks. Furthermore, Auger Cu, Cr and O peaks are present in the spectra. Lead impurities were detected in concentrations below 0.3%. As can be observed the intensity of the spectra is inversely proportional with the chamber pressure. Spectra were taken in pure oxygen at 0.01, 0.1 and 1 mbar (represented as NA in the graphic labels) of pressure and then at 0.05, 0.1, 0.2, 0.5, 1 and 2 mbar of pressure with ozone flow, leading to “equivalent” concentrations of 250, 500, 1000, 2500, 5000 and 10000 ppb of ozone. Lastly a measurement was performed in pure oxygen at 0.05 mbar to prove the total reversibility of the reaction. The ratio Cu:Cr was extracted as 0.6, showing the off-stoichiometry expected for our material. Silicon and titanium were found in concentrations below 2 and 5 %, respectively.

Figure 62 shows the Cu 2p spectra, with the characteristic peaks, Cu $2p_{1/2}$ and Cu $2p_{3/2}$, with binding energies at 933.1 and 953.0 eV, prior to ozone exposure. In this case, no satellite peak is observed, confirming that only Cu^+ is identified in the XPS spectrum. Upon ozone exposure several conclusions might be observed. There is a gradual and continuous shift of the peak position with increasing ozone concentration. Cu $2p_{1/2}$ peak position is shifted from 933.1 eV under pure oxygen to 932.5 eV upon exposure to 10 ppm of ozone. This shift reveals a change in binding energy that can be interpreted either as a change in bandbending by modification of the surface charge in response to a different surface oxygen coverage or as change in bulk doping in response to oxygen incorporation. A change in doping will lead to change in the bulk Fermi level position and to a change of the surface charge [293]. However, due to the oxidizing nature of ozone and the studies performed in chapter 5.2, we expect the adsorption of monoatomic oxygen leading to surface charge transfer, by electron trapping

and a surface bandbending due to the accumulation layer formed at the grains. Nevertheless, some oxygen incorporation cannot be fully excluded.

In figure 63 a) and b), it can be observed a close-up of Cu $2p_{1/2}$ peak. One can notice besides the peak position shift, the formation of a satellite peak at higher binding energies, that can be associated with Cu^{2+} with an associated decrease of intensity of the Cu^{+} peak [294,313,314] . The Cu^{2+} peak intensity increases with ozone partial pressure, whilst the Cu^{+} follows an inverse response. The presence of Cu^{2+} on the material's surface could be attributed to the oxidation of Cu^{+}, upon ozone exposure. This oxidation indicates that the copper sites of the delafossite films or the Cu-O dumbbells in the structure are present in the catalytic decomposition of ozone and the adsorption of monoatomic oxygen.

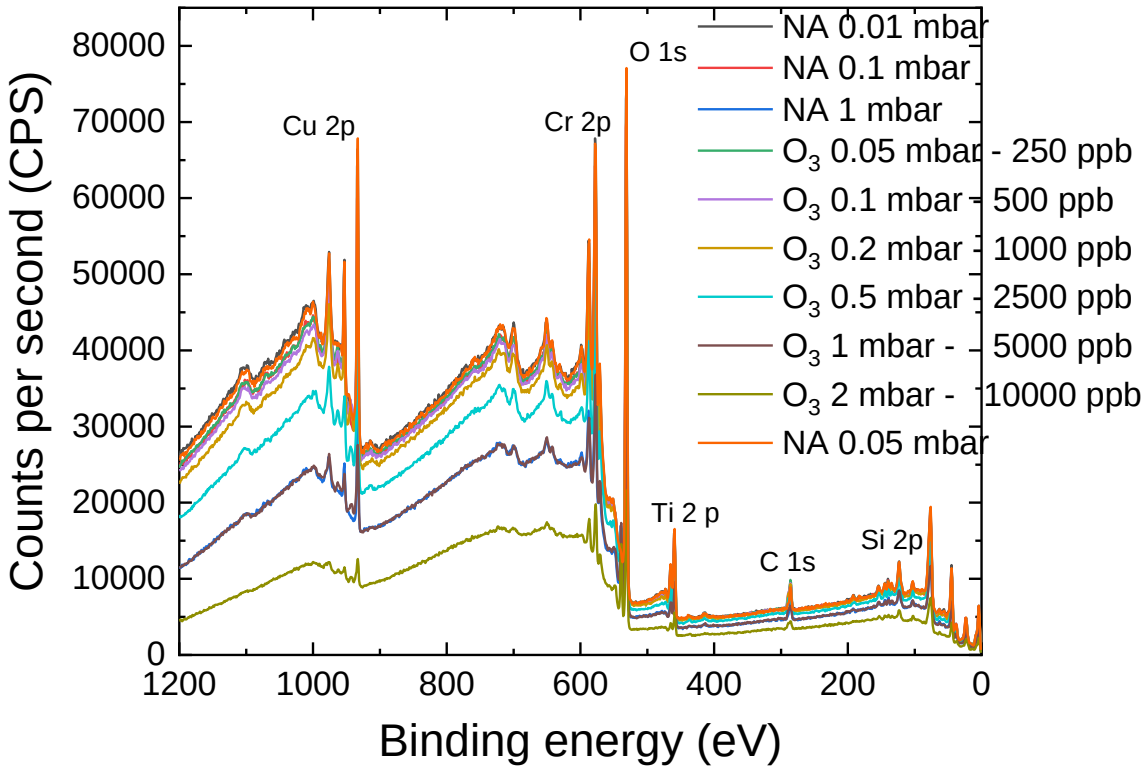

Figure 61 - Full XPS spectra at 100 °C for annealed copper-chromium-oxide thin films, under exposure to 0.01, 0.1 and 1 mbar of pure oxygen and 15% ozone diluted in oxygen in concentrations from 0.05 to 2 mbar. Lastly a pure oxygen spectrum was taken at 0.05 mbar showing the full reversibility of the measurement

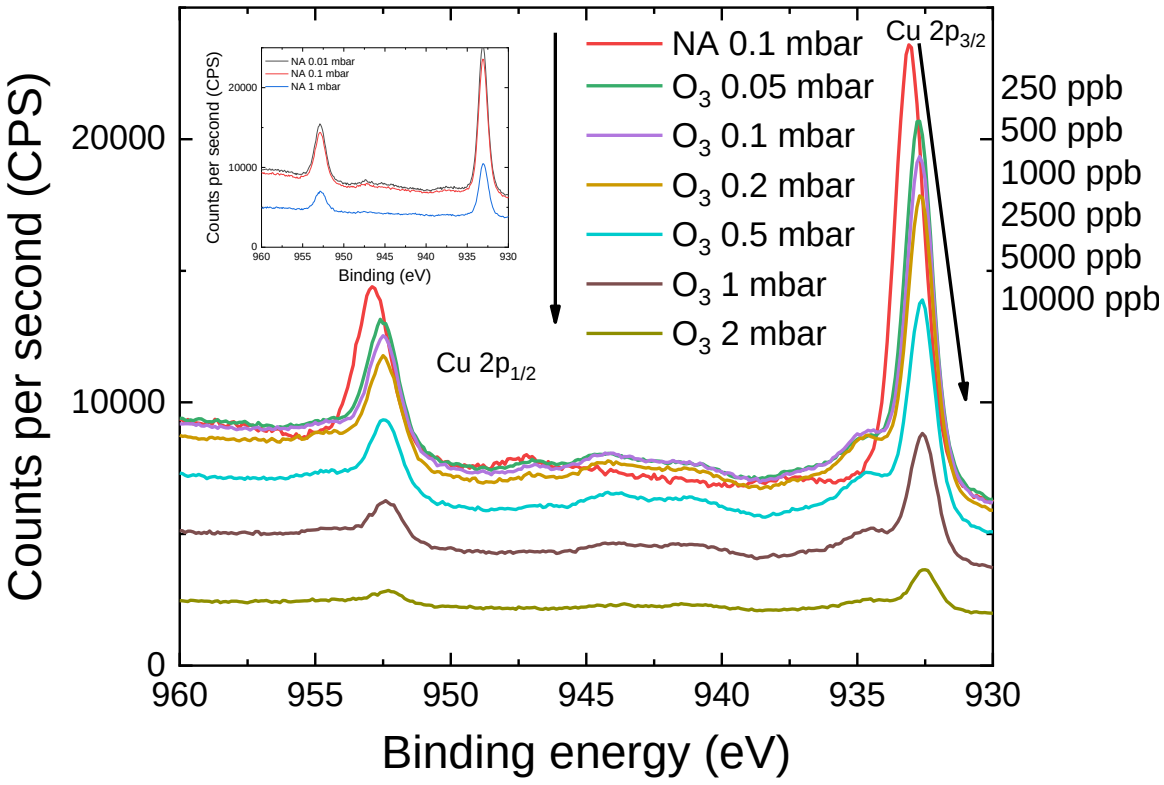

Figure 62 – Cu 2p XPS spectra of copper-chromium-oxide thin film at 100 °C, under pure oxygen and different ozone partial pressures. Arrows for guiding eyes, to represent the peak position shift with increasing ozone partial pressure. Inset showing the stability of the spectra with changes of oxygen concentration.

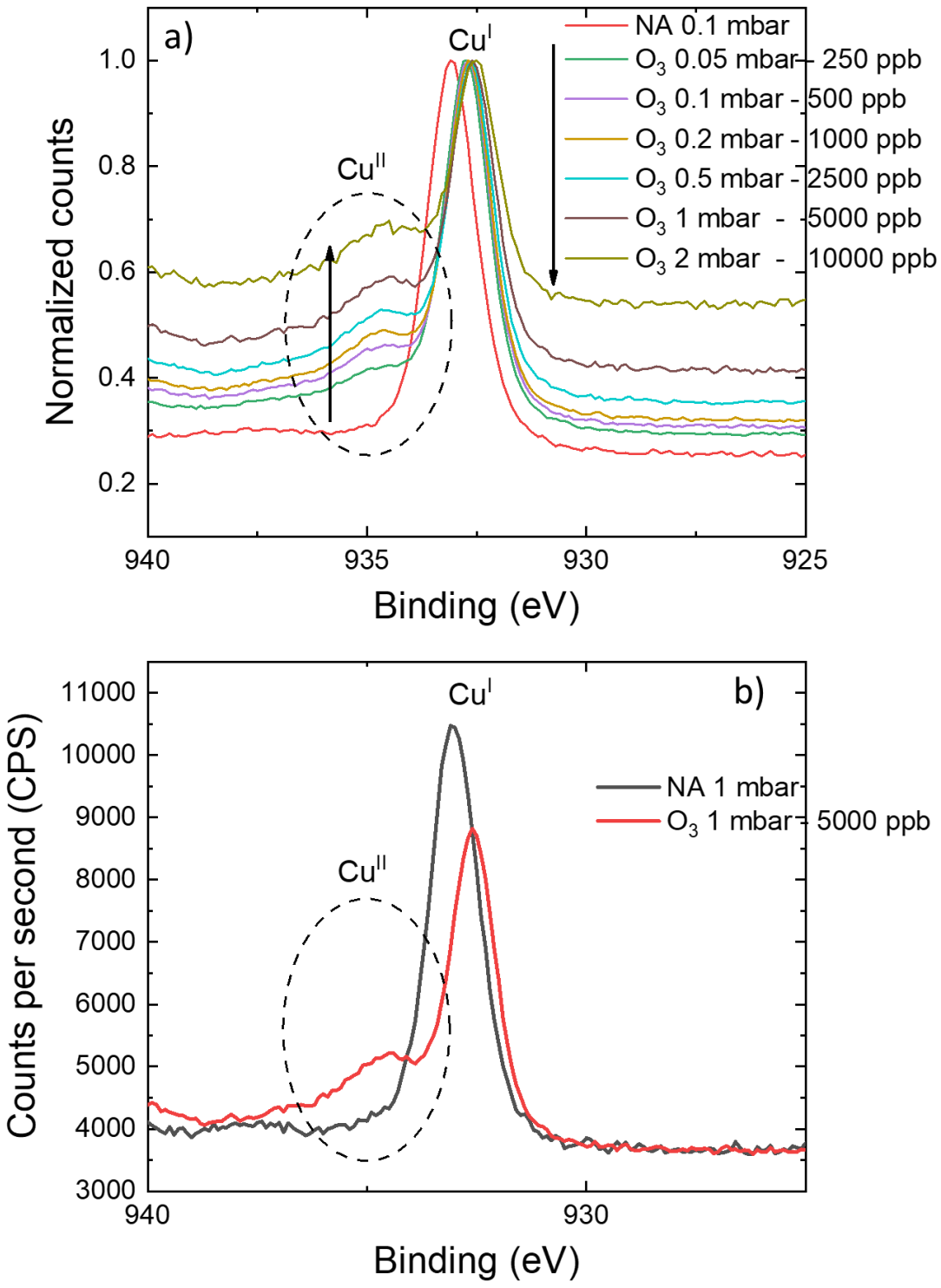

Figure 63 - XPS Cu 2p closeup spectra at 100°C a) under pure oxygen and different ozone concentrations and b) under oxygen and ozone at 1 mbar, showing the partial oxidation of Cu^{+} into Cu^{2+}.

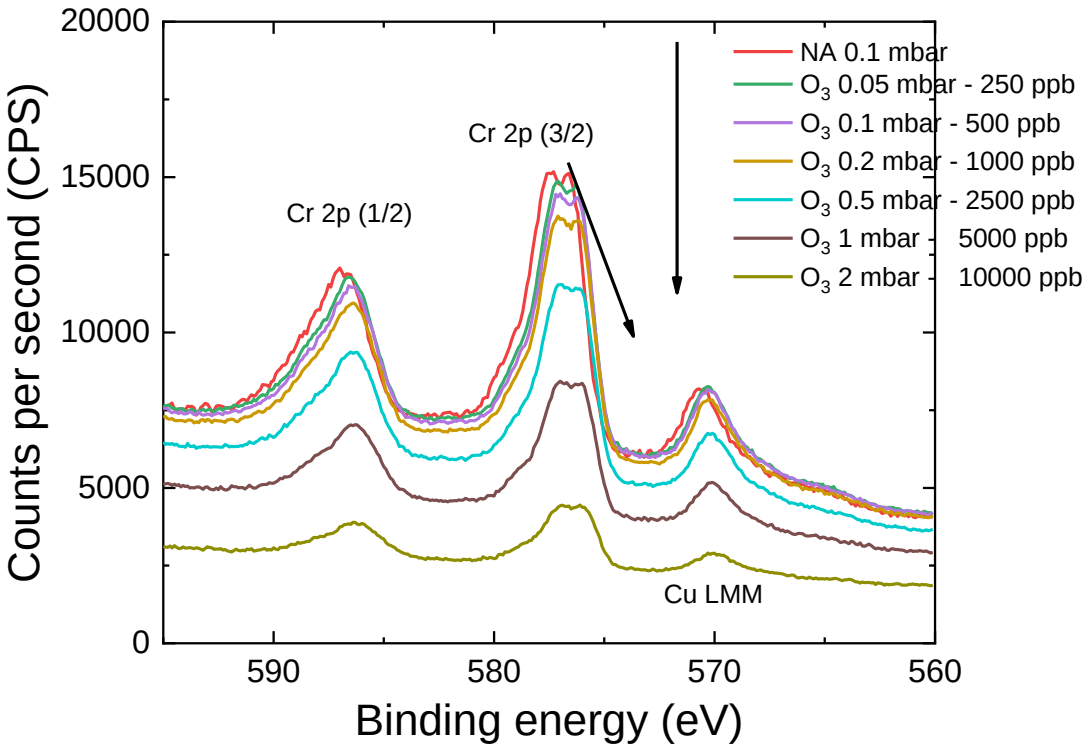

Figure 64 – Cr 2p XPS spectra of copper-chromium-oxide thin film at 100 °C, under pure oxygen and different ozone concentrations.

Figure 64 shows the Cr 2p XPS spectra at 100 °C, under the conditions previously described, for figure 61 and 62. One can observe the Cr $2p_{1/2}$ and Cr $2p_{3/2}$ XPS characteristic peaks at binding energies of 586.9 and 576.6, respectively, before ozone exposure, as well as the Auger Cu LMM peak [14]. The shape of the Cr $2p_{3/2}$ peak, can be explained by Multiplet Splitting, that occurs in core XPS levels whenever there is one (or more) unpaired electron in the valence levels. Multiplet splitting occurs when an atom contains unpaired electrons (e.g. Cr^{3+}, $3p^6 3d^3$) [315]. When a core electron vacancy is created by photoionization, exchange interaction between the unpaired valence electrons and the unpaired electron left in the core level occurs. This interaction produces "split final states" [316]. Multiplet calculations for Cr^{3+}, can be found in [317]. Only Cr^{3+} was found present in the spectra as is expected from copper-chromium delafossites [318].

After ozone exposure, a similar peak displacement can be found, from 576.6 to 576.1 eV upon exposure to 10 ppm of ozone. However, no change in peak behaviour is apparent, with no obvious change in oxidation state, but merely a displacement, that can be associated to change in local carrier concentration.

Furthermore, figure 65 shows the O 1s XPS spectra under the conditions previously described. Once more, a similar displacement as the one found in Cu 2p and Cr 2p, peak

positions was found in O 1s. The confirmation of similar displacements in the three core levels lets us hypothesize a surface bandbending with a similar value ~ 0.55 eV, when the sample is exposed to 10 ppm of ozone at 100°C. Figure 66, shows with great detail the evolution of the peak position with ozone concentration as well as the peak position stability under different O_2 concentrations, further confirming the selectivity of our ozone sensors. Furthermore, upon the introduction of ozone can be seen a small new peak at energies ~ 532 eV. In figure 67, spectra at 1mbar with and without ozone generation are present. It is visible the gaussian behaviour of the XPS peak under oxygen while under ozone the formation of a new peak is evident. This behaviour will be further discussed.

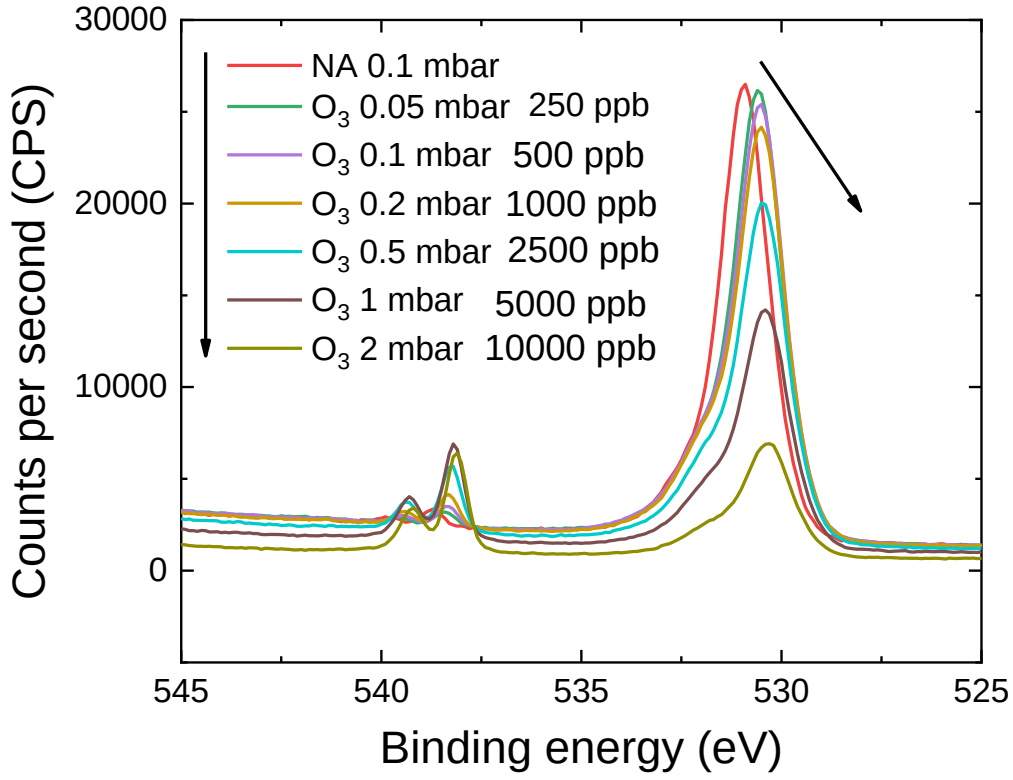

Figure 65 – O 1s XPS spectra of copper-chromium-oxide thin film at 100 °C, under pure oxygen and different ozone concentrations.

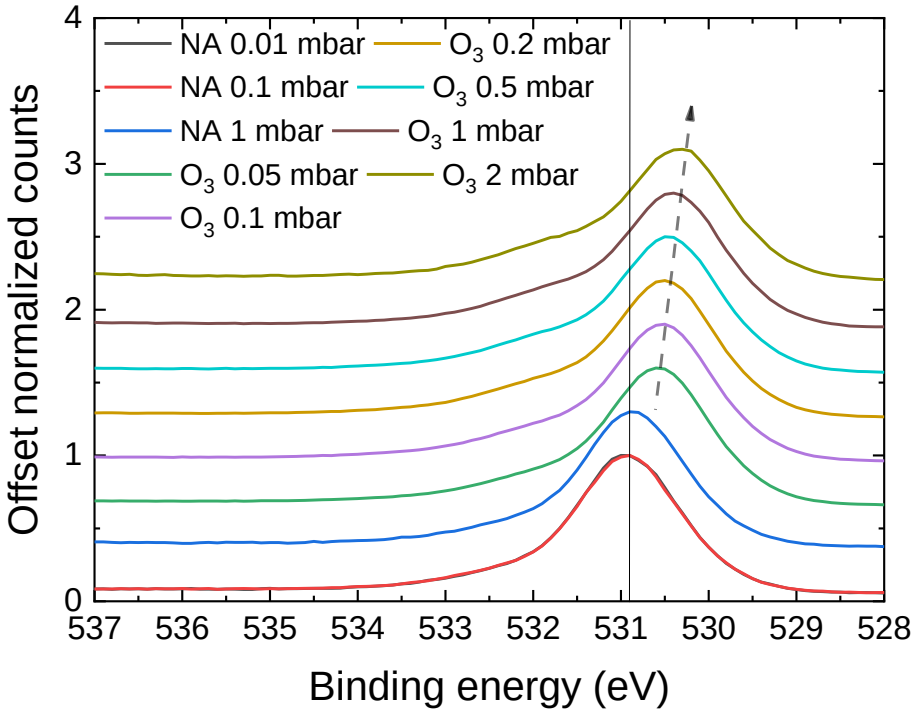

Figure 66 – O 1s XPS close-up spectra of copper-chromium-oxide thin film at 100 °C, under pure oxygen and different ozone concentrations.

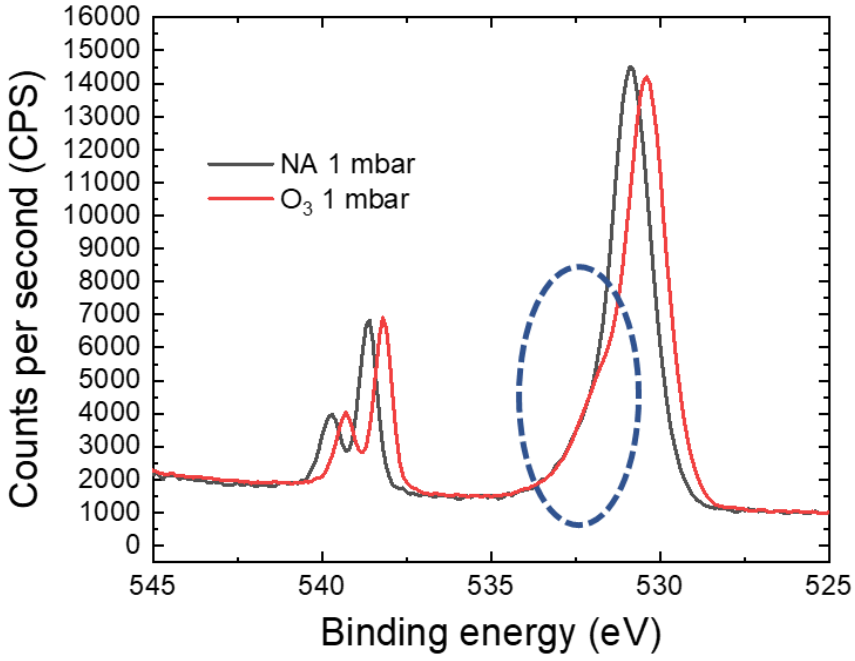

Figure 67 - XPS Cu 2p closeup spectra at 100°C under oxygen and ozone at 1 mbar.

Similar analysis were performed at 50 °C (figures 68 - 70) and 150 °C (figures 71 - 72). The results corroborate what was observed at 100 °C. There is a gradual shift of the core levels of

Cu 2p and O 1s that is proportional to the ozone concentration in the system. In figure 73, can be observed the shift in core level peak positions as function of ozone concentration for the three temperatures studied, 50 °C, 100 °C and 150 °C. One can observe the shift is dependent on the temperature, with 5 ppm of ozone, a shift was measured as ~ 0.4, 0.52 and 0.65, respectively. This indicates that the ozone degradation is a thermally activated process, so that more ozone molecules can readily decompose and adsorb onto our material's surface, leading to the trapping of electrons and therefore the local increase of carrier concentration, translated here by the shift to lower binding energies. Furthermore, figure 73 d), shows the peak position of Cu 2p peak, as function of the chamber pressure, that can be related to the gas partial pressure, with and without ozone. One can notice the relative stability of the peak under oxygen exposure, whilst there is an immediate change and continuous with increase of ozone concentration.

It is noticeable from figures 70 and 72, that the formation of Cu^{2+}, is furthermore increased by the increase in temperature. Figure 74 shows the Cu 2p XPS spectra without ozone and with ozone taken at 1 mbar (5 ppm), at the three studied temperatures, where it is easily noticeable the increase in the new peak at 534.5, suggesting the presence of Cu^{2+}, as well as the relative intensity decrease of the Cu^{+} peak. It can be observed, a higher binding energy change, when the temperature is changed (under pure oxygen conditions), from 932.8 eV at 150°C, to 933 eV at 50°C, for the Cu 2p peak. This is an expected behaviour, due to the semiconducting nature of our copper-chromium-oxide thin film, since the carrier concentration is temperature dependent. Figure 75 shows the Cu^{2+} content as function of temperature and ozone concentration. The analysis without ozone was performed three times, for each temperature, with an error of ± 5% Cu^{2+} content. This analysis can be expanded in a similar way to the one described for the power law behaviour. The resulting exponent, from figure 76, of 0.24, can be considered in line with the one extracted close to 1/3 from the analysis of the sensitivity as function of the ozone concentration. Acknowledging that many approximations were done to extract Cu^{2+} ratio, it is important to notice that it would represent the catalytic decomposition of ozone into monoatomic oxygen, most likely driven by our surface copper sites or copper oxygen dumbbells.

Figure 77 shows the described analysis of the O 1s peak. It can be observed in a similar way, the increasing shift in the O 1s core level with increasing temperature. Furthermore, the change in behaviour of the O 1s peak, previously discussed, that can be associated to chemisorbed oxygen species [319], if even more evident in figure 77 b), where an artificial overlapping of the peaks was performed. It can be also noticed, that this change in behaviour, where a new peak gains prominence is increased by the increase in temperature.

The new oxygen peak observed in O 1s, allows us to conclude that at least up to some extent this reaction is driven by the oxygen surface ionisation. Furthermore, the change in behaviour and oxidation state observed in the Cu 2p spectra, that was not evidenced in the

Cr 2p one, suggest that the catalytic decomposition of ozone and monoatomic oxygen adsorption is governed by the Cu surface sites or the Cu-O dumbbells present in our delafossite surface. The increase in this new O 1s peak is correlated with the increase of ozone partial pressure, but not with the increase in oxygen concentration. Furthermore, it is correlated with the substrate temperature and with the oxidation of Cu^{+} into Cu^{2+}. All this and the full reversibility observed, allows us to hypothesize that either the new oxygen peak observed is either due to surface chemisorbed oxygen or representative of monoatomic oxygen anion (O^{-}) coordinated to the newly oxidized copper or a combination of both.

Figure 78 represents the adsorption induced bandbending upon ozone exposure, under different ozone concentrations. The surface bandbending was measure as 0.4 eV after the exposure to the equivalent concentration of 5 ppm of ozone at 50°C, whilst for the same ozone equivalent concentration was measured as 0.49 and 0.64 eV, at 100 and 150°C, respectively, evidencing the increased bandbending for the same ozone concentration at different temperatures. This can be associated with the temperature dependence of the ozone decomposition.

Figure 79 presents a simple Arrhenius plot showing the dependence of the Cu^{2+} and core level shift as function of temperature, for fixed ozone concentrations. This analysis results in an activation energy, almost one order of magnitude lower than the one extracted from the dynamic model. These results can be interpreted by understanding the specifics of these measurements, where we started from a much lower base pressure, so upon ozone introduction, almost all adsorption sites can be readily available for ozone, as no surface coverage is expected. Furthermore, as there is no humidity in the chamber and the concentration of oxygen is much lower, there are no competitive adsorptions with ozone. This leads to the hypothesis, that the activation energy extracted, about 0.06 eV, should be representative of ozone decomposition. Furthermore, we can assume that in ambient air, the reaction should not be limited by the catalytic decomposition of ozone, but rather by its adsorption on the surface of our material.

In figure 80, is shown the correlation between Cu^{2+} and the core level shift, showing their strong correlation and temperature dependence. This results further corroborate the hypothesis that the ozone catalytic reaction is driven by the copper sites at the surface of our material.

These results bring in a set of new data for the scientific community in general and for the study of ozone adsorption species in particular, on copper-chromium-oxide surface. A lack of comparable data however exists, due to the difficulty in setting up such an experiment and the requirement of a high cost NAP-XPS system. Gassanbauer et al. [293], presented a study of the response of ITO as function of time to oxygen, whilst Lampimaki et al. [320], produced a very interesting study about ozone induced bandbending on TiO_2. However, the influence of temperature or ozone concentration was not studied or reported, leaving us a vacuum of

comparable data. Our results can therefore serve as a foundation for the deeper analysis of surface reaction of metal oxide gas sensors when exposed to their target gases.

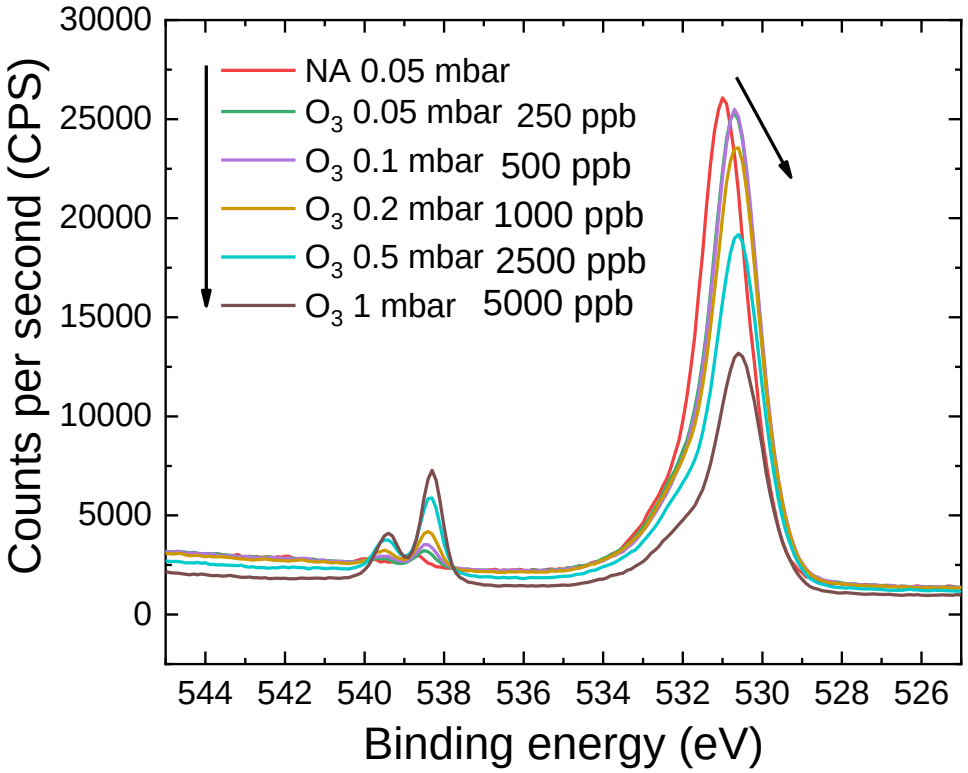

Figure 68 - O 1s XPS spectra of copper-chromium-oxide thin film at 50 °C, under pure oxygen and different ozone concentrations.

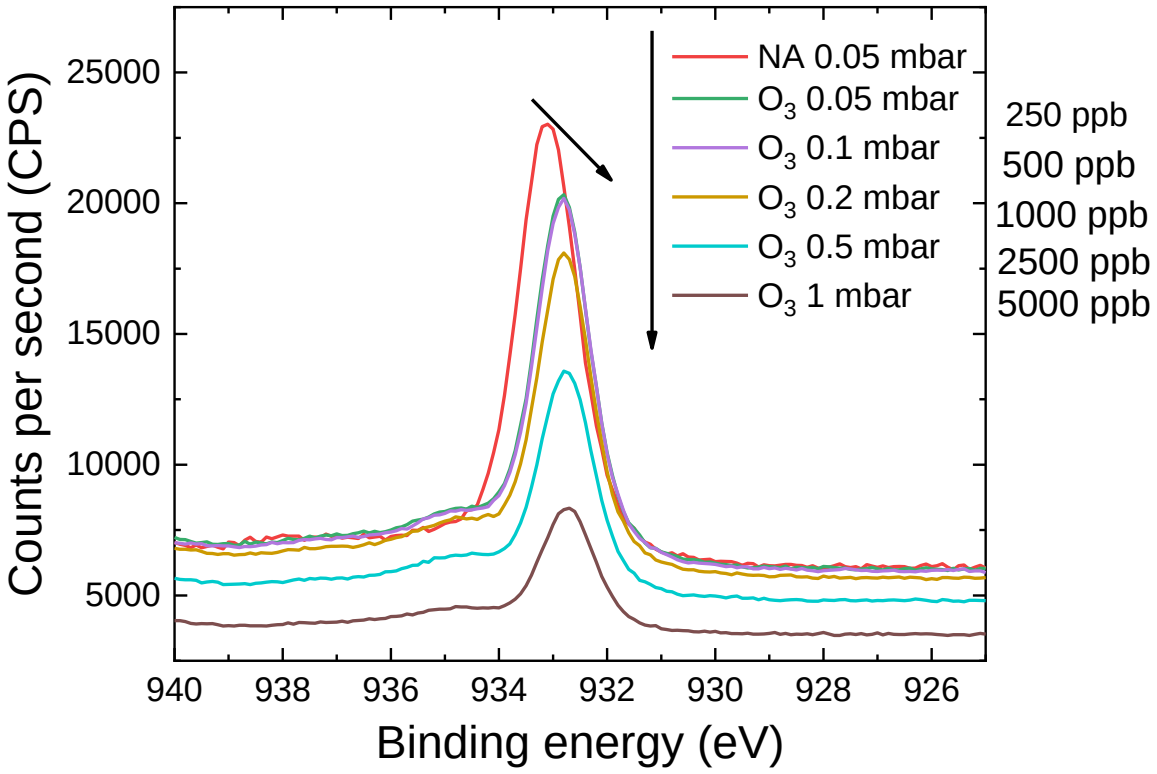

Figure 69 – Cu 2p XPS spectra of copper-chromium-oxide thin film at 50 °C, under pure oxygen and different ozone concentrations.

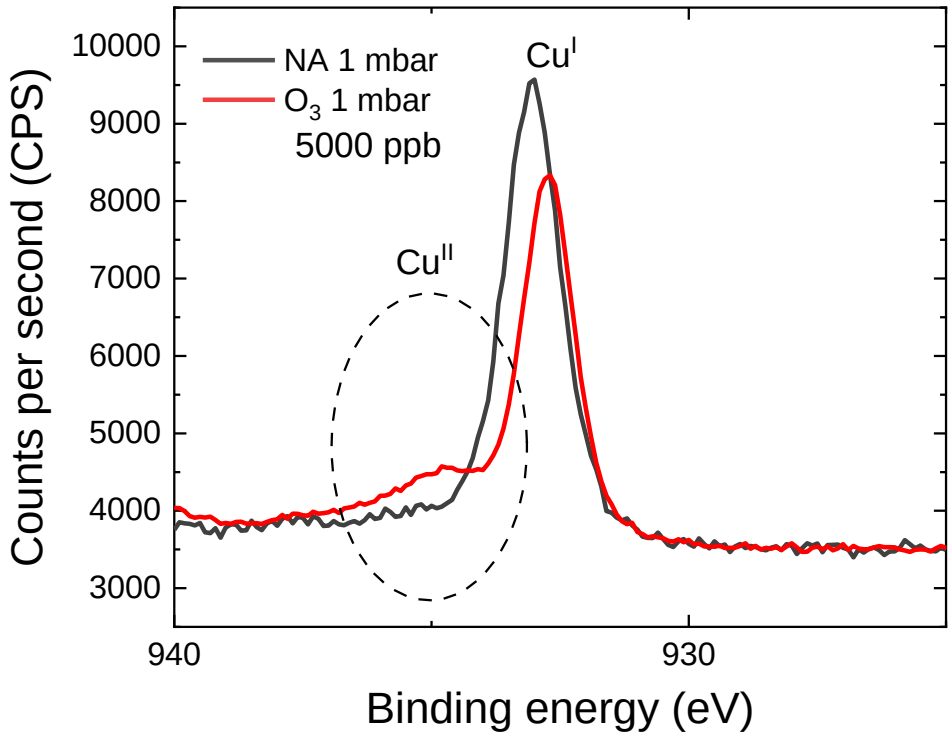

Figure 70 - XPS Cu 2p closeup spectra at 50°C under oxygen and ozone at 1 mbar.

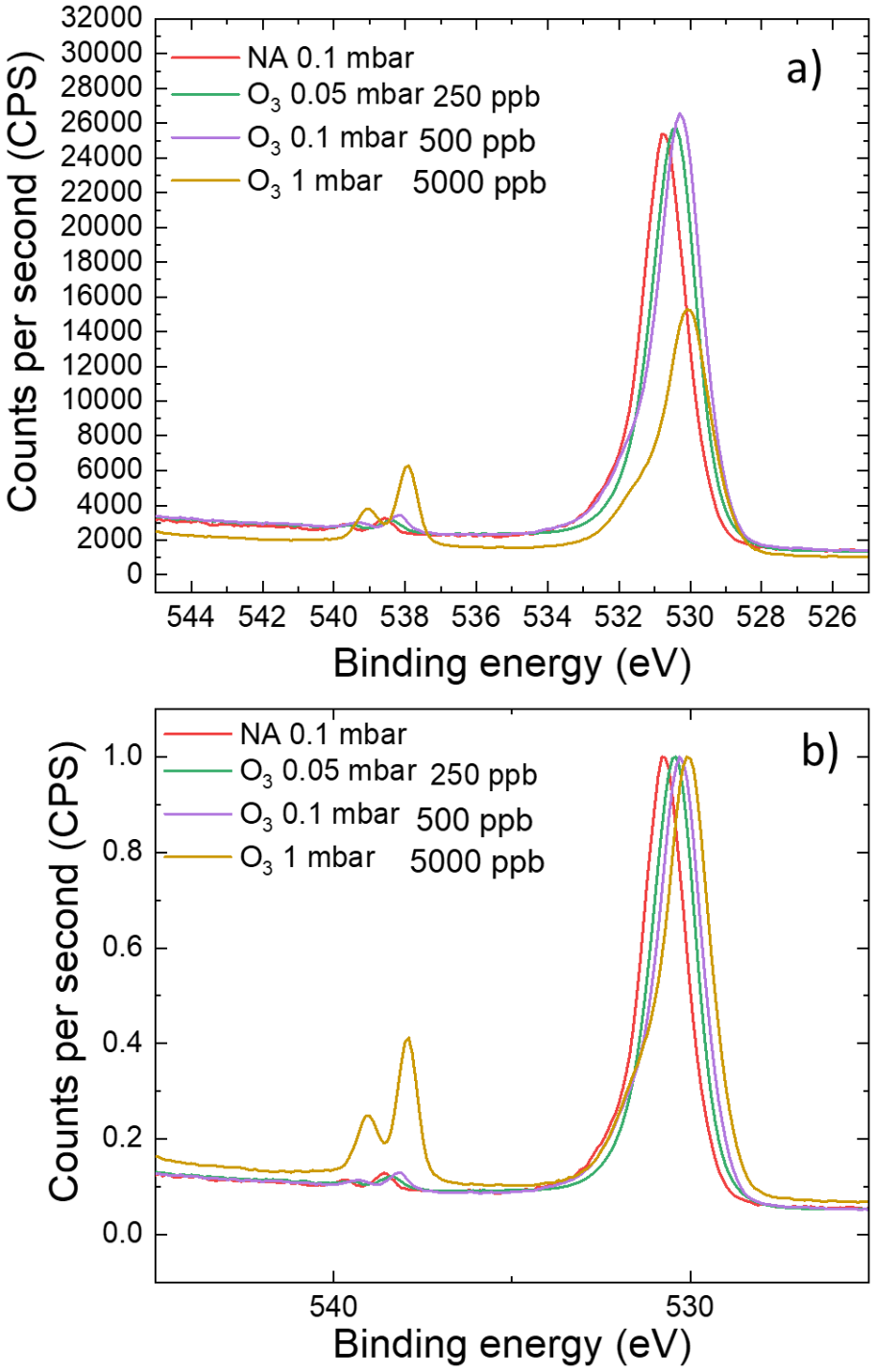

Figure 71 – O 1s XPS spectra of copper-chromium-oxide thin film at 150 °C, under pure oxygen and different ozone concentrations – a) as-is; b) normalized intensity

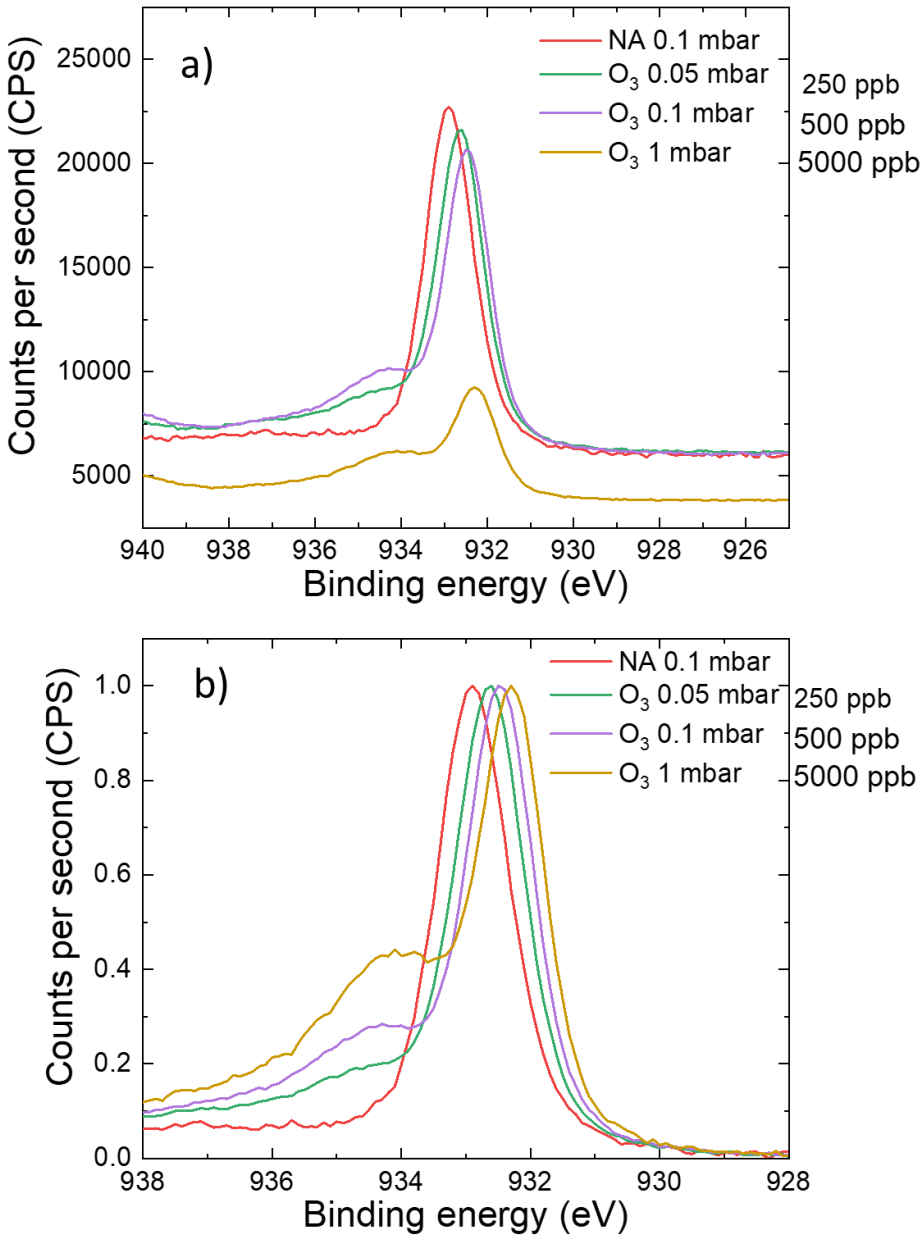

Figure 72 – Cu 2p XPS spectra of copper-chromium-oxide thin film at 150 °C, under pure oxygen and different ozone concentrations – a) as-is; b) normalized intensity

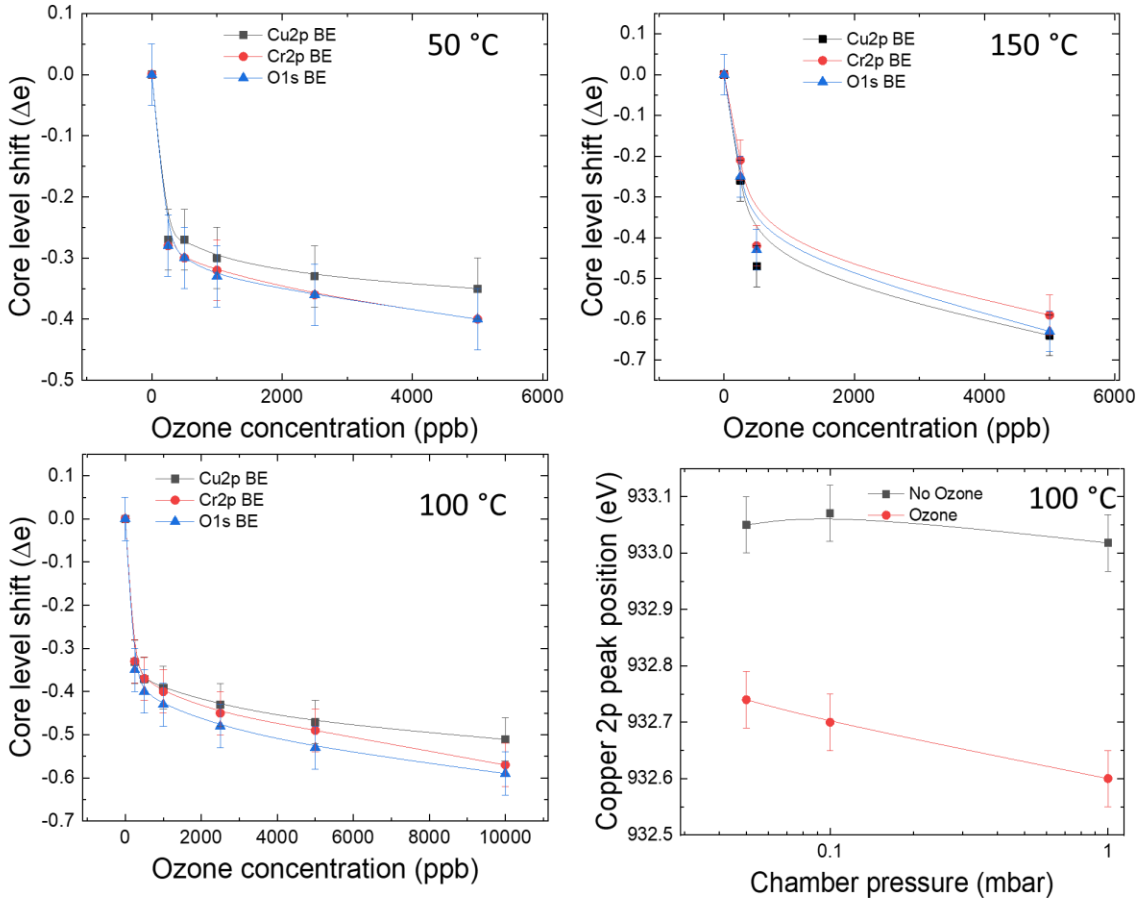

Figure 73 - XPS core level position shift depending on ozone concentration at: 50, 100 and 150°C; d) Copper 2p peak position as function of chamber pressure, under pure oxygen exposure and ozone.

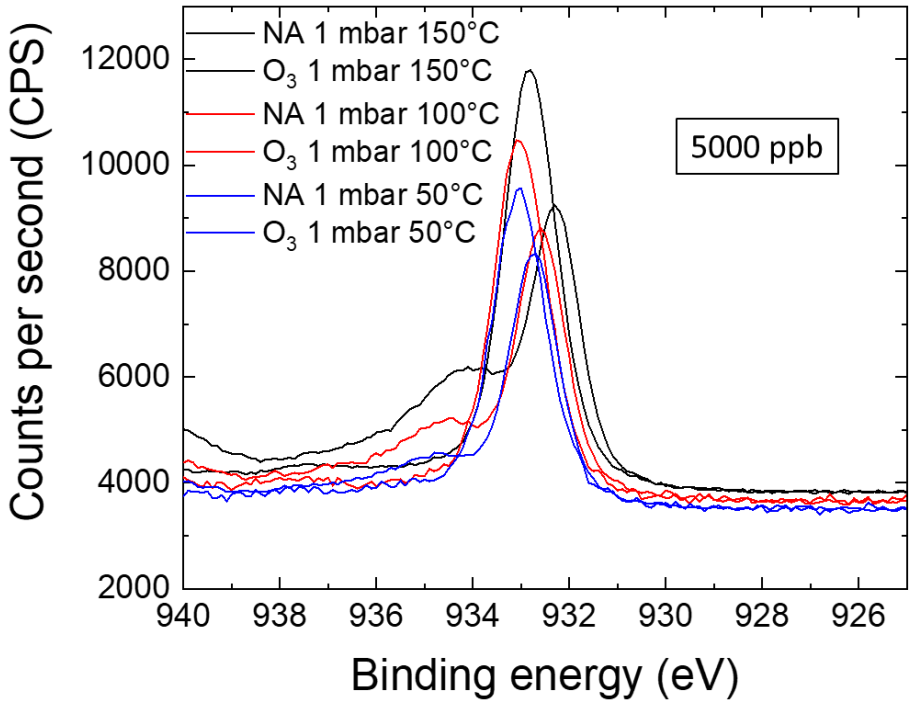

Figure 74 - Cu 2p XPS spectra of copper-chromium-oxide thin film at 50, 100 and 150 °C, under pure oxygen and ozone at 1 mbar (5 ppm)

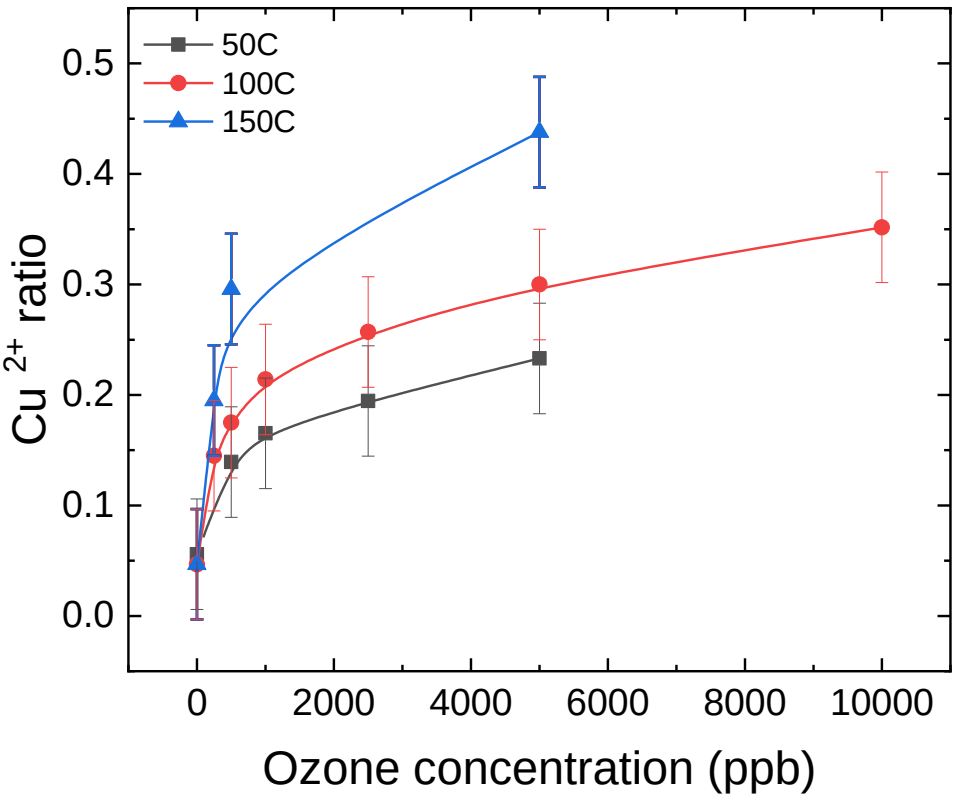

Figure 75 - Cu^{2+} ratio evolution as function of ozone concentration depending on working temperature

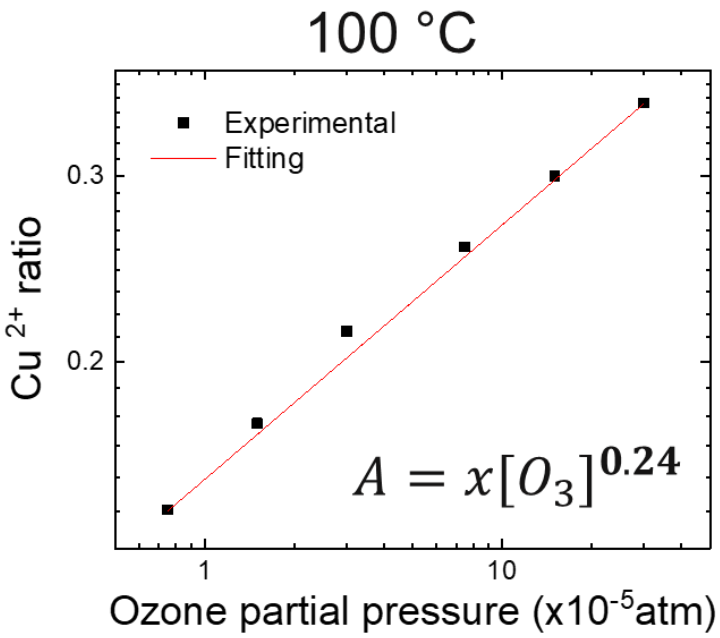

Figure 76 - Cu^{2+} ratio evolution as function of ozone partial pressure, showing its power law behaviour with an exponent of 0.24

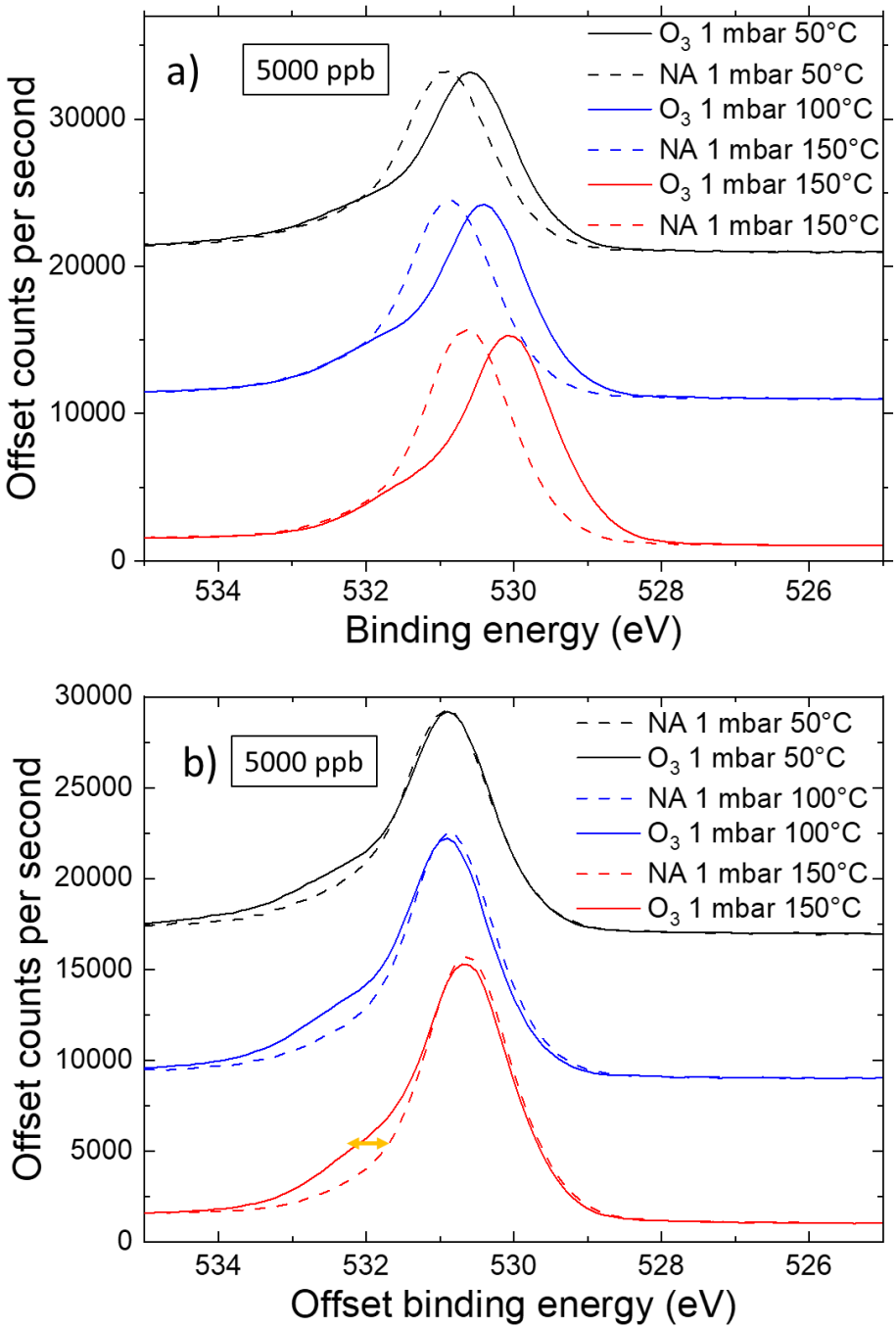

Figure 77 – O 1s XPS spectra of copper-chromium-oxide thin film at 50, 100 and 150 °C, under pure oxygen and ozone at 1 mbar (5 ppm) – a) as is; b) with overlapping peaks

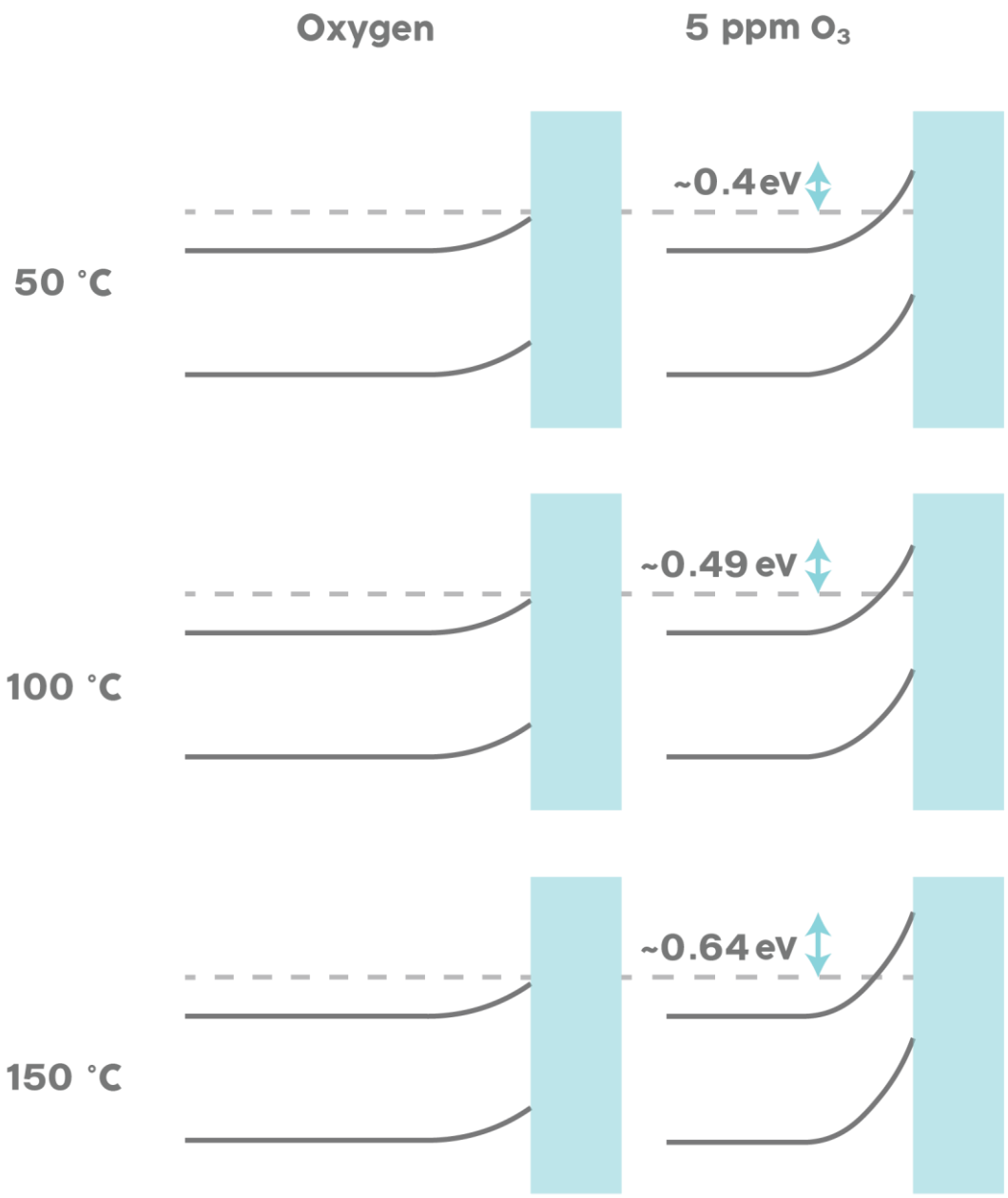

Figure 78 – Representation of the adsorption induced bandbending upon 5 ppm of ozone exposure, at different temperatures. Dotted line just for guiding eyes.

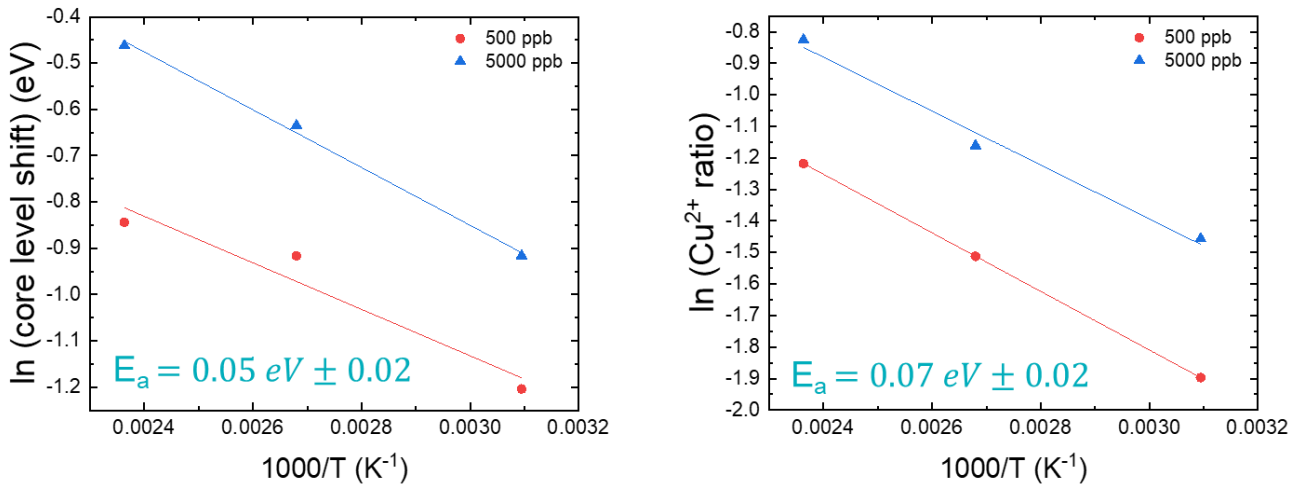

Figure 79 - Energetics of ozone decomposition, extracted as function of core level shift and Cu^{2+} ratio, using an Arrhenius plot

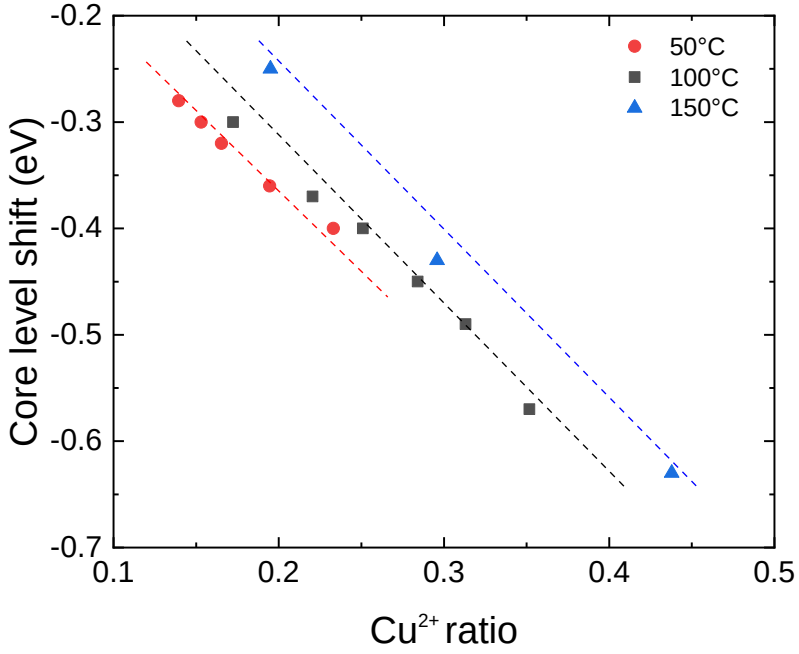

Figure 80 - Dependence of Cu2+ ratio and Core level shift at 50, 100 and 150°C.

5.4. "High" temperature measurements (i.e. >150°C)

The temperature working range of our sensor has been defined as 25 to 150 °C. Ozone exposure at higher temperatures (i.e. > 150 °C), such as 200 °C, seems to promote new responses of our conductometric sensor, as shown in figure 45. In this chapter, we investigate the underlying physical-chemical mechanisms that occur. To this purpose, samples of 32 nm and 140 nm were exposed to 100 ppb of ozone at 200 °C during 26 hours, as shown in figure 81. This was the time necessary for the 32 nm sample to reach a steady state. The sample of 140 nm did not reach a steady state even after 26 hours. This contrasts with the response time until a steady state observed for temperatures below 150 °C, that are usually below 3 hours. The figure inset shows, the response of the thin films to 100 ppb of ozone for 1 hour and the subsequent recovery. One can observe in the case of the 32 nm thin film, the sensing response is up to 150%, whilst exposing the sensor at lower temperatures, leads to lower sensitivities (18, 25 and 41 %, for 75°, 100° and 150 °C, respectively).

Furthermore, an experiment represented in figure 82, was performed. Firstly, the increase in temperature from 25 to 200°C under dry air; next ozone exposure (2.5 ppm) during 4 hours, at 200°C; lastly the temperature was cooled down while the sample was kept exposed to ozone. The ozone flow was stopped, and the sample was left under a dry air flow. 12 hours later the sensor response was measured. It was found that the sensor conductivity was increased by a factor of 6, at 25 °C as compared to its base value at this temperature. This experiment as well as the long-time experienced to reach a plateau suggests a slower and partially irreversible mechanism, that we attribute most likely to the diffusion of atomic oxygen into the delafossite lattice. This was further investigated by XRD measurements. An experiment where the sample was exposed to ozone until a steady state was reached at 100° and 200 °C and quickly cooled down after, was performed. The resulting XRD spectra is presented in figure 83. One can see a clear shift of delafossite (012) peak from ($2\theta = 36.53°$) to ($2\theta = 36.64°$), for the sample exposed at 200 °C to 2.5 ppm of ozone. This shift is also noticeable in the (018) and (110) peaks. This is associated with a change in the lattice parameters. Prior to ozone exposition, the extracted parameter, for "c", along the z axis, is 17.11 ± 0.02 Å, whilst the extracted value after decreases to 17.04 ± 0.02 Å. A small reduction is also found in "a" parameter, from 2.975 ± 0.01 to 2.955 ± 0.01 Å. This shows a small isotropic stress induced on the lattice in the different crystallographic directions. No crystallographic changes were observed after exposure at 100°C. A total reversibility of the increase in conductivity is achieved after exposure at this temperature, supposing long enough time is given (> 4 hours), as shown in figure 50.

Interestingly, an annealing treatment under vacuum at 300 °C leads to a total reversibility of the measurement in minutes and a return to the baseline value of the sensing conductivity as well as a return of the XRD peaks to its initial value.

These results feature a new mechanism in-play at temperatures above 150°C, which therefore modifies significantly the sensing response as well as a possible integration of oxygen into the sensor not easily reversible. Thus, this limits the temperature usage range of our sensors from room temperature to 150°C, which is perfectly matching our goal in researching low-power and highly sensitive/selective ozone sensors. At lower temperatures surface reactions are usually dominant. With the increase of temperature the diffusion of monoatomic oxygen is favoured, albeit being much slower process, compared to adsorption [72]. Gas sensors based on polycrystalline thin-films may have enhanced diffusion of gas molecules along the grain boundary. We can in this case argue that both mechanisms might be present in our films, being the latter more predominant when the temperature is increased, and therefore in-lattice (bulk) diffusion visibly occurs. The process of oxygen incorporation by bulk diffusion has previously been observed by Koretcenkov et al. [9], as the dominant mechanism of sensing response for SnO_2 and TiO_2 sensors, at temperatures above 500 °C. One can correlate with the shift observed on the XRD spectra and the increase in response time until saturation observed in our films above 150 °C with the incorporation of oxygen into the lattice.

In all likeliness there is a small change in stoichiometry of the type $Cu_{0.66}Cr_{1.33}O_{2+x}$. However, conventional quantification techniques such as XPS and SIMS, are not able to quantify it, due to the changes being probably well below 0,1%. If we consider no change in mobility and assume that all carrier concentration change arises from the introduction of oxygen species, we can suppose an increase in oxygen content of the order of $10^{17}cm^{-3}$, whilst the lattice content of stoichiometric oxygen is expected to be 5 orders of magnitude higher [278,283].

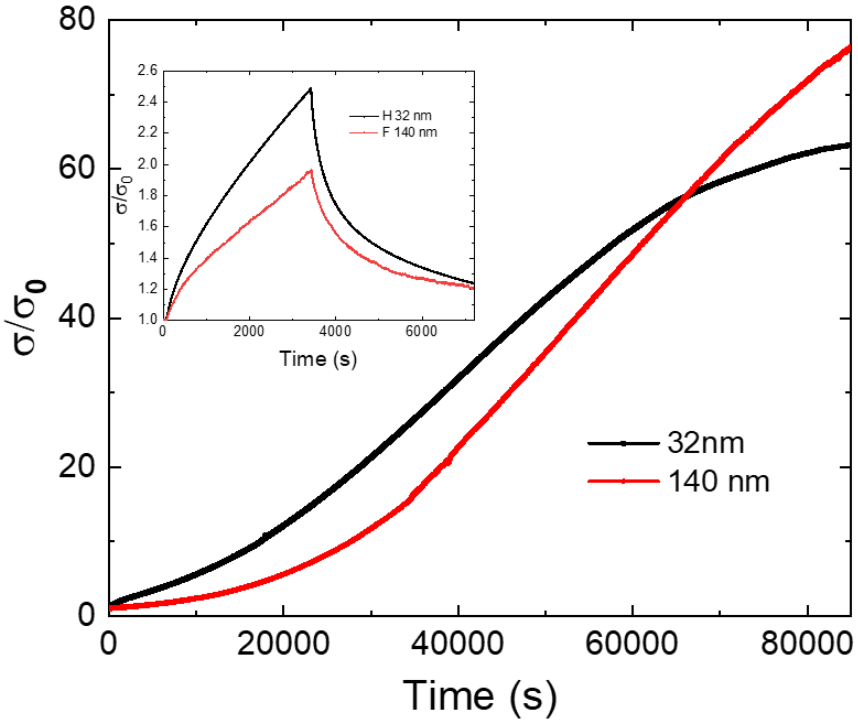

Figure 81 - Sensing characteristics of 32 and 140 nm Cu-Cr-O delafossite annealed at 1050 °C for 300 s, when exposed to 100 ppb of ozone at 200°C. Inset: response to 100 ppb of ozone during 1 hour followed by 1 hour recovery with dry air.

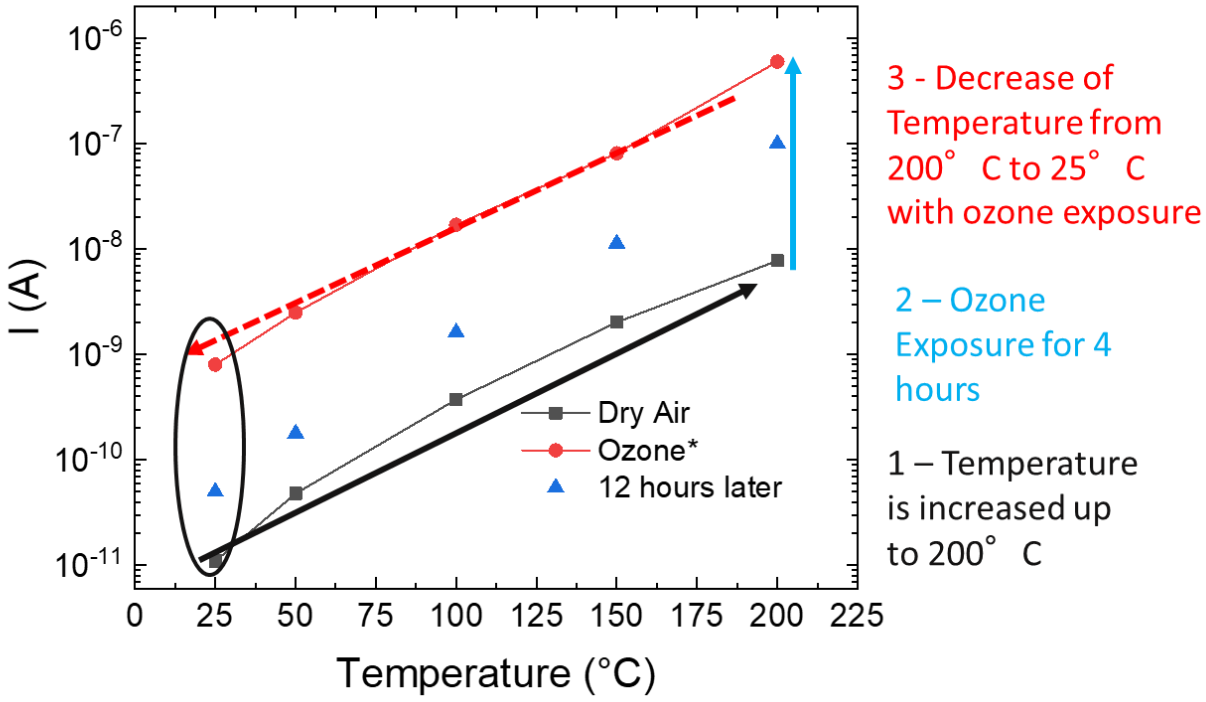

Figure 82 -32 nm thin film annealed at 1050 °C current, with a bias of 1V, at increasing temperatures from 25 to 200 °C. The response is shown under dry air in black. Next there is exposure to 2.5 ppm of ozone during 4 hours and a decrease of the temperature from 200 to 25 °C, with constant ozone exposure. Sample was then left under dry air for 12 hours at 25 °C. The results are 12 hours are present in blue, showing the partially irreversibility of the increase in conductivity.

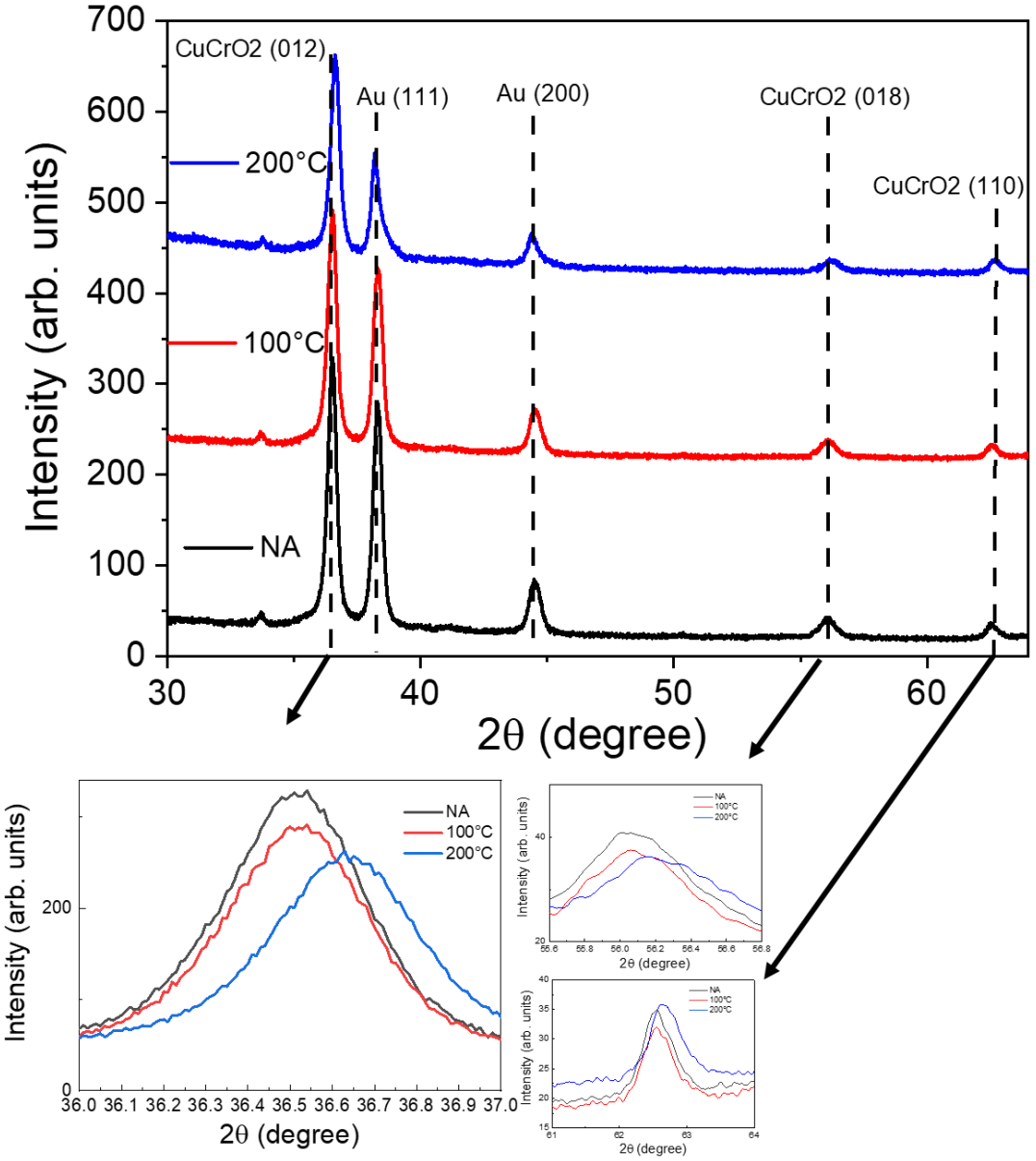

Figure 83 – GIXRD before and after ozone exposure at 100 and 200°C until a steady state was reached followed by a quick cooling down, showing a shift to higher angles of delafossite peaks. A close-up of these peaks is presented.

5.5. Sensing conclusions – Literature comparison

Upon the study of the sensing response of our Cu-Cr-O delafossite thin films, several conclusions can be drawn. It is evident the decrease in resistance upon exposure to any ozone concentration and a recovery to its original value when the ozone injection is stopped. Sensors annealed at 1050 °C lead to the best ozone response while as-deposited delafossite sensors present very low ozone sensitivity. Polycrystalline materials have many interdependent parameters that can influence gas sensing response. Nevertheless, the increase in porosity of the sensors, leading to a higher surface area and the decrease in carrier concentration, leading to a higher Debye length (an increase of up to three orders of magnitude, considering a constant carrier mobility) improve the sensor's response to low ozone concentrations. We were therefore able to show a sensing response to relevant ozone concentrations (as low as 50 ppb) working at temperatures from 25 to 150 °C. These results are a big step when compared with literature, due to the common limitation of ozone sensors to work above 200 °C. A comparison graph of our delafossite and commonly reported ozone sensing materials in the literature is shown in figure 84. Commercially available ozone sensors not only require the high-power consumption to keep temperatures above 200°C as well as require a stabilization and warming period before usage ranging from 6 to 24 hours.

When compared with other delafossite materials proposed, such as $CuAlO_2$ and stoichiometric $CuCrO_2$, for sensing at room temperature these results have shown a decrease in the detection range of 3 orders of magnitude. We further proposed a model to derive a better understanding of key parameters such as the kinetic reaction and delafossite physical properties. From our analysis we may conclude that the reaction is driven by the catalytic decomposition of ozone into monoatomic oxygen. This further explains the very low detection limits observed for our sensors. The selectivity of the sensors when compared with a 20% increase of oxygen concentration has been shown, showing no danger of cross-sensitivity due to ambient oxygen variations.

Novel NAP-XPS measurements with different ozone concentrations and temperatures were performed, leading us to valuable information relative to the bandbending of the surface of our material as function of ozone concentration. Furthermore, we observed the partial oxidation of copper into Cu^{2+} to be dependent on increasing ozone concentration, as well as the formation of a new peak on the oxygen 1s spectra, also proportional to the ozone concentration. This leads to believe that copper sites or Cu-O dumbbells are the responsible for the high catalytic activity of our thin films and its ozone decomposition.

In summary we have found that making use of p-type off-stoichiometric $Cu_{0,66}Cr_{1,33}O_2$ delafossite, with carefully studied annealing treatments, in order to maximize our film porosity and increase its surface area, we can detect low ozone concentrations at

temperatures below 100°C. This allows us to have reversible measurements to small ozone concentrations at lower temperatures, paving the way to low-power solid-state conductometric ozone sensors.

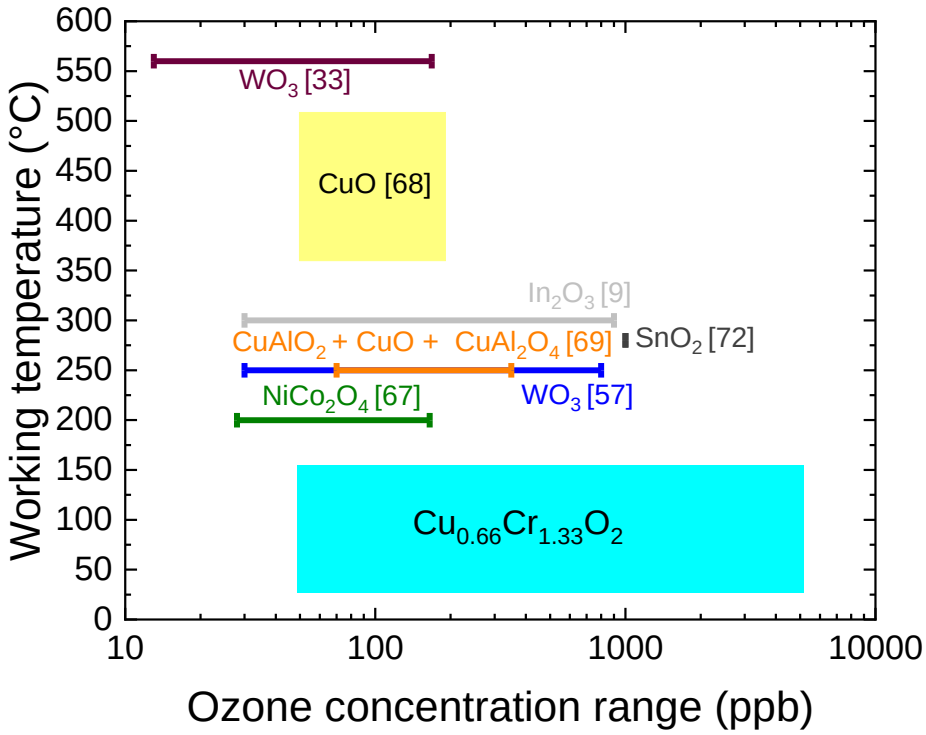

Figure 84 - Comparison of our $Cu_{0.66}Cr_{1.33}O_2$ sensors with literature results, depicting their working temperature and the possible ozone detection range in ppb

6. Future Perspectives

6.1. Device Integration

We have, during this work, successfully maximized the sensing performance of copper-chromium-oxide ozone sensors. One of the purposes of this work is to develop sensors capable of detecting ozone concentrations in the relevant range for human life (i.e. <70 ppb during 8 hours) while keeping the operating costs as low as possible. With this objective it is important to control the conductivity so that it can be easily detected by standard electronic equipment used in low-cost sensor networks. If we assume that the detection limit in the standard electronic equipment used is 0.1 nA, then our high sensitivity sensors, annealed at 1050°C, might not be the most suitable, since the variation of current upon the introduction of 50 ppb of ozone is usually below this range.

If we consider that we want to safely detect (with at least a change in current of 0.1 nA) 20 ppb of ozone, we could then tune the carrier concentration of the film in order to deliver the best sensing response with the given constrains.

In this example and knowing the relation from our analysis in chapter 4.2.1, that

$$I/I_0 = 98 \times [O_3]^{0.31} \tag{43}$$

We can derive the relation $I = 1.164 \times I_0$ and $I - I_0 = 0.1nA$, resulting in $I_0 \sim 0.61$ nA.

If we then consider, that the current is dependent on the conductivity (σ) as:

$$I = \frac{VA\sigma}{l} \tag{44}$$

Where l is the distance between the contacts and A is the product of the thickness (t) and the width (w) of the device. Assuming that w = l and V = 1, we can derive that:

$$\sigma = \frac{I}{t} \tag{45}$$

What would result in the case of our 32 nm thin film, in a minimum conductivity of 1.9×10^{-2} S/cm. Lower conductivities would not be able to produce a change in current in the order of magnitude required. Assuming a mobility of 0.1 cm^2/Vs (the mobility measured for the thin films as deposited), would result in a maximum carrier concentration of 1.2×10^{16} cm^{-3}. Looking at our analysed films in chapter 3.3, it is clear this carrier concentration is lower than the studied for 900°C, whilst probably higher than the carrier concentration present after annealing at 1050°C, as the I_0 of 610 pA, suggests (the measured base current for the films was ~ 200 pA).

On the other hand, if the sensitivity would be decreased, as is to be expected from our analysis of the sensitivity as function of the annealing temperature suggests, would render the device with $1.9 \times 10^{-2}\ \mathrm{S/cm}$ incapable of meeting the specifications here required.

This exercise shows, how the thin film can be modelled in order to meet the required specifications, however, more studies are yet necessary to better understand the variation of the sensitivity with the carrier concentration. For this it is key to be able to accurately measure the mobility / carrier concentration of the copper-chromium-oxide thin films.

The carrier concentration must be then carefully controlled to make sure the device meets the specifications required by the electronic equipment being used and a compromise between the higher sensitivity and higher conductivity has to be reached.

A possibility to overcome this difficulty would be by material engineering in ways the carrier concentration could be decreased whilst increasing the mobility. The operating voltage kept at 1 V during operation, could also be increased, to 10 V, as per standard electronic equipment, for an increased current output. The geometry of the sensor could be modified. The distance between the contacts was kept constant at 500 µm. However, a decrease of the contact distancing to 5 µm, would in theory lead to a response 100 times higher. Interconnected electrodes is even another possibility of increasing the current output without changing the physical properties of the material.

In figure 85 repeatability tests are presented. Here was used the same sample sensor, annealed at 1050°C, with 32 nm of copper-chromium-delafossite. The sensor was exposed 4 times to ozone with 100 ppb diluted in dry air. The measurements were not done in sequence. In fact, they have several months apart. A benchmark comparison with 50 ppb is used. One can notice that there is a reasonable repeatability, but an error can clearly be associated with the measurements. It can be noted up to 5% of sensing response difference upon exposure to 100 ppb of ozone after 5000 s. Nevertheless, it is perfectly reasonable to assume there is a clear distinction in between 50 and 100 ppb of ozone exposure. These differences might arise from several conditions. The manual placement of the probes in the sensing device, leads to differences in the distance of the measurements, the degradation of the gold contacts due to the probe placing and electric error associated with the electrical setup used.

Furthermore, the manual placement of the lamp coverage that controls ozone concentration as described in chapter 2.1, might lead to small variations in ozone concentration. All this coupled with possible starting surface coverages and variations in the lamp power over time and in the sample surface, lead to several error, difficult to isolate. Nevertheless, it is interesting to notice that in any case the sensors present an important repeatability to work as an alarm or a quantitative sensor.

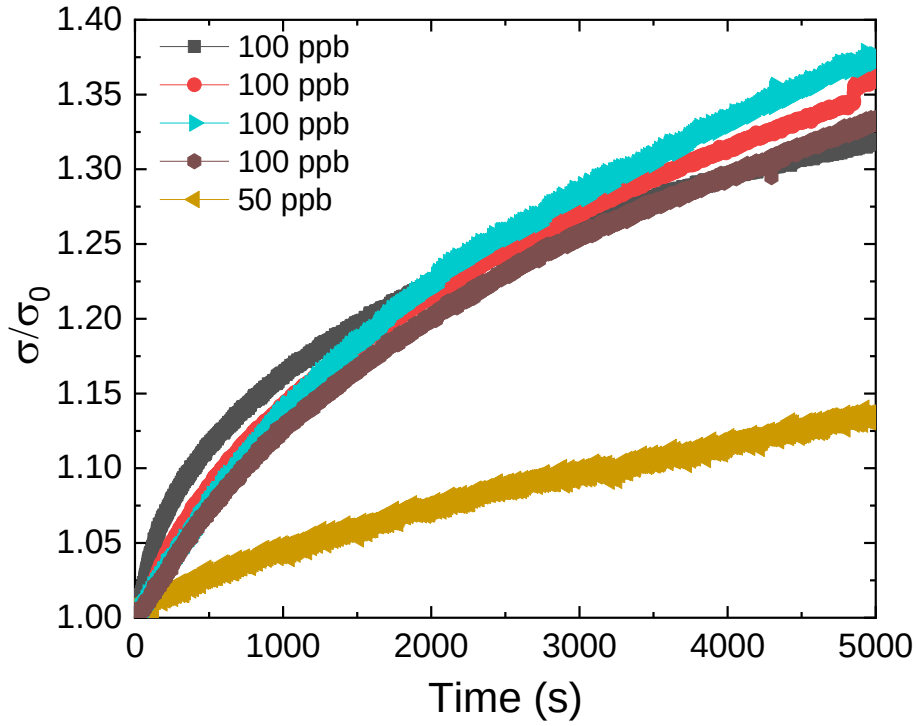

Figure 85 - Repeatability tests - Sensing characteristics at 100°C of 32 nm Cu-Cr-O delafossite thin film annealed at 1050 °C for 300 s, with repeated tests to 100 ppb of ozone. One test at 50 ppb is used for benchmark comparison.

6.2. P-N Junction Development

This chapter is based on a publication. The elaboration of a capable p-n junction, that is the simplest active device, shows the scalability and usability of our off-stoichiometric copper-chromium delafossite. A p-n junction and more complex active devices such as a back-gate transistor, based on an ozone sensitive layer, such as our copper-chromium-oxide, may lead to the creation of a highly sensitive and fast ozone sensor. Several parameters, such as the reverse current in a p-n junction or the turn-on voltage are led by defect density and carrier concentration of the material. Ozone exposure leads to the formation of a surface accumulation layer which has a higher concentration of majority carriers (holes). Due to the nature of the p-n junction, the reverse current, is usually driven by minority carriers, that flow through the depletion region. The fact that ozone exposure leads to trapping of electrons, minority carriers in our copper-chromium-oxide thin film gas sensors, then change the junction reverse current characteristics, as shown per equations 47 and 48. This therefore, may be a powerful tool in a sensing device. Furthermore, the turn-on voltage of the diode is usually defined by the bandalignment of the p and n-type materials. In this case, upon ozone exposure a surface bandbending is created, that may shift the bandalignment and thus the

turn-on voltage of the diode. However, a total bandalignment change can be observed in cases where the grain size, is smaller than the bandbending. Otherwise, a energy screening through the thickness of the film will be observed.

$$I = I_s \exp\left(V/\eta Vt\right) \tag{46}$$

Where I_s is the reverse current of the diode and can be described as:

$$I_s = qA\left(\frac{D_n}{L_n}n_0 + \frac{D_p}{L_p}p_0\right) \tag{47}$$

Where D is the drift current, thermally generated by the charge carriers and L is the minority carrier diffusion length. Upon ozone exposure, the oxygen adsorbates would lead to electron trapping, decreasing the drift electrons available for conduction in the copper-chromium-oxide, decreasing I_s, being then described by:

$$I_s = qA\left(\frac{D_n - \Delta D_n}{L_n}(n_0 - \Delta n_0) + \frac{D_p}{L_p}p_0\right) \tag{48}$$

Where ΔD_n and Δn_0, represent the variation of the drift current generated by the charge carriers, due to electron trapping upon ozone exposure.

6.3. Raman Laser Annealing

Preliminary studies were done in order to understand the feasibility of laser annealing of the delafossite layer. The usage of laser annealing creates several possibilities into sensor development, such as a back-gate transistor architecture for fast sensors recovery, where the study of the electrical properties of the transistor channel may lead to better performing devices. The usage of such devices would allow to go beyond the traditional resistive sensor, having a set of different properties impacted by ozone and a more complete range of electrical parameters, such as the transconductance, turn-on voltage, saturation current or off-current.

For this study we used the Raman laser, with wavelengths 325 and 442 nm, for a possible probing while annealing. A first study was done, probing with the 442 nm wavelength laser, while the sample was heated from RT to 900 °C as shown in figure 86 a). It is noteworthy that the sample as deposited almost doesn't present the copper chromium oxide vibrational peaks, expected at 457 and 709 cm^{-1}. With increased annealing temperature (above 600 °C), these peaks start getting more and more intense. As previously discussed, this may be due to the high number of defects that hinder the vibrations. Thermal treatment promotes defect healing and increases the material crystallinity. With increasing temperature there is a blue shift that can be associated with an increased spacing between the atoms, what is to be expected due to the increased temperature. Figure 86 b), represents the cooling down process, showing the reversibility of the blue shift and the return of the peaks to the expected value, meanwhile the increase in crystallinity and defect healing is not reversible, being observed the Raman vibrational modes at 100 °C. Using the cooling down cycle, we are able to fit the peak position as function of the temperature as shown in figure 87. This calibration curve allows us to extract what is the estimated peak shift depending on the temperature, resulting in the equation:

$$P\ (cm^{-1})\ = 709.85 - 0.034\left(\frac{cm^{-1}}{^{\circ}C}\right)T(^{\circ}\ C) \tag{49}$$

Where P is the peak position, that at RT is 709 cm^{-1}. A change of -0.034 cm^{-1} per °C is therefore expected. This calibration allows us to potentially be able to analyse the local temperature of the thin film, while annealing its top layer. The annealing depth depends only on the laser characteristics.

However, we have found severe limitations, due to the laser power output in our system. The required temperature above 600 °C could not be achieved using the 442 nm laser required to probe the sample. UV-laser (325 nm) annealing was then tested. Annealing steps under ambient atmosphere didn't preserve the delafossite phase, promoting an oxidation of its surface. Optical images are shown in figure 88. XRD analysis shows a formation of Cr_2O_3 phase.

A Linkam probe station was used, in order to create an inert atmosphere during the annealing step. The I-V characteristics of the thin film before and after an annealing step using the 325 nm wavelength laser during 1500 s are shown in figure 89. A decrease in resistance is observed by a factor close to 2. This would roughly correspond to an annealing temperature of 650 °C. For optimization and scalability of this process a stronger laser power is therefore necessary. Part of the laser power may be hindered by absorption of the glass window in the probestation.

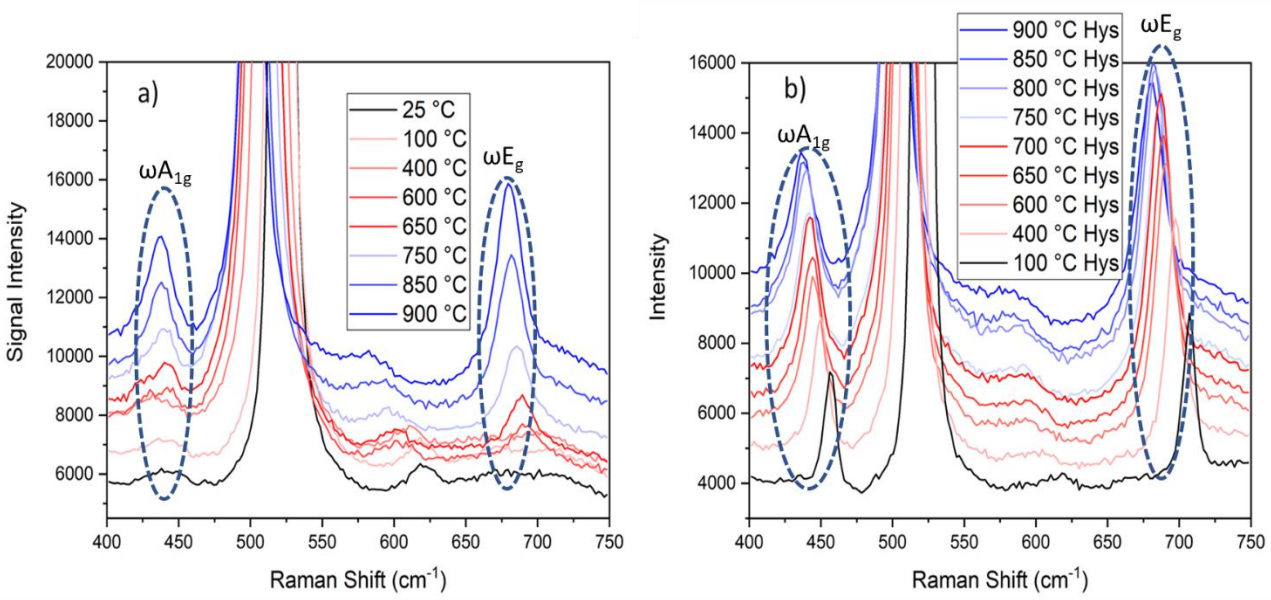

Figure 86 - Raman spectra during annealing process from 25 °C to 900 °C and subsequent cool down

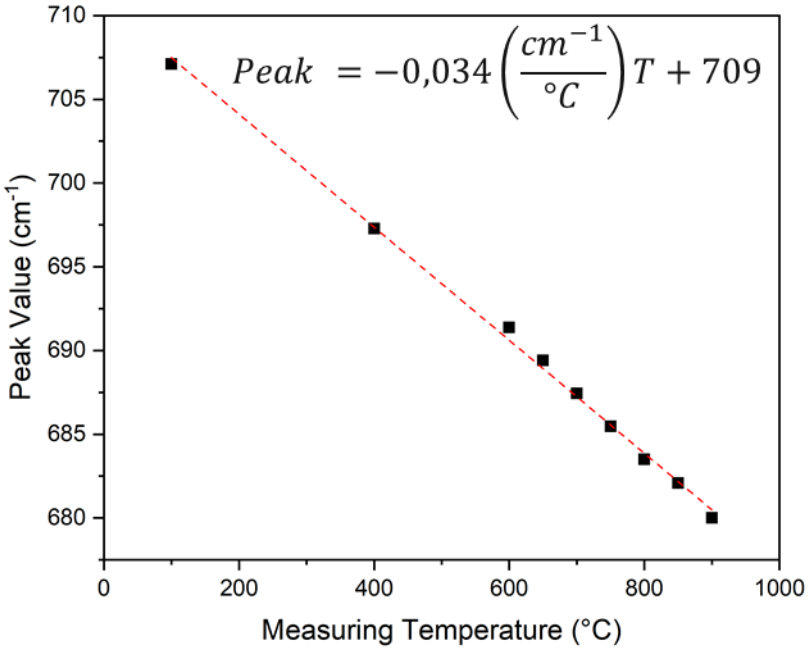

Figure 87 - Fitting of the Raman peak position vs the measuring temperature during the cool down cycle represented in figure 86 b)

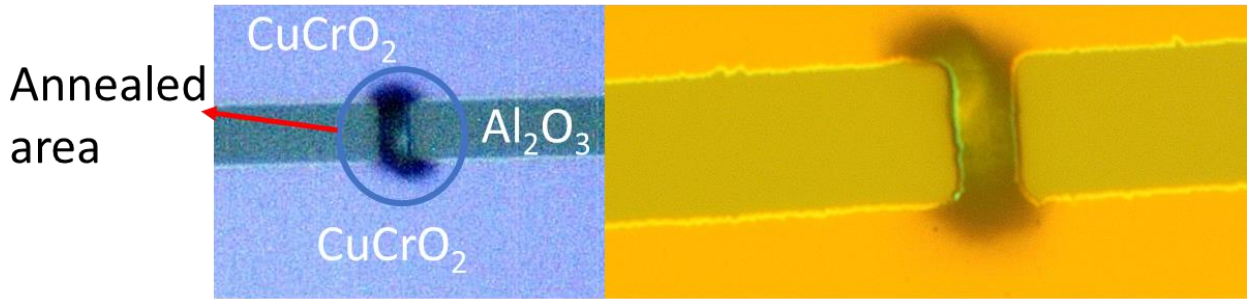

Figure 88 - Optical microscope images of laser annealed area under ambient atmosphere

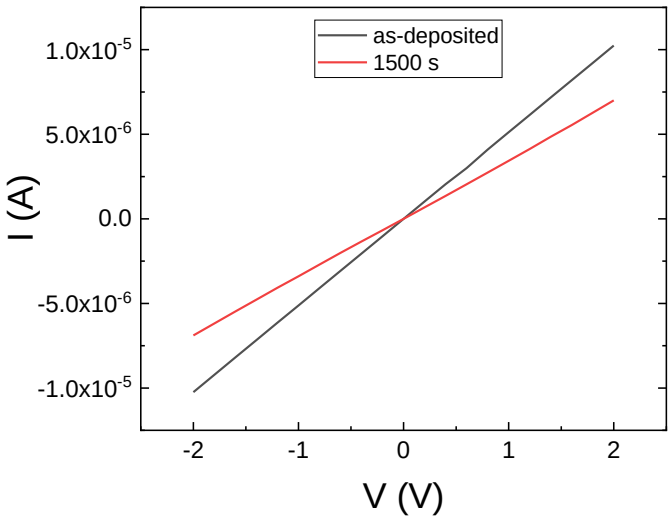

Figure 89 - I-V characteristics of delafossite thin film, annealed under inert conditions, showing a decrease in resistance by a factor close to 2.

6.4. Conclusions

In these perspective studies we show the potential of delafossite to make its way into transparent electronics applications. Many steps still must be further explored, but some building blocks are laid out, showing the possibility to have a fully scalable transparent p-n junction based on $Cu_{0.66}Cr_{1.33}O_2$ and ZnO. P-n junctions can be used as gas sensors, due to the nature of the semiconductors. Upon exposure to the target gas, a bandbending will be created that will lead to different response behaviours.

Laser annealing for controlled depth annealing might be a very interesting tool for a transparent transistor development. Its feasibility might allow the creation of more complex gas sensors based on back-gate transistors. However, with our Raman laser we are limited to a change in resistance of the order of 2. A stronger laser power is therefore necessary while keeping an inert atmosphere. If a stronger laser can be coupled with the Raman system, one has the possibility for an efficient control of the surface temperature, by measuring the Raman peak displacement as shown here.

7. Conclusions and perspectives

The rapid growth of low-cost sensor networks combined with the increased awareness for indoor office pollution has led to a great demand for low cost gas sensors. Among these, ozone sensors have attracted a great deal of attention for two reasons. Firstly, there is a shortage of sensors capable of detection for low ozone concentrations, that are portable, miniaturizable and low cost. Secondly, most of the commonly proposed sensors require high working temperature, leading to a constant power dissipation. Delafossite based sensors have been proposed a decade ago, with sensitivities as low as 50 ppm, whilst the environmental protection agency (EPA), sets the limits of exposure at 70 ppb during 8 hours per day. Despite the fact that delafossite thin films have been studied in the group with the best reported electrical properties for undoped materials, their road to applications was unpaved. Their high number of unsaturated bonds and copper vacancies could lead to a high catalytic activity to ozone.

This thesis was conducted in the framework of MASSENA project agreed between LIST, University of Luxembourg and FNR. This project focused on the study of off-stoichiometric copper-chromium-delafossite properties and the tuning of its properties into applications. Mostly, it was dedicated to the study of the electrical and morphological changes observed in the thin films and how these changes correlate with the ozone sensing response. The thin film properties were influenced by the deposition conditions studied and the post annealing treatments.

$Cu_{0.66}Cr_{1.33}O_2$ thin films are deposited by liquid injection metal organic chemical vapour deposition, a large scale compatible and scalable technique. We have studied the deposition conditions by changing the precursor injection, deposition pressure, substrate temperature and deposition time. Next, we studied the influence of post annealing treatments. We wanted to drive an understanding of how deposition conditions and annealing treatment changes the morphology and electrical properties of delafossite thin films. The effect of the different preparation and annealing conditions was investigated by XRD, SEM, Raman, XPS and AFM characterizations were performed to drive these conclusions.

The different thin films response to ozone was then studied. The influence of the thin films properties on the sensing response was discussed. The working temperature, the influence of ozone concentration and the sensors' selectivity was studied.

We demonstrated that by carefully tuning its properties delafossite materials can be employed as a p-type resistive sensor. Surface area is a key parameter that controls the sensing response for conductometric semiconductor sensors. Normally porosity and grain size are the most efficient ways to control the surface area. We have observed that an increase in the porosity and roughness greatly increases the sensing behaviour of our sensors. This was

achieved by thermal treatments in vacuum. The changes in surface area and the increase of gas permeation are behind the increase in sensitivity with the annealing temperature. The thin films are quire sensitive to ozone at low temperature, but the rapid saturation could not be achieved. For so, we proposed a measuring method based on the dynamic change of current as function of time. The slope of the I(A) - t(s) curve, can give us important information allowing for the fast detection of low ozone concentrations, making the sensor work as a quantitative sensor or as an alarm. The recovery process can also be shortened to some seconds if the temperature is increased above 200 °C, promoting the quick desorption of oxygen adsorbates.

Our dozens of measurements did not lead to a baseline drift, but it is a possibility associated with semiconductor based gas sensors, that due to irreversible reactions and oxygen diffusion into the films, poisoning of the sensors occurs, requiring a recalibration or reset of the sensor. It could be easily achieved by increasing the temperature of the sensor (above 300 °C), promoting the out diffusion of absorbed oxygen.

Our sensor show much improved sensitivity response compared with $CuCrO_2$ microcrystals [12] and $CuAlO_2$ sensors reported in the literature [13]. Unlike commonly reported sensors, where temperatures below 300°C lead to non-reversible measurements, we observed a full recovery of the baseline even at low temperatures. The sensors have shown a great selectivity towards oxygen variation. Deeper studies with different oxidizing and reducing gases could be performed for cross-sensitivity understanding. The kinetic reaction of ozone on the delafossite thin film's surface is led by the catalytic decomposition into atomic oxygen. This helps justifying the selectivity towards molecular oxygen, that was observed.

The working temperature of the sensor has been defined as RT - 150°C. Ozone exposure at higher temperature leads to non-easily reversible changes in the delafossite conductivity due to oxygen species incorporation.

The potential shown by the delafossite thin films can lead to its integration into sensor networks. Furthermore, in most cases the deposition of the films used as ozone sensors in literature works make recourse to not easily scalable techniques, such as sol-gel or physical deposition, due to their increased porosity. In this work fully scalable, miniaturizable and wafer batch compatible techniques were used.

All in all, the high selectivity shown compared with O_2 and high sensitivity allowing for measurements in few tens of ppb range, make our sensors perfectly matching the application case of ozone monitoring and in particular for a function as an alarm alerting of the risks of exposure for the human health and environmental monitoring. The low power consumption and possible integration due to the miniaturization capabilities, allow for its integration into low cost sensor networks and internet of things enabling a detailed mapping of ozone pollution and personal alert in case of risk exposure.

A model of conductivity based on the accumulation layer created by the adsorption of oxygen species leading to a bandbending induced by the surrounding atmosphere was elaborated and compared with the experimental results.

Table 19 makes a comparison of the key features of low-cost ozone sensors, in between different technologies and our sensors. The sensors can work at room temperature, but due to the nature of metal oxide materials and their temperature dependence, it is ideal a working temperature around 100°C. This leads to much lower power consumption than other sensors that require much higher working temperature (> 250°C). These simple sensors, don't make recourse to any external device, leading to easy miniaturization and integration into sensor networks. The response time of the sensors can be quite high, however by using a variation of the slope of response instead of a steady state response we can decrease the response time to competitive values. Our sensors presented high selectivity compared with molecular oxygen, but further studies for the influence of humidity and other oxidizing species are key before usage and commercialization is possible. However, the high performance achieved by the 32 nm thick copper-chromium-oxide films, with changes in current of at least 20% for 50 ppb and 50% for 100 ppb, at low temperature (100°C), leads us to believe the usability of these sensors.

Table 18 - Comparison of key features of different ozone sensing technologies with our copper-chromium-oxide based ozone sensors

Technology / Key Feature	Sensitivity (hundreds of ppb to ppm range)	Selectivity	Cost	Low power consumption	Response time	Miniaturization Integration
Spectroscopy						
Optochemical						
Conductometric metal oxide						
Photo-assisted conductometric						
Electrochemical						
$Cu_{0.66}Cr_{1.33}O_2$ based conductometric						

The in-situ NAP-XPS studies dependent on ozone partial pressure and temperature were a novel and relevant analysis that gives us a window into the ozone decomposition and the adsorption of monoatomic oxygen and can be associated with the models we proposed. We have shown the bandbending created by oxygen adsorbates and the changes in carrier concentration of the material. Furthermore, we have shown these to be dependent on the ozone concentration and the substrate temperature, likely due to the catalytic feature of our very specific delafossite Cu-Cr-O thin-films stoichiometry that induces low-temperature ozone decomposition at its surface. These measurements have allowed us to hypothesize that the Cu atoms or Cu-O dumbbells are responsible for the catalytic activity of our material, since a partial oxidation of the Cu was present, whilst no obvious change was observed in the Cr. The rise of a new peak in the O 1s spectra, suggest the presence of chemisorbed oxygen responsible for the copper oxidation.

This study could even be further deepened by coupling other measurements that would permit to have complementary information and corroboration of the values extracted, for instance in-situ KPFM dependent on temperature and ozone exposure.

Many future studies can be proposed based on this work. It is a work, that opens new perspectives for the integration of copper-chromium-oxide into devices and specially into ozone sensors.

A wider range of combination deposition conditions / annealing treatments could be performed for a deeper understanding of the main driving thin film property for ozone sensing reaction and maximization of its performance. Furthermore, annealing under different atmospheres can be studied to understand its impact on the thin films' morphological properties. Ways to maximize its mobility while controlling the carrier concentration for increased sensor response is a key feature. This could possibly be achieved by changes in annealing atmosphere or integration of other dopants. However, it would be key to have a reliable system for measurement of the copper-chromium-delafossite mobility.

A simple p-n junction was created using ZnO and off-stoichiometric $CuCrO_2$ showing the possibility of integration of the material into active devices. Etching processes and local laser annealing were partially explored, with promising results.

More complex devices can be derived from this study and the integration of copper-chromium-oxide herein studied into other kind of ozone sensors such as based on a p-n junction or a back-gate transistor, where copper-chromium-oxide is used as the sensing layer. The turn on voltage of the devices or the inverse current, might function as sensitive measurements for dangerous ozone concentrations.

In this work the spacing and the electrodes used were unchanged. It was been shown however that this can be an important parameter to increase sensing response [40]. It is of

interest for future works to understand how the spacing in between the electrodes or if the use of interdigitated electrodes can further improve the sensing behaviour.

8. Annex – Deposition conditions

Deposition	Substrate	Silicon Oxide (nm)	Substrate Temperature (°C)	Deposition time (s)	Setpoint	Pressure (mbar)	Injection (g/min)	Conductivity (S/cm)
1	p+ Si	20	450	900	10	12	2	1.53
2	p+ Si	20	450	900	10	12	2	1.25
3	p+ Si	11	450	900	16	12	2	9.50
4	p+ Si	9	450	900	13	12	2	7.16
5	p+ Si	6	475	900	13	12	2	1.26
6	p+ Si	34	450	900	16	12	2	8.19
7	p Si	7	425	900	16	12	2	1.67
8	p Si	21	425	900	16	12	2	4.77
9	p Si	11	450	900	16	12	2	9.74
10	p Si	17	425	900	16	12	2	3.75
11	p Si	18	450	900	16	12	2	9.28
12 (no rotation)	p Si	18	450	900	16	12	2	5.16
13	p+ Si	9	450	900	16	12	2	6.24
14	p+ Si	25	450	900	16	12	2	9.00
15	p+ Si	21	450	900	16	12	2	9.31
16	p Si	8	450	900	16	12	2	7.78
17	p Si	11	450	900	16	12	2	9.09
18	p Si	20	450	900	16	12	2	9.54
19	p Si	20	450	900	16	12	2	8.48
20	p Si	14	450	900	16	12	2	8.48
21	p+ Si	20	450	900	16	12	2	7.16
22	p+ Si	15	450	900	16	12	2	7.16
23	p+ Si	16	450	900	16	12	2	7.61
24	p Si	13	450	900	16	12	2	8.52

Deposition	Substrate	Silicon Oxide (nm)	Substrate Temperature (°C)	Deposition time (s)	Setpoint (cm)	Pressure (mbar)	Injection (g/min)	Conductivity (S/cm)
A1	undoped Si	20	450	900	16	12	2	7.14
A2	undoped Si	20	450	900	16	12	2	9.52
A3	undoped Si	20	450	900	16	12	2	5.71
A4	undoped Si	20	450	1800	16	12	2	6.67
A5	undoped Si	20	450	1800	16	12	2	4.44
A6	undoped Si	20	450	450	16	12	2	9.52
A7	undoped Si	20	450	450	16	12	2	2.86
A8	undoped Si	20	500	900	16	12	2	0.067
A9	undoped Si	20	500	900	16	12	2	0.043
A10	undoped Si	20	550	900	16	12	2	0.002
A11	undoped Si	20	550	900	16	12	2	0.002
A12	undoped Si	20	450	900	16	12	1	0.95
A13	undoped Si	20	450	1800	16	12	1	0.48
A	Sapphire	N/A	450	900	16	12	2	34.17
B	Sapphire	N/A	450	900	16	6	2	2.59
C	Sapphire	N/A	450	900	16	6	2	7.61
D	Sapphire	N/A	450	900	16	12	2	26.66
E	Sapphire	N/A	450	1800	16	12	2	60.34
F	Sapphire	N/A	450	1800	16	12	2	84.47
G	Sapphire	N/A	450	450	16	12	2	12.32
H	Sapphire	N/A	450	450	16	12	2	11.40
I	Sapphire	N/A	450	1800	16	12	2	58.66
J	Sapphire	N/A	450	3600	16	12	2	54.75

9. Bibliography

1. X. Wang, Z. Shen, Z. Tang, G. Li, Y. Lei, Q. Zhang, Y. Zeng, H. Xu, J. Cao, and R. Zhang, 1 (2015).

2. S. C. Lee, S. Lam, and H. K. Fai, **36**, 837 (2001).

3. Environmental Protection Agengy, (n.d.).

4. H. Salonen, T. Salthammer, and L. Morawska, Environ. Int. **119**, 503 (2018).

5. J. J. Zhang, Y. Wei, and Z. Fang, Front. Immunol. **10**, 1 (2019).

6. E. C. Kleinsorge, M. Erben, M. G. Galan, C. Barison, M. E. Gonsebatt, and M. F. Simoniello, Biomarkers **16**, 642 (2011).

7. M. Altayeb, S. M. Sharif, and S. Abdella, 2018 Int. Conf. Comput. Control. Electr. Electron. Eng. ICCCEEE 2018 1 (2018).

8. F. Mao, K. Khamis, S. Krause, J. Clark, and D. M. Hannah, Front. Earth Sci. **7**, 1 (2019).

9. G. Korotcenkov, V. Brinzari, and B. K. Cho, J. Sensors **2016**, (2016).

10. A. Dey, Mater. Sci. Eng. B Solid-State Mater. Adv. Technol. **229**, 206 (2018).

11. G. W. Hunter, S. Akbar, S. Bhansali, M. Daniele, P. D. Erb, K. Johnson, C.-C. Liu, D. Miller, O. Oralkan, P. J. Hesketh, P. Manickam, and R. L. Vander Wal, J. Electrochem. Soc. **167**, 037570 (2020).

12. S. Zhou, X. Fang, Z. Deng, D. Li, W. Dong, R. Tao, G. Meng, and T. Wang, Sensors Actuators, B Chem. **143**, 119 (2009).

13. X. G. Zheng, K. Taniguchi, A. Takahashi, Y. Liu, and C. N. Xu, Appl. Phys. Lett. **85**, 1728 (2004).

14. P. Lunca-Popa, J. Afonso, P. Grysan, J. Crêpellière, R. Leturcq, and D. Lenoble, Sci. Rep. **8**, 7216 (2018).

15. S. Chapman, London, Edinburgh, Dublin Philos. Mag. J. Sci. **10**, 369 (1930).

16. P. J. D. Peterson, A. Aujla, K. H. Grant, A. G. Brundle, M. R. Thompson, J. Vande Hey, and R. J. Leigh, Sensors (Switzerland) **17**, 1 (2017).

17. T. Ching, E. Marcus, M. David, M. Haniff, and N. H. Ngajikin, *Ozone Sensor Review from the Fundamental Perspective* (2012).

18. M. David, M. H. Ibrahim, S. M. Idrus, A. I. Azmi, N. H. Ngajikin, T. C. En Marcus, M. Yaacob, M. R. Salim, and A. A. Aziz, J. Teknol. **73**, 23 (2015).

19. M. David, M. H. Ibrahim, S. M. Idrus, A. I. Azmi, N. H. Ngajikin, T. C. En Marcus, M. Yaacob, M. R. Salim, and A. A. Aziz, J. Teknol. **73**, 23 (2015).

20. G. Korotcenkov and B. K. Cho, Sensors Actuators, B Chem. **161**, 28 (2012).

21. S. Vallejos, V. Khatko, K. Aguir, K. A. Ngo, J. Calderer, I. Gràcia, C. Cané, E. Llobet, and X.

Correig, Sensors Actuators, B Chem. **126**, 573 (2007).

22. N. Fann, A. D. Lamson, S. C. Anenberg, K. Wesson, D. Risley, and B. J. Hubbell, **32**, (2012).

23. W. J. Collins, R. G. Derwent, B. Garnier, C. E. Johnson, M. G. Sanderson, and D. S. Stevenson, **108**, 1 (2003).

24. Y. Wang, B. Hu, G. Tang, D. Ji, H. Zhang, J. Bai, X. Wang, and Y. Wang, **133**, 450 (2013).

25. R. P. Tuckett, Clim. Chang. 3 (2009).

26. WHO, (2005).

27. J. I. Levy, S. M. Chemerynski, and J. A. Sarnat, Epidemiology **16**, 458 (2005).

28. European Environment Agency (EEA), *Air Quality in Europe - 2020 Report* (2020).

29. A. Ezcurra, B. Benech, A. Echelecou, J. M. Santamaría, I. Herrero, and E. Zulueta, **74**, 367 (2013).

30. J. Staehelin, J. Thudium, R. Buehler, A. Volz-Thomas, and W. Graber, Atmos. Environ. **28**, 75 (1994).

31. D. G. Poppendieck, D. Rim, and A. K. Persily, Environ. Sci. Technol. **48**, 2067 (2014).

32. S. R. Utembe, G. M. Hansford, M. G. Sanderson, R. A. Freshwater, K. F. E. Pratt, D. E. Williams, R. A. Cox, and R. L. Jones, Sensors Actuators, B Chem. **114**, 507 (2006).

33. N. Yamazoe and N. Miura, Sensors Actuators B. Chem. **20**, 95 (1994).

34. V. Yushkov, A. Oulanovsky, N. Lechenuk, I. Roudakov, K. Arshinov, F. Tikhonov, L. Stefanutti, F. Ravegnani, U. Bonafé, and T. Georgiadis, J. Atmos. Ocean. Technol. **16**, 1345 (1999).

35. H. Güsten, G. Heinrich, R. W. H. Schmidt, and U. Schurath, J. Atmos. Chem. **14**, 73 (1992).

36. A. J. BERNANOSE and M. G. RÉNÉ, in *OZONE Chem. Technol.* (AMERICAN CHEMICAL SOCIETY, 1959), pp. 2–7.

37. D. Sauter, U. Weimar, G. Noetzel, J. Mitrovics, and W. Göpel, Sensors Actuators B Chem. **69**, 1 (2000).

38. D. Parrish and F. Fehsenfeld, Atmos. Environ. **34**, 1921 (2000).

39. S. O'Keeffe, C. Fitzpatrick, and E. Lewis, Sensors Actuators B-Chemical - Sens. ACTUATOR B-CHEM **125**, 372 (2007).

40. G. Korotcenkov, Mater. Sci. Eng. R Reports **61**, 1 (2008).

41. T. Takada, K. Suzuki, and M. Nakane, Sensors Actuators B. Chem. **13**, 404 (1993).

42. T. Wagner, J. Hennemann, C. D. Kohl, and M. Tiemann, Thin Solid Films **520**, 918 (2011).

43. S. R. Kim, H. K. Hong, C. H. Kwon, D. H. Yun, K. Lee, and Y. K. Sung, Sensors Actuators, B Chem. **66**, 59 (2000).

44. M. Epifani, E. Comini, J. Arbiol, R. Díaz, N. Sergent, T. Pagnier, P. Siciliano, G. Faglia, and J. R. Morante, Sensors Actuators, B Chem. **130**, 483 (2008).

45. A. Gurlo, N. Bârsan, M. Ivanovskaya, U. Weimar, and W. Göpel, Sensors Actuators, B Chem. **47**, 92 (1998).

46. T. Doll, A. Fuchs, I. Eisele, G. Faglia, S. Groppelli, and G. Sberveglieri, Sensors Actuators, B Chem. **49**, 63 (1998).

47. M. Ivanovskaya, A. Gurlo, and P. Bogdanov, Sensors Actuators, B Chem. **77**, 264 (2001).

48. R. Martins, E. Fortunato, P. Nunes, I. Ferreira, A. Marques, M. Bender, N. Katsarakis, V. Cimalla, and G. Kiriakidis, J. Appl. Phys. **96**, 1398 (2004).

49. S. Christoulakis, M. Suchea, E. Koudoumas, M. Katharakis, N. Katsarakis, and G. Kiriakidis, Appl. Surf. Sci. **252**, 5351 (2006).

50. M. Bender, E. Gagaoudakis, E. Douloufakis, E. Natsakou, N. Katsarakis, V. Cimalla, G. Kiriakidis, E. Fortunato, P. Nunes, A. Marques, and R. Martins, Thin Solid Films **418**, 45 (2002).

51. F. S. Sen Chien, C. R. Wang, Y. L. Chan, H. L. Lin, M. H. Chen, and R. J. Wu, Sensors Actuators, B Chem. **144**, 120 (2010).

52. L. S. R. Rocha, C. R. Foschini, C. C. Silva, E. Longo, and A. Z. Simões, Ceram. Int. **42**, 4539 (2016).

53. A. C. Catto, L. F. da Silva, C. Ribeiro, S. Bernardini, K. Aguir, E. Longo, and V. R. Mastelaro, RSC Adv. **5**, 19528 (2015).

54. J. Guérin, K. Aguir, M. Bendahan, and C. Lambert-Mauriat, Sensors Actuators, B Chem. **104**, 289 (2005).

55. D. E. Williams, S. R. Aliwell, K. F. E. Pratt, D. J. Caruana, R. L. Jones, R. A. Cox, G. M. Hansford, and J. Halsall, Meas. Sci. Technol. **13**, 923 (2002).

56. A. Labidi, E. Gillet, R. Delamare, M. Maaref, and K. Aguir, Sensors Actuators, B Chem. **120**, 338 (2006).

57. M. Bendahan, J. Guérin, R. Boulmani, and K. Aguir, Sensors Actuators, B Chem. **124**, 24 (2007).

58. W. Qu and W. Wlodarski, Sensors Actuators, B Chem. **64**, 42 (2000).

59. J. Guérin, M. Bendahan, and K. Aguir, Sensors Actuators, B Chem. **128**, 462 (2008).

60. K. Aguir, C. Lemire, and D. B. B. Lollman, Sensors Actuators, B Chem. **84**, 1 (2002).

61. E. Gagaoudakis, M. Bender, E. Douloufakis, N. Katsarakis, E. Natsakou, V. Cimalla, and G. Kiriakidis, Sensors Actuators, B Chem. **80**, 155 (2001).

62. S. O'Brien, M. G. Nolan, M. Çopuroglu, J. A. Hamilton, I. Povey, L. Pereira, R. Martins, E. Fortunato, and M. Pemble, Thin Solid Films **518**, 4515 (2010).

63. G. Kiriakidis, M. Bender, N. Katsarakis, E. Gagaoudakis, E. Hourdakis, E. Douloufakis, and V. Cimalla, Phys. Status Solidi Appl. Res. **185**, 27 (2001).

64. J. Xuan, G. Zhao, M. Sun, F. Jia, X. Wang, T. Zhou, G. Yin, and B. Liu, (2020).

65. G. Korotcenkov, V. Brinzari, J. R. Stetter, I. Blinov, and V. Blaja, Sensors Actuators, B Chem. **128**, 51 (2007).

66. M. Z. Atashbar, B. Gong, H. T. Sun, W. Wlodarski, and R. Lamb, Thin Solid Films **354**, 222 (1999).

67. N. Joshi, L. F. Da Silva, H. Jadhav, J. C. M'Peko, B. B. Millan Torres, K. Aguir, V. R. Mastelaro, and O. N. Oliveira, RSC Adv. **6**, 92655 (2016).

68. A. Bejaoui, J. Guerin, J. A. Zapien, and K. Aguir, Sensors Actuators, B Chem. **190**, 8 (2014).

69. C. Baratto, R. Kumar, G. Faglia, K. Vojisavljević, and B. Malič, Sensors Actuators, B Chem. **209**, 287 (2015).

70. N. Yamazoe and K. Shimanoe, Sensors Actuators, B Chem. **128**, 566 (2008).

71. A. Naydenov, R. Stoyanova, and D. Mehandjiev, J. Mol. Catal. A. Chem. **98**, 9 (1995).

72. G. Korotcenkov, S. D. Han, B. K. Cho, and V. Brinzari, Crit. Rev. Solid State Mater. Sci. **34**, 1 (2009).

73. V. R. Mastelaro, S. C. Zílio, L. F. Da Silva, P. I. Pelissari, M. I. B. Bernardi, J. Guerin, and K. Aguir, Sensors Actuators, B Chem. **181**, 919 (2013).

74. G. Chabanis, I. P. Parkin, and D. E. Williams, Meas. Sci. Technol. **14**, 76 (2003).

75. D. E. Williams and K. F. E. Pratt, Sensors Actuators, B Chem. **70**, 214 (2000).

76. Z. Hua, C. Tian, D. Huang, W. Yuan, C. Zhang, X. Tian, M. Wang, and E. Li, Sensors Actuators B Chem. **267**, 510 (2018).

77. J. Guérin, K. Aguir, and M. Bendahan, Sensors Actuators, B Chem. **119**, 327 (2006).

78. S. M. Sze, *Book Review: Semiconductor Devices — Physics and Technology* (1986).

79. I. Langmuir, J. Am. Chem. Soc. **40**, 1361 (1918).

80. R. Nix, (2021).

81. O. Sahu and N. Singh, *Significance of Bioadsorption Process on Textile Industry Wastewater* (Elsevier Ltd., 2018).

82. L. Gajdosik, Sensors Actuators B Chem. **106**, 691 (2005).

83. M. https://doi. org/10. 1007/97.-1-4615-3656-7_2 Wolkenstein T. (1991) The Various Types of Adsorption. In: Electronic Processes on Semiconductor Surfaces during Chemisorption. Springer, Boston, *No Title* (n.d.).

84. M. Gillet, K. Aguir, M. Bendahan, and P. Mennini, Thin Solid Films **484**, 358 (2005).

85. S. Thirumalairajan, V. R. Mastelaro, and C. A. Escanhoela, ACS Appl. Mater. Interfaces **6**, 21739 (2014).

86. V. Demarne, A. Grisel, R. Sanjinés, D. Rosenfeld, and F. Lévy, Sensors Actuators B. Chem. **7**, 704 (1992).

87. N. Caicedo, R. Leturcq, J. P. Raskin, D. Flandre, and D. Lenoble, Sensors Actuators, B Chem. **297**, 126602 (2019).

88. Z. Liu, T. Yamazaki, Y. Shen, T. Kikuta, and N. Nakatani, Sensors Actuators, B Chem. **128**, 173 (2007).

89. T. Hyodo, N. Nishida, Y. Shimizu, and M. Egashira, Sensors Actuators, B Chem. **83**, 209 (2002).

90. V. Golovanov, M. A. Mäki-Jaskari, T. T. Rantala, G. Korotcenkov, V. Brinzari, A. Cornet, and J. Morante, Sensors Actuators, B Chem. **106**, 563 (2005).

91. M. Ulrich, A. Bunde, and C. D. Kohl, Appl. Phys. Lett. **85**, 242 (2004).

92. N. Bârsan, M. Hübner, and U. Weimar, Sensors Actuators, B Chem. **157**, 510 (2011).

93. N. Bârsan, R. Grigorovici, R. Ionescu, M. Motronea, and A. Vancu, Thin Solid Films **171**, 53 (1989).

94. N. Barsan and U. Weimar, J. Electroceramics **7**, 143 (2001).

95. S. C. Naisbitt, K. F. E. Pratt, D. E. Williams, and I. P. Parkin, Sensors Actuators, B Chem. **114**, 969 (2006).

96. A. Rothschild and Y. Komem, J. Appl. Phys. **95**, 6374 (2004).

97. M. Suchea, N. Katsarakis, S. Christoulakis, S. Nikolopoulou, and G. Kiriakidis, Sensors Actuators, B Chem. **118**, 135 (2006).

98. G. Korotcenkov, V. Macsanov, V. Tolstoy, V. Brinzari, J. Schwank, and G. Fagila, Sensors Actuators, B Chem. **96**, 602 (2003).

99. G. E. de Souza Brito, C. V. Santilli, and S. H. Pulcinelli, Colloids Surfaces A Physicochem. Eng. Asp. **97**, 217 (1995).

100. M. N. Rumyantseva, A. M. Gaskov, N. Rosman, T. Pagnier, and J. R. Morante, Chem. Mater. **17**, 893 (2005).

101. N. F. Uvarov and V. V. Boldyrev, Usp. Khim. **70**, 327 (2001).

102. T. G. G. Maffeïs, G. T. Owen, C. Malagù, G. Martinelli, M. K. Kennedy, F. E. Kruis, and S. P. Wilks, Surf. Sci. **550**, 21 (2004).

103. B. Yu, L. Guo, Z. Yang, C. Zhu, F. Gan, G. Zhang, G. Tang, X. Wu, and W. Chen, Phys. Lett. Sect. A Gen. At. Solid State Phys. **251**, 67 (1999).

104. H. Zhang, Y. Liu, K. Zhu, G. Siu, Y. Xiong, and C. Xiong, J. Phys. Condens. Matter **10**, 11121 (1998).

105. A. Diéguez, A. Romano-Rodríguez, A. Vilà, and J. R. Morante, J. Appl. Phys. **90**, 1550 (2001).

106. A. M. Mazzone and V. Morandi, Sensors Actuators, A Phys. **126**, 56 (2006).

107. E. Lucas, S. Decker, A. Khaleel, A. Seitz, S. Fultz, A. Ponce, W. Li, C. Carnes, and K. J. Klabunde, Chem. - A Eur. J. **7**, 2505 (2001).

108. J. Schalwig, P. Kreisl, S. Ahlers, and G. Müller, IEEE Sens. J. **2**, 394 (2002).

109. U. Betz, M. Kharrazi Olsson, J. Marthy, M. F. Escolá, and F. Atamny, Surf. Coatings Technol. **200**, 5751 (2006).

110. Z. Chen, W. Li, R. Li, Y. Zhang, G. Xu, and H. Cheng, Langmuir **29**, 13836 (2013).

111. A. Barnabé, Y. Thimont, M. Lalanne, L. Presmanes, and P. Tailhades, J. Mater. Chem. C **3**, 6012 (2015).

112. K. H. L. Zhang, K. Xi, M. G. Blamire, and R. G. Egdell, J. Phys. Condens. Matter **28**, 383002 (2016).

113. M. Grundmann, F. Klüpfel, R. Karsthof, P. Schlupp, F.-L. Schein, D. Splith, C. Yang, S. Bitter, and H. von Wenckstern, J. Phys. D. Appl. Phys. **49**, 213001 (2016).

114. J. Afonso, R. Leturcq, P. L. Popa, and D. Lenoble, J. Mater. Sci. Mater. Electron. **30**, 1760 (2019).

115. K. Nomura, T. Kamiya, and H. Hosono, Adv. Mater. **23**, 3431 (2011).

116. K. Nomura, H. Ohta, A. Takagi, T. Kamiya, M. Hirano, and H. Hosono, Nature **432**, 488 (2004).

117. P.-W. Chen, C.-T. Chang, T.-F. Ko, S.-C. Hsu, K.-D. Li, and J.-Y. Wu, Sci. Rep. **10**, 8430 (2020).

118. C. G. Granqvist, Thin Solid Films **564**, 1 (2014).

119. M. Z. Sialvi, R. J. Mortimer, G. D. Wilcox, A. M. Teridi, T. S. Varley, K. G. U. Wijayantha, and C. A. Kirk, ACS Appl. Mater. Interfaces **5**, 5675 (2013).

120. Q. Liu, Q. Chen, Q. Zhang, Y. Xiao, X. Zhong, G. Dong, M.-P. Delplancke-Ogletree, H. Terryn, K. Baert, F. Reniers, and X. Diao, J. Mater. Chem. C **6**, 646 (2018).

121. H. Ohta, M. Orita, M. Hirano, and H. Hosono, J. Appl. Phys. **89**, 5720 (2001).

122. S. Kim, S. jin Kim, K. heon Kim, H. Kim, and T. G. Kim, Phys. Status Solidi **211**, 2569 (2014).

123. C. Battaglia, A. Cuevas, and S. De Wolf, Energy Environ. Sci. **9**, 1552 (2016).

124. F. Menchini, M. L. Grilli, T. Dikonimos, A. Mittiga, L. Serenelli, E. Salza, R. Chierchia, and M. Tucci, Phys. Status Solidi **13**, 1006 (2016).

125. C. Baratto, R. Kumar, G. Faglia, K. Vojisavljević, and B. Malič, Sensors Actuators B Chem. **209**, 287 (2015).

126. B. Tong, Z. Deng, B. Xu, G. Meng, J. Shao, H. Liu, T. Dai, X. Shan, W. Dong, S. Wang, S. Zhou, R. Tao, and X. Fang, ACS Appl. Mater. Interfaces **10**, 34727 (2018).

127. D. Upadhyay, B. Roondhe, A. Pratap, and P. K. Jha, Appl. Surf. Sci. **476**, 198 (2019).

128. T. P. Mokoena, H. C. Swart, and D. E. Motaung, J. Alloys Compd. **805**, 267 (2019).

129. H.-J. Kim and J.-H. Lee, Sensors Actuators B Chem. **192**, 607 (2014).

130. D. Bhattacharya, D. Ghoshal, D. Mondal, B. K. Paul, J. Pal, B. Gupta, N. Bose, P. Nandy, M. Basu, and S. Das, Ceram. Int. (2020).

131. A. Tsukazaki, A. Ohtomo, T. Onuma, M. Ohtani, T. Makino, M. Sumiya, K. Ohtani, S. F. Chichibu, S. Fuke, Y. Segawa, H. Ohno, H. Koinuma, and M. Kawasaki, Nat. Mater. **4**, 42 (2005).

132. J. L. Lyons, A. Janotti, and C. G. Van de Walle, Appl. Phys. Lett. **95**, 252105 (2009).

133. O. Bierwagen and J. S. Speck, Appl. Phys. Lett. **101**, 102107 (2012).

134. X. Chen, L. Zhao, and Q. Niu, J. Electron. Mater. **41**, 3382 (2012).

135. A. Alshahrie, S. Joudakzis, A. A. Al-Ghamdi, L. M. Bronstein, and W. E. Mahmoud, Ceram. Int. **45**, 7984 (2019).

136. H. Sato, T. Minami, S. Takata, and T. Yamada, Thin Solid Films **236**, 27 (1993).

137. J. A. Caraveo-Frescas, P. K. Nayak, H. A. Al-Jawhari, D. B. Granato, U. Schwingenschlögl, and H. N. Alshareef, ACS Nano **7**, 5160 (2013).

138. Y. Ogo, H. Hiramatsu, K. Nomura, H. Yanagi, T. Kamiya, M. Hirano, and H. Hosono, Appl. Phys. Lett. **93**, 032113 (2008).

139. E. Fortunato, R. Barros, P. Barquinha, V. Figueiredo, S.-H. K. Park, C.-S. Hwang, and R. Martins, Appl. Phys. Lett. **97**, 052105 (2010).

140. E. Chikoidze, A. Fellous, A. Perez-Tomas, G. Sauthier, T. Tchelidze, C. Ton-That, T. T. Huynh, M. Phillips, S. Russell, M. Jennings, B. Berini, F. Jomard, and Y. Dumont, Mater. Today Phys. **3**, 118 (2017).

141. N. Ueda, H. Hosono, R. Waseda, and H. Kawazoe, Appl. Phys. Lett. **70**, 3561 (1997).

142. M. Orita, H. Hiramatsu, H. Ohta, M. Hirano, and H. Hosono, Thin Solid Films **411**, 134 (2002).

143. J. Asbalter and A. Subrahmanyam, J. Vac. Sci. Technol. A Vacuum, Surfaces, Film. **18**, 1672 (2000).

144. K. Ueda, S. Inoue, S. Hirose, H. Kawazoe, and H. Hosono, Appl. Phys. Lett. **77**, 2701 (2000).

145. H. Hiramatsu, K. Ueda, H. Ohta, M. Hirano, T. Kamiya, and H. Hosono, Appl. Phys. Lett. **82**, 1048 (2003).

146. K. Ueda, S. Inoue, H. Hosono, N. Sarukura, and M. Hirano, Appl. Phys. Lett. **78**, 2333 (2001).

147. H. Hiramatsu, K. Ueda, H. Ohta, M. Hirano, M. Kikuchi, H. Yanagi, T. Kamiya, and H. Hosono, Appl. Phys. Lett. **91**, 012104 (2007).

148. C. . Windisch, G. . Exarhos, K. . Ferris, M. . Engelhard, and D. . Stewart, Thin Solid Films **398–399**, 45 (2001).

149. K. Dileep, B. Loukya, P. Silwal, A. Gupta, and R. Datta, J. Phys. D. Appl. Phys. **47**, 405001 (2014).

150. M. Dekkers, G. Rijnders, and D. H. A. Blank, Appl. Phys. Lett. **90**, 021903 (2007).

151. H. J. Kim, I. C. Song, J. H. Sim, H. Kim, D. Kim, Y. E. Ihm, and W. K. Choo, J. Appl. Phys. **95**, 7387 (2004).

152. H. Mizoguchi, M. Hirano, S. Fujitsu, T. Takeuchi, K. Ueda, and H. Hosono, Appl. Phys. Lett. **80**, 1207 (2002).

153. N. Mansourian-Hadavi, S. Wansom, N. H. Perry, A. R. Nagaraja, T. O. Mason, L. H. Ye, and A. J. Freeman, Phys. Rev. B - Condens. Matter Mater. Phys. **81**, 1 (2010).

154. T. Kim, B. Yoo, Y. Youn, M. Lee, A. Song, K.-B. Chung, S. Han, and J. K. Jeong, ACS Appl. Mater. Interfaces **11**, 40214 (2019).

155. A. Bhatia, G. Hautier, T. Nilgianskul, A. Miglio, J. Sun, H. J. Kim, K. H. Kim, S. Chen, G.-M. Rignanese, X. Gonze, and J. Suntivich, Chem. Mater. **28**, 30 (2016).

156. E. Bobeico, F. Varsano, C. Minarini, and F. Roca, Thin Solid Films **444**, 70 (2003).

157. A. Kudo, H. Yanagi, H. Hosono, and H. Kawazoe, Appl. Phys. Lett. **73**, 220 (1998).

158. H. Kawazoe, H. Yanagi, K. Ueda, and H. Hosono, MRS Bull. **25**, 28 (2000).

159. K. H. L. Zhang, Y. Du, A. Papadogianni, O. Bierwagen, S. Sallis, L. F. J. Piper, M. E. Bowden, V. Shutthanandan, P. V. Sushko, and S. A. Chambers, Adv. Mater. **27**, 5191 (2015).

160. E. Arca, K. Fleischer, and I. V. Shvets, Appl. Phys. Lett. **99**, 2011 (2011).

161. E. Norton, L. Farrell, S. D. Callaghan, C. McGuinness, I. V. Shvets, and K. Fleischer, Phys. Rev. B **93**, 115302 (2016).

162. A. N. Banerjee and K. K. Chattopadhyay, Prog. Cryst. Growth Charact. Mater. **50**, 52 (2005).

163. G. Hautier, A. Miglio, G. Ceder, G.-M. Rignanese, and X. Gonze, Nat. Commun. **4**, 2292 (2013).

164. J. E. Sansonetti and W. C. Martin, J. Phys. Chem. Ref. Data **34**, 1559 (2005).

165. H. Raebiger, S. Lany, and A. Zunger, Phys. Rev. B **76**, 045209 (2007).

166. Z. Wang, P. K. Nayak, J. A. Caraveo-Frescas, and H. N. Alshareef, Adv. Mater. **28**, 3831 (2016).

167. A. Zunger, Appl. Phys. Lett. **83**, 57 (2003).

168. H. Kawazoe, M. Yasukawa, H. Hyodo, M. Kurita, H. Yanagi, and H. Hosono, Nature **389**, 939 (1997).

169. H. Kawazoe, M. Yasukawa, H. Hyodo, M. Kurita, H. Yanagi, and H. Hosono, Nature **389**, 939 (1997).

170. K. Koumoto, H. Koduka, and W. S. Seo, J. Mater. Chem. **11**, 251 (2001).

171. A. P. Mackenzie, Reports Prog. Phys. **80**, 032501 (2017).

172. D. S. Ginley, H. Hosono, and D. C. Paine, *Handbook of Transparent Conductors* (Springer US, Boston, MA, 2011).

173. R. S. Ajimsha, K. A. Vanaja, M. K. Jayaraj, P. Misra, V. K. Dixit, and L. M. Kukreja, Thin Solid Films **515**, 7352 (2007).

174. J. Tate, M. K. Jayaraj, A. D. Draeseke, T. Ulbrich, A. W. Sleight, K. A. Vanaja, R. Nagarajan, J. F. Wager, and R. L. Hoffman, Thin Solid Films **411**, 119 (2002).

175. D. Xiong, H. Wang, W. Zhang, X. Zeng, H. Chang, X. Zhao, W. Chen, and Y. B. Cheng, J. Alloys Compd. **642**, 104 (2015).

176. P. Lunca-Popa, J. Botsoa, M. Bahri, J. Crêpellière, P. Desgardin, J. N. Audinot, T. Wirtz, D. Arl, O. Ersen, M. F. Barthe, and D. Lenoble, Sci. Rep. **10**, 1 (2020).

177. B. J. Ingram, G. B. González, T. O. Mason, D. Y. Shahriari, A. Barnabè, D. Ko, and K. R. Poeppelmeier, Chem. Mater. **16**, 5616 (2004).

178. H. Yanagi, S. I. Inoue, K. Ueda, H. Kawazoe, H. Hosono, and N. Hamada, J. Appl. Phys. **88**, 4159 (2000).

179. C. Ruttanapun, J. Appl. Phys. **114**, (2013).

180. D. O. Scanlon, A. Walsh, and G. W. Watson, Chem. Mater. **21**, 4568 (2009).

181. M. Snure and A. Tiwari, Appl. Phys. Lett. **91**, 3 (2007).

182. K. Ueda, T. Hase, H. Yanagi, H. Kawazoe, H. Hosono, H. Ohta, M. Orita, and M. Hirano, J. Appl. Phys. **89**, 1790 (2001).

183. R. Srinivasan, B. Chavillon, C. Doussier-Brochard, L. Cario, M. Paris, E. Gautron, P. Deniard, F. Odobel, and S. Jobic, J. Mater. Chem. **18**, 5647 (2008).

184. H. Yanagi, T. Hase, S. Ibuki, K. Ueda, and H. Hosono, Appl. Phys. Lett. **78**, 1583 (2001).

185. L. Liu, K. Bai, H. Gong, and P. Wu, Phys. Rev. B **72**, 125204 (2005).

186. M. Sasaki and M. Shimode, J. Phys. Chem. Solids **64**, 1675 (2003).

187. M. Singh, V. N. Singh, and B. R. Mehta, J. Nanosci. Nanotechnol. **8**, 3889 (2008).

188. R. Nagarajan, A. D. Draeseke, A. W. Sleight, and J. Tate, J. Appl. Phys. **89**, 8022 (2001).

189. T. Arnold, D. J. Payne, A. Bourlange, J. P. Hu, R. G. Egdell, L. F. J. Piper, L. Colakerol, A. De Masi, P.-A. Glans, T. Learmonth, K. E. Smith, J. Guo, D. O. Scanlon, A. Walsh, B. J. Morgan, and G. W. Watson, Phys. Rev. B **79**, 075102 (2009).

190. N. Duan, A. W. Sleight, M. K. Jayaraj, and J. Tate, Appl. Phys. Lett. **77**, 1325 (2000).

191. B. J. Ingram, B. J. Harder, N. W. Hrabe, T. O. Mason, and K. R. Poeppelmeier, Chem. Mater. **16**, 5623 (2004).

192. Y. Kakehi, K. Satoh, T. Yotsuya, K. Masuko, T. Yoshimura, A. Ashida, and N. Fujimura, J. Cryst. Growth **311**, 1117 (2009).

193. R. Nagarajan, N. Duan, M. K. Jayaraj, J. Li, K. A. Vanaja, A. Yokochi, A. Draeseke, J. Tate, and A. W. Sleight, Int. J. Inorg. Mater. **3**, 265 (2001).

194. R. Manoj, M. Nisha, K. A. Vanaja, and M. K. Jayaraj, Bull. Mater. Sci. **31**, 49 (2008).

195. M. K. Jayaraj, A. D. Draeseke, J. Tate, and A. W. Sleight, Thin Solid Films **397**, 244 (2001).

196. Y. Ono, K. Satoh, T. Nozaki, and T. Kajitani, Jpn. J. Appl. Phys. **46**, 1071 (2007).

197. S. Saadi, A. Bouguelia, and M. Trari, Sol. Energy **80**, 272 (2006).

198. Q.-L. Liu, Z.-Y. Zhao, R.-D. Zhao, and J.-H. Yi, J. Alloys Compd. **819**, 153032 (2020).

199. Y. Ma, X. Zhou, Q. Ma, A. Litke, P. Liu, Y. Zhang, C. Li, and E. J. M. Hensen, Catal. Letters **144**, 1487 (2014).

200. R. S. Yu and C. M. Wu, Appl. Surf. Sci. **282**, 92 (2013).

201. T. Okuda, Y. Beppu, Y. Fujii, T. Kishimoto, K. Uto, T. Onoe, N. Jufuku, S. Hidaka, N. Terada, and S. Miyasaka, J. Phys. Conf. Ser. **150**, 0 (2009).

202. T. Okuda, N. Jufuku, S. Hidaka, and N. Terada, Phys. Rev. B - Condens. Matter Mater. Phys. **72**, 4 (2005).

203. M. Amami, C. V. Colin, P. Strobel, and A. Ben Salah, Phys. B Condens. Matter **406**, 2182 (2011).

204. A. Maignan, C. Martin, R. Frésard, V. Eyert, E. Guilmeau, S. Hébert, M. Poienar, and D. Pelloquin, Solid State Commun. **149**, 962 (2009).

205. F. Lin, C. Gao, X. Zhou, W. Shi, and A. Liu, J. Alloys Compd. **581**, 502 (2013).

206. J. Y. Yang, X. D. Shen, V. Pomjakushin, L. Keller, E. Pomjakushina, Y. W. Long, M. Kenzelmann, A. T. Apostolov, I. N. Apostolova, J. M. Wesselinowa, P. Pokhriyal, A. Bhakar, P. Rajput, M. N. Singh, P. Sagdeo, T. Kim, M. An, and S. Jeon, AIP Adv. **101**, 0 (2020).

207. T. W. Chiu, B. S. Yu, Y. R. Wang, K. Te Chen, and Y. Te Lin, J. Alloys Compd. **509**, 2933 (2011).

208. Z. Y. Liu, G. Y. Wang, X. P. Liu, and Y. J. Wang, Ranliao Huaxue Xuebao/Journal Fuel Chem. Technol. **41**, 1473 (2013).

209. C. Taddee, T. Kamwanna, and V. Amornkitbamrung, Appl. Surf. Sci. **380**, 237 (2016).

210. K. Hayashi, K. Sato, T. Nozaki, and T. Kajitani, Jpn. J. Appl. Phys. **47**, 59 (2008).

211. N. Barot, P. K. Mehta, A. Rao, R. Thomas, and Y. K. Kuo, J. Alloys Compd. **791**, 134 (2019).

212. P. Lunca Popa, J. Crêpellière, R. Leturcq, and D. Lenoble, Thin Solid Films **612**, 194 (2016).

213. D. O. Scanlon, A. Walsh, B. J. Morgan, G. W. Watson, D. J. Payne, and R. G. Egdell, Phys. Rev. B - Condens. Matter Mater. Phys. **79**, 1 (2009).

214. D. O. Scanlon, K. G. Godinho, B. J. Morgan, and G. W. Watson, J. Chem. Phys. **132**, (2010).

215. D. O. Scanlon and G. W. Watson, J. Mater. Chem. 3655 (2011).

216. T. Yokobori, M. Okawa, K. Konishi, R. Takei, K. Katayama, S. Oozono, T. Shinmura, T. Okuda, H. Wadati, E. Sakai, K. Ono, H. Kumigashira, M. Oshima, T. Sugiyama, E. Ikenaga, N. Hamada, and T. Saitoh, Phys. Rev. B - Condens. Matter Mater. Phys. **87**, 1 (2013).

217. D. O. Scanlon and G. W. Watson, J. Mater. Chem. **21**, 3655 (2011).

218. M. Han, K. Jiang, J. Zhang, W. Yu, Y. Li, Z. Hu, and J. Chu, J. Mater. Chem. **22**, 18463 (2012).

219. W. Ketir, S. Saadi, and M. Trari, J. Solid State Electrochem. **16**, 213 (2012).

220. O. Crottaz and F. Kubel, **47**, 2646 (1996).

221. O. Crottaz and F. Kubel, Z. Krist. **10**, 1996 (1996).

222. O. Aktas, K. D. Truong, T. Otani, G. Balakrishnan, M. J. Clouter, T. Kimura, and G. Quirion, J. Phys. Condens. Matter **24**, (2012).

223. S. Wu, Z. Deng, W. Dong, J. Shao, and X. Fang, Thin Solid Films **595**, 124 (2015).

224. J. Y. Yang, X. D. Shen, V. Pomjakushin, L. Keller, E. Pomjakushina, Y. W. Long, M. Kenzelmann, A. T. Apostolov, I. N. Apostolova, J. M. Wesselinowa, P. Pokhriyal, A. Bhakar, P. Rajput, M. N. Singh, P. Sagdeo, T. Kim, M. An, and S. Jeon, AIP Adv. **101**, 0 (2020).

225. T. Arnold, D. J. Payne, A. Bourlange, J. P. Hu, R. G. Egdell, L. F. J. Piper, L. Colakerol, A. De Masi, P.-A. Glans, T. Learmonth, K. E. Smith, J. Guo, D. O. Scanlon, A. Walsh, B. J. Morgan, and G. W. Watson, Phys. Rev. B **79**, 075102 (2009).

226. R. S. Yu and C. M. Wu, Appl. Surf. Sci. **282**, 92 (2013).

227. L. Farrell, E. Norton, C. M. Smith, D. Caffrey, I. V. Shvets, and K. Fleischer, J. Mater. Chem. C **4**, 126 (2015).

228. L. Farrell, E. Norton, B. J. O'dowd, D. Caffrey, I. V. Shvets, and K. Fleischer, Appl. Phys. Lett. **107**, 1 (2015).

229. D. O. Scanlon and G. W. Watson, J. Mater. Chem. **21**, 3655 (2011).

230. J. Tate, H. L. Ju, J. C. Moon, A. Zakutayev, A. P. Richard, J. Russell, and D. H. McIntyre, Phys. Rev. B - Condens. Matter Mater. Phys. **80**, 1 (2009).

231. M. Poienar, V. Hardy, B. Kundys, K. Singh, A. Maignan, F. Damay, and C. Martin, J. Solid State Chem. **185**, 56 (2012).

232. G. Dong, M. Zhang, X. Zhao, H. Yan, C. Tian, and Y. Ren, Appl. Surf. Sci. **256**, 4121 (2010).

233. M. A. Marquardt, N. A. Ashmore, and D. P. Cann, Thin Solid Films **496**, 146 (2006).

234. J. Crêpellière, P. L. Popa, N. Bahlawane, R. Leturcq, F. Werner, S. Siebentritt, and D. Lenoble, J. Mater. Chem. C **4**, 4278 (2016).

235. W. Ketir, S. Saadi, and M. Trari, J. Solid State Electrochem. **16**, 213 (2012).

236. B. J. Ingram, G. B. González, T. O. Mason, D. Y. Shahriari, A. Barnabè, D. Ko, and K. R. Poeppelmeier, Chem. Mater. **16**, 5616 (2004).

237. L. Farrell, K. Fleischer, D. Caffrey, D. Mullarkey, E. Norton, and I. V. Shvets, Phys. Rev. B - Condens. Matter Mater. Phys. **91**, 1 (2015).

238. I. Sinnarasa, Y. Thimont, L. Presmanes, A. Barnabé, and P. Tailhades, Nanomaterials **7**, (2017).

239. R. Bywalez, S. Götzendörfer, and P. Löbmann, J. Mater. Chem. **20**, 6562 (2010).

240. J. Crêpellière, Metalorganic Chemical Vapour Deposition of P-Type Delafossite CuCrO2 Semiconductor Thin Films: Characterization and Application to Transparent p-n Junction, University of Luxembourg, 2016.

241. J. and T. K. Yamashita, J. Phys. Chem. Solids 34 (1958).

242. A. J. Bosman and H. J. Van Daal, **8732**, (2017).

243. J. Nell, B. J. Wood, S. E. Dorris, and T. O. Mason, J. Solid State Chem. **82**, 247 (1989).

244. B. J. Ingram, G. B. González, T. O. Mason, D. Y. Shahriari, A. Barnabè, D. Ko, and K. R. Poeppelmeier, Chem. Mater. **16**, 5616 (2004).

245. B. J. Ingram, T. O. Mason, R. Asahi, K. T. Park, and A. J. Freeman, Phys. Rev. B - Condens. Matter Mater. Phys. **64**, 1551141 (2001).

246. S. N. F. Mott and E. A. Davis, *Electronic Processes in Non-Crystalline Materials* (1979).

247. T. S. Tripathi and M. Karppinen, Adv. Electron. Mater. **3**, 1 (2017).

248. M. J. Han, Z. H. Duan, J. Z. Zhang, S. Zhang, Y. W. Li, Z. G. Hu, and J. H. Chu, J. Appl. Phys. **114**, 0 (2013).

249. T. S. Tripathi and M. Karppinen, Phys. Procedia **75**, 488 (2015).

250. S. Mahapatra and S. A. Shivashankar, Chem. Vap. Depos. **9**, 238 (2003).

251. P. W. Sadik, M. Ivill, V. Craciun, and D. P. Norton, Thin Solid Films **517**, 3211 (2009).

252. D. Li, X. Fang, A. Zhao, Z. Deng, W. Dong, and R. Tao, Vacuum **84**, 851 (2010).

253. J. Wang, T. B. Daunis, L. Cheng, B. Zhang, J. Kim, and J. W. P. Hsu, ACS Appl. Mater. Interfaces **10**, 3732 (2018).

254. J. Wang, P. Zheng, D. Li, Z. Deng, W. Dong, R. Tao, and X. Fang, J. Alloys Compd. **509**, 5715 (2011).

255. J. Cui, H. Cao, W. Zhou, L. Chen, X. Zhai, L. Yu, T. Zheng, and P. Yang, Mater. Lett. **163**, 28 (2016).

256. A. C. Rastogi, S. H. Lim, and S. B. Desu, J. Appl. Phys. **104**, (2008).

257. S. H. Lim, S. Desu, and A. C. Rastogi, J. Phys. Chem. Solids **69**, 2047 (2008).

258. R. S. Yu and C. M. Wu, Appl. Surf. Sci. **282**, 92 (2013).

259. S. Wu, Z. Deng, W. Dong, J. Shao, and X. Fang, Thin Solid Films **595**, 124 (2015).

260. T. S. Tripathi and M. Karppinen, Phys. Procedia **75**, 488 (2016).

261. S. Götzendörfer, C. Polenzky, S. Ulrich, and P. Löbmann, Thin Solid Films **518**, 1153 (2009).

262. H. S. and M. A. P. Y. and F. S. and A. Billard, J. Phys. D. Appl. Phys. **49**, 185105 (2016).

263. J. Crêpellière, P. Lunca Popa, N. Bahlawane, R. Leturcq, F. Werner, S. Siebentritt, and L. D., J. Mater. Chem. 31 (2016).

264. H. Y. Chen, J. T. Wu, and C. Huang, Thin Solid Films **605**, 180 (2016).

265. M. Han, J. Wang, Q. Deng, J. Wang, W. Li, P. Zhang, C. Li, and Z. Hu, J. Alloys Compd. **647**, 1028 (2015).

266. E. Chikoidze, M. Boshta, M. Gomaa, T. Tchelidze, D. Daraselia, D. Japaridze, A. Shengelaya, Y. Dumont, and M. Neumann-Spallart, J. Phys. D. Appl. Phys. **49**, (2016).

267. W. Liu, J. Phys. Conf. Ser. **1637**, 012062 (2020).

268. D. O. Scanlon and G. W. Watson, J. Phys. Chem. Lett. **1**, 3195 (2010).

269. P. Lunca Popa, J. Crêpellière, P. Nukala, R. Leturcq, and D. Lenoble, Appl. Mater. Today **9**, 184 (2017).

270. M. Ahmadi, M. Asemi, and M. Ghanaatshoar, Appl. Phys. Lett. **113**, (2018).

271. D. Li, X. Fang, Z. Deng, W. Dong, R. Tao, S. Zhou, J. Wang, T. Wang, Y. Zhao, and X. Zhu, J. Alloys Compd. **486**, 462 (2009).

272. H. Sun, M. A. P. Yazdi, S. C. Chen, C. K. Wen, F. Sanchette, and A. Billard, J. Mater. Sci. **52**, 11537 (2017).

273. H. Katayama-Yoshida, T. Koyanagi, H. Funashima, H. Harima, and A. Yanase, Solid State Commun. **126**, 135 (2003).

274. R. Nagarajan, N. Duan, M. K. Jayaraj, J. Li, K. A. Vanaja, A. Yokochi, A. Draeseke, J. Tate, and A. W. Sleight, Int. J. Inorg. Mater. **3**, 265 (2001).

275. H. Jiang and D. A. Stewart, ACS Appl. Mater. Interfaces **9**, 16296 (2017).

276. K. Hayashi, K. Sato, T. Nozaki, and T. Kajitani, Jpn. J. Appl. Phys. **47**, 59 (2008).

277. E. C. and M. B. and M. G. and T. T. and D. D. and D. J. and A. S. and Y. D. and M. Neumann-Spallart, J. Phys. D. Appl. Phys. **49**, 205107 (2016).

278. A. Barnabe, Y. Thimont, M. Lalanne, L. Presmanes, and P. Tailhades, J. Mater. Chem. C **3**, 6012 (2015).

279. A. Barnabé, Y. Thimont, M. Lalanne, L. Presmanes, and P. Tailhades, J. Mater. Chem. C **3**, 6012 (2015).

280. Z. Deng, X. Fang, D. Li, R. Tao, W. Dong, T. Wang, S. Zhou, G. Meng, and X. Zhu, Proc. SPIE **7381**, 73812Z (2009).

281. Z. Deng, X. Fang, D. Li, S. Zhou, R. Tao, W. Dong, T. Wang, G. Meng, and X. Zhu, J. Alloys Compd. **484**, 619 (2009).

282. X. Pang, M. D. Shaw, A. C. Lewis, L. J. Carpenter, and T. Batchellier, Sensors Actuators B. Chem. **240**, 829 (2017).

283. P. Lunca Popa, J. Crêpellière, R. Leturcq, and D. Lenoble, Thin Solid Films **612**, 194 (2016).

284. J. Crepelliere, (2016).

285. P. Lunca Popa, J. Crêpellière, P. Nukala, R. Leturcq, and D. Lenoble, Appl. Mater. Today **9**, 184 (2017).

286. H. Bluhm, Situ Charact. Thin Film Growth 75 (2011).

287. (n.d.).

288. M. C. Biesinger, C. Brown, J. R. Mycroft, R. D. Davidson, and N. S. McIntyre, Surf. Interface Anal. **36**, 1550 (2004).

289. N. M. Stark, D. J. Yelle, and U. P. Agarwal, Lignin Polym. Compos. 49 (2016).

290. D. R. Baer and S. Thevuthasan, Handb. Depos. Technol. Film. Coatings 749 (2010).

291. L. Pielsticker, R. Nicholls, S. Beeg, C. Hartwig, G. Klihm, R. Schlögl, S. Tougaard, and M. Greiner, Surf. Interface Anal. **53**, 605 (2021).

292. R. R. Mather, Surf. Modif. Text. 296 (2009).

293. Y. Gassenbauer, R. Schafranek, A. Klein, S. Zafeiratos, M. Hävecker, A. Knop-Gericke, and R. Schlögl, Solid State Ionics **177**, 3123 (2006).

294. M. Salmeron and R. Schlögl, Surf. Sci. Rep. **63**, 169 (2008).

295. R. Schlaf and B. Parkinson, J. Phys. Chem. B - J PHYS CHEM B **103**, (1999).

296. S. Zhou, X. Fang, Z. Deng, D. Li, W. Dong, R. Tao, G. Meng, T. Wang, and X. Zhu, J. Cryst. Growth **310**, 5375 (2008).

297. C. Hartwig, K. Schweinar, T. E. Jones, S. Beeg, F. P. Schmidt, R. Schlögl, and M. Greiner, J. Chem. Phys. **154**, (2021).

298. W. T. Lim, P. W. Sadik, D. P. Norton, S. J. Pearton, and F. Ren, Appl. Surf. Sci. **254**, 2359 (2008).

299. W. T. Lim, P. W. Sadik, D. P. Norton, S. J. Pearton, Y. L. Wang, and F. Ren, Electrochem. Solid-State Lett. **10**, 178 (2007).

300. V. Rogé, N. Bahlawane, G. Lamblin, I. Fechete, F. Garin, A. Dinia, and D. Lenoble, J. Mater. Chem. A **3**, 11453 (2015).

301. P. Lunca-popa, J. Botsoa, M. Bahri, J. Crêpellière, P. Desgardin, J. Audinot, T. Wirtz, D. Arl, O. Ersen, and M. Barthe, 2 (n.d.).

302. P. Lunca-Popa, J. Botsoa, M. Bahri, J. Crêpellière, P. Desgardin, J. N. Audinot, T. Wirtz, D. Arl, O. Ersen, M. F. Barthe, and D. Lenoble, Sci. Rep. **10**, 1 (2020).

303. A. A. Istratov, C. Flink, H. Hieslmair, S. A. McHugo, and E. R. Weber, Mater. Sci. Eng. B Solid-State Mater. Adv. Technol. **72**, 99 (2000).

304. Y. G. CELEBI, August, 1998, Texas Tech University, 1998.

305. Zeitschrift Für Krist. - Cryst. Mater. **211**, 482 (1996).

306. W. Dannhauser and P. A. Vaughan, J. Am. Chem. Soc. **77**, 896 (1955).

307. A. Garg, A. Mishra, K. Pandey, and S. Sharma, J. Appl. Phys. **116**, (2014).

308. O. Aktas, K. D. Truong, T. Otani, G. Balakrishnan, M. J. Clouter, T. Kimura, and G. Quirion, J. Phys. Condens. Matter **24**, 1 (2012).

309. P. H. Fang and W. S. Brower, Phys. Rev. **129**, 1561 (1963).

310. M. F. Coelho, M. A. Rivas, G. Vilão, E. M. Nogueira, and T. P. Iglesias, J. Chem. Thermodyn. **132**, 164 (2019).

311. M. G. Sung, K. Y. Lim, H. J. Cho, S. R. Lee, S. A. Jang, Y. S. Kim, M. S. Joo, J. H. Lee, T. Y. Kim, H. S. Yang, S. H. Pyi, and J. W. Kim, Japanese J. Appl. Physics, Part 1 Regul. Pap. Short Notes Rev. Pap. **46**, 2134 (2007).

312. K. Elers, *Copper Diffusion Barrier Deposition on Integrated Circuit Devices by Atomic Layer Deposition Technique* (2008).

313. H. Liu, J. Xie, P. Liu, and B. Dai, Catalysts **6**, 1 (2016).

314. B. Jee, P. St. Petkov, G. N. Vayssilov, T. Heine, M. Hartmann, and A. Pöppl, J. Phys. Chem. C **117**, 8231 (2013).

315. (n.d.).

316. (n.d.).

317. R. P. Gupta and S. K. Sen, Phys. Rev. B **12**, 15 (1975).

318. J. Christopher and C. S. Swamy, J. Mater. Sci. **27**, 1353 (1992).

319. L. Liu, T. Li, Z. Yi, F. Chi, Z. Lin, X. Zhang, and K. Xu, Sensors Actuators, B Chem. **297**, 126815 (2019).

320. M. Lampimäki, V. Zelenay, A. Křepelová, Z. Liu, R. Chang, H. Bluhm, and M. Ammann, ChemPhysChem **14**, 2419 (2013).

10. Publication List

P. Lunca Popa, **J. Afonso,** P. Grysan, J. Crêpellière, R. Leturcq and D. Lenoble, Tuning the electrical properties of the p-type transparent conducting oxide Cu1−xCr1+xO2 by controlled annealing, Scientific Reports volume 8, Article number: 7216 (2018)

J. Afonso, P. Lunca Popa, R. Leturcq and D. Lenoble, Transparent p-Cu0.66Cr1.33O2/n-ZnO heterojunction prepared in a five-step scalable process, Journal of Materials Science: Materials in Electronics volume 30, pages 1760–1766 (2019)

M. Moreira*, **J. Afonso***, J. Crêpellière, D. Lenoble and P. Lunca Popa, A review on the p-type transparent CuCrO2 delafossite, in submission process

João R. Afonso*, Petru Lunca-Popa, Damien Lenoble, Jean-Pierre Raskin and Mark Greiner, Thin film $Cu_{0.66}Cr_{1.33}O_2$ property engineering for ozone sensing devices, in preparation

Patents

J. Afonso, D. Lenoble, OZONE SENSOR WITH OFF-STOCHEOMETRIC DELAFOSSITE-TYPE COPPER OXIDE, Filled on 19/05/2021

Oral presentation

Defect engineering in off-stoichiometric copper chromium oxide for emerging transparent devices, **J. Afonso**, P. Grysan, J. Crêpellière, P. Lunca-Popa, R. Leturcq, D. Lenoble, EMRS 2019 Fall meeting, Warsaw, Poland

Transparent p-$Cu_{0.66}Cr_{1.33}O_2$/n-ZnO heterojunction prepared in a five-step scalable process, J. Afonso, P. Lunca Popa, R. Leturcq, D. Lenoble, Nano S&T-2018, Potsdam, Germany

Journal of Materials Science: Materials in Electronics (2019) 30:1760–1766
https://doi.org/10.1007/s10854-018-0448-4

Transparent p-$Cu_{0.66}Cr_{1.33}O_2$/n-ZnO heterojunction prepared in a five-step scalable process

João Afonso[1] · Renaud Leturcq[1] · Petru Lunca Popa[1] · Damien Lenoble[1]

Received: 13 August 2018 / Accepted: 24 November 2018 / Published online: 28 November 2018

Abstract
Transparent and electrical conducting p-type off-stoichiometric copper–chromium oxide thin films were used to build p-$Cu_{0.66}Cr_{1.33}O_2$/n-ZnO heterojunctions. The junctions were fabricated in a novel and simple five step process including metal organic chemical vapour deposition, atomic layer deposition, chemical wet etching, and optical lithography. One last step of thermal annealing, with varying temperatures of 650 and 700 °C, is added in order to tune the electrical properties of delafossite and consequently the electrical features of p–n junctions. This work was developed to address the lack of transparent and industrially scalable rectifying p–n junctions that can open multiple application paths in transparent electronics. A competitive ideality factor η of 6.6 and a transmittance in the visible range of 50% were achieved. An understanding of the electronic response of junctions is presented herein as well as a deepening comprehension of the physical properties of materials, with the bands alignment and the Fermi level tuning.

1 Introduction

In the recent years, wide bandgap semiconductors have been investigated in order to build a transparent p–n junction. Challenges still exist in creating a heterojunction that combines a relevant bands alignment with a satisfying rectifying behaviour while remaining optically transparent over the visible wavelength range [1]. Simple transparent p–n junctions can derive into photodetectors and photovoltaic cells and can open paths to more complex device as transparent transistors [2]. From this perspective, transparent conductive oxides (TCOs) are a special kind of materials that combine high electrical conductivity, interesting carrier mobility and large optical bandgap [3, 4]. Homo-junctions were explored in the past, mainly focused on the zinc oxide [2]. Despite that its p-type conductivity was reported (under non-equilibrium conditions) [5], the problem of dopants asymmetry inducing furthermore the lack of reliability of the p-type layer impedes an adequate utilization of ZnO homo-junctions. The best electrical performances, combining high I_{ON}/I_{OFF} ratio and ideality factor closer to 1 were reported by Grundmann et al. [2] for NiO/ZnO ($I_{ON}/I_{OFF} = 2\times10^{10}$ at ±2 V and an ideality factor $\eta = 1.9$) and for CuI/ZnO ($I_{ON}/I_{OFF} = 6\times10^{6}$ at ±2 V and an ideality factor $\eta = 2.1$). The ratio between the diode forward current and the off-state current, measured at a given ± V, is a standard measurement of the quality of the diode, by the distinction of a clear ON and OFF state. The ideality factor is a factor that relates how close the diode behaves compared with the ideal equation, which is a factor related to the carriers recombination, where 1, represents normally a diode limited by the minority carriers. However the measured transmittance was under 50% for both cases, a value not well fitted for transparency. Moreover, the fabrication method was pulsed laser deposition (PLD), a high-cost technique with important limitations in terms of industrial uses, since it is nearly impossible to prepare uniform thin films on a large scale area [6].

Among n-type TCOs, indium tin oxide (ITO) is already widely used in flat panel displays, touch screens or light emitting diodes. Nonetheless the high cost of indium and its toxicity reclaim alternative solutions and at the moment the most promising one seems to be the zinc oxide (ZnO), a direct bandgap semiconductor with suitable electrical and optical properties (Eg = 3.4 eV [7], transmittance above 80% in the visible region [8–10]), high chemical resistance and low fabrication cost compared with ITO. ZnO, in its undoped or doped forms (Al:ZnO or Ga:ZnO) starts already to find their way into applications [11–14].

✉ João Afonso
joao.afonso@list.lu

[1] Materials Research and Technology Department (MRT), Luxembourg Institute of Science and Technology (LIST), 41 rue de Brill, 4422 Belvaux, Luxembourg

Whilst the problem of finding an adequate n-type semiconductor seems to be solvable/solved, the search for a matching p-type semiconductor is still ongoing. The challenge in achieving a capable p-type TCO rise from the intrinsic electronic structure of metal oxides with the top of the valence band composed by strongly localized oxygen 2*p* orbitals. This results furthermore in difficulties in introducing shallow acceptors and consequently high effective masses of carriers [13]. In 1997, Kawazoe et al. [14], suggested a new method for the modulation of the valence band for AMO_2 (with A = Cu or Ag and M = Al, Sc, Cr, Fe, Ga, or Y) [15] with the delafossite structure. This modulation is explained by the covalent bonding between Cu $3d^{10}$ and O $2p^6$ (with close energy levels), resulting in a dispersion of the top valence band that furthermore ameliorates holes delocalisation. This model explains thus the higher holes mobility (above 1 $cm^2\ V^{-1}\ s^{-1}$) achieved in this type of materials when comparing with other TCOs [18]. Among copper delafossites, $CuCrO_2$ presents a high density of states of 3*d* cations (Cr^{3+}) near the valence band maximum allowing thus the covalent mixing between the chromium and oxygen atoms and a good dopability [17]. The interest in these particular materials has grown since Nagarajan et al. [19] reported the highest conductivity (220 S cm^{-1}) of delafossite compounds for Mg doped $CuCrO_2$ whilst they measured an optical transparency of 30% in the case of 270 nm thin films. There are usually two ways of doping $CuCrO_2$ thin films, intrinsic doping which is attributed to copper vacancies and oxygen interstitials, and extrinsic doping of which Mg is the most common, but also Fe, N or Zn can be considered [13]. Recent papers report the fabrication of a new peculiar phase of copper chromium delafossite characterized by an important deficit of copper. High electric conductivities and adequate transparency in visible range [16] were measured for such thin films, deposited using chemical vapour deposition.

With the controlled tunability of carrier concentration and good increase of optical transmittance over the annealing processes [17] this particular material might became a viable option for the introduction and study of a transparent p–n junction [18]. As-deposited films present high carrier concentration, up to 10^{22} cm^{-3}, attributed to chains of missing copper [19]. Although of great interest for p-type TCO applications, these high values are unsuitable for building reliable p–n junctions. Fortunately, the metastable nature of these peculiar defects makes possible the tuning of carrier concentration by using thermal annealing steps. During such processes the copper chains vacancies are progressively healed while the films stoichiometry and morphology remain unaltered. By using annealing temperatures within 650–900 °C range the carrier concentration was diminished from 10^{21} to 10^{17} cm^{-3} while the electrical conductivity and drift mobility were varied few orders of magnitude. More important, the manipulation of Fermi level and the improvement of optical transmittance from 38% to values above 60% were reported [17].

Several works reporting previously the fabrication of $CuCrO_2$/ZnO p–n junctions were using only PLD [20–23] as the fabrication method. As already mentioned, this fabrication method is not suitable for industrial applications due to its lack of efficient scalability. The present paper suggests a new versatile and technological readable approach combining MOCVD, ALD, lithography followed by an annealing step in order to create a better interface and to produce a more favourable band-alignment. This process, schematically illustrated in Fig. 1 provides a promising, simple, straightforward and cheap fabrication method, easily scalable into large area for industrial purposes (Fig. 1). The junction was annealed at 650 °C and at 700 °C. The electrical and optical behaviour of the junction is therefore compared for these annealing temperatures, together with a deeper investigation of the changes in the physical properties of materials.

2 Materials and methods

$Cu_{0.66}Cr_{1.33}O_2$ films were deposited on a sapphire substrate using Direct Liquid Injection—Metal Organic Chemical Vapour Deposition system DLI-MOCVD, (MC200 from Annealsys). The used copper and chromium precursors are bis[2,2,6,6-tetramethyl-3,5-heptanedionato] copper(II) and tris[2,2,6,6- tetramethyl-3,5-heptanedionato]chromium(III), respectively ($Cu(thd)_2$ and $Cr(thd)_3$, Strem Chemicals). Cyclohexane solutions with a total precursor concentration of $[Cu(thd)_2] = [Cr(thd)_3] = 2{,}5$ mM were used. The total canister solution used was 1 L of Cyclohexane with

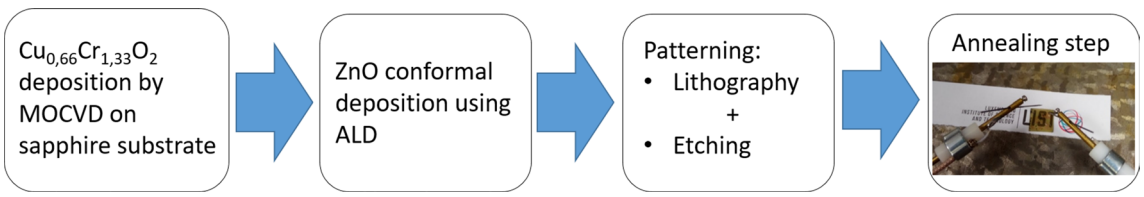

Fig. 1 Schematic production chain of p–n junction, representing the five steps to reach a rectifying diode

1.075 g Cu(thd) + 1.5 g Cr(thd). The deposition parameters used were: substrate temperature of 450 °C, oxygen flow of 2000 sccm, nitrogen flow of 850 sccm and the total process pressure was 12 mbar. The process used followed the previous optimization detailed by Lunca Popa et al. [18]. ALD deposition of ZnO was next deposited, on glass substrate for the thin film study and on top of the delafossite film, deposited on sapphire to make a p–n junction, following the process described by Roge et al. [24] at 150 °C. Argon was used as purge and carrier gas, for 500 cycles and with a pulse sequence: Diethylzinc (DEZ, $Zn(C_2H_5)_2$) pulse 150 ms—purge 10 s—H_2O pulse 200 ms—purge 10 s.

The annealing processes were performed at 650 and 700 °C in a Rapid Thermal Annealing reactor (from Annealsys) at a pressure of 0.3 mbar under a nitrogen flow of 25 sccm. The temperature step for heating and cooling was 5 °C s^{-1}. The annealing time considered includes only the plateau regime. Prior to deposition, the substrates were cleaned in acetone and ethanol and dried with nitrogen jet.

Kevin Probe Force Microscopy (KPFM) measurements have been performed on a Bruker Innova using the surface potential mode as amplitude modulation. Surface topography is obtained in the first pass and the surface potential is measured on the second pass. Freshly cleaved highly-oriented pyrolitic graphite (HOPG) is used as reference. The measurements are performed under dry N_2 atmosphere to avoid contaminations on the surface.

The films morphology and thickness were inspected using scanning electron microscopy (SEM) using 10 kV of acceleration voltage. The structure of the grown films was studied by X-Ray Diffraction (XRD) using a Bruker D8 Discover system using monochromatic Cu Kα radiation (l = 1.54 Å) at 40 kV and 40 mA. The scans were performed in the grazing incidence (GI) geometry using a scanning step of 0.02°.

The patterning processes were performed by means of lithography. First a layer of HDMSwas spin-coated at 4000 rpm for 30 s, with an with an acceleration of 1000 rpm s^{-2}. It was then baked for 60 s at 115 °C. Then a layer of Shipley S1813 was spin-coated for 60 s at 4000 rpm, with an acceleration of 1000 rpm s^{-2}, leading to a 1.2 µm layer. After it was baked for 60 s at 115 °C. The exposition was made with a MLA 150 from Heidelberg Instruments using a dose of 90 mJ cm^{-2}. After exposure, the samples were developed using MF319 for 40 s and rinsed for 30 s. The samples were dipped in $FeCl_2$ at 0.1% for 15 s to etch the ZnO, with an expected etched thickness of 100 nm.

The electrical characterization of the junction used a configuration with two points at different voltage, with a voltage sweep and measuring the current between the two tungsten tips. The sweep tip was kept on the $Cu_{0.66}Cr_{1.33}O_2$ contacted with silver paste and constant 0 V was kept on ZnO pads. The carrier concentration of ZnO was measured using Hall-effect measurements with a magnet of 0.562 T using Van der Pauw configuration. In the case of the delafossite, these values were extracted from the measurement of the Seebeck coefficient, using small polaron model.

3 Results and discussion

The fabrication of transparent diodes based on ZnO and $Cu_{0.66}Cr_{1.33}O_2$, started with the deposition of $Cu_{0.66}Cr_{1.33}O_2$ on sapphire substrate at 450 °C followed by ZnO deposited at 150 °C. Sapphire was chosen as a substrate due to its high temperature stability being adequate for wide temperature range studies.

The thickness of films as measured by cross-sectional SEM, was found to be 250 nm for $Cu_{0.66}Cr_{1.33}O_2$. The zinc oxide layer was measured by elipsometry on a silicon sample located next to the sapphire sample during the ALD deposition, resulting in 65 nm as shown in Fig. 2. As deposited ZnO presents a carrier concentration of 5×10^{19} cm^{-3}, with an associated conductivity of 120 S cm^{-1}. While delafossite films present a carrier concentration of 2×10^{21} cm^{-3}, with an associated conductivity of 20 S cm^{-1}. Films present high electrical conductivities, that leads to an ohmic behaviour of the junction, showing a non-rectifying response as later described. The annealing effects on the delafossite have been reported in our previous work [17]. A decrease of the carrier concentration for temperatures above 650 °C was observed. With 700 °C annealing for 15 min, a decrease of the carrier concentration to 10^{19} cm^{-3} is obtained, for the delafossite films. On the other hand annealing ZnO at 650 °C for 15 min has also a significant impact reducing the carrier concentration to values below 10^{18} cm^{-3}.

Figure 3 depicts a projection of the band-diagram of the films, using the combination of data from Refs. [25–27] and the results of measurements of the work function for the different annealing temperatures. The reported electron affinities for ZnO and $CuCrO_2$ suggests a type-II band alignment in between our delafossite and ZnO.

KPFM measurements were performed on samples, corresponding to the different annealing temperatures presented herein, as-deposited, 650 °C and 700 °C. The measurements were performed alternatively between HOPG reference and the sample, in order to compensate for drifts due to contaminations of the tip. In order to compensate the vacuum levels misalignment KPFM insert a voltage VDC = (Φtip − Φsample)/e where, Φtip (Pt–Ir) = 5.5 eV. The work function ΔΦ is measured according to:

$$E_F - E_V = (\chi + Eg) - \Delta\Phi \quad (1)$$

where χ is the electronic affinity (2.1 eV for copper chromium delafossite [27], 4.3 eV for zinc oxide [25, 26]), Eg is the band gap (3.2 eV for copper chromium delafossite [27], 3.4 eV for zinc oxide [25, 26]). We assume the these values

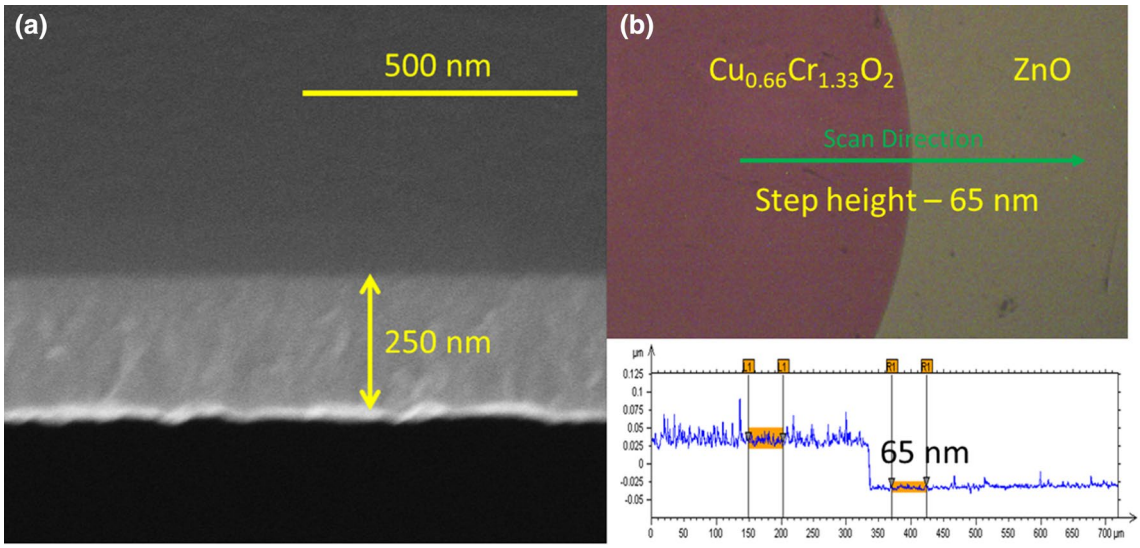

Fig. 2 **a** Cross-sectional SEM showing the delafossite film thickness, with approximate 250 nm, deposited on sapphire substrate. **b** Optical image of the device after etching of ZnO, with the presented scan using for profilometry and the resulting step, with 65 nm

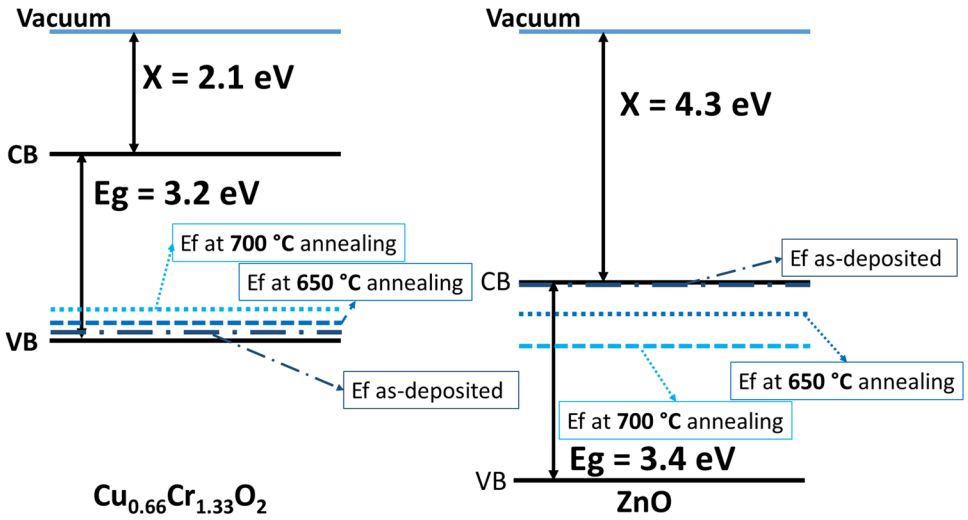

Fig. 3 Projection of the band-diagram using the combination of data from Refs. [25–27], where was extracted the electronic affinity, with the measurements of the work function for the different annealing temperatures (as-deposited, after 650 °C annealing and after 700 °C annealing) performed by KPFM, presenting a type-II band alignment in between our delafossite and ZnO

(X,E_g) are insignificantly affected by annealing [19, 28] and thus holds for both cases of annealed and as-deposited.

In Fig. 3 is shown the change of the Fermi level as extracted from KPFM measurements upon annealing. In both films, the Fermi level shifts towards midgap position after annealing. This might be correlated with the decrease in carrier concentration, as previously described. This prooves the controllable tuning of the Fermi level with the annealing steps.

Furthermore the optical transmittance dependence on the annealing conditions is represented in Fig. 4, for individual films. An increase in optical transmittance from 38 up to 50% is measured for the case of $Cu_{0.66}Cr_{1.33}O_2$ whilst no major difference was observed in the case of ZnO after the annealing step. $Cu_{0.66}Cr_{1.33}O_2$ and ZnO transmittance measurements were performed on sapphire and glass substrates, respectively. The optical properties of the junction were investigated for the junction, deposited in sapphire, annealed at 700 °C in between 400 and 800 nm resulting in an optical transmittance of 48%, which could be further increased using another substrate (moving from sapphire to glass).

Fig. 5 shows the grazing incidence X-Ray diffractograms in the interest range of films (a) delafossite deposited on sapphire substrate, (b) ZnO deposited on glass substrate, (c) final junction, with stacked ZnO and delafossite on a sapphire substrate, after a thermal annealing step at 700 °C. The diffraction peak of delafossite can be clearly attributed to the (012) diffraction plan, ($2\theta = 36.4°$), with a seemingly preferential orientation, as previously discussed

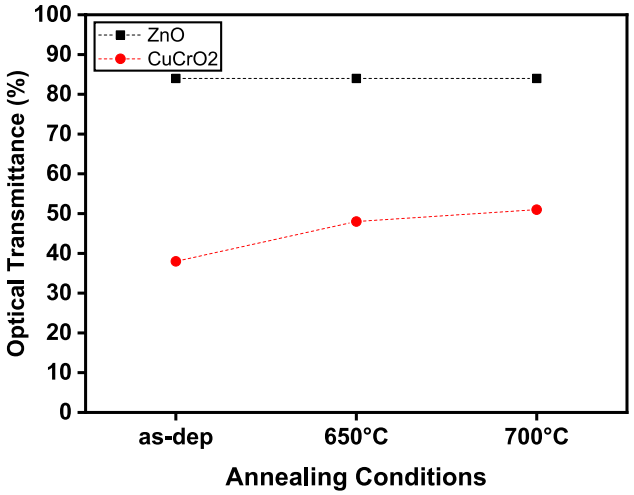

Fig. 4 Optical transmittance of ZnO thin films deposited on glass and delafossite thin films deposited on sapphire respectively, with the variation in the annealing temperature, error bars are comprised in the thickness of data points, dotted lines are represented for guiding eyes of readers

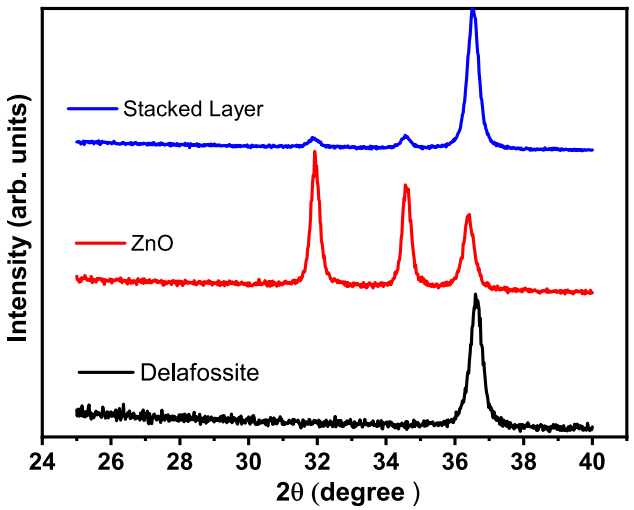

Fig. 5 GIXRD patterns with incidence angle of 0.35°; a delafossite thin film, b ZnO thin film and c stacked layer of delafossite-ZnO after a thermal annealing step at 700 °C

[19]. ZnO diffraction patterns exhibited three distinct peaks, that might be associated to (100), (002) and (101) planes according to pdf card 04-006-2557, ($2\theta = 31.8°$, 34.4° and 36.3°, respectively). Regarding the diode sample, the representative peaks of delafossite and ZnO thin films are observed, with a major response to the delafossite (012) plane. There is a seemingly preferential orientation of the ZnO deposited on delafossite as compared with ZnO thin films deposited on glass, leading to a relative bigger contribution of the (002) peak as compared with the (100). The (101) peak might be hidden within more prominent in the delafossite (012) peak.

The chemical composition of the junction as a function of depth was analysed using Secondary-Ion Mass Spectrometry (SIMS), as represented in Fig. 6. Layers are chemically stable with no inter-layer diffusion.

The optical transmittance of the junction was measured in the optical range 400–800 nm after annealing at 700 °C for 15 m, with a resulting transmittance of 50%, for the bilayer deposited on sapphire substrates.

Electrical properties of the junction were then studied, with a focus on the ratio of forward to reverse current, I_{ON}/I_{OFF}, calculated at ± 4 V.

Prior to annealing, no rectifying behaviour is presented by the junction. After the first annealing at 650 °C, a rectifying diode behaviour, with $I_{ON}/I_{OFF} = 7$, was measured. Another thermal treatment at 700 °C was subsequently done improving furthermore the electrical results. Room temperature I–V characteristics of the junction (a) without thermal annealing, (b) with thermal annealing at 650 °C and (c) with thermal annealing at 700 °C are presented in Fig. 7.

The best $I_{ON}/I_{OFF} = 13$ was achieved after the annealing at 700 °C. The increase was mainly due to the reduction of I_{OFF}, which may be attributed to the reduction of interface traps and recombination centres [23]. However, there is a trade-off with the increase in performance due to the better junction quality with the reduced forward current with higher annealing temperature, since the turn-on voltage of the device increases, as we extract hereafter.

The I–V curve of the junction after the thermal treatment at 700 °C, is also presented in Fig. 7, with a fitting as of an ideal diode, following the Eq. (2):

$$I = I_1 \exp(V/\eta Vt) - I_2 \quad (2)$$

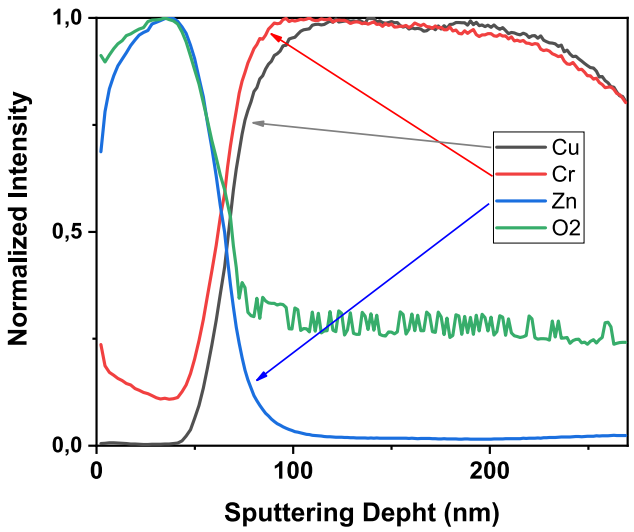

Fig. 6 SIMS analysis of junction annealed at 700 °C, with a layer of zinc oxide on top of our delafossite

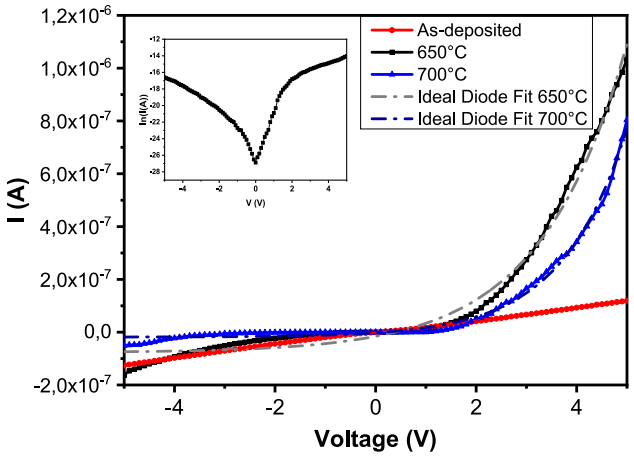

Fig. 7 Current–voltage characteristics of p- $Cu_{0.66}Cr_{1.33}O_2$/n-ZnO diode with, (a) no thermal treatment, (b) annealed at 650 °C, (c) annealed at 700 °C, comparing with an ideal diode fitting, Eq. (2) for (b and c). Inset semi log current–voltage characteristics of the p–n junction annealed at 700 °C used for extraction of the ideality factor

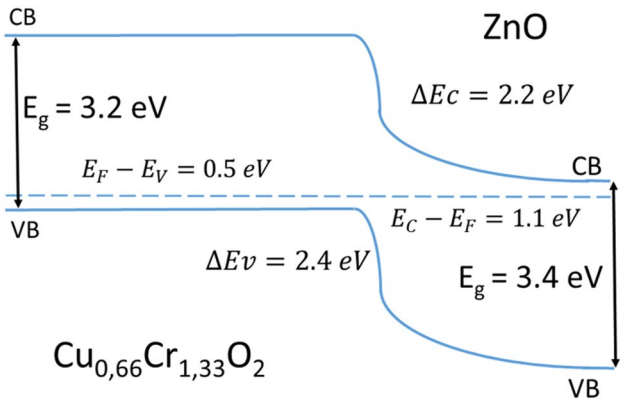

Fig. 8 Band diagram schematic according to data from literature and workfunction calculated from KPFM measurements, ΔEc represents the energy difference of conduction bands for delafossite—zinc oxide, being 2.2 eV, while ΔEv is the analogous for the valence band difference, being 2.4 eV; E_F represents the Fermi level calculated, while it is presented in case of delafossite the difference E_F–E_v representing the difference between the Fermi level and the Valence Band with a value of 0.5 eV for the junction annealed at 700 °C and in case of ZnO the difference E_c–E_F, representing the difference of the Conduction band and the Fermi level with a value of 1.1 eV for 700 °C annealing

where, Vt = kT/e; η is the diode ideality factor; V is the applied voltage and is considered $I_1 \neq I_2$ due to a shunt resistance effect for small voltages, I_2 being the reverse saturation current. The reverse current was extracted, $I_{OFF} = -15$ nA, as the current at − 4 V.

For V > 4 V, the linear response of the curve is governed by the junction series resistance, allowing to extract the series resistance value with a linear I–V fitting between 4 < V < 5. The extracted value is Rs = 2 MΩ, a quite large value. Comparing Eq. (2), with the commonly used diode Eq. (3), it was extracted Rsh = 1.8 kΩ.

$$I = I_0\left(\exp\left(\frac{Vq}{\eta KbT}\right) - 1\right) + \frac{V}{Rsh} \tag{3}$$

The turn-on voltage (V_{on}) of the heterojunction, was estimated to be 1.4 V for the junction annealed at 700 °C and 0.9 V for the 650 °C. The shift of the I–V curves is due to the reduction of recombination centres at the interface [23]. The I_0, presented in Eq. 3, was extracted with the value 16 nA. The ideality factor of the junction was calculated using a linear fit in the semi-log current vs voltage characteristic of the junction in between 0.2 < V < 0.6, resulting in η = 6.3 (Fig. 7 inset). These high ideality factor values are commonly reported in the case of wide gap heterojunctions and values even higher were reported [2, 21].

According to Shah et al. [29], the ideality factor is the sum of the several ideality factors present in the many local rectifying junctions of the device and thus values > 2 are expected. Zekry et al. [30, 31], claim that this value can also be justified by the recombination of carriers at the interface of the heterojunction, as well as the effect provided by the metal-semiconductor contacts. This might be non-ohmic and have a relatively high resistance that can impact the extracted ideality factor. The films roughness and the different crystalline orientations introducing mismatches, defects and inhomogeneities at the interface can also result in η > 2 [32].

A type-II band diagram of a p–n junction is exhibited in Fig. 8. The workfunction of both sides of the junction after annealing at 700 °C were considered. One should notice that the diagram represents a formation of an ideal junction, neglecting defects at the interface. An increase of the ZnO workfunction and a decrease in the case of $Cu_{0.66}Cr_{1.33}O_2$ compared with the values of the films as-deposited, are reported.

|qΔEc| = 2.2 V, what in a perfect diode would roughly correspond to the turn-on voltage of the diode. The calculated η = 6.3 ideality factor suggests a high interface defect density or may be attributed to the presence of chromium excess for delafossite thin films inducing midgap impurity levels. Therefore a value smaller than the expected 2.2 V is enough to flatten the bands and allow conduction that justifies the smaller turn-on voltage than the one theoretically expected.

4 Conclusion

A transparent p–n junction was created based on highly conductive p-type Cu–Cr–O and n-type ZnO thin films deposited on a sapphire substrate. The electrical behaviour of the

junction depends on the post-annealing temperature due to the reported tuning of the Fermi level and carrier concentrations tuning during such thermal treatment. A junction with a rectifying behaviour and an optical transmittance of 50% was finally developed. The ideality factor achieved was $\eta \sim 6$, still needs to be improved when compared to the best values reported in literature, of $\eta \sim 2$, for junctions with similar transmittance values. The chemical composition of the junction remains unchanged with high temperature annealing steps up to 700 °C. An increase in optical transmittance can be expected by using a more transparent substrate, such as glass, keeping the process safely below 600 °C. The junction was developed as within a 5-step process including techniques easily scalable for a large area deposition, unlike the best performing junctions in the literature, which make recourse to PLD techniques. A higher rectification factor, I_{ON}/I_{OFF}, should be optimized engineering a lower series resistance and a better interface engineering may lead to even more performant junction and lower ideality factor.

In conclusion, a simple and scalable process for fabricate a p-$Cu_{0.66}Cr_{1.33}O_2$/n-ZnO transparent junction was demonstrate. This might be of interest in electronic applications based on the principle of transparent diodes.

Acknowledgements This project was supported by the Luxembourg National Research Fund (FNR), Luxembourg (DEPTOS—Defect Engineering in p-type oxides semiconductors—project number C12/MS/3959502) and Luxembourg (Project PRIDE—project number 15/10935404/MASSENA). We would like to thank Mr. Patrick Grysan and Ms. Nathalie Valle for their valuable technical support.

References

1. A. Facchetti, T.J. Marks (eds.), *Transparent Electronics: From Synthesis to Applications* (2010). https://doi.org/10.1002/9780470710609
2. M. Grundmann, F. Klüpfel, R. Karsthof, P. Schlupp, F.-L. Schein, D. Splith, C. Yang, S. Bitter, H. von Wenckstern, J. Phys. D Appl. Phys. **49**, 213001 (2016)
3. E. Muchuweni, T.S. Sathiaraj, H. Nyakotyo, Heliyon **3**, e00285 (2017)
4. A.J. Leenheer, J.D. Perkins, M.F.A.M. van Hest, J.J. Berry, R.P. O'Hayre, D.S. Ginley, Phys. Rev. B **77**, 115215 (2008)
5. Y.-T. Chuang, J.-W. Liou, W.-Y. Woon, Nanotechnology **28**, 35603 (2017)
6. H. Kim, in *Pulsed Laser Deposition of Thin Films*, ed. by R. Eason (Wiley, Hoboken, 2006), pp. 239–260
7. J. Laube, D. Nbling, H. Beh, S. Gutsch, D. Hiller, M. Zacharias, Thin Solid Films **603**, 377 (2016)
8. S. Sharma, S. Vyas, C. Periasamy, P. Chakrabarti, Superlattices Microstruct. **75**, 378 (2014)
9. P. Banerjee, W.-J. Lee, K.-R. Bae, S.B. Lee, G.W. Rubloff, J. Appl. Phys. **108**, 43504 (2010)
10. J.-H. Lee, K.-H. Ko, B.-O. Park, J. Cryst. Growth **247**, 119 (2003)
11. S. O'Brien, M.G. Nolan, M. Çopuroglu, J.A. Hamilton, I. Povey, L. Pereira, R. Martins, E. Fortunato, M. Pemble, Thin Solid Films **518**, 4515 (2010)
12. J. Pan, C. Zhao, X. Wei, C. Chi, W. Zhao, C. Song, Y. Zheng, C. Li, Nanotechnology **29**, 085202 (2018). https://doi.org/10.1088/1361-6528/aaa327
13. K.H.L. Zhang, K. Xi, M.G. Blamire, R.G. Egdell, J. Phys. Condens. Matter **28**, 383002 (2016)
14. H. Kawazoe, M. Yasukawa, H. Hyodo, M. Kurita, H. Yanagi, H. Hosono, Nature **389**, 939 (1997)
15. J. Crêpellière, P. Lunca Popa, N. Bahlawane, R. Leturcq, F. Werner, S. Siebentritt, D. Lenoble, J. Mater. Chem. 31, 412–417 (2016)
16. H. Sun, M.A.P. Yazdi, F. Sanchette, A. Billard, J. Phys. D Appl. Phys. **49**, 185105 (2016)
17. P. Lunca-Popa, J. Afonso, P. Grysan, J. Crêpellière, R. Leturcq, D. Lenoble, Sci. Rep. **8**, 7216 (2018)
18. P. Lunca Popa, J. Crêpellière, R. Leturcq, D. Lenoble, Thin Solid Films **612**, 194 (2016)
19. P. Lunca Popa, J. Crêpellière, P. Nukala, R. Leturcq, D. Lenoble, Appl. Mater. Today **9**, 184 (2017)
20. T.-W. Chiu, K. Tonooka, N. Kikuchi, Thin Solid Films **516**, 5941 (2008)
21. R.S. Ajimsha, K.A. Vanaja, M.K. Jayaraj, P. Misra, V.K. Dixit, L.M. Kukreja, Thin Solid Films **515**, 7352 (2007)
22. H. Yanagi, K. Ueda, H. Ohta, M. Orita, M. Hirano, H. Hosono, Solid State Commun. **121**, 15 (2001)
23. A.N. Banerjee, K.K. Chattopadhyay, Cent. Eur. J. Phys. **6**, 57 (2008)
24. V. Rogé, N. Bahlawane, G. Lamblin, I. Fechete, F. Garin, A. Dinia, D. Lenoble, J. Mater. Chem. A **3**, 11453 (2015)
25. Y. Zhang, G. Yousong, Y. Huang, X. Yan, Q. Liao, *Controllable Synthesis, Structure and Property Modulation and Device Application of One-Dimensional Nanomaterials* (World Scientific, Singapore, 2011)
26. T. Tharsika, A.S.M.A. Haseeb, S.A. Akbar, M.F. Mohd, Sabri, W.Y. Hoong, Sensors (Switzerland) **14**, 14586 (2014)
27. J. Wang, Y. Lee, J.W.P. Hsu, J. Mater. Chem. C **4**, 3607 (2016)
28. J. Husna, M.M. Aliyu, M.A. Islam, P. Chelvanathan, Energy Proc. **25**, 55 (2012)
29. J.M. Shah, Y.L. Li, T. Gessmann, E.F. Schubert, J. Appl. Phys. **94**, 2627 (2003)
30. A. Zekry, M. Abdel-Naby, H.F. Ragaie, F.E. El Akkad, IEEE Trans. Electron Devices **40**, 259 (1993)
31. K. Kirah, A. Zekry, H.F. Ragaie, W.F. Fikry, J. Electrochem. Soc. **145**, 332 (1998)
32. F.L. Schein, H. Von Wenckstern, M. Grundmann, Appl. Phys. Lett. **102**, 092109 (2013)